Spin-Correlated Optical Properties of Ferromagnetic Nanostructures

Kelly M. Walsh

A dissertation

submitted in partial fulfillment of the requirements

for the degree of

Doctor of Philosophy

University of Washington

2024

Reading Committee:

Daniel R. Gamelin, Chair

Brandi M. Cossairt

Douglas A. Reed

Program Authorized to Offer Degree:

Chemistry

University of Washington

Abstract

Spin-Correlated Optical Properties of Ferromagnetic Nanostructures

Kelly M. Walsh

Chair of the Supervisory Committee:

Daniel R. Gamelin

Department of Chemistry

The advancement of next-generation spin-based electronics will be aided by the development of materials whose optical responses are defined by spontaneous ferromagnetic ordering. Here, this dissertation leverages the chemical tunability of nanostructured materials to rationally design ferromagnets with spin-correlated optical responses, addressing the fundamental materials chemistry challenge that lies at the heart of achieving paradigm-shifting opto-spintronic technologies. Chapter 2 investigates the magnetic and magneto-optical properties of $CsEuCl_3$ perovskite nanocrystals and thin films through a combination of photoluminescence and magnetic circular dichroism spectroscopies, elucidating the *f–d* nature of the $CsEuCl_3$ optical properties and uncovering ferromagnetic ordering stemming from the same *f–d* origin. Chapter 3 develops new functionalities in the well-studied – yet recently overlooked – family of ferromagnetic Cr^{2+} 2D perovskites with magnon-assisted spin-flip transitions that provide an

optical probe of magnetic ordering. This chapter expands the chemistry of these materials, focused on the previously unreported compositions PEA_2CrX_4 (PEA^+ = phenethylammonium, X = Cl, Br). The steric bulk of the PEA^+ cation dictates the overall chemical reactivity of these materials, imparting robust ambient stability to these otherwise famously hygroscopic compounds, and directing the formation of lateral $PEA_2Cr(Cl,Br)$ magneto-heterostructures in partial vapor-phase anion-exchange experiments. Chapter 4 transforms the broadband luminescence of the archetypal van der Waals ferromagnets CrX_3 (X = Cl, Br, I) through dopant incorporation of spin-bearing Yb^{3+} narrow-line emitters. The Yb^{3+} magnetization is pinned to that of the CrI_3 host through strong Yb^{3+}–Cr^{3+} magnetic exchange coupling, evidenced *via* the Yb^{3+} circularly polarized luminescence. The Yb^{3+}–Cr^{3+} magnetic exchange coupling arises through halide-mediated superexchange pathways that are highly dependent on the Yb^{3+}-halide covalency. The influence of covalency in Yb^{3+}:CrX_3 is investigated through a host of photoluminescence experiments, identifying anomalously high Yb^{3+}-iodide covalency in Yb^{3+}:CrI_3. In total, this dissertation accomplishes magnetic and magneto-optical tunability of metal-halide nanostructures across a range of compositions and morphologies, employing the chemical and spectroscopic toolboxes to design ferromagnets with spin-correlated optical properties.

To mom and dad, for always nurturing my love of school and learning.

To Thomas, my partner in everything.

Acknowledgements

Earning a PhD, while a deeply personal accomplishment, is not one that is done in isolation. A tremendous number of people have helped me through this journey, both during my graduate studies and through all the times that led me here. I am lucky to have been supported by excellent educators and mentors over the years and am particularly grateful to my parents for enabling and encouraging my academic journey. I can genuinely say I have had so much fun during my PhD learning and growing as a scientist, in large part because of my advisor Daniel, who taught me how to be creative about science. Thank you to my PhD committee and the broader UW Chemistry and scientific community for always cheering for me. My research group has been invaluable not only in the lab but also for being some of my best friends. I love you all.

I have been profoundly lucky to get to share my life with my husband Thomas. I cannot express how much support I have had from him, how much we have gotten to enjoy Seattle, and how much he has encouraged me to be the best version of myself. Thank you, Thomas, for pushing me to pursue my dreams, and thank you for letting me be part of yours. You are truly my very best friend and the best life partner I could ask for. This accomplishment is ours to share. I love you dearly.

TABLE OF CONTENTS

Chapter 1. Introduction

Some of the most promising next-generation spin-based electronics (spintronics) schemes are based on light-driven magnetic switching,[1, 2] yet many state-of-the-art spintronics either have no optical component,[3, 4] or rely on proximity effects between a spin-functional layer and a separate, optically functional layer.[5-8] It therefore remains a fundamental materials challenge to design systems with the necessary connection between magnetism and optical responsivity. Most magnetic materials are found as solid-state extended lattices,[9-11] but control of their opto-electronic and magnetic responses requires precise knowledge of, and mastery over, the chemistry that dictates the lattice covalency, bond angles, and atomistic spatial arrangements.[12-16] The worlds of solid-state physics and chemistry may at first seem incongruent – however, the dominant surface-to-volume ratio of the nanoscale enables precise chemical transformations of extended lattices not achievable in the bulk. Nanostructured materials with reduced dimensionality, therefore, serve as the perfect platform to achieve chemical tunability of opto-electronic and magnetic functionalities.

Over the past several decades there has been ample development of metal-halide perovskites at reduced dimensionalities, including as colloidal nanocrystals[17-19] and two-dimensional (2D) structural analogs.[20-22] Separately, the discovery of 2D magnetism in isolated monolayers of CrI_3[23] and $Cr_2Ge_2Te_6$[24] has led to pronounced research attention on magnetic van der Waals materials. Accordingly, these platforms serve as ideal candidates for developing ferromagnetic nanostructures with spin-correlated optical functionalities. While there are numerous examples of materials in these categories exhibiting magneto-optical coupling,[1, 25-28] it is foundationally different for optical responsivities to be defined by – and pinned to – the spontaneous lattice long-range magnetic order. In the former case, an external magnetic field is required to elicit or initialize the desired magneto-optical interactions, yet in the latter it is the internal molecular field that induces the magneto-optical interactions. This dissertation addresses this gap by using chemical methods to design ferromagnetic nanostructures whose optical responses are dictated by the lattice spontaneous magnetization. Chapter 1 provides a brief primer on magnetic ordering, followed by an overview of the chemistry and spin-correlated optical properties of the three metal-halide ferromagnets discussed in Chapters 2-4.

1.1 Magnetic ordering & magnetic superexchange

Nonzero spin angular momentum is a key requisite to magnetism. Many magnetic systems are composed of metal centers with unpaired electrons, with net magnetic properties dictated by the interaction between electrons across metal centers. Non-interacting metal centers experience paramagnetism, where all spins orient independently from one another. Interactions between metal centers can give rise to ordered magnetism, where all spins orient in a cooperative manner, either parallel or antiparallel to one another in ferromagnetic and antiferromagnetic ordering, respectively. These magnetic exchange interactions occur when there is a nonzero probability of an electron on one metal center residing on the adjacent metal center. Direct magnetic exchange

between metal centers arises from strong interactions *via* direct orbital overlap (such as through metal-metal bonding). Magnetic superexchange occurs in systems with weakly interacting metal centers, where orbital overlap between metal centers is facilitated by a non-magnetic bridging ion. There are other magnetic exchange mechanisms such as Ruderman-Kittel-Kasuya-Yosida (RKKY) exchange,[29-31] but for the ferromagnetic metal-halide systems discussed in this dissertation, superexchange interactions dictate the ferromagnetism.

While superexchange was initially understood by studying molecular systems,[9, 14, 32] the same basic principles apply to metal-metal interactions in extended lattices. The strength of the magnetic exchange is described by the Heisenberg-Dirac-van Vleck spin Hamiltonian[33-35] in equation 1

$$H_{exchange} = -2\sum_{i,j} J_{ij} S_i S_j \quad (1)$$

where J_{ij} is the magnetic exchange constant and S_i, S_j are the spins of metal ions i and j, respectively. The exchange integral describing the magnitude of J is given in equation 2[14, 32]

$$J = -K_{ab} + \frac{(E_A - E_S)^2}{2U_0} \quad (2)$$

where K_{ab} describes the potential exchange component and the second term describes the kinetic exchange component. Here, E_A and E_S are the energies of the antisymmetric and symmetric combinations of the interacting orbitals and U_0 is composed of the one- and two-center electron exchange energies. When $J > 0$ ferromagnetic alignment is preferred while when $J < 0$ antiferromagnetic alignment is preferred. The experimentally observed J value is an average of all combinations of orbital interactions between metal centers.

Ferromagnets are characterized by spontaneous magnetization that occurs below a critical temperature.[36] Below the critical temperature, called the Curie temperature T_C, all spins are aligned and magnetic ordering can exist across macroscopic length scales. Elevated temperatures introduce thermal spin fluctuations that misalign the spins until a ferromagnetic-to-paramagnetic phase transition occurs above T_C. The value of T_C is determined by J according to the molecular field treatment given by equation 3[37]

$$T_C = \frac{2zJS(S+1)}{3k_B} \quad (3)$$

where z is the number of nearest-neighbors, J is the magnetic exchange constant, S is the spin angular momentum, and k_B is the Boltzmann constant. From equations 2 and 3 it is clear that the degree of covalency between the metal center and bridging ion is the key in dictating the magnetic superexchange constant and consequently the magnetic ordering temperature. These are the foundational phenomena that dictate the magnetism of the metal-halide ferromagnets of Chapters 2-4.

1.2 Ferromagnetism in the three-dimensional perovskite $CsEuCl_3$

Perovskite materials are characterized by an ABX_3 stoichiometry composed of corner-sharing $[BX_6]^{y-}$ octahedra, with the A-site cation sitting in the void formed by the octahedral connections.[38] Over the past several decades, extensive research attention has been given to the semiconducting lead-halide perovskite compositions (A = monovalent cation, B = Pb, X = Cl, Br, I) owing to their high photoluminescence quantum yields,[39-41] strong absorption cross-sections,[42,43] and compositionally tunable band gaps.[44, 45] Following the report of the solution-phase synthesis of colloidal $CsPbX_3$ nanocrystals,[18] the broader family of metal-halide perovskite nanocrystals has experienced an explosion of research development, particularly directed toward the chemistry and photophysics of these materials.[17, 19, 46] Incorporation of paramagnetic dopants has been used to bestow magneto-optical functionality to otherwise diamagnetic perovskite compositions.[28, 47] In Mn^{2+}:$CsPbCl_3$, the paramagnetic Mn^{2+} dopants couple to the $CsPbCl_3$ exciton yielding a spin-

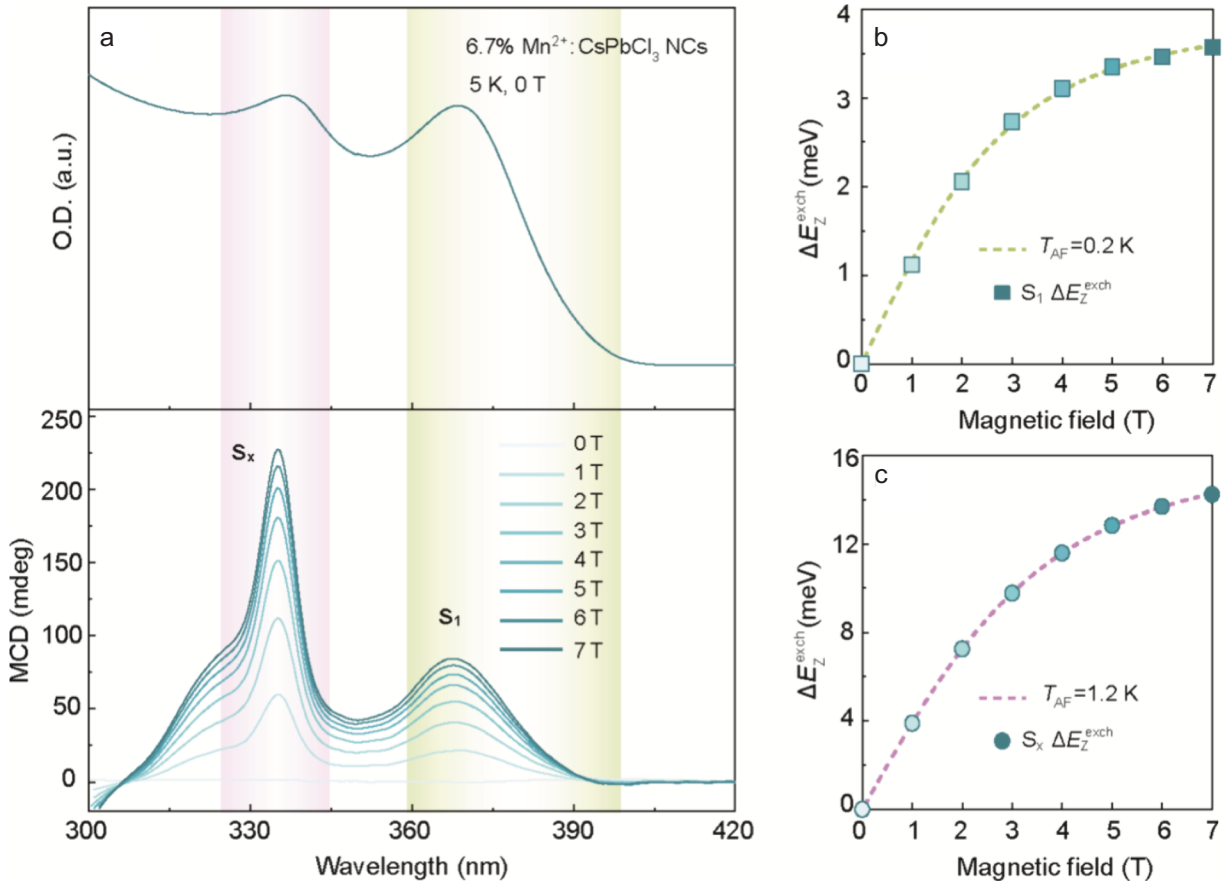

Figure 1.1. (a) Absorption (top) and magnetic circular dichroism (bottom) spectra of Mn^{2+}:$CsPbCl_3$ nanocrystals collected as a function of applied external magnetic field. (b,c) Extracted exchange-induced Zeeman splitting energies of the $CsPbCl_3$ S_2 and S_x excitons. The magnetization behavior is dictated by the Mn^{2+} magnetization described by a Brillouin function (dashed) for an ideal Curie paramagnet. Reproduced with permission from Yeh, I.-H.; Ghobadifard, M.; Feng, L.; Galievsky, V.; Radovanovic, P. V. *Nano Lett.* **2024**, *24*, 10554-10561. Copyright 2024 American Chemical Society.

induced Zeeman splitting, evidenced by magnetic circular dichroism experiments (Figure 1.1).[28] While Mn^{2+}:$CsPbCl_3$ holds promise as a *dilute* magnetic semiconductor, the development of *magnetically concentrated* perovskites exhibiting long-range magnetic order is still lacking. Although there are several reports of ferromagnetic ordering in these magnetically dilute perovskite lattices,[48-51] their fleetingly small magnetization indicates the existence of weak magnetic domains with disputable long-range character.[52]

Several perovskite compositions employ divalent, open-shell transition metal B-sites, yet all studied to date are antiferromagnetic[53-55] – including $KCrF_3$[56, 57] whose 2D chloride and bromide analogs exhibit ferromagnetic ordering (*vide infra)*. Therefore, in targeting ferromagnetic ABX_3 perovskites, the search for a suitable magnetic B-site cation must expand outside the first-row transition metals. Europium is one of the few lanthanides that is stable in the divalent oxidation state owing to the stability of its half-filled $4f^7$ valence shell, making it readily amenable to the perovskite structure. Additionally, given its high spin value ($S_{Eu} = 7/2$), Eu^{2+} is an intriguing candidate for exploring magnetic ABX_3 perovskites. Despite reports of the $CsEuCl_3$ perovskite structure[58, 59] and colloidal nanocrystal synthesis,[60] up until the work described in Chapter 2 there

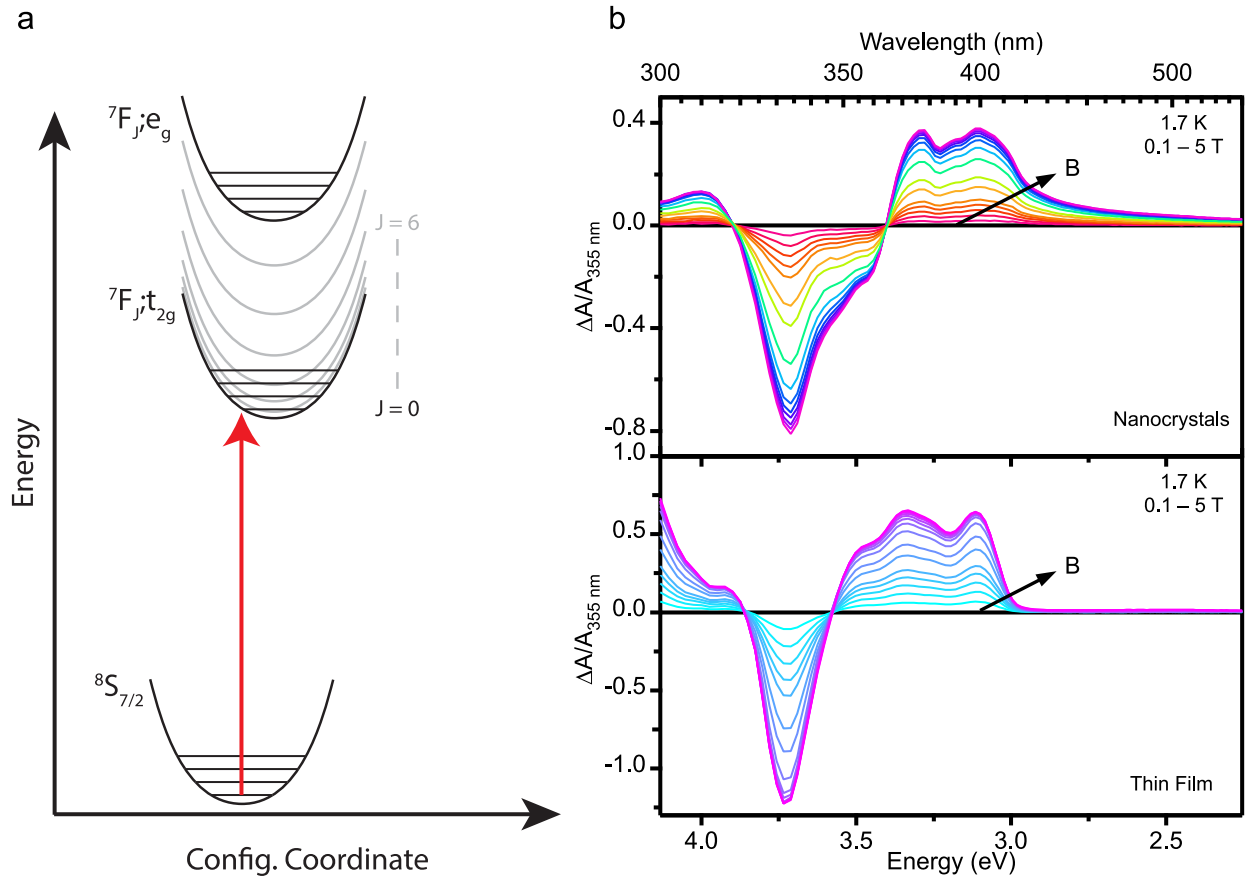

Figure 1.2. (a) Single configurational coordinate diagram of Eu^{2+} $4f^7 \rightarrow 5d^1$ transition. (b) $CsEuCl_3$ MCD spectra of the same transition described in (a). The MCD fine structure arises from the J = 0 – 6 transitions of the ^7F_J excited state. Reproduced with permission from Walsh, K. M.; Pressler, K.; Crane, M. J.; Gamelin, D. R. *ACS Nano* **2022**, *16*, 2569-2576. Copyright 2022 American Chemical Society.

exist no studies on its magnetic or magneto-optical behavior.

Previous literature assigned the optical features of $CsEuCl_3$ to band-like excitonic transitions.[60] The work described in Chapter 2 instead reveals that the $CsEuCl_3$ optical features originate from localized Eu^{2+}-centered $4f^7 \rightarrow 5d^1$ transitions (Figure 1.2a) through a combination of variable-temperature photoluminescence and magnetic circular dichroism (MCD) experiments.[61] The invariable photoluminescence energy as a function of sample morphology and temperature indicates that the transition is highly localized. The photoluminescence lifetime at 15 K was measured to be 233 ns, comparable to that of Eu^{2+} doped into alkali halides.[62] The photoluminescence lifetime shortens to 12 ns at 298 K which indicates thermally activated energy migration and subsequent nonradiative recombination, consistent with the low room-temperature photoluminescence quantum yield. These observations – along with the corresponding temperature dependence of the photoluminescence intensity – characterize the localized nature of the $CsEuCl_3$ photoluminescence. MCD spectroscopy (Figure 1.2b) reveals that the absorption transitions arise from the same $4f^7 \rightarrow 5d^1$ electronic origin.

Notably, Chapter 2 additionally uncovers ferromagnetic ordering in $CsEuCl_3$ nanocrystals and thin films through MCD spectroscopy. In brief, MCD probes the differential absorption between left and right circularly polarized light. Upon application of an external magnetic field, degenerate energy levels are split into their spin sublevels due to the Zeeman effect, with the extent of splitting dictated by the electronic g value and the strength of the external magnetic field.[63] Since left and right circularly polarized light have different optical selection rules ($\Delta m_J = \pm 1$), MCD spectroscopy can be used to definitively assign the origin of electronic transitions. MCD also probes the sample magnetization; the $CsEuCl_3$ MCD data collected as a function of continuous magnetic field sweeps are shown in Figure 1.3a revealing magnetic hystereses that arise from ferromagnetic ordering.

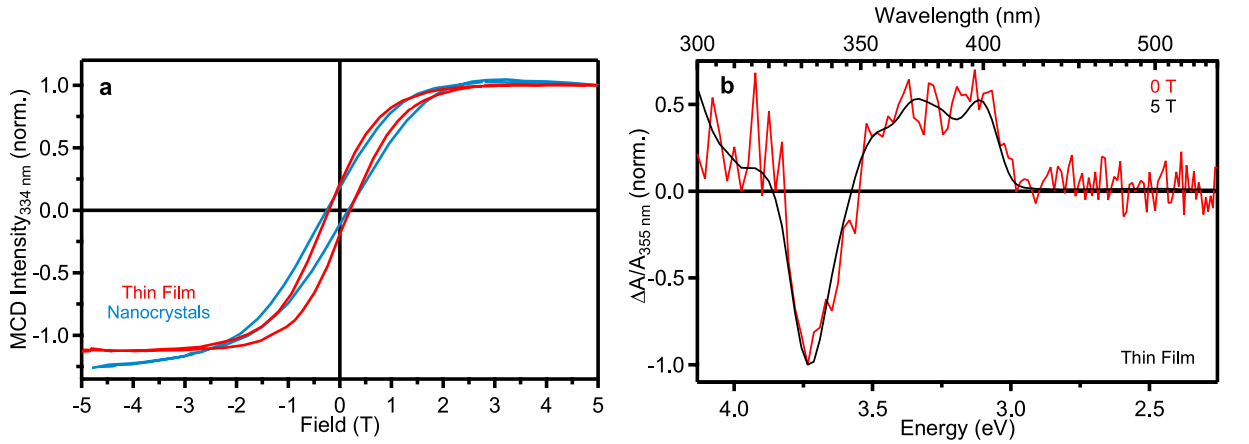

Figure 1.3. (a) MCD intensity of $CsEuCl_3$ nanocrystals and thin films collected during continuous magnetic field sweeps revealing magnetic hystereses and ferromagnetic ordering. (b) 5 T and 0 T (remanence) MCD spectra of a $CsEuCl_3$ thin film. The overlay between the two spectra indicates that the ferromagnetism arises from $CsEuCl_3$ and not a spurious impurity. Reproduced with permission from Walsh, K. M.; Pressler, K.; Crane, M. J.; Gamelin, D. R. *ACS Nano* **2022**, *16*, 2569-2576. Copyright 2022 American Chemical Society.

At zero external magnetic field most materials will show zero MCD signal since the degenerate spin sublevels will have equivalent absorption of left and right circularly polarized light. Instead, remanent $CsEuCl_3$ MCD signal is observed at zero external field, indicating that the spin sublevels are split by the *internal* molecular field arising from the spontaneous lattice ferromagnetic ordering. The similarity between the remanent MCD spectrum and high-field spectrum indicates that the Eu^{2+} *f–d* lowest-lying optical transition is the same pathway that gives rise to ferromagnetic ordering. This is consistent with the related class of europium chalcogenide (EuE, E = O, S, Se, Te) magnetic semiconductors which have optical properties defined by the same Eu^{2+}-centered $4f^7 \rightarrow 5d^1$ transition as $CsEuCl_3$. The magnetism of these materials arises from a combination of indirect exchange (interaction between the localized magnetic moment of one Eu^{2+} and a delocalized 5*d* orbital in the conduction band) and a chalcogen-mediated superexchange pathway between the 4*f* ground state of one Eu^{2+} and the empty 5*d* orbital of the adjacent Eu^{2+}.[11, 64, 65]

The results of Chapter 2 identify $CsEuCl_3$ as the only ferromagnetic ABX_3 perovskite studied to date. Additionally, the connection between the magnetism and optical properties of this material further distinguishes $CsEuCl_3$ among other non-magnetic and magnetically dilute metal-halide perovskites. The observation of ferromagnetism in both $CsEuCl_3$ colloidal nanocrystals and thermally evaporated thin film opens opportunities to implement these materials in a range of applications, leveraging the enhanced nanoscale processability *via* inkjet printing[66, 67] or the scalability of large-area film deposition.[68]

Despite the advantages of these materials, one drawback is their low ferromagnetic ordering temperature ($T_C \approx 3$ K).[61] Given the relatively high ionicity of the metal-halide perovskite lattice and shielded nature of the *f* electrons that participate in magnetic exchange pathways, the Eu^{2+}–Eu^{2+} magnetic exchange coupling is limitingly small. Additionally, the subsequent report of antiferromagnetic ordering in polycrystalline powders of $CsEuCl_3$[69] indicates that the ferromagnetic and antiferromagnetic exchange interactions are in close competition similar to the EuE semiconductors,[11, 64] with a possibly non-negligible magnetic dependence on internal lattice disorder. While the work of Chapter 2 establishes the paradigm for this dissertation, further exploration of optically functional low-dimensional ferromagnetic perovskites is motivated by targeting higher T_C values, as investigated in Chapter 3.

1.3 Magnon-assisted spin-flip transitions in A_2CrX_4 two-dimensional perovskites

Though technically distinct from the three-dimensional ABX_3 perovskite family,[38] two-dimensional A_2BX_4 (A = monovalent cation, B = divalent metal, X = Cl, Br, I) "perovskites" can be related to their 3D analogs by means of severing the axial coordinations of the metal-halide octahedra, yielding quasi-two-dimensional sheets of corner-sharing octahedra propagating along the (0, 0, l) crystallographic plane.[70, 71] The monovalent A-site cation is coulombically bound within the cuboctahedral pockets on either side of the inorganic sheet, meaning each inorganic layer is separated by two layers of the A-site cation. These A-site cations are in turn separated from one another by a van der Waals gap, enabling wide accommodation of inorganic and organic

(typically alkylammonium) A-site identities.[21, 71] In the literature there are many structure types that are referred to as 2D perovskites,[38, 71, 72] yet here, only the Ruddlesden-Popper family described above are discussed. There exist several magnetic 2D perovskite compositions,[73-76] with the ferromagnetic A_2CrX_4 family being most notable.[77-79] While the semiconducting nature of the lead-halide and tin-halide 2D perovskites makes them particularly attractive for optoelectronic applications,[80-85] the spin-correlated optical properties of the Cr^{2+}-based 2D perovskites distinguish them among their non-magnetic analogs for application in next-generation opto-*spintronic* technologies.

The family of ferromagnetic A_2CrX_4 2D perovskites were investigated deeply in the 1970s and 1980s, where namely Peter Day and coworkers established the fundamental physical characteristics of these materials.[77, 86, 87] Both the all-inorganic (A = Cs^+, K^+, Rb^+) and hybrid organic-inorganic (A = alkylammonium) compositions adopt the K_2NiF_4 structure as part of the Ruddlesden-Popper family of layered 2D perovskites.[77] The unequal occupation of the e_g set of *d* orbitals arising from the Cr^{2+} d^4 electron configuration leads to a spontaneous Jahn-Teller elongation along the molecular *z*-axis that stabilizes the d_{z^2} orbital relative to the $d_{x^2-y^2}$ (Figure 1.4).[88, 89] This Jahn-Teller elongation yields a tetragonally distorted pseudo-D_{4h} point symmetry for each $[CrX_6]^{4-}$ octahedron.

Due to the axial zero field splitting experienced by Cr^{2+} from second-order spin-orbit coupling effects, the Jahn-Teller axis lies within the basal plane of the inorganic sheet[78] where the elongation axis of one octahedron is the short axis of the adjacent in an antiferrodistortive pattern (Figure 1.5a). This cooperative Jahn-Teller effect leads to the d_{z^2} orbital on one Cr^{2+} ordering orthogonally to that of the adjacent Cr^{2+} ion. Therefore, in the absence of magnetic exchange, the Cr^{2+} spins would alternate along the Jahn-Teller molecular distortion axes (0, 0, 1). Instead, through a superexchange mechanism mediated by the bridging halide anion, the Cr^{2+} spins

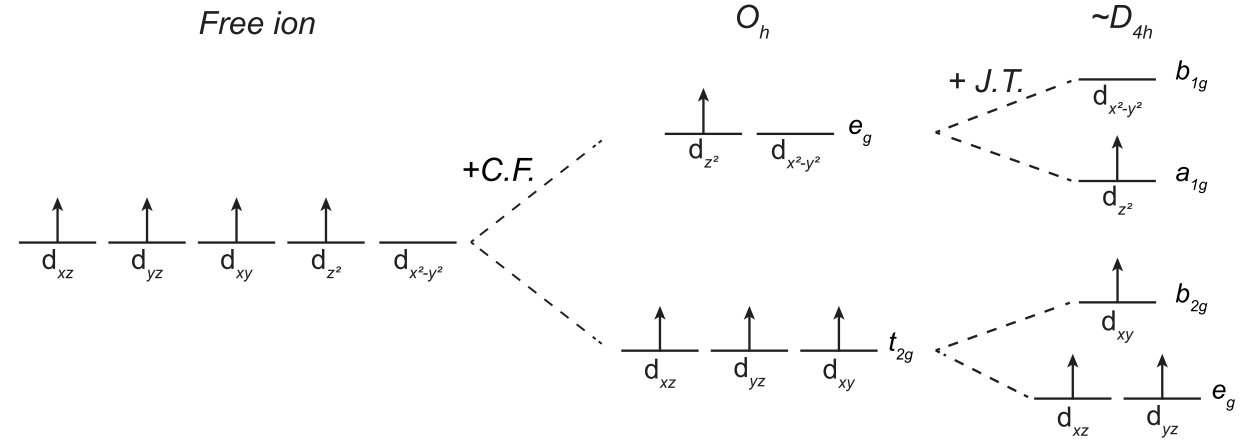

Figure 1.4. Electron configuration diagram describing Cr^{2+} in A_2CrX_4. In the free ion picture, all 5 *d* orbitals are degenerate. With the introduction of an octahedral crystal field, the *d* orbitals are split into their t_{2g} and e_g components. The unequal occupation of the e_g orbital set leads to a spontaneous Jahn-Teller distortion that causes an elongation along the molecular *z*-axis, leading to an approximate D_{4h} symmetry of each $[CrX_6]^{4-}$ octahedron in A_2CrX_4.

ferromagnetically align along the angle bisecting the intersection of the molecular axes, as evidenced by neutron diffraction experiments.[89, 90] This ferromagnetic alignment arises from a kinetic superexchange pathway in which the electron from the filled d_{z^2} orbital on one Cr^{2+} delocalizes into the empty $d_{x^2-y^2}$ orbital† on the adjacent as illustrated in Figure 1.5b,c. Despite the fact that the recent interest in 2D van der Waals ferromagnets has been invigorated by observation of 2D magnetism in isolated monolayers of $Cr_2Ge_2Te_6$[24] and CrI_3[23], A_2CrX_4 has long been understood to be a purely 2D ferromagnet, showing no influence of interlayer spacing on the magnetic ordering temperature.[77, 79]

The distinguishing characteristic of this family of materials is the fact that their ferromagnetism is intimately linked to their optical properties. A_2CrX_4 are transparent insulators with absorption spectra characterized by a near-UV ligand-to-metal charge-transfer transition, a Jahn-Teller-split spin-allowed feature in the near-IR, and two sharp spin-flip transitions in the visible (Figure 1.6a).[87, 91, 92] These spin-flip transitions are strikingly intense given their spin-forbidden nature and exhibit an anomalous temperature dependence, as highlighted in Figure 1.6b which compares the temperature-dependent absorption intensity of K_2CrCl_4[92] to that of the hyperbolic cotangent function describing a typical phonon-coupled vibronic hotband.[93] Also interestingly, the d^4 Tanabe-Sugano diagram[94] (and even more so the D_{4h} ligand field energy diagram[95]) predicts many more spin-flip transitions than the two that are observed. Both observations can be explained by the mechanism in which these spin-flip features gain intensity.

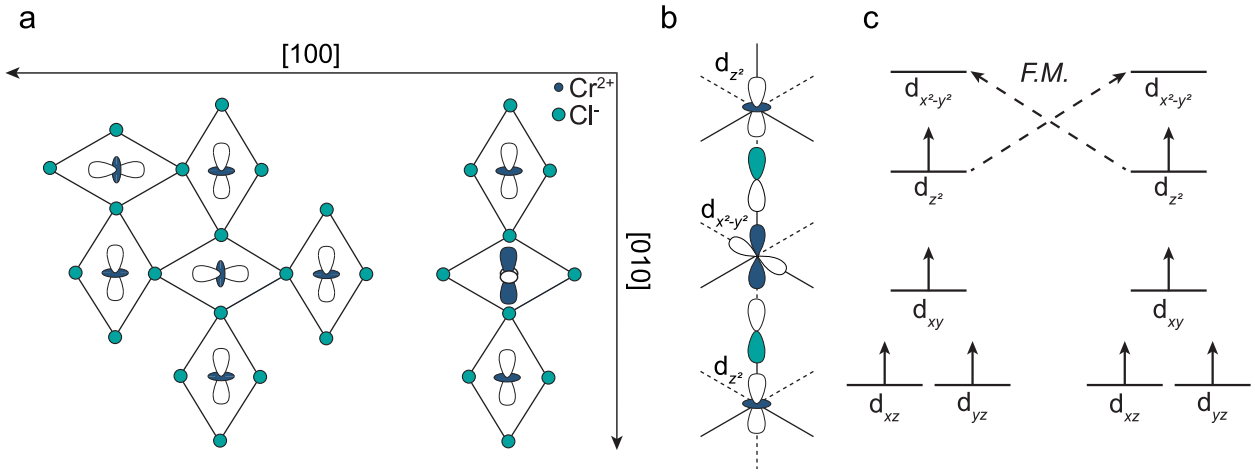

Figure 1.5. (a) Cartoon illustration of the antiferrodistortive ordering of the Jahn-Teller elongation axes within the (0, 0, 1) plane and the consequential orbital ordering pattern. The crystallographic planes are labeled based on the parent K_2NiF_4. (b) Orbital ordering between adjacent Cr^{2+} atoms, mediated by the halide *p* orbitals. (c) Ferromagnetic superexchange pathway arising from the antiferrodistortive orbital ordering motif.

† Here it is worth reminding that the cartesian solution to the d_{z^2} spherical harmonic is more rigorously notated as $d_{2z^2-x^2-y^2}$, which further highlights the orbital overlap that enables the ferromagnetic superexchange interaction.

In A_2CrX_4, spin-flip excitations gain intensity by coupling to lattice spin fluctuations, as is also the case for other magnetic insulators.[96] In a magnetically ordered lattice, thermally induced spin fluctuations propagate through the lattice as quantized spin waves (magnons). These magnetic spin fluctuations result in deviations from the ordered spin state, which in ferromagnets reduces the overall lattice spin projection. At elevated temperatures the Cr^{2+}-centered quintet-to-triplet spin-flip excitations (ΔS = -1) gain allowedness by coupling to the annihilation of a thermally populated magnon, yielding net spin conservation (illustrated in Figure 1.6c,d). On the basis of spin conservation, only "pure" spin-flip transitions with no change in orbital occupancy will result in the dramatic magnon-related temperature dependence observed in these materials. Additionally, only spin-flip excitations involving the relevant magnetic exchange orbitals can couple to lattice magnon modes. Therefore, the two visible features observed in A_2CrX_4 can be attributed to excitations involving a spin flip on the d_{z^2} orbital, namely the $^5B_{1g} \rightarrow {}^3B_{1g}$ transitions

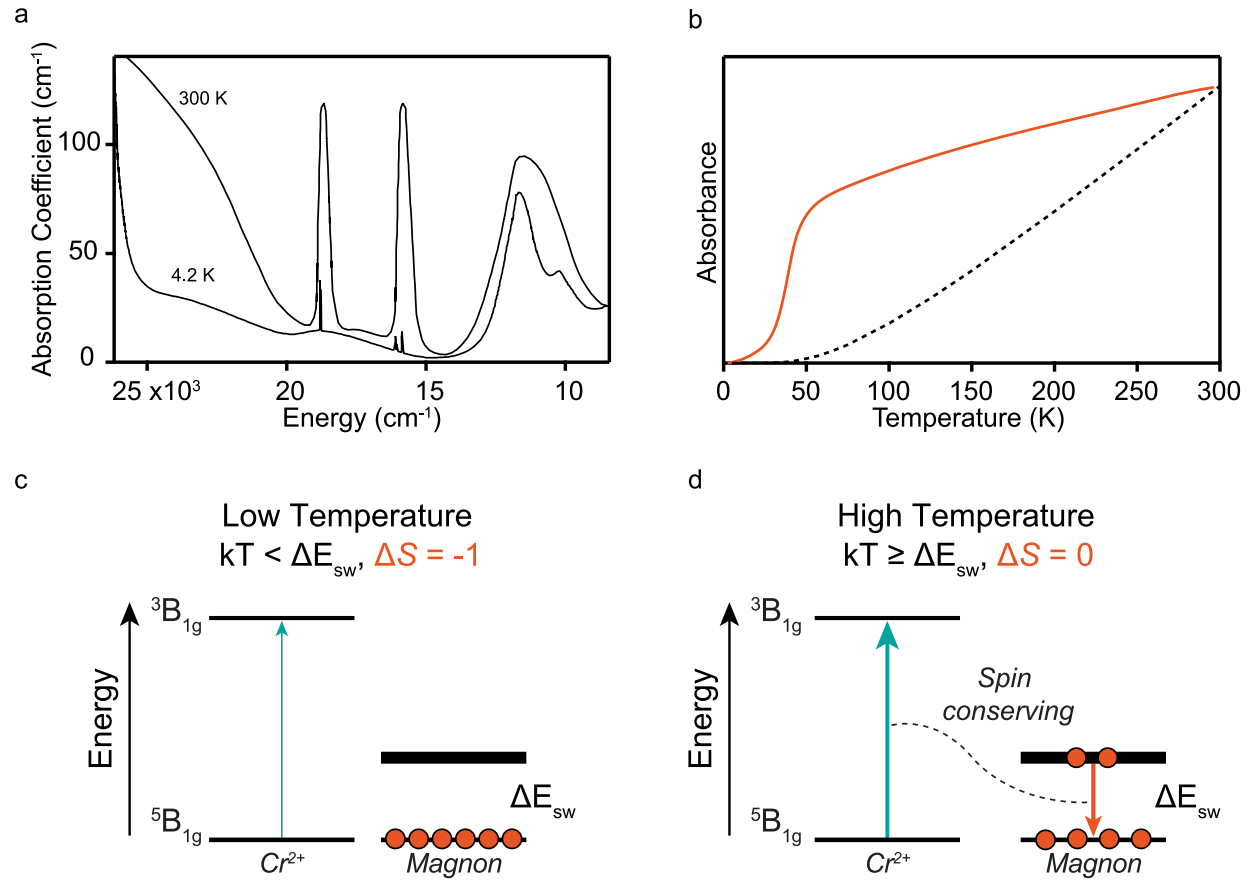

Figure 1.6. (a) Absorption spectra of K_2CrCl_4 collected at 300 K and 4.2 K. (b) Temperature dependence of the integrated absorption intensity of K_2CrCl_4 (orange) compared to the typical temperature dependence of a vibronic hotband (dashed), scaled and offset for sake of comparison. Adapted with permission from Day, P.; Gregson, A. K.; Leech, *Phys. Rev. Lett.* **1973**, *30*, 19. Schema describing the (c) low-temperature "pure" forbidden spin-flip electronic transition and the (d) spin-conserving thermally activated magnon-assisted spin flip transition, where ΔE_{SW} is the spin-wave gap, or the magnon energy.

(using D_{4h} notation) originating from the ^3F and ^3H free ion parentages. Therefore, the temperature-dependent intensities of these spin-flip features map the thermal population of magnons within the lattice, thus providing a purely optical probe of the lattice magnetization.[78] Furthermore, owing to their highly localized nature, these spin-flip transitions are sensitive to short-range magnetic order that persists well above the long-range magnetic ordering temperature.

Despite the unique properties of these materials, there has been little research effort directed toward their further development in the past several decades. This is perhaps attributable to the fact that these materials are famously hygroscopic owing to the facile oxidation of Cr^{2+} to Cr^{3+}.[79, 87, 97] In the lead-halide analogs it was found that using a bulky organic A-site such as phenethylammonium (PEA^+) results in enhanced ambient stability relative to similar compositions with smaller A-sites.[21, 81] In addition to the steric bulk, it is hypothesized that the pi-pi stacking of the PEA^+ aromatic rings is also important for the exclusion of both oxygen and water. The first half of Chapter 3 demonstrates that this utility can be extended to the ferromagnetic A_2CrX_4 composition PEA_2CrCl_4, yielding unmatched ambient stability in these compounds.[98] The second half of Chapter 3 reports unprecedented compositional tunability of this family of materials *via* post-synthetic anion exchange to achieve the previously unreported ferromagnetic composition of PEA_2CrBr_4.[99] Furthermore, it is demonstrated that the PEA^+ cation again plays a pivotal role by prohibiting interlayer anion diffusion, directing the formation of lateral 2D $PEA_2Cr(Cl,Br)_4$ magneto-heterostructures. These magneto-heterostructures have no

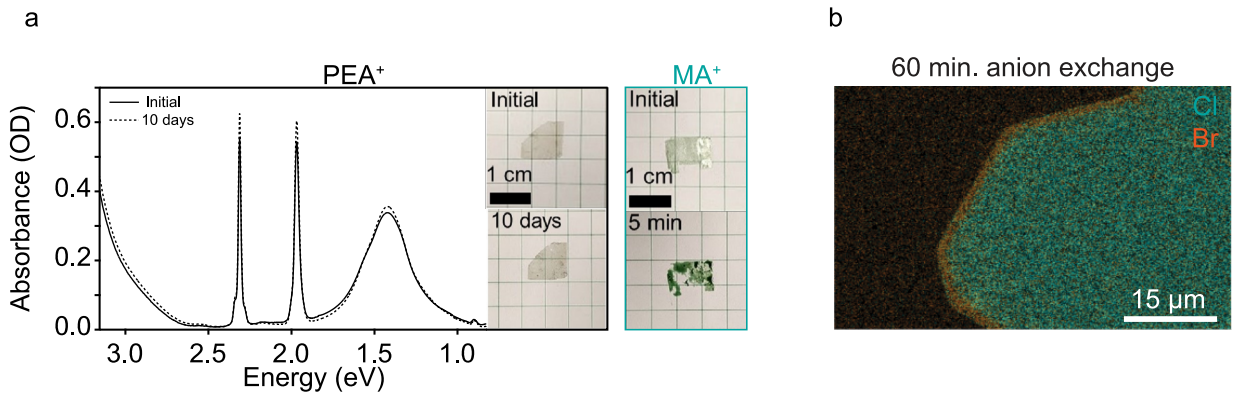

Figure 1.7. (a) Absorption spectrum of as-synthesized PEA_2CrCl_4 (solid) and after 10 days of ambient exposure (dashed). The inset shows images of the same flake taken at corresponding timepoints, demonstrating robust ambient stability with no optical or visual changes. Images to the right are of an analogous composition made using methylammonium (MA^+), demonstrating that the smaller A-site cation prompts nearly instantaneous crystal degradation upon exposure to air. Adapted with permission from Smith, R. T.; Walsh, K. M.; Jiang, Q.; Chu, J.-H..; Gamelin, D. R. *Chem. Mater.* **2024**, *36*, 1571-1578. Copyright 2024 American Chemical Society. (b) SEM-EDS image collected after a 60 min. vapor-phase anion exchange reaction performed on an exfoliated flake of single-crystalline PEA_2CrCl_4 with the chloride signal plotted in teal and the bromide signal plotted in orange. The presence of the lateral heterostructure motif indicates the dominant exchange pathway is 2D, propagating within the layers Adapted with permission from Walsh, K. M.; Smith, R. T.; Gamelin, D. R. *J. Am. Chem. Soc.* **2024**, *146*, *29159-29168.* Copyright 2024 American Chemical Society.

analogy in the bulk and may lead to novel spin effects arising from the competition between the PEA_2CrCl_4 and PEA_2CrBr_4 magnetic domains. Importantly, heterostructure formation is only afforded by the 2D nature of the anion diffusion kinetics, meaning this architecture is inherently incompatible with the 3D diffusion kinetics observed in higher-dimensionality ABX_3 perovskites. Overall, the results of Chapter 3 demonstrate that the 2D perovskite synthetic toolbox – which has been well-developed for analogous metal-halide compositions – can be translated to A_2CrX_4 ferromagnets.

Chapters 2 and 3 leverage the wealth of chemistry that has been developed for nanostructured metal-halide perovskites to achieve optical functionalities that are inherently connected to the ferromagnetic spontaneous magnetization. Chapters 2 and 3 approach this dissertation's goal from opposition directions: Chapter 2 investigates the previously unreported magnetic and magneto-optical properties of $CsEuCl_3$ metal-halide perovskite nanocrystals and thin films while Chapter 3 targets a well-studied 2D perovskite ferromagnet to engender new chemical functionalities. These chapters demonstrate the successful use of chemistry to rationally design optically functional ferromagnets across a range of compositions. Chapter 4 is an extension of this work, achieving magnetic pinning of a Yb^{3+} narrow-line emitter doped into the archetypal van der Waals ferromagnet CrX_3 (X = Cl, Br, I).

1.4 Yb^{3+} dopant sensitization in the van der Waals ferromagnets CrX_3

For decades, the prevailing theory established by Mermin and Wagner was that ordered magnetism could not exist at the 2D limit, since the gapless magnon density of states would elicit disruptive spin fluctuations at any finite temperature.[100] In response, several theories arose stating

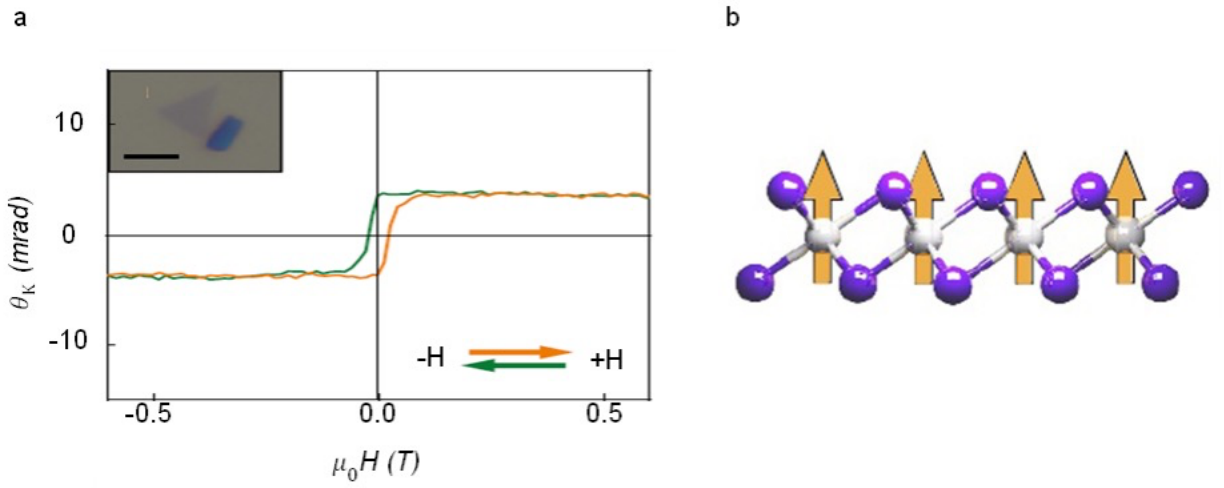

Figure 1.8. (a) Magneto-optical Kerr effect signal from a monolayer of CrI_3, with the inset showing an optical microscope image of the flake. The magnetic hysteresis indicates ferromagnetism, which is schematically illustrated in (b). Reproduced with permission from Huang, B.; Clark, G.; Navarro-Moratalla, E.; Klein, D. R.; Cheng, R.; Seyler, K. L.; Zhong, D.; Schmidgall, E.; McGuire, M. A.; Cobden, D. H.; Yao, W.; Xiao, D.; Jarillo-Herrero, P.; Xu, X. *Nature* **2017,** *546*, 270-273.

that 2D magnetic order can be stabilized against these thermal spin fluctuations by magnetocrystalline anisotropy.[101, 102] Though there exist several model systems to experimentally test these theories in the bulk (such as the family of layered A_2CrX_4 perovskites discussed in the previous section), 2D magnetism was not probed at the atomically thin limit until reports of stable ferromagnetism in isolated monolayers of CrI_3[23] and $Cr_2Ge_2Te_6$.[24] These discoveries prompted vigorous investigation of magnetic van der Waals materials. CrI_3 has received particular attention yielding discoveries such as layer-dependent magnetic ordering,[23] giant magnetoresistance,[3] and proximity effects in magnetic van der Waals heterostructures[5, 6] with studies extending to the chloride and bromide compositions as well.

Despite the fervent attention on the magnetic properties of CrX_3, (X = Cl, Br, I) study of its optical properties is conversely lacking. This is due to the fact that the CrX_3 emission properties are defined by the Cr^{3+} $^4T_{2g} \rightarrow {}^4A_{2g}$ *d–d* transition, which is inherently broad due to its excited-state Jahn-Teller distortion.[103, 104] The breadth of this emission feature severely limits the photonic functionality of CrI_3 – for comparison, the room-temperature optical linewidths of the van der Waals semiconductors WSe_2 and $MoSe_2$ are nearly ~5x narrower than that of CrI_3 at 15 K.[105-107] Incorporation of impurity dopants has long been used to transform the optical properties of materials, yet this utility was previously undemonstrated in CrI_3.[108-115]

In searching for a suitable luminescent dopant, the trivalent lanthanides are attractive candidates owing to their narrow-line emission, characteristic of the highly shielded *f* orbitals that participate in the *f–f* optical transitions. Despite the advantage of the narrow linewidths, the parity-forbidden nature of the *f–f* transitions results in very low absorption coefficients. To overcome this, proper donor-acceptor spectral matching can result in Ln^{3+}-centered *f–f* luminescence that is sensitized *via* energy transfer from the excited state of the host. Figure 1.9 illustrates the spectral overlap of the trivalent lanthanide excited states[116] and that of CrX_3. It is particularly suitable to match the acceptor energy to the photoluminescence, rather than absorption, energy of CrX_3; the photoluminescence spectrum is representative of the equilibrium excited state (following the spontaneous Jahn-Teller-induced excited-state reorganization) that will participate in energy transfer. While Figure 1.9 indicates there are several Ln^{3+} candidates with suitable spectral matching, Yb^{3+} shows excellent spectral matching for the entire CrX_3 family and has only one $^2F_{5/2}$ excited state, streamlining spectroscopic analysis. Initially, it was unclear whether the disparity in ionic radii of Yb^{3+} and Cr^{3+} (0.615 Å vs 0.868 Å)[117] would accommodate dopant incorporation into the lattice. Nonetheless, Chapter 4 finds that Yb^{3+} incorporates into the entire CrX_3 family, substituting for the octahedral Cr^{3+} site.[118, 119] The CrX_3 lattice relaxes the Yb^{3+}-induced strain by expanding the interlayer van der Waals gap, highlighting the utility of the soft 2D van der Waals interactions. In all CrX_3 compositions Yb^{3+} shows sensitized *f–f* luminescence (Figure 1.10a).[119]

To date, there are no other reports of luminescent dopants incorporated into a ferromagnetic lattice. The closest example is a recent report studying the luminescence of native defects in the ferromagnetic semiconductor CrSBr, though in this example the defect incorporation is random and uncontrollable.[120] The study of magneto-optical interactions between spin-bearing dopants and a ferromagnetic host is therefore wholly unexplored. To probe the magnetic behavior of the Yb^{3+} dopants, the Yb^{3+} circularly polarized luminescence was monitored as a function of applied external magnetic field, as illustrated in Figure 1.10b.[118] Analogous to the magnetic circular dichroism experiment, magnetic circularly polarized luminescence probes the differential emission of left and right circularly polarized light, where the Zeeman-split spin sublevels can be interrogated by the nature of circular polarization spin selection rules.[63] Notably, the Yb^{3+} polarization ratio saturates around ~0.2 T – nearly 100x lower than would be expected to saturate a S = ½ Curie paramagnet.[16, 118] The zoomed-in inset of panel b shows the Yb^{3+} polarization ratio centered around 0 T, showing a coercivity of 55 mT, comparable to that of bulk CrI_3. Furthermore, Figure 1.10c monitors the same Yb^{3+} polarization ratio as a function of temperature, which perfectly tracks with the magnetic ordering of bulk CrI_3. Together, these

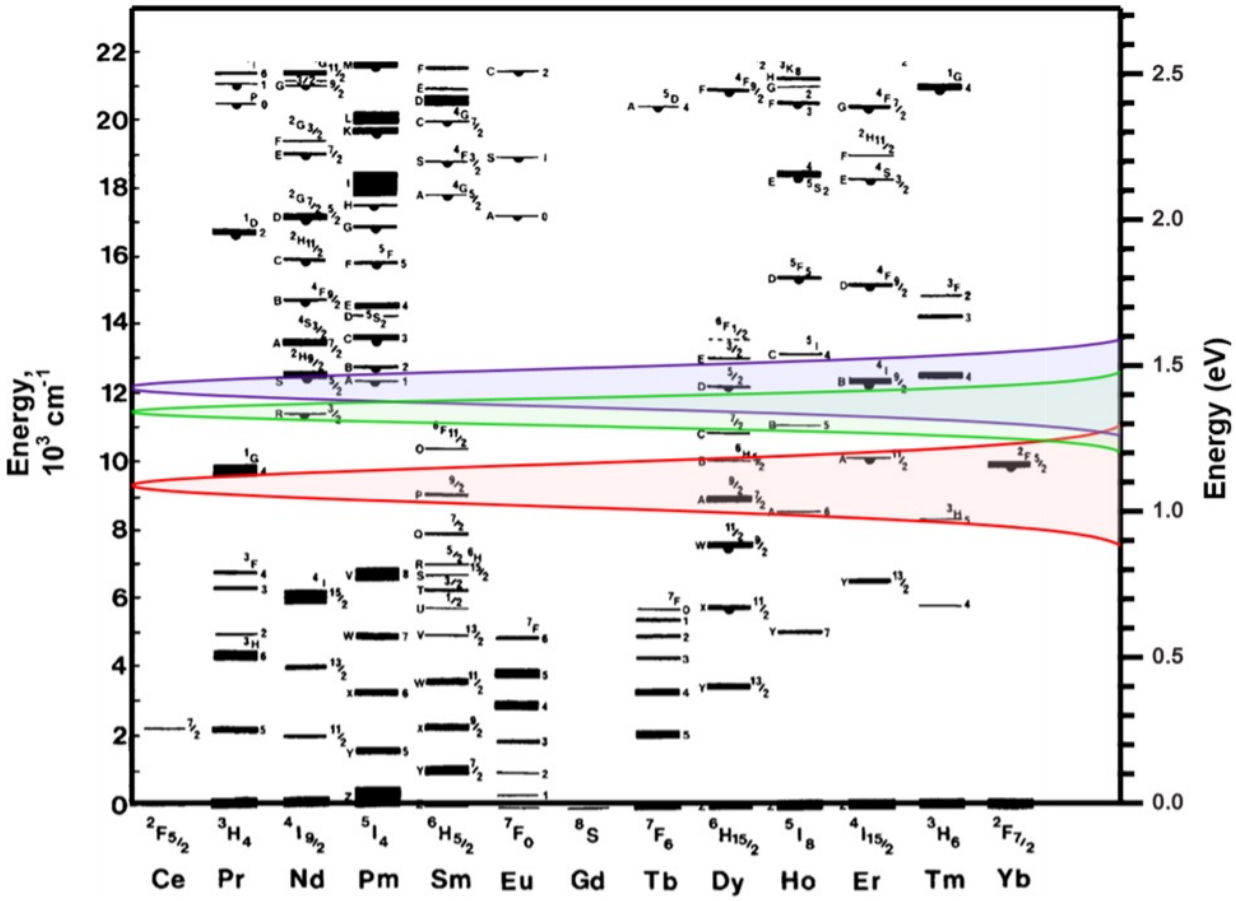

Figure 1.9. Dieke diagram showing the energies of the Ln^{3+} electronic states (left axis) overlaid with the photoluminescence of CrI_3 (red), $CrBr_3$ (green), and $CrCl_3$ (purple) (right axis), illustrating the expected electronic overlap between the CrX_3 donor and Ln^{3+} acceptor.

results indicate that the Yb^{3+} magnetization is pinned to that of the ferromagnetic CrI_3 host through strong Yb^{3+}–Cr^{3+} exchange interactions. This exchange interaction arises from an iodide-mediated superexchange pathway, where the metal-iodide covalency plays a key factor in the degree of magnetic exchange. This is particularly intriguing given that the highly shielded nature of the Yb^{3+} *f* orbitals is typically thought to make Yb^{3+} insensitive to its surrounding ligand field environment. The Yb^{3+}-X covalency is investigated in Chapter 4.3 and highlights the anomalously high Yb^{3+}-iodide covalency in Yb^{3+}:CrI_3.

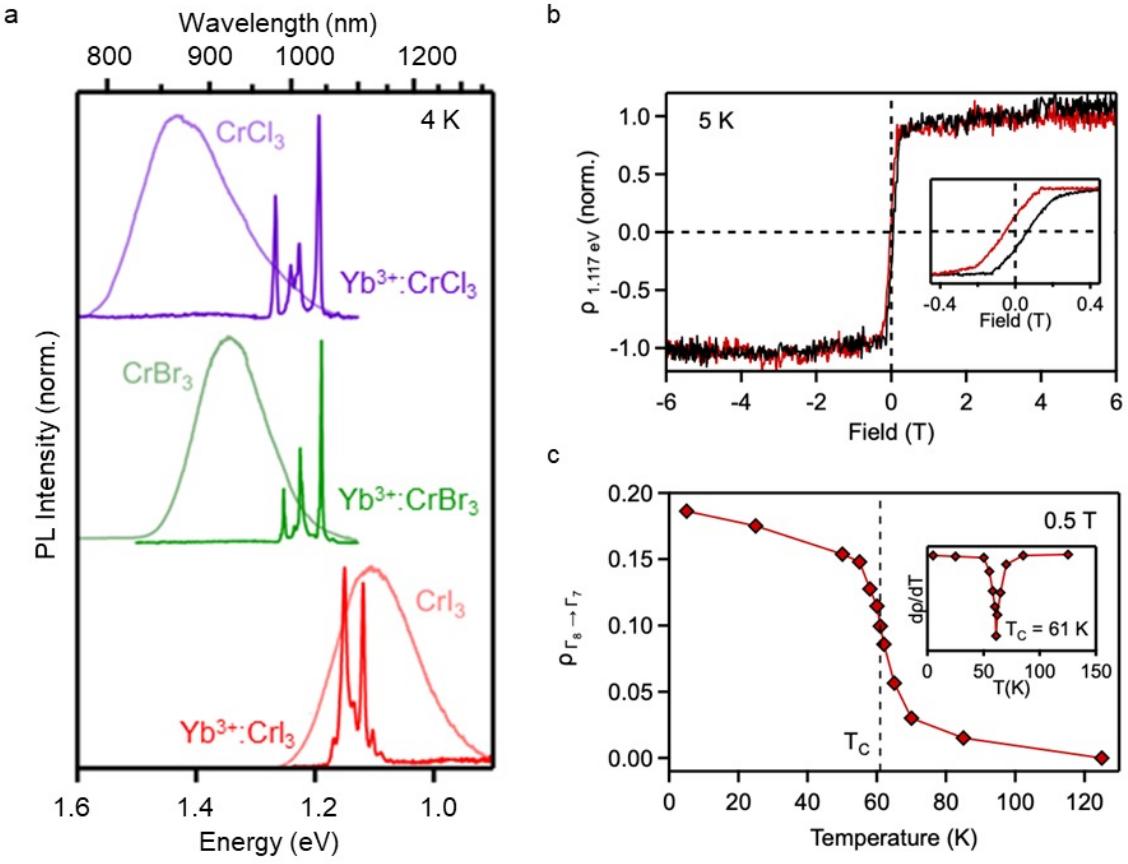

Figure 1.10. (a) Photoluminescence spectra of CrX_3 (X = Cl, Br, I) overlaid with the corresponding Yb^{3+}:CrX_3 spectra. Reproduced with permission from Snoeren; T. J.; Pressler, K.; Kluherz, K. T.; Walsh, K. M.; De Yoreo, J. J.; Gamelin, D. R. *J. Am. Chem. Soc.* **2023**, *145*, 17427-17434. (b) Yb^{3+} circularly polarized photoluminescence ratio ($\rho = (\sigma^- - \sigma^+)/(\sigma^- + \sigma^+)$) monitoring the $\Gamma^8 \rightarrow \Gamma^7$ transition while sweeping the magnetic field in both the positive and negative directions. The inset shows a zoom-in of the data centered around 0 T, showing a coercive field of ~55 mT, comparable to that of bulk CrI_3. (c) Scatter plot of the same Yb^{3+} $\Gamma^8 \rightarrow \Gamma^7$ polarization ratio as a function of temperature, highlighting the correspondence with the CrI_3 magnetic ordering. Reproduced with permission from Pressler, K.; Snoeren, T. J.; Walsh, K. M.; Gamelin, D. R. *Nano Letters* **2023**, *23*, 1320-1326. Copyright 2024 American Chemical Society

1.5 Summary and outlook

In summary, this dissertation establishes a wide-ranging set of principles for achieving spin correlated optical properties in ferromagnetic nanostructures. It is demonstrated that nanoscale advantages can facilitate broad chemical tunability, including colloidal nanocrystal preparation, 2D magnetic heterostructures, and incorporation of designer spin-bearing optical dopants. Furthermore, this work illustrates expansive use of the spectroscopic toolbox to gain a fundamental understanding of the magnetic and magneto-optical interactions in these systems. Precise control over the atomistic interactions is particularly important for tuning the local metal-metal magnetic exchange, with particular emphasis on the covalency of the bridging ligand with the metal centers. Mastery over both the chemistry and magneto-optical spectroscopies yields a synergistic cycle of materials development toward achieving optical spin correlations in ferromagnetic nanostructures. In addition to gaining fundamental insights into these ferromagnetic metal-halide nanostructures, this work opens opportunities to achieve optically manipulated magnetism in future studies.

1.6 References

1. Gish, J. T.; Lebedev, D.; Song, T. W.; Sangwan, V. K.; Hersam, M. C. Van der Waals Opto-Spintronics. *Nat. Electron.* **2024,** *7*, 336-347.
2. Siegrist, F.; Gessner, J. A.; Ossiander, M.; Denker, C.; Chang, Y.-P.; Schröder, M. C.; Guggenmos, A.; Cui, Y.; Walowski, J.; Martens, U.; Dewhurst, J. K.; Kleineberg, U.; Münzenberg, M.; Sharma, S.; Schultze, M. Light-Wave Dynamic Control of Magnetism. *Nature* **2019,** *571*, 240-244.
3. Song, T.; Cai, X.; Tu, M. W.-Y.; Zhang, X.; Huang, B.; Wilson, N. P.; Seyler, K. L.; Zhu, L.; Taniguchi, T.; Watanabe, K.; McGuire, M. A.; Cobden, D. H.; Xiao, D.; Yao, W.; Xu, X. Giant Tunneling Magnetoresistance in Spin-Filter van der Waals Heterostructures. *Science* **2018,** *360*, 1214-1218.
4. Cenker, J.; Sivakumar, S.; Xie, K.; Miller, A.; Thijssen, P.; Liu, Z.; Dismukes, A.; Fonseca, J.; Anderson, E.; Zhu, X.; Roy, X.; Xiao, D.; Chu, J.-H.; Cao, T.; Xu, X. Reversible Strain-Induced Magnetic Phase Transition in a van der Waals Magnet. *Nat. Nanotechnol.* **2022,** *17*, 256-261.
5. Zhong, D.; Seyler, K. L.; Linpeng, X.; Cheng, R.; Sivadas, N.; Huang, B.; Schmidgall, E.; Taniguchi, T.; Watanabe, K.; McGuire, M. A.; Yao, W.; Xiao, D.; Fu, K.-M. C.; Xu, X. Van der Waals Engineering of Ferromagnetic Semiconductor Heterostructures for Spin and Valleytronics. *Sci. Adv.* **2017,** *3*, e1603113.
6. Seyler, K. L.; Zhong, D.; Huang, B.; Linpeng, X.; Wilson, N. P.; Taniguchi, T.; Watanabe, K.; Yao, W.; Xiao, D.; McGuire, M. A.; Fu, K.-M. C.; Xu, X. Valley Manipulation by Optically Tuning the Magnetic Proximity Effect in WSe2/CrI3 Heterostructures. *Nano Lett.* **2018,** *18*, 3823-3828.
7. Huang, B.; McGuire, M. A.; May, A. F.; Xiao, D.; Jarillo-Herrero, P.; Xu, X. Emergent phenomena and proximity effects in two-dimensional magnets and heterostructures. *Nat. Mater.* **2020,** *19*, 1276-1289.
8. Kim, Y.-H.; Zhai, Y.; Lu, H.; Pan, X.; Xiao, C.; Gaulding, E. A.; Harvey Steven, P.; Berry Joseph, J.; Vardeny Zeev, V.; Luther Joseph, M.; Beard Matthew, C. Chiral-Induced Spin Selectivity Enables a Room-Temperature Spin Light-Emitting Diode. *Science* **2021,** *371*, 1129-1133.
9. Goodenough, J. B., *Magnetism and the Chemical Bond*. Interscience Publishers: New York, 1963.
10. Zener, C. Interaction Between the *d* Shells in the Transition Metals. *Phys. Rev.* **1951,** *81*, 440-444.
11. Wachter, P. Optical Electrical and Magnetic Properties of the Europium Chalcogenides and the Rare Earth Pnictides. *Crit. Rev. Solid State Sci.* **1972,** *3*, 189-241.
12. Di Bartolo, B., *Optical Properties of Ions in Solids*. Plenum Press: New York, 1975.
13. Hoffmann, R. How Chemistry and Physics Meet in the Solid State. *Angewandte Chemie International Edition in English* **1987,** *26*, 846-878.
14. Hay, P. J.; Thibeault, J. C.; Hoffmann, R. Orbital Interactions in Metal Dimer Complexes. *J. Am. Chem. Soc.* **1975,** *97*, 4884-4899.
15. Weihe, H.; Güdel, H. U. Quantitative Interpretation of the Goodenough−Kanamori Rules: A Critical Analysis. *lnorg. Chem.* **1997,** *36*, 3632-3639.
16. Kahn, O., *Molecular Magnetism*. VCH: New York, NY, 1993.
17. Dey, A.; Ye, J.; De, A.; Debroye, E.; Ha, S. K.; Bladt, E.; Kshirsagar, A. S.; Wang, Z.; Yin, J.; Wang, Y.; Quan, L. N.; Yan, F.; Gao, M.; Li, X.; Shamsi, J.; Debnath, T.; Cao,

M.; Scheel, M. A.; Kumar, S.; Steele, J. A.*, et al.* State of the Art and Prospects for Halide Perovskite Nanocrystals. *ACS Nano* **2021,** *15*, 10775-10981.
18. Protesescu, L.; Yakunin, S.; Bodnarchuk, M. I.; Krieg, F.; Caputo, R.; Hendon, C. H.; Yang, R. X.; Walsh, A.; Kovalenko, M. V. Nanocrystals of Cesium Lead Halide Perovskites ($CsPbX_3$, X = Cl, Br, and I): Novel Optoelectronic Materials Showing Bright Emission with Wide Color Gamut. *Nano Lett.* **2015,** *15*, 3692-3696.
19. Akkerman, Q. A.; Rainò, G.; Kovalenko, M. V.; Manna, L. Genesis, Challenges and Opportunities for Colloidal Lead Halide Perovskite Nanocrystals. *Nat. Mater.* **2018,** *17*, 394-405.
20. Mao, L.; Stoumpos, C. C.; Kanatzidis, M. G. Two-Dimensional Hybrid Halide Perovskites: Principles and Promises. *J. Am. Chem. Soc.* **2019,** *141*, 1171-1190.
21. Li, X.; Hoffman, J. M.; Kanatzidis, M. G. The 2D Halide Perovskite Rulebook: How the Spacer Influences Everything from the Structure to Optoelectronic Device Efficiency. *Chem. Rev.* **2021,** *121*, 2230-2291.
22. Mao, L.; Chen, J.; Vishnoi, P.; Cheetham, A. K. The Renaissance of Functional Hybrid Transition-Metal Halides. *Acc. Mater. Res.* **2022,** *3*, 439-448.
23. Huang, B.; Clark, G.; Navarro-Moratalla, E.; Klein, D. R.; Cheng, R.; Seyler, K. L.; Zhong, D.; Schmidgall, E.; McGuire, M. A.; Cobden, D. H.; Yao, W.; Xiao, D.; Jarillo-Herrero, P.; Xu, X. Layer-Dependent Ferromagnetism in a van der Waals Crystal Down to the Monolayer Limit. *Nature* **2017,** *546*, 270-273.
24. Gong, C.; Li, L.; Li, Z.; Ji, H.; Stern, A.; Xia, Y.; Cao, T.; Bao, W.; Wang, C.; Wang, Y.; Qiu, Z. Q.; Cava, R. J.; Louie, S. G.; Xia, J.; Zhang, X. Discovery of Intrinsic Ferromagnetism in Two-Dimensional van der Waals Crystals. *Nature* **2017,** *546*, 265-269.
25. Neumann, T.; Feldmann, S.; Moser, P.; Delhomme, A.; Zerhoch, J.; Van De Goor, T.; Wang, S.; Dyksik, M.; Winkler, T.; Finley, J. J.; Plochocka, P.; Brandt, M. S.; Faugeras, C.; Stier, A. V.; Deschler, F. Manganese doping for enhanced magnetic brightening and circular polarization control of dark excitons in paramagnetic layered hybrid metal-halide perovskites. *Nat. Commun.* **2021,** *12*.
26. Zhang, K.; Zhao, J.; Hu, Q.; Yang, S.; Zhu, X.; Zhang, Y.; Huang, R.; Ma, Y.; Wang, Z.; Ouyang, Z.; Han, J.; Han, Y.; Tang, J.; Tong, W.; Zhang, L.; Zhai, T. Room-Temperature Magnetic Field Effect on Excitonic Photoluminescence in Perovskite Nanocrystals. *Adv. Mater.* **2021**, 2008225.
27. Wang, M.; Yang, Z.; Zhang, C. Polarized Photoluminescence from Lead Halide Perovskites. *Advanced Optical Materials* **2021,** *n/a*, 2002236.
28. Yeh, I. H.; Ghobadifard, M.; Feng, L.; Galievsky, V.; Radovanovic, P. V. Origin of Dopant-Carrier Exchange Coupling and Excitonic Zeeman Splitting in Mn^{2+}-Doped Lead Halide Perovskite Nanocrystals. *Nano Lett.* **2024,** *24*, 10554-10561.
29. Ruderman, M. A.; Kittel, C. Indirect Exchange Coupling of Nuclear Magnetic Moments by Conduction Electrons. *Phys. Rev.* **1954,** *96*, 99-102.
30. Kittel, C., *Introduction to Solid State Physics*. 8th ed.; Wiley: Hoboken, NJ, 2005.
31. Kittel, C., Indirect Exchange Interactions in Metals. In *Solid State Phys.*, Seitz, F.; Turnbull, D.; Ehrenreich, H., Eds. Academic Press: 1969; Vol. 22, pp 1-26.
32. Anderson, P. W., Theory of Magnetic Exchange Interactions:Exchange in Insulators and Semiconductors. In *Solid State Phys.*, Seitz, F.; Turnbull, D., Eds. Academic Press: 1963; Vol. 14, pp 99-214.
33. Dirac, P. A. M.; Fowler, R. H. On the Theory of Quantum Mechanics. *Proceedings of the Royal Society of London. Series A, Containing Papers of a Mathematical and Physical Character*

1997, *112*, 661-677.
34. Heisenberg, W. Mehrkörperproblem und Resonanz in der Quantenmechanik. *Z. Phys.* **1926,** *38*, 411-426.
35. Van Vleck, J. H., *The Theory of Electric and Magnetic Susceptibilities*. Oxford University Press: London, 1965.
36. Fisher, M. E. The Theory of Equilibrium Critical Phenomena. *Rep. Prog. Phys.* **1967,** *30*, 615.
37. Coey, J. M. D., *Magnetism and Magnetic Materials*. 1 ed.; Cambridge University Press: Cambridge, 2001.
38. Akkerman, Q. A.; Manna, L. What Defines a Halide Perovskite? *ACS Energy Lett.* **2020,** *5*, 604-610.
39. Di Stasio, F.; Christodoulou, S.; Huo, N.; Konstantatos, G. Near-Unity Photoluminescence Quantum Yield in $CsPbBr_3$ Nanocrystal Solid-State Films *via* Postsynthesis Treatment with Lead Bromide. *Chem. Mater.* **2017,** *29*, 7663-7667.
40. Zhong, Q.; Cao, M.; Xu, Y.; Li, P.; Zhang, Y.; Hu, H.; Yang, D.; Xu, Y.; Wang, L.; Li, Y.; Zhang, X.; Zhang, Q. L-Type Ligand-Assisted Acid-Free Synthesis of $CsPbBr_3$ Nanocrystals with Near-Unity Photoluminescence Quantum Yield and High Stability. *Nano Lett.* **2019,** *19*, 4151-4157.
41. Dutta, A.; Behera, R. K.; Pal, P.; Baitalik, S.; Pradhan, N. Near-Unity Photoluminescence Quantum Efficiency for All $CsPbX_3$ (X=Cl, Br, and I) Perovskite Nanocrystals: A Generic Synthesis Approach. *Angew. Chem. Int. Ed.* **2019,** *58*, 5552-5556.
42. Manser, J. S.; Christians, J. A.; Kamat, P. V. Intriguing Optoelectronic Properties of Metal Halide Perovskites. *Chem. Rev.* **2016,** *116*, 12956–13008.
43. De Roo, J.; Ibáñez, M.; Geiregat, P.; Nedelcu, G.; Walravens, W.; Maes, J.; Martins, J. C.; Van Driessche, I.; Kovalenko, M. V.; Hens, Z. Highly Dynamic Ligand Binding and Light Absorption Coefficient of Cesium Lead Bromide Perovskite Nanocrystals. *ACS Nano* **2016,** *10*, 2071-2081.
44. Shamsi, J.; Urban, A. S.; Imran, M.; De Trizio, L.; Manna, L. Metal Halide Perovskite Nanocrystals: Synthesis, Post-Synthesis Modifications, and Their Optical Properties. *Chem. Rev.* **2019,** *119*, 3296–3348.
45. Creutz, S. E.; Crites, E. N.; De Siena, M. C.; Gamelin, D. R. Anion Exchange in Cesium Lead Halide Perovskite Nanocrystals and Thin Films Using Trimethylsilyl Halide Reagents. *Chem. Mater.* **2018,** *30*, 4887-4891.
46. Stoumpos, C. C.; Kanatzidis, M. G. The Renaissance of Halide Perovskites and Their Evolution as Emerging Semiconductors. *Acc. Chem. Res.* **2015,** *48*, 2791-2802.
47. De Siena, M. C.; Sommer, D. E.; Creutz, S. E.; Dunham, S. T.; Gamelin, D. R. Spinodal Decomposition During Anion Exchange in Colloidal Mn^{2+}-Doped $CsPbX_3$ (X = Cl, Br) Perovskite Nanocrystals. *Chem. Mater.* **2019,** *31*, 7711-7722.
48. Náfrádi, B.; Szirmai, P.; Spina, M.; Lee, H.; Yazyev, O. V.; Arakcheeva, A.; Chernyshov, D.; Gibert, M.; Forró, L.; Horváth, E. Optically Switched Magnetism in Photovoltaic Perovskite $CH_3NH_3(Mn:Pb)I_3$. *Nat. Commun.* **2016,** *7*, 13406.
49. Ren, L.; Wang, Y.; Wang, M.; Wang, S.; Zhao, Y.; Cazorla, C.; Chen, C.; Wu, T.; Jin, K. Tuning Magnetism and Photocurrent in Mn-Doped Organic–Inorganic Perovskites. *J. Phys. Chem. Lett.* **2020,** *11*, 2577-2584.
50. Rajamanickam, N.; Chowdhury, T. H.; Isogami, S.; Islam, A. Magnetic Properties in $CH_3NH_3PbI_3$ Perovskite Thin Films by Mn Doping. *J. Phys. Chem. C* **2021,** *125*, 20104-20112.

51. Ning, W.; Bao, J.; Puttisong, Y.; Moro, F.; Kobera, L.; Shimono, S.; Wang, L.; Ji, F.; Cuartero, M.; Kawaguchi, S.; Abbrent, S.; Ishibashi, H.; De Marco, R.; Bouianova Irina, A.; Crespo Gaston, A.; Kubota, Y.; Brus, J.; Chung Duck, Y.; Sun, L.; Chen Weimin, M., *et al.* Magnetizing Lead-Free Halide Double Perovskites. *Sci. Adv.* **2020,** *6*, eabb5381.
52. Sajedi, M.; Luo, C.; Siemensmeyer, K.; Krivenkov, M.; Chen, K.; Taylor, J. M.; Flatken, M. A.; Radu, F.; Rader, O. Search for Ferromagnetism in Mn-Doped Lead Halide Perovskites. *Communications Physics* **2023,** *6*, 80.
53. Hirakawa, K.; Hirakawa, K.; Hashimoto, T. Magnetic Properties of Potassium Iron Group Fluorides KMF_3. *J. Phys. Soc. Jpn.* **1960,** *15*, 2063-2068.
54. Kedzie, R. W.; Shane, J. R.; Kestigian, M.; Croft, W. J. Resonance Observation of Antiferromagnetic Ordering in RbMnCl3, CsMnCl3, and KMnCl3. *J. Appl. Phys.* **1965,** *36*, 1195-1196.
55. Goodenough, J. B.; Longo, M., Magnetic Properties of Perovskite and Perovskite-Related Compounds (Tab. 6). In *Landolt-Börnstein - Group III Condensed Matter*, Springer-Verlag Berlin Heidelberg: 1970; Vol. 4a, p 214.
56. Cousseins, J.-C.; Kozak, A. d. Sur les Fluorures Doubles de Chrome Bivalent de Potassium ou de Rubidium. *Comptes rendus hebdomadaires des séances de l'Académie des sciences. Série C, Sciences chimiques* **1966,** *263*, 1533.
57. Scatturin, V.; Corliss, L.; Elliott, N.; Hastings, J. Magnetic structures of 3d transition metal double fluorides, $KMeF_3$. *Acta Crystallogr.* **1961,** *14*, 19-26.
58. Meyer, G. Neue Chlor-PeroWskite Mit Zweiwertigen Lanthaniden: $CsLn^{II}Cl_3$ (Ln^{II} = Sm, Eu, Tm, Yb). *Die Naturwissenschaften* **1978,** *65*, 258-258.
59. Nocera, D. G.; Morss, L. R.; Fahey, J. A. Preparation, Crystal Structure, and Enthalpy of Formation of Cesium Europium(II) Chloride, $CsEuCl_3$. *J. lnorg. Nucl. Chem.* **1980,** *42*, 55-59.
60. Huang, J.; Lei, T.; Siron, M.; Zhang, Y.; Yu, S.; Seeler, F.; Dehestani, A.; Quan, L. N.; Schierle-Arndt, K.; Yang, P. Lead-Free Cesium Europium Halide Perovskite Nanocrystals. *Nano Lett.* **2020,** *20*, 3734-3739.
61. Walsh, K. M.; Pressler, K.; Crane, M. J.; Gamelin, D. R. Ferromagnetism and Spin-Polarized Luminescence in Lead-Free $CsEuCl_3$ Perovskite Nanocrystals and Thin Films. *ACS Nano* **2022,** *16*, 2569-2576.
62. Rubio, O. J. Doubly-Valent Rare-Earth Ions in Halide Crystals. *Journal of Physics and Chemistry of Solids* **1991,** *52*, 101-174.
63. Schatz, P. N.; Piepho, S. B., *Group Theory in Spectroscopy: With Applications to Magnetic Circular Dichroism*. Wiley: New York, 1983.
64. Mauger, A.; Godart, C. The Magnetic, Optical, and Transport Properties of Representatives of a Class of Magnetic Semiconductors: The Europium Chalcogenides. *Phys. Rep.* **1986,** *141*, 51-176.
65. Boncher, W.; Dalafu, H.; Rosa, N.; Stoll, S. Europium Chalcogenide Magnetic Semiconductor Nanostructures. *Coord. Chem. Rev.* **2015,** *289-290*, 279-288.
66. Cohen, T. A.; Sharp, D.; Kluherz, K. T.; Chen, Y.; Munley, C.; Anderson, R. T.; Swanson, C. J.; De Yoreo, J. J.; Luscombe, C. K.; Majumdar, A.; Gamelin, D. R.; Mackenzie, J. D. Direct Patterning of Perovskite Nanocrystals on Nanophotonic Cavities with Electrohydrodynamic Inkjet Printing. *Nano Lett.* **2022,** *22*, 5681-5688.
67. Guymon, G. G.; Sharp, D.; Cohen, T. A.; Gibbs, S. L.; Manna, A.; Tzanetopoulos, E.; Gamelin, D. R.; Majumdar, A.; MacKenzie, J. D. Electrohydrodynamic Printing-Based Heterointegration of Quantum Dots on Suspended Nanophotonic Cavities. *Advanced Materials*

Technologies **2024,** *9*, 2301921.
68. Crane, M. J.; Kroupa, D. M.; Roh, J. Y.; Anderson, R. T.; Smith, M. D.; Gamelin, D. R. Single-Source Vapor Deposition of Quantum-Cutting Yb3+:CsPb(Cl1–xBrx)3 and Other Complex Metal-Halide Perovskites. *ACS Applied Energy Materials* **2019,** *2*, 4560-4565.
69. Straus, D. B.; Klimczuk, T.; Xu, X.; Cava, R. J. Antiferromagnetic Order in the Rare-Earth Halide Perovskites CsEuBr3 and CsEuCl3. *Chem. Mater.* **2022,** *34*, 10772-10777.
70. Stoumpos, C. C.; Cao, D. H.; Clark, D. J.; Young, J.; Rondinelli, J. M.; Jang, J. I.; Hupp, J. T.; Kanatzidis, M. G. Ruddlesden–Popper Hybrid Lead Iodide Perovskite 2D Homologous Semiconductors. *Chem. Mater.* **2016,** *28*, 2852-2867.
71. Saparov, B.; Mitzi, D. B. Organic–Inorganic Perovskites: Structural Versatility for Functional Materials Design. *Chem. Rev.* **2016,** *116*, 4558-4596.
72. Mao, L.; Teicher, S. M. L.; Stoumpos, C. C.; Kennard, R. M.; DeCrescent, R. A.; Wu, G.; Schuller, J. A.; Chabinyc, M. L.; Cheetham, A. K.; Seshadri, R. Chemical and Structural Diversity of Hybrid Layered Double Perovskite Halides. *J. Am. Chem. Soc.* **2019,** *141*, 19099-19109.
73. Huang, B.; Zhang, J.-Y.; Huang, R.-K.; Chen, M.-K.; Xue, W.; Zhang, W.-X.; Zeng, M.-H.; Chen, X.-M. Spin-Reorientation-Induced Magnetodielectric Coupling Effects in Two Layered Perovskite Magnets. *Chem. Sci.* **2018,** *9*, 7413-7418.
74. van Amstel, W. D.; de Jongh, L. J. Magnetic Measurements on $(CH_3NH_3)_2MnCl_4$, a Quasi Two-Dimensional Heisenberg Antiferromagnet. *Solid State Commun.* **1972,** *11*, 1423-1429.
75. de Jongh, L. J.; Botterman, A. C.; de Boer, F. R.; Miedema, A. R. Transition Temperature of the Two-Dimensional Heisenberg Ferromagnet with S=½. *J. Appl. Phys.* **1969,** *40*, 1363-1365.
76. Polyakov, A. O.; Arkenbout, A. H.; Baas, J.; Blake, G. R.; Meetsma, A.; Caretta, A.; van Loosdrecht, P. H. M.; Palstra, T. T. M. Coexisting Ferromagnetic and Ferroelectric Order in a $CuCl_4$-based Organic–Inorganic Hybrid. *Chem. Mater.* **2012,** *24*, 133-139.
77. Day, P. Correlation of Structures and Properties of Ferromagnetic Tetrahalogenochromate(II) Salts. *J. Magn. Magn. Mater.* **1986,** *54-57*, 1442-1446.
78. Briat, B.; Bramwell, S. T.; Canit, J. C.; Day, P.; Thorne, J. R. G. Spin Dynamics and Absorption-Band Profiles for the Planar Two-Dimensional Easy-Plane Ionic Ferromagnet Rb_2CrCl_4. *Proc. R. Soc. London, Ser. A* **1997,** *415*, 277-302.
79. Bellitto, C.; Day, P. Organic-Intercalated Halogenochromates(II): Low-Dimensional Magnets. *J. Mater. Chem.* **1992,** *2*, 265-271.
80. Era, M.; Morimoto, S.; Tsutsui, T.; Saito, S. Organic-Inorganic Heterostructure Electroluminescent Device Using a Layered Perovskite Semiconductor $(C_6H_5C_2H_4NH_3)_2PbI_4$. *Appl. Phys. Lett.* **1994,** *65*, 676-678.
81. Smith, I. C.; Hoke, E. T.; Solis-Ibarra, D.; McGehee, M. D.; Karunadasa, H. I. A Layered Hybrid Perovskite Solar-Cell Absorber with Enhanced Moisture Stability. *Angew. Chem. Int. Ed.* **2014,** *53*, 11232-11235.
82. Grancini, G.; Nazeeruddin, M. K. Dimensional Tailoring of Hybrid Perovskites for Photovoltaics. *Nat. Rev. Mater.* **2019,** *4*, 4-22.
83. Smith, M. D.; Connor, B. A.; Karunadasa, H. I. Tuning the Luminescence of Layered Halide Perovskites. *Chem. Rev.* **2019,** *119*, 3104-3139.
84. Zhang, F.; Lu, H.; Tong, J.; Berry, J. J.; Beard, M. C.; Zhu, K. Advances in Two-Dimensional Organic–Inorganic Hybrid Perovskites. *Energy Environ. Sci.* **2020,** *13*, 1154-1186.
85. Chen, Y.; Sun, Y.; Peng, J.; Tang, J.; Zheng, K.; Liang, Z. 2D Ruddlesden–Popper

Perovskites for Optoelectronics. *Adv. Mater.* **2018,** *30*, 1703487.
86. Bellitto, C.; Day, P. Bis(monoalkylammonium) Tetrachlorochromates(II): A New Series of Two-Dimensional Ionic Ferromagnets. *J. Chem. Soc., Chem. Commun.* **1976**, 870-871.
87. Day, P. New Transparent Ferromagnets. *Acc. Chem. Res.* **1979,** *12*, 236-243.
88. Münninghoff, G.; Hellner, E.; Fyne, P. J.; Day, P.; Hutchings, M. T.; Tasset, F. Mangetic Moment Distribution in the Ionic Ferromagnet Rb_2CrCl_4. *Le Journal de Physique Colloques* **1982,** *43*, 243-247.
89. Janke, E.; Hutchings, M. T.; Day, P.; Walker, P. J. Neutron Diffraction Study of the Crystal and Magnetic Structure of Rb_2CrCl_4: A Two-Dimensional Ionic Ferromagnet. *J. Phys. C: Solid State Phys.* **1983,** *16*, 5959.
90. Hutchings, M. T.; Als-Nielsen, J.; Lindgard, P. A.; Walker, P. J. Neutron Scattering Investigation of the Temperature Dependence of Long-Wavelength Spin Waves in Ferromagnetic Rb_2CrCl_4. *J. Phys. C: Solid State Phys.* **1981,** *14*, 5327.
91. Bellitto, C.; Brunner, H.; Güdel, H. Optical Spectroscopy of One- and Two-Dimensional Ionic Magnets of Cr^{2+}: $CsCrCl_3$, $(CH_3)_4NCrCl_3$, $(CH_3)_4NCrBr_3$, $CrCl_2$, $(C_2H_5NH_3)_2CrCl_4$, and $(C_2H_5NH_3)_2CrBr_4$. *lnorg. Chem.* **1987,** *26*, 2750-2754.
92. Day, P.; Gregson, A. K.; Leech, D. H. Optical Properties of Ferromagnetic K_2CrCl_4. *Phys. Rev. Lett.* **1973,** *30*, 19-22.
93. Ballhausen, C. J., *Introduction to Ligand Field Theory*. McGraw-Hill: New York (State), 1962.
94. Tanabe, Y.; Sugano, S. On the Absorption Spectra of Complex Ions II. *J. Phys. Soc. Jpn.* **1954,** *9*, 766-779.
95. König, E.; Kremer, S., *Ligand field energy diagrams*. Plenum Press: New York, 1977.
96. Kojima, N., Elementary Excitations in Magnetically Ordered Materials. In *Magneto-optics*, Sugano, S.; Kojima, N., Eds. Springer: Berlin, 2000; pp 37-74.
97. Bellitto, C.; Day, P. Magnetic Susceptibility and Optical Spectra of the Organic-Intercalated Two-Dimensional Ferromagnets Bis(monomethylammonium)- and Bis(monoethylammonium) tetrachlorochromate(II). *J. Chem. Soc., Dalton Trans.* **1978**, 1207-1212.
98. Smith, R. T.; Walsh, K. M.; Jiang, Q.; Chu, J.-H.; Gamelin, D. R. An Air-Stable and Exfoliable Ferromagnetic Two-Dimensional Perovskite, $(Phenethylammonium)_2CrCl_4$. *Chem. Mater.* **2024,** *36*, 1571-1578.
99. Walsh, K. M.; Smith, R. T.; Gamelin, D. R. Anion Exchange and Lateral Heterostructure Formation in Ferromagnetic $PEA_2Cr(Cl,Br)_4$ Two-Dimensional Perovskites. *J. Am. Chem. Soc.* **2024,** *146*, 29159-29168.
100. Mermin, N. D.; Wagner, H. Absence of Ferromagnetism or Antiferromagnetism in One- or Two-Dimensional Isotropic Heisenberg Models. *Phys. Rev. Lett.* **1966,** *17*, 1133-1136.
101. Kosterlitz, J. M.; Thouless, D. J. Ordering, Metastability and Phase Transitions in Two-Dimensional Systems. *Journal of physics. C, Solid state physics* **1973,** *6*, 1181-1203.
102. Gibertini, M.; Koperski, M.; Morpurgo, A. F.; Novoselov, K. S. Magnetic 2D Materials and Heterostructures. *Nat. Nanotechnol.* **2019,** *14*, 408-419.
103. Güdel, H. U.; Snellgrove, T. R. Jahn-Teller Effect in the $^4T_{2g}$ State of Chromium(III) in Dicesium Sodium Indium(III) Hexachloride. *lnorg. Chem.* **1978,** *17*, 1617-1620.
104. Wilson, R. B.; Solomon, E. I. Spectroscopic Studies of the Photoactive $^4T_{2g}$ Excited State of Hexaamminechromium(III). *lnorg. Chem.* **1978,** *17*, 1729-1736.
105. Yan, T.; Qiao, X.; Liu, X.; Tan, P.; Zhang, X. Photoluminescence Properties and

Exciton Dynamics in Monolayer WSe_2. *Appl. Phys. Lett.* **2014,** *105*, 101901.
106. Luis Enrique Parra, L.; Loïc, M.; Joanna, W.; Aditya, S.; Etienne, L.; Michelangelo, R.; Takashi, T.; Kenji, W.; Stéphane, B. Single- and Narrow-Line Photoluminescence in a Boron Nitride-Supported $MoSe_2$/Graphene Heterostructure. *Comptes Rendus. Physique* **2021,** *22*, 77-88.
107. Seyler, K. L.; Zhong, D.; Klein, D. R.; Gao, S.; Zhang, X.; Huang, B.; Navarro-Moratalla, E.; Yang, L.; Cobden, D. H.; McGuire, M. A.; Yao, W.; Xiao, D.; Jarillo-Herrero, P.; Xu, X. Ligand-Field Helical Luminescence in a 2D Ferromagnetic Insulator. *Nat. Phys.* **2018,** *14*, 277-281.
108. Cox, P. A., *Electronic Structure and Chemistry of Solids*. Oxford University Press: Oxford, 1987.
109. Henderson, B.; Imbusch, G. F., *Optical Spectroscopy of Inorganic Solids*. Oxford University Press: Oxford, 1989.
110. Kittel, C., *Introduction to Solid State Physics*. 8 ed.; Wiley: New York, 2004.
111. Bassett, L. C.; Alkauskas, A.; Exarhos, A. L.; Fu, K.-M. C. Quantum defects by design. *Nanophotonics* **2019,** *8*, 1867-1888.
112. Tran, T. T.; Elbadawi, C.; Totonjian, D.; Lobo, C. J.; Grosso, G.; Moon, H.; Englund, D. R.; Ford, M. J.; Aharonovich, I.; Toth, M. Robust Multicolor Single Photon Emission from Point Defects in Hexagonal Boron Nitride. *ACS Nano* **2016,** *10*, 7331-7338.
113. Hong, J.; Jin, C.; Yuan, J.; Zhang, Z. Atomic Defects in Two-Dimensional Materials: From Single-Atom Spectroscopy to Functionalities in Opto-/Electronics, Nanomagnetism, and Catalysis. *Adv. Mater.* **2017,** *29*, 1606434.
114. Milstein, T. J.; Kroupa, D. M.; Gamelin, D. R. Picosecond Quantum Cutting Generates Photoluminescence Quantum Yields Over 100% in Ytterbium-Doped $CsPbCl_3$ Nanocrystals. *Nano Lett.* **2018,** *18*, 3792-3799.
115. Reinhard, C.; Valiente, R.; Güdel, H. U. Exchange-Induced Upconversion in Rb_2MnCl_4:Yb^{3+}. *The Journal of Physical Chemistry B* **2002,** *106*, 10051-10057.
116. Dieke, G. H.; Crosswhite, H. M.; Crosswhite, H., *Spectra and Energy Levels of Rare Earth Ions in Crystals*. Interscience Publishers: New York, 1968.
117. Shannon, R. Revised Effective Ionic Radii and Systematic Studies of Interatomic Distances in Halides and Chalcogenides. *Acta Crystallographica Section A* **1976,** *32*, 751-767.
118. Pressler, K.; Snoeren, T. J.; Walsh, K. M.; Gamelin, D. R. Magnetic Amplification at Yb^{3+} "Designer Defects" in the van der Waals Ferromagnet CrI_3. *Nano Lett.* **2023,** *23*, 1320-1326.
119. Snoeren, T. J.; Pressler, K.; Kluherz, K. T.; Walsh, K. M.; De Yoreo, J. J.; Gamelin, D. R. Luminescence and Covalency in Ytterbium-Doped CrX_3 (X = Cl, Br, I) van der Waals Compounds. *J. Am. Chem. Soc.* **2023,** *145*, 17427-17434.
120. Klein, J.; Song, Z.; Pingault, B.; Dirnberger, F.; Chi, H.; Curtis, J. B.; Dana, R.; Bushati, R.; Quan, J.; Dekanovsky, L.; Sofer, Z.; Alù, A.; Menon, V. M.; Moodera, J. S.; Lončar, M.; Narang, P.; Ross, F. M. Sensing the Local Magnetic Environment through Optically Active Defects in a Layered Magnetic Semiconductor. *ACS Nano* **2023,** *17*, 288-299.

Portions of Chapter 1 are in preparation for publication, reproduced with permission from Walsh, K. M.; Gamelin, D. R.

Chapter 2. Ferromagnetism and Spin-Polarized Luminescence in Lead-Free $CsEuCl_3$ Perovskite Nanocrystals and Thin Films

Chapter 2 describes this dissertation's paradigmatic study and illustrates the utility of magneto-optical spectroscopies in revealing the electronic origins of optical transitions and probing the relationship between spin and optical functionalities.

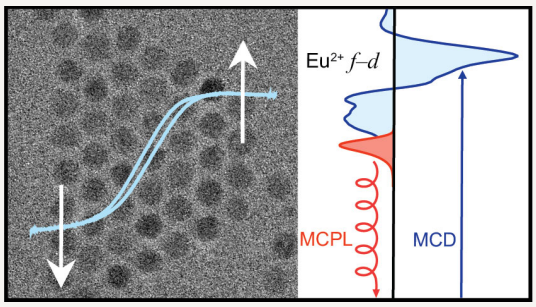

2.1 Overview

The emergence of next-generation spintronic and spin-photonic technologies will be aided by the development of materials showing strongly coupled magnetic, electronic, and optical properties. Through a combination of magneto-photoluminescence and magnetic circular dichroism spectroscopies we demonstrate strong magneto-optical responses from $CsEuCl_3$ perovskite nanocrystals and thin films in the near-UV/visible region, stemming from the *f*–*d* transitions centered at the B-site Eu^{2+} cations. We show that this material undergoes a ferromagnetic phase transition at ~3 K in both the nanocrystal and thin-film samples, resulting in complete spin alignment and indicating intrinsic ferromagnetism. We also report the observation of spin-polarized photoluminescence in the presence of a magnetic field at cryogenic temperatures, saturating with a large polarization ratio ($\Delta I/I = (I_L - I_R)/(I_L + I_R)$) of nearly 30% at modest magnetic fields (~2 T). These results highlight $CsEuCl_3$ as an intrinsically ferromagnetic, luminescent metal-halide perovskite with potentially interesting implications for future spin-based technologies using perovskites.

2.2 Introduction

Ferromagnetic EuE (E = O, S, Se, Te) semiconductors have long been employed for demonstration of spintronic functionality in transport measurements.[1] These materials have been prepared across a range of morphologies, including both bulk and nanocrystalline forms.[1-3] Despite the strong oscillator strength of the Eu^{2+} *f*–*d* transition that defines their band gaps, these materials show weak photoluminescence (PL) in the bulk[4, 5] and little or no intrinsic PL in nanocrystals. Materials that combine luminescence with ferromagnetism provide an additional magneto-optical degree of freedom that could prove attractive for basic research toward next-generation spin-photonic technologies. Recently, metal-halide perovskites have received pronounced attention due to their high PL quantum yields,[6, 7] tunable band gaps,[8, 9] and large absorption coefficients.[10, 11] Despite several studies of the spin properties of non-magnetic lead-halide perovskites,[12-14] magnetic perovskites remain underdeveloped. Previous reports of

magnetic perovskites have relied on open-shell dopants such as Mn^{2+} or Fe^{3+} to impart magnetic functionality. In some cases, ferromagnetic ordering is observed but with small magnetic moments that indicate its origin in ferromagnetic domains or inclusions, with the majority of the dopant population remaining paramagnetic.[15-18] Some observations have demonstrated weak coupling between such magnetism and the optical properties of the materials.[19] Further advances in the development of magnetic metal-halide perovskites will generate attractive opportunities to access spin-controlled electronic and photonic properties, or photon-controlled spin properties, in this versatile class of materials.

Here, we report on the magneto-optical properties of the perovskite $CsEuCl_3$ prepared in both nanocrystalline and bulk (thin-film) morphologies. Although the nanocrystal synthesis of this material has been recently reported,[20] the magnetic or magneto-optical properties of these nanocrystals have not yet been reported. Even in the bulk literature there are very few studies of $CsEuCl_3$, and none that have addressed its magnetism or magneto-optical properties. Using magnetic circular dichroism (MCD) spectroscopy, we now show that $CsEuCl_3$ displays a very strong magneto-optical response in the near-UV/visible region associated with its Eu^{2+} *f–d* optical band gap. Moreover, we identify a magnetic phase transition to a ferromagnetic phase showing a sizable magnetic hysteresis below ~3 K. We also report variable-temperature PL measurements, demonstrating strongly enhanced luminescence at low temperatures. Magneto-PL measurements further demonstrate the emission of circularly polarized light with a polarization ratio of nearly 30% at relatively small magnetic fields. The magneto-optical responses of $CsEuCl_3$ greatly exceed those reported for any other metal-halide perovskites to date. These distinctive magnetic and magneto-optical properties in $CsEuCl_3$, in conjunction with its perovskite structure and its accessibility through both chemical and vapor-deposition routes, may have promising ramifications for future spin-based technologies built around metal-halide perovskites.

2.3 Results and discussion

Colloidal $CsEuCl_3$ nanocrystals were prepared following literature procedures (see section 2.5 Methods).[20] Figure 2.1a,b show TEM images of the $CsEuCl_3$ nanocrystals studied here. The nanocrystals are spherically shaped and nearly monodisperse, with d = 10.1 ± 0.7 nm. Figure 2.1c shows a photograph of the thermally evaporated $CsEuCl_3$ thin film also studied here (see section 2.5 Methods). This film, grown on a quartz substrate, has excellent transparency and shows negligible scattering. The film thickness is estimated to be 80 nm based on quartz crystalline microbalance readings during deposition. Figure 2.1d plots powder X-ray diffraction data collected for the nanocrystals and thin film. These data show peaks consistent with perovskite $CsEuCl_3$; the experimental data are referenced against the tetragonal phase, but it is not possible to distinguish between cubic (*Pm*-3m, a = b = c = 5.62 Å, ICSD Coll. Code 31463)[21] and tetragonal (*P*4*mm*, a = b = 5.59 Å, c = 5.62 Å, ICSD Coll. Code 201316)[22] structures from these data. A similar structural ambiguity was also encountered in the analogous lead-halide perovskites.[23] The peak intensity ratios in the thin-film data indicate preferential growth along the [200] direction. We also note the presence of a weak shoulder on the [200] diffraction peak in the nanocrystal data that is not

present in the thin-film XRD data. The peaks are not sufficiently resolved to definitively identify this shoulder, but it could conceivably come from an impurity that is not removed by our sample purification steps. The $CsEuCl_3$ nanocrystals and thin films are unstable in air due to facile oxidation of Eu^{2+} to Eu^{3+},[20] and the asterisks in Figure 2.1d denote additional features that arise from the encapsulating Kapton tape used for the air-free X-ray diffraction measurements (see section 2.5 Methods).

Figure 2.2a plots room-temperature absorption, PL, and PLE spectra collected for the $CsEuCl_3$ nanocrystals. The absorption spectrum shows an intense band with pronounced structure centered around 3.7 eV. At higher energies, the main absorption feature decreases in intensity and a second, deep- UV feature displays a gradual onset. The main PL feature is centered around 2.88 eV (430 nm), close to the absorption onset. A second, less-intense PL feature is observed at ~2.2 eV, with large batch-to-batch variations in its intensity. The PLE spectra of both PL features follow the nanocrystal absorption spectrum well. The low-energy PL does not increase in intensity when the nanocrystals are exposed to air (see Appendix A), ruling out the possibility that it arises from aerobic degradation of the $CsEuCl_3$. Moreover, the PLE data (Figure 2.2a) show that this second peak is sensitized by $CsEuCl_3$ itself, meaning that the anomalous Eu^{2+} is intimately connected to the $CsEuCl_3$ lattice. Collectively, the data point to this second PL feature arising from additional Eu^{2+} species within the $CsEuCl_3$ lattice, for example, associated with point defects, rather than from lattice decomposition products.

Figure 2.2b shows variable-temperature PL spectra collected from these $CsEuCl_3$ nanocrystals. The PL intensity decreases with increasing temperature but its energy is temperature- independent, contrary to what would be expected for an excitonic transition. Instead, the data in Figure 2.2a,b are consistent with the spectroscopy of $CsEuCl_3$ being dominated by localized Eu^{2+} $4f^6 5d^1 - 4f^7$ transitions. In the octahedral B-site coordination environment of $CsEuCl_3$, the empty Eu^{2+} $5d$ orbitals of the $4f^7(^8S_{7/2})$ ground state are split into t_{2g} and e_g sets, with the t_{2g} set becoming the lowest unoccupied orbitals. The structured absorption band centered at ~3.5 eV thus corresponds to the $4f^7(^8S_{7/2}) \rightarrow 4f^6(^7F_J)5d^1(t_{2g})$ transition, with fine structure arising from

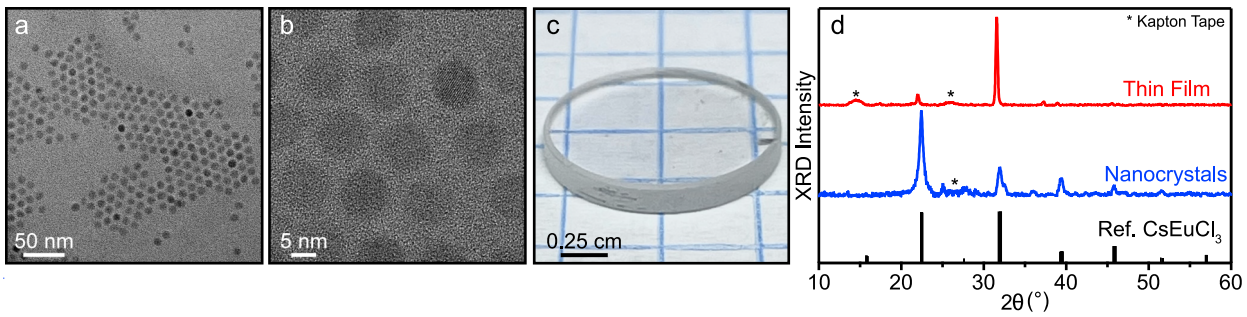

Figure 2.1. (a,b) TEM images of $CsEuCl_3$ nanocrystals. (c) Photograph of the thermally evaporated $CsEuCl_3$ thin film. (d) Powder X-ray diffraction patterns of $CsEuCl_3$ nanocrystals and $CsEuCl_3$ thin film compared to a $CsEuCl_3$ reference pattern (tetragonal, ICSD Coll. Code 201316). The asterisks correspond to additional scattering peaks due to the Kapton tape used for air-free encapsulation.

spin−orbit splittings within the $4f^6 5d^1$ excited-state configuration. The growing absorption above ~4.0 eV is attributed to the onset of $4f^7(^8S_{7/2}) \rightarrow 4f^6(^7F_J)5d^1(e_g)$ transitions.

Figure 2.2c plots PL decay curves for these $CsEuCl_3$ nanocrystals collected at a series of temperatures from 15 to 300 K. From these data, the PL decays with a time constant of ~233 ns at 15 K that decreases to ~12 ns at room temperature. In bulk Eu^{2+}-doped alkali halides, the Eu^{2+} $4f^6 5d^1 \rightarrow 4f^7$ lifetime is reported to be temperature independent with a value of ~850 ns, reasonably approximated as the Eu^{2+} radiative lifetime in these lattices.[24, 25] Eu^{2+}-doped $CsCaCl_3$ single crystals also show a PL decay time of ~1 μs at ~45 K,[26] but their anomalous temperature dependence makes direct comparison with the $CsEuCl_3$ PL difficult. Overall, the 15 K nanocrystal PL lifetime of 233 ns observed here is consistent with assignment of this PL as a Eu^{2+} $4f^6 5d^1 \rightarrow 4f^7$ transition.

Figure 2.2d summarizes the variable-temperature PL data from Figure 2.2b,c and shows that the $4f^6 5d^1 \rightarrow 4f^7$ PL lifetime and intensity both decrease with increasing temperature in

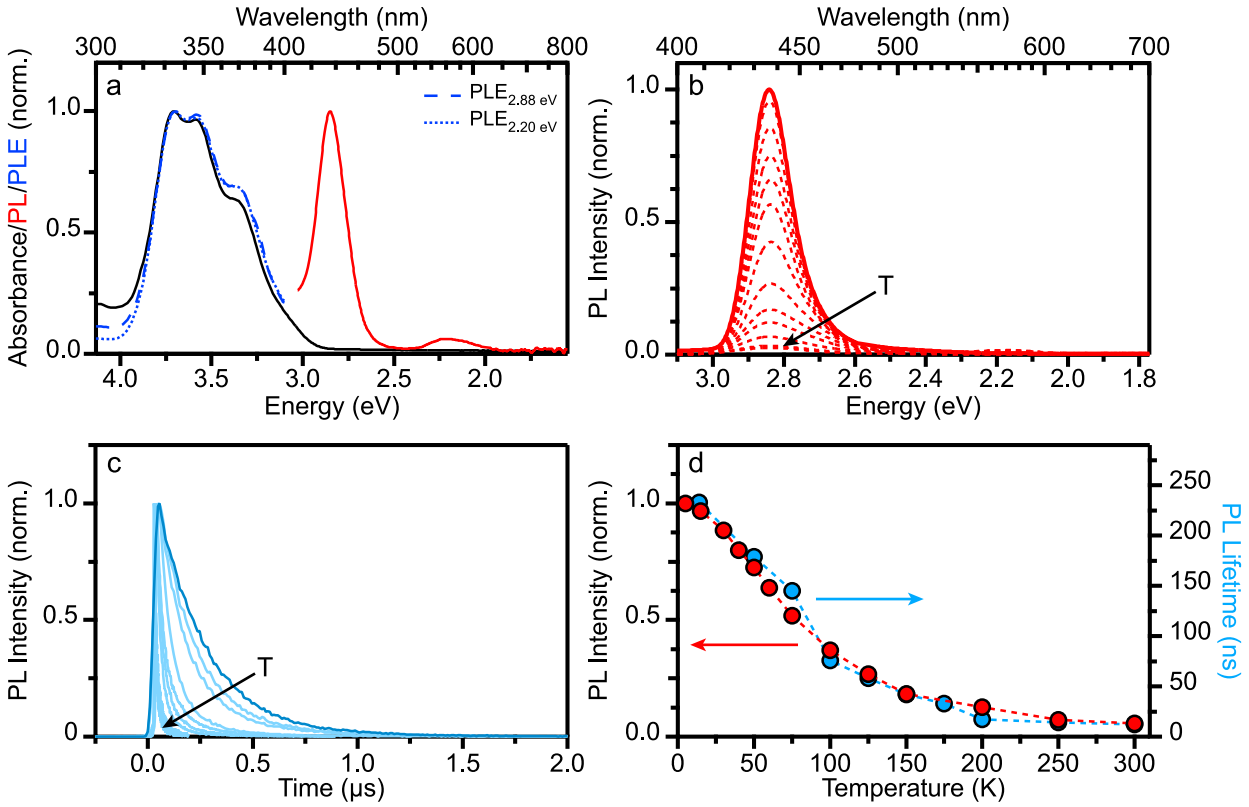

Figure 2.2. (a) Room-temperature absorption (black), PL (red), and PLE (blue) spectra of colloidal $CsEuCl_3$ nanocrystals. (b) Variable-temperature PL spectra of $CsEuCl_3$ nanocrystals collected between 5 – 300 K, excited with 375 nm light. (c) Variable-temperature TRPL spectra of $CsEuCl_3$ nanocrystals excited with 355 nm laser pulses fired at a repetition rate of 50 Hz, collected between 15 – 300 K. All PL lifetimes were fit with bi-exponential decay functions. The room-temperature average decay time was 12 ns, and the average decay time increased to 233 ns at 15 K. (d) Scatter plot of integrated PL intensities (red) and average PL lifetimes (blue) plotted as a function of temperature.

the same manner, indicating the presence of thermally activated nonradiative losses with a very small energy barrier. Indeed, both metrics drop by ~95% over this temperature range, consistent with the low room-temperature PLQY (~2%) reported previously.[20] Most likely, this temperature dependence stems from accelerating intrananocrystal energy migration enabled by thermal broadening of the absorption and emission bands, which increases donor−acceptor spectral overlap. Energy migration commonly leads to nonradiative relaxation in related materials with high concentrations of luminescent centers, because the excitation can sample a large volume during its lifetime and thus has a high probability of finding a trap. Notably, the weaker, low-energy PL from Figure 2.2a is not observed in the low-temperature PL spectra shown in Figure 2.2b and appears only above ~200 K (see Appendix A), consistent with thermally activated energy migration and trapping. In a previous report, the room-temperature PLQY of $CsEuCl_3$ nanocrystals was improved from 2 to 6% after a postsynthetic halide surface treatment.[20] This modest PLQY enhancement may suggest that at least some nonradiative losses in these nanocrystals can be attributed to surface trapping, but it also suggests the prevalence of internal lattice defects as well. A similar and even broader sub-bandgap PL feature is observed in the $CsEuCl_3$ thin films as well, but this feature disappears with annealing (see Appendix A), consistent with the relevant trap involving a native defect. In many Eu^{2+}-doped halide crystals, Eu^{2+} can occupy multiple lattice sites with different coordination numbers,[27, 28] leading to multiple PL peaks and nonradiative recombination sites; trapping in $CsEuCl_3$ is thus tentatively attributed to such defects, for example, a combination of Eu_{Cs}, Eu_i, and $Eu_{surface/grain\ boundary}$. Further improvement of this material's PLQY at high temperatures will therefore require suppressing formation of internal lattice defects. Overall, these observations indicate thermally activated energy migration in $CsEuCl_3$ that results in efficient energy trapping at both nonradiative and emissive defect sites.

Because Eu^{2+} is magnetic, magneto-optical spectroscopies were applied to investigate the transitions seen by absorption and PL in more detail. Figure 2.3a plots $CsEuCl_3$ nanocrystal MCD spectra collected at 1.7 K as a function of magnetic fields between 0.1 and 5.0 T. These spectra show a derivative-shaped MCD band centered around 3.5 eV and an additional positive MCD feature around 4.0 eV, coinciding with the energetic positions of the observed absorption features. The $CsEuCl_3$ MCD spectrum resembles those of dilute Eu^{2+} dopants in other halide lattices (Eu^{2+}:CsCl and Eu^{2+}:$CsNaEuCl_3$,[29] see Appendix A), consistent with assignment of this electronic transition in $CsEuCl_3$ as the $4f^7(^8S_{7/2}) \rightarrow 4f^6(^7F_J)5d(t_{2g})$ transition of Eu^{2+}. These data show a trend of increasing MCD intensity with increasing magnetic field. All components of the MCD fine structure gain intensity with increasing field and saturate at the highest fields in a similar manner.

Figure 2.3b plots parallel data collected for the $CsEuCl_3$ thin film shown in Figure 2.1. The thin-film spectra are very similar to the nanocrystal data, with the main differences being narrower features at 3.1 and 3.7 eV and the absence of the low-energy MCD tail observed in the nanocrystal spectra. Due to the much larger surface-to-volume ratios of the nanocrystals, we interpret these spectral differences as reflecting the contributions of surface or near-surface Eu^{2+}

ions with slightly different coordination environments to the nanocrystal spectra. Indeed, the additional MCD component present in the nanocrystals (see Appendix A) is similar to the MCD spectra of $Eu(OCN)_2$ nanocrystals;[30] $Eu(OCN)_2$ crystallizes in a layered structure, resulting in a Eu^{2+} coordination environment that may be similar to the proposed surface Eu^{2+} ions in $CsEuCl_3$. Overall, the MCD spectra observed for $CsEuCl_3$ are characteristic of Eu^{2+} ions in halide crystals and confirm assignment of the dominant $CsEuCl_3$ nanocrystal absorption band to the *f–d* transitions of B-site Eu^{2+} ions. Notably, the MCD signal amplitudes in $CsEuCl_3$ (e.g., $\Delta A/A_{max} \sim 1.2$, Figure 2.3b) are a factor of ~20× larger than those of $CsPbBr_3$ ($\Delta A/A_{max} \sim 0.06$[31]) under similar measurement conditions and even a factor of ~2× larger than those of Mn^{2+}:CdSe quantum dots showing giant excitonic Zeeman splittings,[32] highlighting the very large magneto-optical response of $CsEuCl_3$.

The $CsEuCl_3$ MCD intensities decrease with increasing temperature (see Appendix A), consistent with our assignment of this as C-term MCD intensity[33] reliant upon magnetization of the Eu^{2+} ground state. The full variable-temperature, variable- field MCD data sets for these two $CsEuCl_3$ samples are summarized in Figure 2.3c,d, plotted as MCD isotherms ($I(B)_T$ *vs* $\mu_B B/kT$). The 1.7 K isotherms in Figure 2.3c,d both approach saturation at large B/T, consistent with a

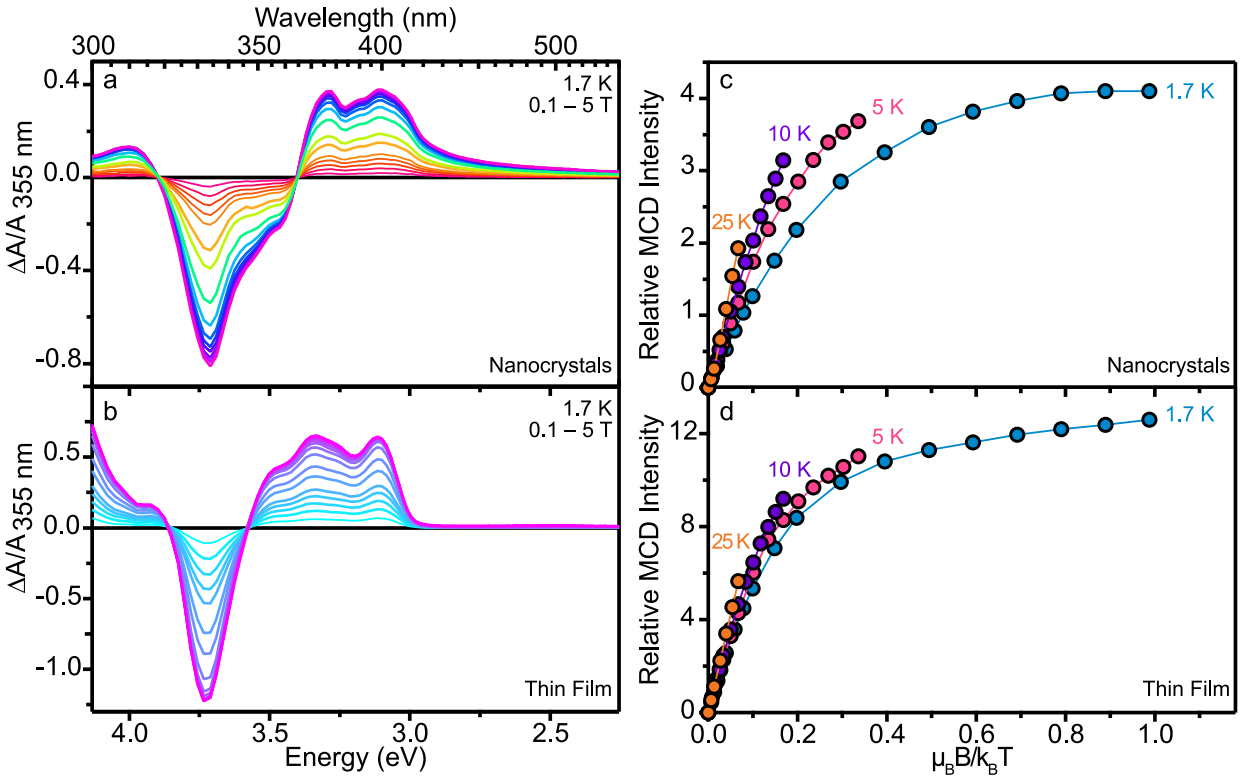

Figure 2.3. Variable-field MCD spectra of $CsEuCl_3$ nanocrystals (a) and thin film (b) collected between 0.1 and 5 T at 1.7 K. (c,d) Scatter plots of total integrated MCD intensity vs $\mu_B B/k_B T$. The temperature dependence and saturation at large B/T are consistent with a paramagnetic ground state. The nesting of isotherms indicates a temperature-dependent Boltzmann population distribution over a split ground-state manifold.

dominant C-term contribution. Further, the isotherms for different temperatures do not all lie on top of one another as for a simple paramagnet but instead show nesting indicative of a more complicated magnetic ground state. Often, such nesting reflects splittings of magnetic ground states through either first- or second-order spin−orbit interactions, the latter coupled with low-symmetry distortions, but the $^8S_{7/2}$ ground state of Eu^{2+} has no first-order orbital angular momentum and its valence *f*-shell electrons are only weakly influenced by low-symmetry crystal fields. Indeed the crystal-field splitting of the Eu^{2+} ground state is typically smaller than k_BT across all temperatures[29] and is therefore not responsible for this nesting.

To probe the magnetic ground state further, field-sweep MCD measurements were performed at the lowest temperature achievable in our MCD instrument, ~ 1.7 K. Figure 2.4a plots the normalized MCD intensities of the strong negative feature centered around 3.71 eV (334 nm) for both the nanocrystal and thin-film samples, measured during continuous "positive"

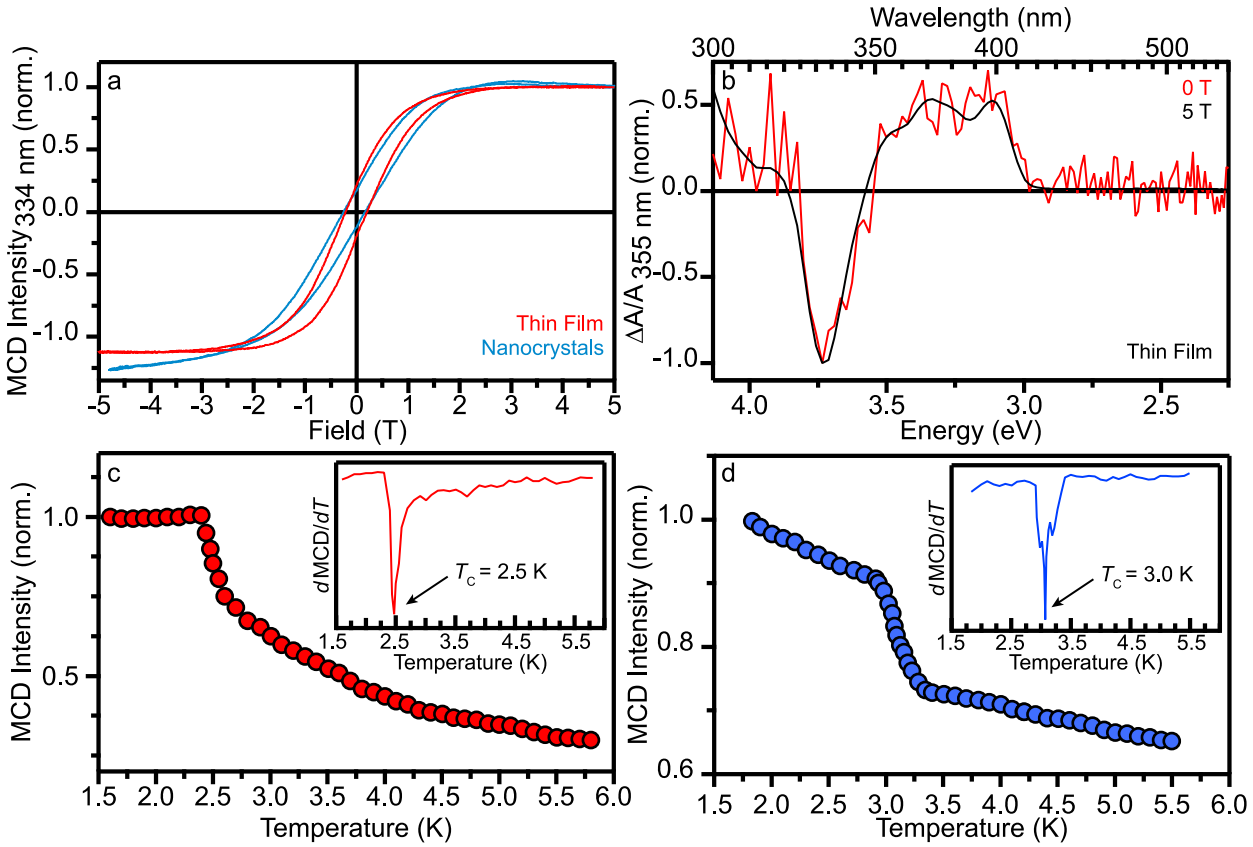

Figure 2.4. 1.7 K magnetic field-sweep data for $CsEuCl_3$ nanocrystals and thin film, collected by monitoring the MCD intensity of the feature centered around 3.71 eV (334 nm) as a function of applied magnetic field. (b) 0 T (remanent) MCD spectrum of the $CsEuCl_3$ thin film collected at 1.7 K following hysteresis measurement, plotted together with the 5 T spectrum of the same sample measured under the same conditions and scaled for comparison. (c,d) Curie temperature plots of the thin film and nanocrystal samples collected at 0.15 T monitoring the MCD intensity centered around 3.71 eV (334 nm) as a function of temperature. The Curie temperatures were found to be ca. 2.5 and 3.0 K for the thin film and nanocrystals, respectively.

and "negative" magnetic-field sweeps at 1.7 K. The data for both samples reveal clear magnetic hystereses characterized by a remanence of ~12% and a coercivity of 0.2 T. Figure 2.4b shows that the MCD spectrum measured at 0 T (remanence) is superimposable upon the high-field (5 T) MCD spectrum of the same sample, indicating that this remanent magnetization is associated with $CsEuCl_3$ itself rather than with impurities or other spurious sources. The saturation observed at high fields, particularly cleanly in the thin film, demonstrates that all Eu^{2+} participate in this magnetic ordering, and not just a small subset of Eu^{2+} ions. The nanocrystals may require larger fields to achieve full saturation because of contributions from surface Eu^{2+} that are poorly integrated into the ferromagnetic ordering. This interpretation is supported by variable-temperature measurements. Figure 2.4c,d plot the normalized 0.15 T MCD intensities of the same 3.17 eV feature for the thin film and nanocrystals as a function of temperature. These data show distinct discontinuities in the magnetization, attributable to the ferromagnetic phase transition. The insets in Figure 2.4c,d plot dMCD/dT, from which Curie temperatures of $T_C \sim 2.5$ and 3.0 K are obtained for the thin film and nanocrystals, respectively. Whereas the thin-film magnetization plateaus below the ordering temperature, the nanocrystal magnetization continues to rise slightly, supporting the interpretation above that surface Eu^{2+} contributes a paramagnetic signal on top of the nanocrystal ferromagnetism in the latter.

The rich magnetism of $CsEuCl_3$ demonstrated above should also manifest itself in the PL of these materials. Figure 2.5a plots circularly resolved PL spectra of the $CsEuCl_3$ nanocrystals measured at 1.7 K in applied magnetic fields of 0−5 T. The data show a large disparity between left- and right-circularly polarized PL intensities in an applied magnetic field. Figure 2.5b plots the PL polarization ratio, $\Delta I/I = (I_L - I_R)/(I_L + I_R)$. These data show a rapidly increasing degree of circular polarization with increasing magnetic field, saturating at $\Delta I/I \sim 0.29$, indicating strongly spin-polarized PL from perovskite $CsEuCl_3$ nanocrystals. For comparison, $\Delta I/I$ is ~0.05 for $MAPbI_3$ thin films under similar measurement conditions.[34] We note that $\Delta I/I$ in $CsEuCl_3$ reaches saturation at a lower field than needed to saturate the MCD intensity at the same temperature (see Appendix A); the

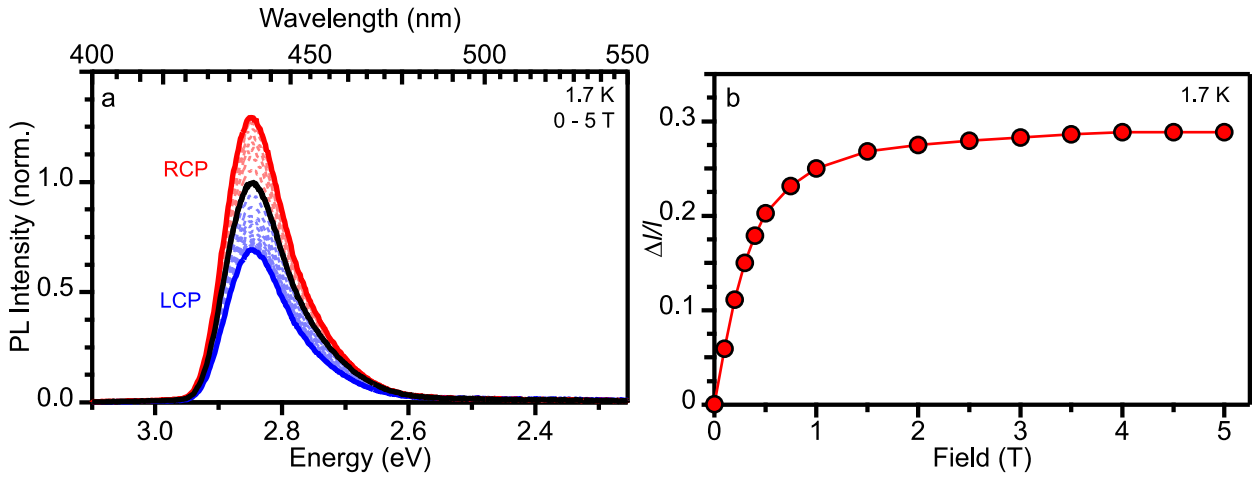

Figure 2.5. (a) $CsEuCl_3$ nanocrystal MCPL spectra collected at 1.7 K between 0 – 5 T. (b) Scatter plot of nanocrystal MCPL polarization ratio ($\Delta I/I$) *vs* magnetic field at 1.7 K.

MCPL field dependence reflects the magnetization (and potentially also spin-relaxation dynamics) of the emissive excited state rather than magnetization of the ground state.

Characterization of the $CsEuCl_3$ electronic structure, as informed by the optical and magneto-optical spectroscopies described above, is fundamentally important for assessing the potential of this material for future spin-based applications. Using MCD and PL spectroscopies, we show here that the strong first absorption band of $CsEuCl_3$ is a Eu^{2+} *f–d* transition, similar to EuE (E = O, S, Se, Te) ferromagnetic semiconductors.[2] This assignment defines the nature of the optical gap in $CsEuCl_3$. The data reported here suggest that this transition is fairly isolated, similar to the *f–d* transitions of Eu^{2+} ions diluted into other chloride lattices. This result is consistent with the absence of confinement effects in the energy of this transition upon changing from thin-film to nanocrystal morphologies. The primary difference observed between the $CsEuCl_3$ nanocrystals and thin films is that the nanocrystals show additional spectral and magnetic contributions relative to the thin films, attributed to surface Eu^{2+}.

The magnetic properties reported here for $CsEuCl_3$ are not found in any other metal-halide perovskites. Ferromagnetic ordering of Eu^{2+} spins is observed with T_C = 2.5−3.0 K. The similar magnetic hystereses and ordering temperatures in nanocrystals and thin films indicate that this ferromagnetism is intrinsic to bulk $CsEuCl_3$. Importantly, all Eu^{2+} participate in this ferromagnetic ordering, contrasting $CsEuCl_3$ with the several magnetically doped metal-halide perovskite and related semiconductors recently reported to show ferromagnetism;[15-18] in the latter, the magnetic ions are present at relatively low concentrations (compared to $CsEuCl_3$) and only minority populations appear to order ferromagnetically. Those materials are thus arguably better described as metal-halide perovskites containing ferromagnetic inclusions or domains, whereas $CsEuCl_3$ is a *bona fide* ferromagnetic metal-halide perovskite. We note that another class of 2D hybrid metal-halides has also shown ferromagnetism in some compositions, *e.g.*, $(RNH_2)_2MCl_4$ (M = Cr, Cu; R = alkyl),[35, 36] but these bear little resemblance to the perovskite structure.[37]

The excited-state localization observed spectroscopically implies that this ferromagnetism results from Eu^{2+}-Eu^{2+} *f–d*- and super-exchange, as in the canonical EuE magnetic semiconductors.[1] For comparison, ferromagnetism has also been reported in $EuCl_2$ and EuI_2 (T_C = 1.6 – 1.8 K; 9- and 7-coordinate, respectively), but it is absent in $EuBr_2$ (8-coordinate) and $(C_4H_9NH_3)_2EuI_4$ down to 1.1 and 1.8 K, respectively.[38, 39] Much more stable ferromagnetism is observed in the EuE lattices (E = O, S, Se; T_C = 70, 16, 6 K, respectively).[40, 41] Although MCD spectroscopy does not show the same large *d*-band spin splittings in $CsEuCl_3$ as found in, *e.g.*, EuS nanocrystals,[42] the observation of ferromagnetic ordering in a metal-halide perovskite may present interesting opportunities for integration of magnetism into existing or future perovskite technologies. For example, the strong spin- polarizable PL found in $CsEuCl_3$ introduces an attractive functionality for potential spin-photonics applications not found in other perovskites. Moreover, $CsEuCl_3$ shares the same lattice structure and similar lattice parameters with other popular metal-halide perovskites based on Pb^{2+} and Sn^{2+}, and it may therefore be possible to grow architectures interfacing ferromagnetic $CsEuCl_3$ with commensurate metal-halide perovskites such as $CsPbCl_3$ or $CsSnCl_3$ that possess complementary functionalities, thereby expanding the

possibilities for manipulating the optoelectronic properties of perovskites. Heterointerfacing of this type may also be accessible on the nanoscale using wet-chemical methods.

2.4 Conclusion

Spectroscopic results are presented that elucidate the fundamental electronic structure of $CsEuCl_3$, both in nanocrystals and in bulk form. PL in this material is assigned to the *f*–*d* optical transition of Eu^{2+} in the B site of the perovskite $CsEuCl_3$ lattice, and the corresponding *f*–*d* absorption band defines the optical gap of the material. The absorption, MCD, and PL data all indicate that this transition is fairly localized. Variable-temperature PL measurements suggest efficient energy migration within photoexcited $CsEuCl_3$ that accelerates with increasing temperature and that leads to trapping and nonradiative relaxation. In the nanocrystals, for example, the PL intensity decreases by a factor of ∼20 between 5 K and room temperature. MCD spectroscopy also reveals ferromagnetic ordering with T_C = 2.5−3.0 K in $CsEuCl_3$, and magneto- PL demonstrates spin-polarizable emission with maximum polarization ratios of ∼30%. This strong ferromagnetism combined with the strong low-temperature PL and the large coupling between the magnetism and the electronic transitions of $CsEuCl_3$ distinguish this material among metal-halide perovskites. When combined with the scalability of thermal evaporation methods for large-area thin-film growth and the processability of colloidal nanocrystals, these results present $CsEuCl_3$ as an attractive and flexible candidate for integration of magnetism into future spintronic or spin-photonic architectures based on metal-halide perovskites.

2.5 Methods

Chemicals. Unless otherwise stated, all chemicals were used as purchased without further purification. Nanocrystal syntheses employed Cs_2CO_3 (99% Alpha Aesar), $EuCl_3$ (99.99%, Sigma- Aldrich), 1-octadecene (ODE, 90% Sigma-Aldrich), oleylamine (OAm, 70% Sigma-Aldrich), oleic acid (OA, 90%, Sigma-Aldrich), and trioctylphosphine (TOP, 97% Sigma-Aldrich). Thin films were prepared with $EuCl_2$ (99.99%, Sigma-Aldrich) and CsCl (99.999%, Strem).

Preparation of Eu^{2+} precursor. One mmol of $EuCl_3$ was added to 5 mL of OAm and evacuated at 120 °C for 60 min. The solution was then reacted at 300 °C under N_2 for 40 min, upon which it was left to cool to room temperature and transferred to a glovebox for future use.

Preparation of Cs-Oleate. 0.2 g Cs_2CO_3 was added to 7.5 mL ODE and 0.7 mL OA. The solution was evacuated at 120 °C for 60 min, or until all residual carbonic acid was removed. The flask was then switched to N_2 and heated to 150 °C for 30 min.

Preparation of $CsEuCl_3$ nanocrystals. The $CsEuCl_3$ nanocrystal synthesis was adapted from a previous literature report.[20] In a standard reaction, 5 mL ODE, 0.5 mL TOP, and 0.25 mL OA were degassed at 120 °C for 60 min, upon which the reaction flask was switched to N_2 and 2 mL of the Eu^{2+}-precursor was added. The temperature was raised to 250 °C and held for 25 min. Then, 2 mL of Cs-oleate was added to the Eu^{2+} flask and the reaction proceeded for 45 min after the temperature restabilized at 250 °C. The reaction was quenched with a room-temperature water bath, and 6 mL of hexanes was added. The product was separated from the reaction solution by centrifuging at 8000 rpm for 5 min, followed by resuspension of the pellet in hexane, and repeated once. After the second resuspension in hexane, the nanocrystals were purified via further centrifugation at 4000 rpm for 1 min, where the supernatant was collected and finally centrifuged at 2000 rpm for 2 min. The suspended nanocrystalline product was then collected. $CsEuCl_3$ decomposes in air, so all sample synthesis, handling, transport, and measurement was performed with careful exclusion of air.

Preparation of Thin Films. Thin-film samples were prepared on quartz substrates via thermal evaporation. In a standard $CsEuCl_3$ deposition, $EuCl_2$ and CsCl were simultaneously evaporated in stoichiometric amounts at a rate of ~0.25 Å/s, as monitored by quartz crystal microbalances. After deposition, the film was annealed at 300 °C for 30 min under inert atmosphere. Eu^{2+}-doped CsCl thin films were prepared by simultaneous thermal evaporation of $EuCl_2$ and CsCl with no postdeposition annealing. $CsEuCl_3$ decomposes in air, so all sample synthesis, handling, transport, and measurement was performed with careful exclusion of air.

Analytical characterization. Thin film and nanocrystal samples were encapsulated in Kapton tape under inert conditions prior to collecting X-ray diffraction data. X-ray diffraction measurements were performed using a Bruker D8 Discover Microfocus diffractometer with a Cu Kα source (1.54 Å). Transmission electron microscope images were collected using a Technai G2 F20 Supertwin TEM operating at 200 kV.

Electronic absorption, PL, time-resolved PL spectroscopies. Electronic absorption spectra were collected at room temperature using Cary 60 and Cary 5000 spectrometers. Variable-

temperature photoluminescence (PL) and time-resolved photo- luminescence (TRPL) data were collected by sandwiching drop cast nanocrystals between two quartz disks and loading into a closed-cycle helium cryostat. Continuous-wave PL spectra were collected by exciting the sample with a 375 nm diode laser and detected on a liquid-nitrogen-cooled CCD mounted on a monochromator. Time- resolved PL data were collected by irradiating the sample with 355 nm light generated from the third harmonic of an Ekspla Nd:YAG laser firing at a repetition rate of 50 Hz, with the PL detected by a Hamamatsu R928 photomultiplier tube mounted on a monochromator. PL excitation (PLE) measurements as well as some thin-film PL measurements were performed using an Edinburgh FLS1000 fluorometer equipped with a xenon flash lamp and visible PMT detector. PLE measurements were performed by monitoring the PL intensity at the desired wavelength while tuning the excitation wavelength, and PL measurements on this instrument were performed using 375 nm excitation.

Magnetic circular dichroism (MCD), magnetic circularly polarized luminescence (MCPL) spectroscopies. Nanocrystal samples for magneto-optical measurements were prepared as a mull suspension by mixing dried nanocrystals with polydimethylsiloxane, then sandwiched between two quartz disks. Thin film samples were prepared by thermally depositing directly onto a quartz disk. Magneto-optical data were collected by loading samples into a superconducting magneto-optical cryostat equipped with a variable- temperature sample compartment (Cryo-Industries SMC-1659 OVT) oriented in the Faraday configuration. MCD spectra were collected using an Aviv 40DS spectropolarimeter. MCPL spectra were collected using 375 nm laser diode excitation. The sample PL was guided along the magnetic field axis through a liquid crystal variable retardation plate set to $\lambda/4$ at the emission maximum, followed by a linear polarizer to separate left- and right-circularly polarized components. The PL was then passed through a fiber-optic cable and detected on a liquid nitrogen-cooled CCD mounted on a monochromator. MCPL ratios are defined as $\Delta I/I = (I_L - I_R)/(I_L + I_R)$ following sign conventions outlined in Piepho and Schatz.[14] At liquid helium temperatures all sample depolarization ratios were checked by matching the CD signal of a chiral molecule placed before and after the sample along the optical path. The depolarization ratios of all samples were ~5%.

2.6 References

1. Mauger, A.; Godart, C. The Magnetic, Optical, and Transport Properties of Representatives of a Class of Magnetic Semiconductors: The Europium Chalcogenides. *Phys. Rep.* **1986,** *141*, 51-176.
2. Wachter, P. Optical Electrical and Magnetic Properties of the Europium Chalcogenides and the Rare Earth Pnictides. *Crit. Rev. Solid State Sci.* **1972,** *3*, 189-241.
3. Boncher, W.; Dalafu, H.; Rosa, N.; Stoll, S. Europium Chalcogenide Magnetic Semiconductor Nanostructures. *Coord. Chem. Rev.* **2015,** *289-290*, 279-288.
4. Tsu, R.; Esaki, L. Luminescence Spectra of Europium Chalcogenides: EuO, EuS, and EuSe. *Phys. Rev. Lett.* **1970,** *24*, 455-459.
5. Hulin, M. D.; Hanus, J.; Benoit A La Guillaume, C.; Reed, T. G. Luminescence of EuTe and Other Europium Chalcogenides. *Solid State Commun.* **1970,** *8*, 1525-1528.
6. Di Stasio, F.; Christodoulou, S.; Huo, N.; Konstantatos, G. Near-Unity Photoluminescence Quantum Yield in $CsPbBr_3$ Nanocrystal Solid-State Films *via* Postsynthesis Treatment with Lead Bromide. *Chem. Mater.* **2017,** *29*, 7663-7667.
7. Koscher, B. A.; Swabeck, J. K.; Bronstein, N. D.; Alivisatos, A. P. Essentially Trap-Free $CsPbBr_3$ Colloidal Nanocrystals by Postsynthetic Thiocyanate Surface Treatment. *J. Am. Chem. Soc.* **2017,** *139*, 6566-6569.
8. Protesescu, L.; Yakunin, S.; Bodnarchuk, M. I.; Krieg, F.; Caputo, R.; Hendon, C. H.; Yang, R. X.; Walsh, A.; Kovalenko, M. V. Nanocrystals of Cesium Lead Halide Perovskites ($CsPbX_3$, X = Cl, Br, and I): Novel Optoelectronic Materials Showing Bright Emission with Wide Color Gamut. *Nano Lett.* **2015,** *15*, 3692-3696.
9. Shamsi, J.; Urban, A. S.; Imran, M.; De Trizio, L.; Manna, L. Metal Halide Perovskite Nanocrystals: Synthesis, Post-Synthesis Modifications, and Their Optical Properties. *Chem. Rev.* **2019,** *119*, 3296–3348.
10. Manser, J. S.; Christians, J. A.; Kamat, P. V. Intriguing Optoelectronic Properties of Metal Halide Perovskites. *Chem. Rev.* **2016,** *116*, 12956–13008.
11. De Roo, J.; Ibáñez, M.; Geiregat, P.; Nedelcu, G.; Walravens, W.; Maes, J.; Martins, J. C.; Van Driessche, I.; Kovalenko, M. V.; Hens, Z. Highly Dynamic Ligand Binding and Light Absorption Coefficient of Cesium Lead Bromide Perovskite Nanocrystals. *ACS Nano* **2016,** *10*, 2071-2081.
12. Belykh, V. V.; Yakovlev, D. R.; Glazov, M. M.; Grigoryev, P. S.; Hussain, M.; Rautert, J.; Dirin, D. N.; Kovalenko, M. V.; Bayer, M. Coherent Spin Dynamics of Electrons and Holes in $CsPbBr_3$ Perovskite Crystals. *Nat. Commun.* **2019,** *10*, 673.
13. Utzat, H.; Sun, W.; Kaplan Alexander, E. K.; Krieg, F.; Ginterseder, M.; Spokoyny, B.; Klein Nathan, D.; Shulenberger Katherine, E.; Perkinson Collin, F.; Kovalenko Maksym, V.; Bawendi Moungi, G. Coherent Single-Photon Emission from Colloidal Lead Halide Perovskite Quantum Dots. *Science* **2019,** *363*, 1068-1072.
14. Crane, M. J.; Jacoby, L. M.; Cohen, T. A.; Huang, Y.; Luscombe, C. K.; Gamelin, D. R. Coherent Spin Precession and Lifetime-Limited Spin Dephasing in $CsPbBr_3$ Perovskite Nanocrystals. *Nano Lett.* **2020,** *20*, 8626-8633.
15. Ning, W.; Bao, J.; Puttisong, Y.; Moro, F.; Kobera, L.; Shimono, S.; Wang, L.; Ji, F.; Cuartero, M.; Kawaguchi, S.; Abbrent, S.; Ishibashi, H.; De Marco, R.; Bouianova Irina, A.; Crespo Gaston, A.; Kubota, Y.; Brus, J.; Chung Duck, Y.; Sun, L.; Chen Weimin, M.*, et al.* Magnetizing Lead-Free Halide Double Perovskites. *Sci. Adv.* **2020,** *6*, eabb5381.
16. Náfrádi, B.; Szirmai, P.; Spina, M.; Lee, H.; Yazyev, O. V.; Arakcheeva, A.;

Chernyshov, D.; Gibert, M.; Forró, L.; Horváth, E. Optically Switched Magnetism in Photovoltaic Perovskite CH_3NH_3(Mn:Pb)I_3. *Nat. Commun.* **2016,** *7*, 13406.
17. Ren, L.; Wang, Y.; Wang, M.; Wang, S.; Zhao, Y.; Cazorla, C.; Chen, C.; Wu, T.; Jin, K. Tuning Magnetism and Photocurrent in Mn-Doped Organic–Inorganic Perovskites. *J. Phys. Chem. Lett.* **2020,** *11*, 2577-2584.
18. Rajamanickam, N.; Chowdhury, T. H.; Isogami, S.; Islam, A. Magnetic Properties in $CH_3NH_3PbI_3$ Perovskite Thin Films by Mn Doping. *J. Phys. Chem. C* **2021,** *125*, 20104-20112.
19. Zhang, K.; Zhao, J.; Hu, Q.; Yang, S.; Zhu, X.; Zhang, Y.; Huang, R.; Ma, Y.; Wang, Z.; Ouyang, Z.; Han, J.; Han, Y.; Tang, J.; Tong, W.; Zhang, L.; Zhai, T. Room-Temperature Magnetic Field Effect on Excitonic Photoluminescence in Perovskite Nanocrystals. *Adv. Mater.* **2021**, 2008225.
20. Huang, J.; Lei, T.; Siron, M.; Zhang, Y.; Yu, S.; Seeler, F.; Dehestani, A.; Quan, L. N.; Schierle-Arndt, K.; Yang, P. Lead-Free Cesium Europium Halide Perovskite Nanocrystals. *Nano Lett.* **2020,** *20*, 3734-3739.
21. Meyer, G. Neue Chlor-PeroWskite Mit Zweiwertigen Lanthaniden: $CsLn^{II}Cl_3$ (Ln^{II} = Sm, Eu, Tm, Yb). *Die Naturwissenschaften* **1978,** *65*, 258-258.
22. Nocera, D. G.; Morss, L. R.; Fahey, J. A. Preparation, Crystal Structure, and Enthalpy of Formation of Cesium Europium(II) Chloride, $CsEuCl_3$. *J. lnorg. Nucl. Chem.* **1980,** *42*, 55-59.
23. Cottingham, P.; Brutchey, R. L. On the Crystal Structure of Colloidally Prepared $CsPbBr_3$ Quantum Dots. *Chem. Commun.* **2016,** *52*, 5246-5249.
24. Pedrero, E. N.; Hernández, J. A.; Flores, C. J.; García-Bórquez, A.; Tocho, J. O.; Villagrán-Muniz, M.; García Solé, J.; Murrieta, H. S. Analysis of the Optical Behaviour of Eu^{2+} Ions in CsCl Crystals. *Phys. Status Solidi B* **1997,** *203*, 591-598.
25. Muñoz, G. H.; De La Cruz, C. L.; Muñoz, A. F.; Rubio, J. O. High-Temperature Luminescence Properties of Eu^{2+}-Activated Alkali Halide Phosphor Materials. *J. Mater. Sci. Lett.* **1988,** *7*, 1310-1312.
26. Tyagi, M.; Zhuravleva, M.; Melcher, C. L. Theoretical and Experimental Characterization of Promising New Scintillators: Eu^{2+} Doped $CsCaCl_3$ and $CsCaI_3$. *J. Appl. Phys.* **2013,** *113*, 203504.
27. López, F. J.; Murrieta, H. S.; Hernández, J. A.; Rubio, J. O. Optical Absorption and Luminescence Investigations of the Precipitated Phases of Eu^{2+} in NaCl and KCl Single Crystals. *Phys. Rev. B* **1980,** *22*, 6428-6439.
28. Rubio, J. O.; Murrieta, H. S.; Hernández, J. A.; López, F. J. Addendum to "Optical Absorption and Luminescence Investigations of the Precipitated Phases of Eu^{2+} in NaCl and KCl Single Crystals". *Phys. Rev. B* **1981,** *24*, 4847-4851.
29. Banerjee, A. K.; Schwartz, R. W. The Absorption, Magnetic Circular Dichroism and Emission of Eu^{2+} in Cubic Elpasolites. *J. Phys. Chem. Solids* **1981,** *42*, 1057-1060.
30. Hasegawa, Y.; Koide, K.; Tsurui, M.; Kitagawa, Y.; Nakanishi, T.; Doi, Y.; Hinatsu, Y.; Fushimi, K. Circularly Polarized Absorption and Luminescence of Semiconductor Eu-OCN Nanocrystals in the Blue Region of the Electromagnetic Spectrum. *ChemPhysChem* **2020,** *21*, 2019-2024.
31. Jacoby, L. M.; Crane, M. J.; Gamelin, D. R. Coherent Spin Dynamics in Vapor-Deposited $CsPbBr_3$ Perovskite Thin Films. *Chem. Mater.* **2022,** *34*, 1937-1945.
32. Nelson, H. D.; Bradshaw, L. R.; Barrows, C. J.; Vlaskin, V. A.; Gamelin, D. R. Picosecond Dynamics of Excitonic Magnetic Polarons in Colloidal Diffusion-Doped $Cd_{1-x}Mn_xSe$ Quantum Dots. *ACS Nano* **2015,** *9*, 11177-11191.

33. Schatz, P. N.; Piepho, S. B., *Group Theory in Spectroscopy: With Applications to Magnetic Circular Dichroism*. Wiley: New York, 1983.
34. Zhang, C.; Sun, D.; Yu, Z.-G.; Sheng, C.-X.; McGill, S.; Semenov, D.; Vardeny, Z. V. Field-Induced Spin Splitting and Anomalous Photoluminescence Circular Polarization in $CH_3NH_3PbI_3$ Films at High Magnetic Field. *Phys. Rev. B* **2018,** *97*, 134412.
35. Bellitto, C.; Day, P. Bis(monoalkylammonium) Tetrachlorochromates(II): A New Series of Two-Dimensional Ionic Ferromagnets. *J. Chem. Soc., Chem. Commun.* **1976**, 870-871.
36. Polyakov, A. O.; Arkenbout, A. H.; Baas, J.; Blake, G. R.; Meetsma, A.; Caretta, A.; van Loosdrecht, P. H. M.; Palstra, T. T. M. Coexisting Ferromagnetic and Ferroelectric Order in a $CuCl_4$-based Organic–Inorganic Hybrid. *Chem. Mater.* **2012,** *24*, 133-139.
37. Akkerman, Q. A.; Manna, L. What Defines a Halide Perovskite? *ACS Energy Lett.* **2020,** *5*, 604-610.
38. Sanchez, J. P.; Friedt, J. M.; Bärnighausen, H.; Van Duyneveldt, A. J. Structural, Magnetic, and Electronic Properties of Europium Dihalides EuX_2 (X = Cl, Br, I). *lnorg. Chem.* **1985,** *24*, 408-415.
39. Mitzi, D. B.; Liang, K. Preparation and Properties of $(C_4H_9NH_3)_2EuI_4$: A Luminescent Organic−Inorganic Perovskite with a Divalent Rare-Earth Metal Halide Framework. *Chem. Mater.* **1997,** *9*, 2990-2995.
40. Menyuk, N.; Dwight, K.; Reed, T. B. Critical Magnetic Properties and Exchange Interactions in EuO. *Phys. Rev. B* **1971,** *3*, 1689-1698.
41. Van Houten, S. Magnetic Interaction in EuS, EuSe, and EuTe. *Phys. Lett.* **1962,** *2*, 215-216.
42. Asuigui, D. R. C.; De Siena, M. C.; Fainblat, R.; James, D.; Gamelin, D. R.; Stoll, S. L. Giant Band Splittings in EuS and EuSe Magnetic Semiconductor Nanocrystals. *Chem. Commun.* **2020,** *56*, 5843–5846.

Chapter 3. Selective Chemical Reactivity in Spin-Photonic $A_2Cr(Cl,Br)_4$ Two-Dimensional Perovskite Ferromagnets

Chapter 3 demonstrates the ability to tune the dimensionality of the chemical reactivity of a family of two-dimensional Cr^{2+} ferromagnets, enabling new functionalities including ambient stability and magneto-heterostructures. These Cr^{2+} 2D perovskites exhibit magnon-assisted spin-flip absorption transitions which provide a purely optical probe of spin correlation in this material, making them particularly attractive spin-photonic platforms.

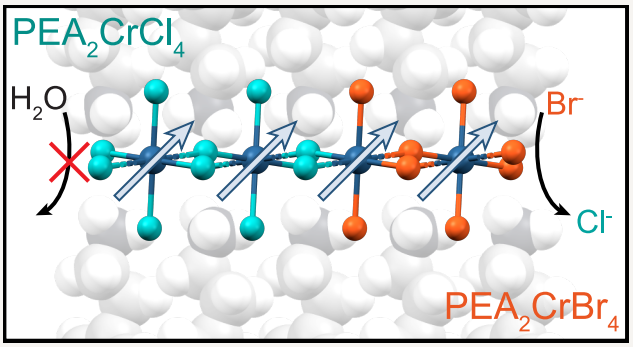

The contents of section 3.2 are adapted with permission from Smith, R. T.; Walsh, K. M.; Jiang, Q.; Chu, J.-H..; Gamelin, D. R. *Chem. Mater.* **2024**, *36*, 1571-1578. Copyright 2024 American Chemical Society. The contents of section 3.3 are reproduced with permission from Walsh, K. M.; Smith, R. T.; Gamelin, D. R. *J. Am. Chem. Soc.* **2024**, *146*, 29159-29168. Copyright 2024 American Chemical Society.

3.1 Overview

Synthesis and structural characterization of the 2D hybrid-perovskite ferromagnet $(PEA)_2CrCl_4$ (PEA^+ = phenethylammonium) are reported in section 3.2. We report that $(PEA)_2CrCl_4$ is ferromagnetically ordered with $T_C = 44$ K and shows rich temperature-dependent absorption in the visible region that reflects coupling of Cr^{2+} optical spin-flip transitions to 2D magnons. We find that the steric bulk of the PEA^+ cation dictates the overall chemical reactivity of this material, imparting robust ambient stability to these otherwise famously hygroscopic compounds. Post-synthetic vapor-phase anion exchange of PEA_2CrCl_4 is reported in section 3.3. Anion exchange using vaporous trimethylsilyl bromide (TMS-Br) is shown to drive complete conversion of solution-processed PEA_2CrCl_4 polycrystalline thin films to PEA_2CrBr_4. 5 K magnetic circular dichroism spectroscopy indicates ferromagnetic ordering in these PEA_2CrCl_4 and PEA_2CrBr_4 films. *Via* partial anion exchange of exfoliated flakes of PEA_2CrCl_4 single crystals, we demonstrate that it is possible to generate abrupt lateral Cl/Br magneto-heterointerfaces. The sterically inhibitive PEA^+ is also found to suppress 3D diffusion, which is highlighted by parallel anion-exchange experiments on MA_2CrCl_4 (MA^+ = methylammonium), which instead show 3D exchange. Comparison of anion-exchange reactions in analogous perovskites shows that 2D bromide diffusion is slowest in PEA_2CrCl_4, attributed to the antiferrodistortive ordering found in this composition. In addition to demonstrating ambient stability, post-synthetic composition control, and heterostructure formation in ferromagnetic Cr-based 2D perovskites for the first time, these results also advance our fundamental chemical understanding of this relatively unexplored family of ferromagnetic 2D perovskites, broadening opportunities for investigation and control of novel spin effects in low-dimensional metal-halide perovskites.

3.2 An air-stable and exfoliable ferromagnetic two-dimensional perovskite, (phenethylammonium)$_2$CrCl$_4$

3.2.1 Introduction

Recent advances in hybrid inorganic/organic metal-halide perovskites have revealed exciting opportunities for the development of new optoelectronic materials, stimulating an explosion of research into the synthesis, structure/function relationships, and applications of these materials.[1-5] Most of this perovskite renaissance has focused on semiconducting perovskites of Pb^{2+} and Sn^{2+}, driven in large part by the chemical tunability of their physical properties and the high efficiencies of lead-iodide-based (e.g., $CH_3NH_3PbI_3$, or $MAPbI_3$) photovoltaics.[1, 3, 4, 6, 7] An intriguing family of leadfree layered metal-halide perovskites is the chromium-based compounds, A_2CrX_4, where A = RNH_3^+ (e.g., $MeNH_3^+$, $EtNH_3^+$, $BzNH_3^+$) and X = Cl^-, Br^-.[8-10] These compounds and their all-inorganic analogs (A = K^+, Cs^+, Rb^+) attracted a great deal of interest in the 1970s and 1980s after they were discovered to be a unique class of "transparent ferromagnets",[11] but they have received virtually no attention since.[12, 13] Most work on hybrid A_2CrX_4 compounds was thus performed before the explosion of research into hybrid lead-based 2D perovskites, and further investigation of their chemistry and properties is warranted.

One challenge confronting these materials is their atmospheric instability. A_2CrX_4 compounds have historically been extremely hygroscopic and subject to facile Cr^{2+} oxidation in air;[9] they are much less stable than analogous hybrid lead-halide perovskites. Creation of A_2CrX_4 compositions that are more stable in ambient atmosphere will ease further investigation of their properties and applications. From observations with hybrid lead-halide perovskites,[13,16] we hypothesized that hybrid A_2CrX_4 compounds could be stabilized by using larger, more hydrophobic organic cations. For example, replacing small cations like methylammonium with the larger phenethylammonium (PEA) enhances lead-halide perovskite stability in ambient conditions,[14-17] and long-chain alkylammonium-based $(C_nH_{2n+1}NH_3)_2PbI_4$ 2D perovskites (n = 14, 16, 18) show increasing stability with increasing n.[18] Air-stable A_2CrX_4 compounds have not been demonstrated previously, presenting an opportunity to test the efficacy of this strategy in a more challenging materials system.

Here, we report the synthesis of large crystals of the new hybrid compound $(PEA)_2CrCl_4$, via an antisolvent vapor-diffusion method. In stark contrast with the structurally analogous methylammonium compound $(MeNH_3)_2CrCl_4$, these $(PEA)_2CrCl_4$ crystals show remarkably good stability in air over many days. Since few X-ray crystal structures of A_2CrCl_4 compounds exist, the structure of $(PEA)_2CrCl_4$ was determined by single-crystal diffraction. This structure shows sheets of distorted $[CrCl_6]^{4-}$ octahedra spaced by PEA bilayers with a van der Waals gap between them. We further demonstrate that these crystals can be mechanically exfoliated down to single monolayers with micrometer lateral dimensions. Magnetic measurements on a bulk $(PEA)_2CrCl_4$ single crystal show in-plane ferromagnetic ordering with T_C = 44 K, and electronic absorption measurements at zero field allow the spontaneous 2D magnetic ordering to be monitored via evolution of Cr^{2+} spin-flip excitations. These findings highlight $(PEA)_2CrCl_4$ as an

attractive candidate for studies of A_2CrX_4 magnetism and magneto-optics from the bulk to the monolayer limit, and they pave the way for its use as a model system for further experimentation with magnetic hybrid perovskites.

3.2.2 Results and discussion

Figure 3.1 summarizes the synthesis and basic characterization of the $(PEA)_2CrCl_4$ crystals reported here. Growth of A_2CrX_4-type crystals by antisolvent vapor diffusion has not been reported previously. Figure 3.1a describes the chemical reaction involved. Figure 3.1b shows a typical $(PEA)_2CrCl_4$ crystal obtained from this synthesis. The crystal has lateral dimensions of ~6 cm^2, thickness of <1 mm, and is nearly transparent in the visible region. Figure 3.1c shows an optical image of the crystal under a microscope, taken with 100× magnification. Step edges with well-defined faceting are observed on the crystal surface. Figure 3.1d shows X-ray diffraction data collected for an oriented $(PEA)_2CrCl_4$ crystal using a powder diffractometer. Select peaks are indexed according to the single-crystal X-ray structure (*vide infra*). The peaks in

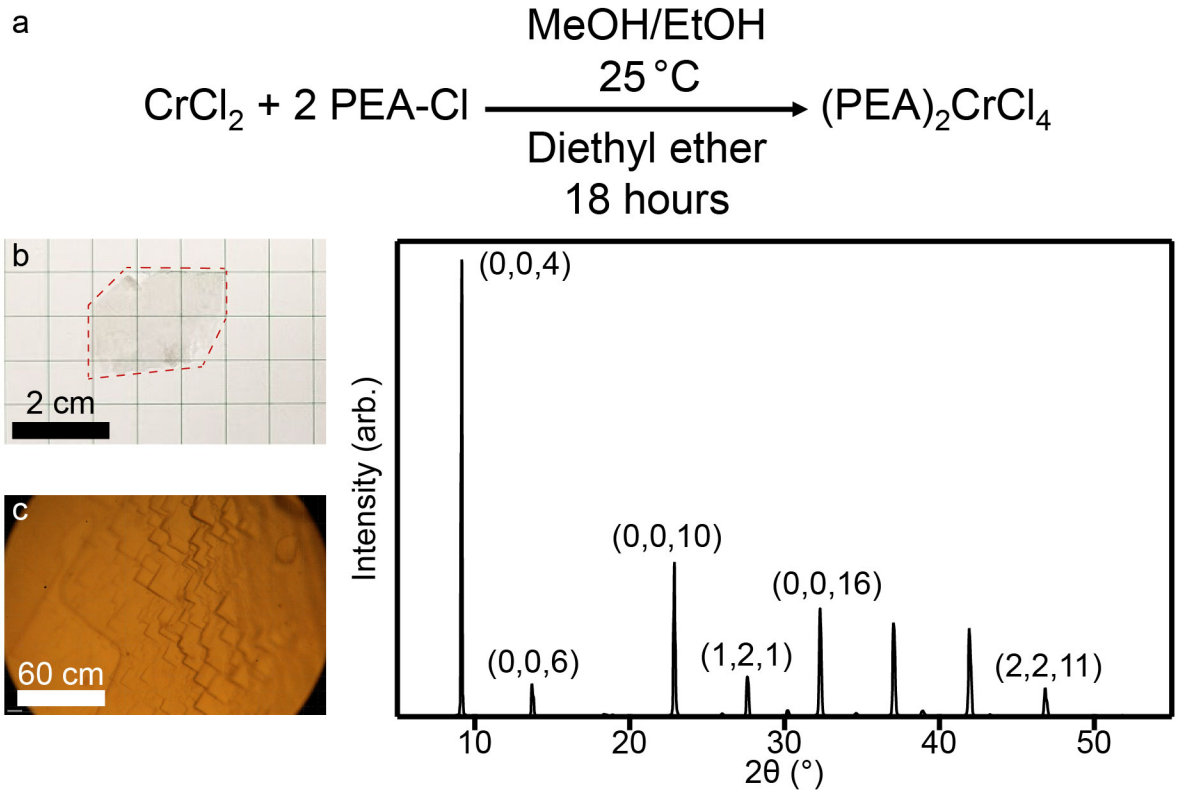

Figure 3.1. (a) $(PEA)_2CrCl_4$ crystals are formed by the vapor diffusion of diethyl ether (antisolvent) into an alcohol solution of Cr^{2+} and PEA precursors at room temperature. (b) Photograph of a $(PEA)_2CrCl_4$ crystal, showing distinct faceting. A dashed red line outlines the crystal as a guide for the eye. The scale bar is 2 cm. (c) Optical microscope image of a $(PEA)_2CrCl_4$ crystal showing multiple step edges. The scale bar is 60 μm. (d) X-ray diffraction pattern of an oriented $(PEA)_2CrCl_4$ crystal collected on a powder diffractometer, with select peaks indexed.

Figure 3.1d primarily correspond to (00*l*) reflections, highlighting the crystal's orientation and layer stacking along the *l* direction.

Most structural information for A_2CrCl_4 compounds has come from neutron-scattering measurements,[19-21] and single-crystal X-ray structures have only been reported for a few compounds.[13, 22, 23] Because $(PEA)_2CrCl_4$ has not been synthesized previously, its structure was determined by single-crystal X-ray diffraction. Figure 3.2a summarizes the 100 K structure. Consistent with other hybrid A_2CrX_4 compounds, $(PEA)_2CrCl_4$ adopts the K_2NiF_4 structure type and has orthorhombic symmetry, forming in the 2D (Ruddlesden−Popper) perovskite phase with extended sheets of six-coordinate Cr^{2+} cations bridged by chloride anions. These inorganic sheets are separated by two layers of organic A-site PEA cations with a van der Waals gap between them. The interlayer separation is 1.92 nm, which is the second largest known for any A_2CrX_4 compound.[24]

Each Cr^{2+} ion shows a large tetragonal elongation of its first coordination sphere (Figure 3.2b), with two Cr−Cl bonds ~0.4 Å longer than the other four. The elongation axes lie in the *ab* plane but order antiferrodistortively such that neighboring Cr^{2+} elongation axes are orthogonal to one another (Figure 3.2c). This cooperative Jahn−Teller distortion is a signature of the A_2CrCl_4 family of compounds.[25] The elongated bond lengths of ~2.8 Å and the Cr−Cl−Cr angle of 166.3° are comparable to those of other hybrid A_2CrX_4 compounds (see Appendix B).[8] $(PEA)_2CrCl_4$ also

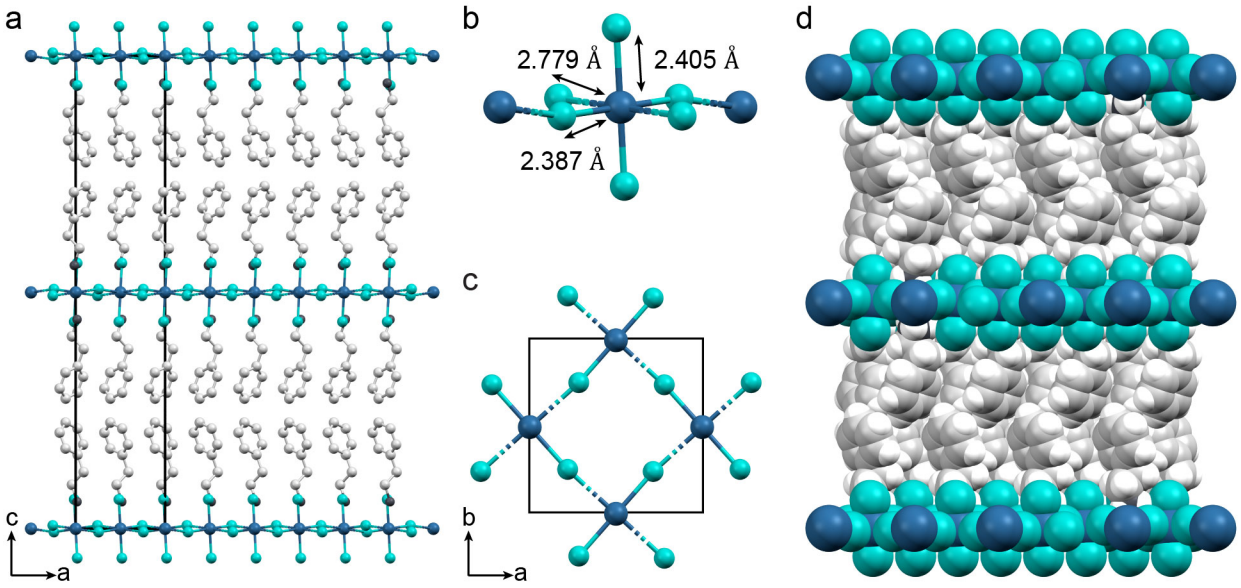

Figure 3.2. Single-crystal X-ray structure of $(PEA)_2CrCl_4$ collected at 100 K. (a) Edge view of the $(PEA)_2CrCl_4$ structure, illustrating 2D sheets of interconnected $[CrCl_6]^{4-}$ octahedra stacked with PEA spacers. The black lines indicate the unit cell. (b) Individual $[CrCl_6]^{4-}$ octahedron and its Cr−Cl bond lengths. The dashed bonds highlight the in-plane tetragonal elongation. (c) Top-down view of the middle 2D inorganic layer in the unit cell of panel (a), showing antiferrodistortive ordering of the Cr^{2+} Jahn−Teller elongation axes (dashed bonds). (d) Space-filling representation of the edge view of $(PEA)_2CrCl_4$ shown in panel (a).

shows some octahedral tilting (θ_a = +5.98° and θ_b = ± 5.04°, where θ_i refers to the tilt angle toward crystallographic axis *i*, see Appendix B), as is common for many halide perovskites.[26-29] Figure 3.2d shows a space filling representation of the same edge as that shown in Figure 3.2a.

$(PEA)_2CrCl_4$ is found to be remarkably stable in an ambient environment. To illustrate this observation, the known compound $(MeNH_3)_2CrCl_4$ was also prepared by the same synthesis method. Figure 3.3a compares two photographs of the same individual $(MeNH_3)_2CrCl_4$ crystal: the first taken when the crystal was initially exposed to air and the second after 5 min in air. As prepared, the crystal is transparent and essentially colorless, just like that of $(PEA)_2CrCl_4$ (Figure 3.1b). After only 5 min in air, however, the $(MeNH_3)_2CrCl_4$ crystal completely decomposed, showing large areas that have been etched and other areas that are discolored by oxidation. In contrast, $(PEA)_2CrCl_4$ crystals show no detectable decomposition on the same time scale. Figure 3.3b compares two photographs of $(PEA)_2CrCl_4$ after initial exposure to air and after 10 full days in air. Even with this long exposure, the crystal's morphology remains unchanged. Figure 3.3c shows powder X-ray diffraction data collected on a similar $(PEA)_2CrCl_4$ crystal over the course of 15 days in air, normalized to the peak at 2θ ≈ 14°. After 10 days, the data show no significant

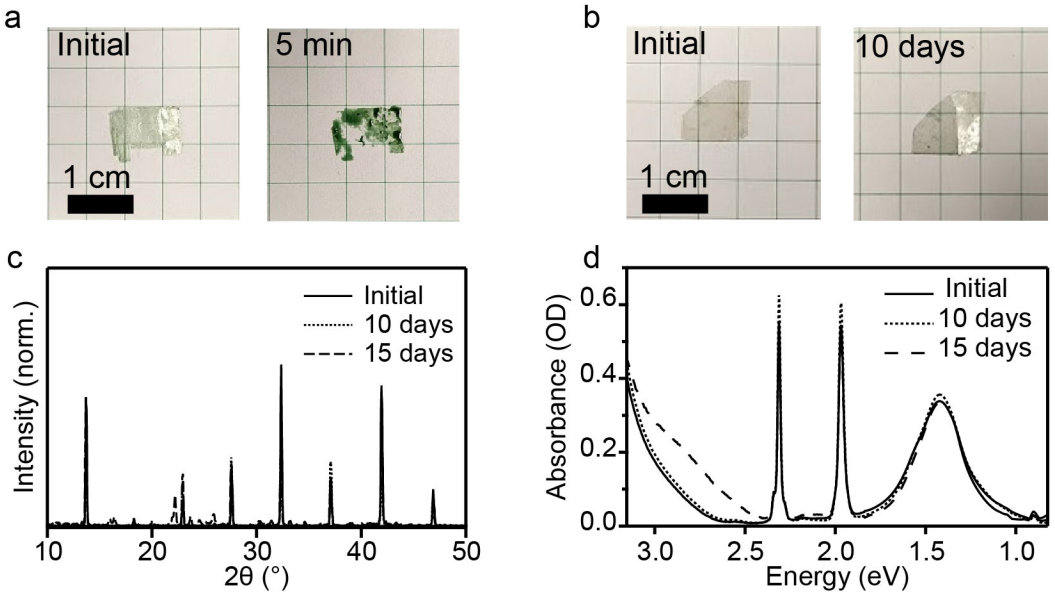

Figure 3.3. Air stability of the $(PEA)_2CrCl_4$ crystals. (a) Photographs of a crystal of $(MeNH_3)_2CrCl_4$ taken after initial air exposure (left) and after 5 min in air (right) showing rapid decomposition. Scale bar = 1 cm. (b) Photographs showing a similar crystal of $(PEA)_2CrCl_4$ taken after initial air exposure (left) and after 10 days in air (right), showing retention of the crystal's integrity. Scale bar = 1 cm. (c) XRD data for a $(PEA)_2CrCl_4$ crystal stored in air were collected upon initial exposure, after 10 days in air, and after 15 days in air. The initial and 10 day data are essentially indistinguishable. Peaks from a new decomposition phase become evident in the 15 day data, but the original phase is still dominant. (d) Room-temperature absorption spectra of a $(PEA)_2CrCl_4$ crystal stored in air, collected upon initial exposure, after 10 days in air, and after 15 days in air. The initial and 10-day data are again essentially indistinguishable. After 15 days in air, a broad decomposition band centered at ~2.9 eV is evident.

change, and only after 15 days is diffraction from a decomposition phase evident. The original phase is still dominant. Similarly, absorption spectroscopy (Figure 3.3d) shows superimposable spectra for the first ~10 days, and only after ~10–15 days is a new broad band at ~2.8 eV evident that reflects the very slow oxidation. This increased air stability could be due to the greater hydrophobicity of PEA.[14-18] Notably, close packing of PEA in the ordered structure fills space effectively (Figure 3.2d, see also Appendix B), which helps protect chromium from the surrounding atmosphere.

By changing the size of the R group on the alkylammonium cations, seminal experiments performed decades ago demonstrated that the ferromagnetism of A_2CrX_4 compounds is not significantly dependent on interlayer spacing.[9, 25] From these results, it was concluded that the A_2CrX_4 compounds are two-dimensional easy-plane ionic ferromagnets, although the monolayer was never isolated. More recently, A_2CrX_4 compounds have also been predicted to be good candidates for mechanical exfoliation,[12] but they have not yet been studied in this way. To test the feasibility of mechanical exfoliation, we attempted to exfoliate $(PEA)_2CrCl_4$ single crystals using the Scotch-tape method, transferring the resulting materials onto SiO_2 wafers under gentle heating. Figure 3.4a shows a large-area optical microscope image of a representative exfoliation. Many flakes with lateral dimensions of several micrometers are observed. The white arrow indicates a particularly thin flake. Figure 3.4b shows an AFM image collected in this area, which reveals a single monolayer of $(PEA)_2CrCl_4$, confirmed by the height-scan data shown in Figure 3.4c. The thickness of this flake was determined to be 1.67 nm. The average monolayer thickness found by measuring the step heights of several flakes was determined to be 2.0 ± 0.1 nm (see Appendix B). This thickness agrees well with the monolayer thickness expected from single-crystal X-ray diffraction (~1.9 nm interlayer spacing). These data thus represent the first

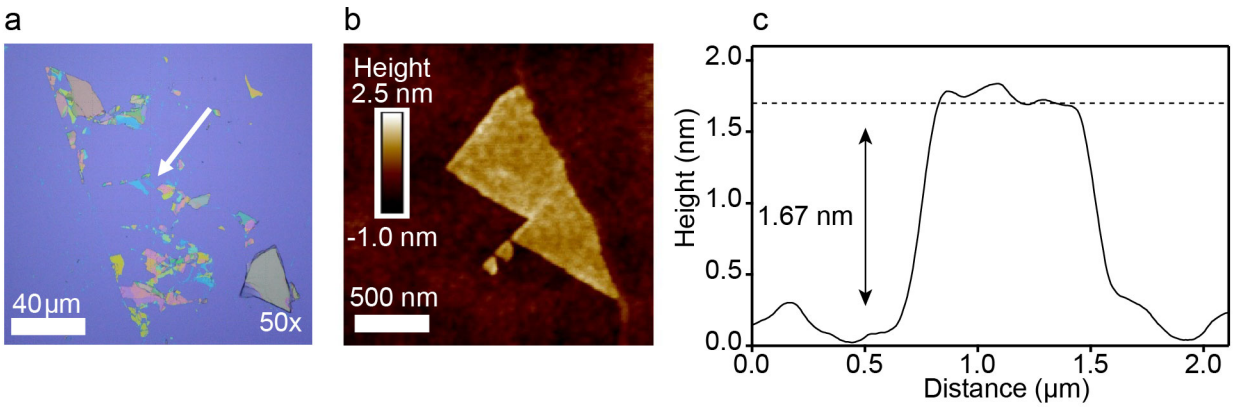

Figure 3.4. (a) Large-area optical image of a mechanically exfoliated $(PEA)_2CrCl_4$ crystal. The white arrow indicates the region where the AFM data of Figure 4b,c were collected. Scale bar: 40 μm. (b) AFM image of the region from Figure 4a indicated by the white arrow (2.0 × 2.0 μm area). Scale bar: 500 nm. (c) AFM height plot for the flake shown in Figure 4b, indicating a height of ~1.67 nm, consistent with a single $(PEA)_2CrCl_4$ monolayer. Averaging over many AFM measurements of step heights in several other flakes gives an average monolayer height of 2.0 ± 0.1 nm (see Appendix B).

exfoliation of any A_2CrX_4 compound, demonstrating the ability to isolate even an individual monolayer. Importantly, AFM data for exfoliated samples (see Appendix B) show no detectable change after up to 3 days in air, indicating that the protection provided by PEA against atmospheric degradation is retained, even in such thin crystals. These results demonstrate that $(PEA)_2CrCl_4$ is well suited to serve as a practical model system for the physical investigation of exfoliated A_2CrCl_4 compounds.

The magnetic properties of a $(PEA)_2CrCl_4$ single crystal were examined using vibrating sample magnetometry and the results are summarized in Figure 3.5. Figure 3.5a plots field-cooled (FC) and zero-field-cooled (ZFC) molar susceptibility (χ) *vs* temperature for a single crystal with a 0.01 T magnetic field oriented in the crystallographic *ab* plane ($H \perp c$), bisecting the angle defined by the Cr^{2+} molecular axes ($\varphi = 45°$). The data show a rapid increase in χ below

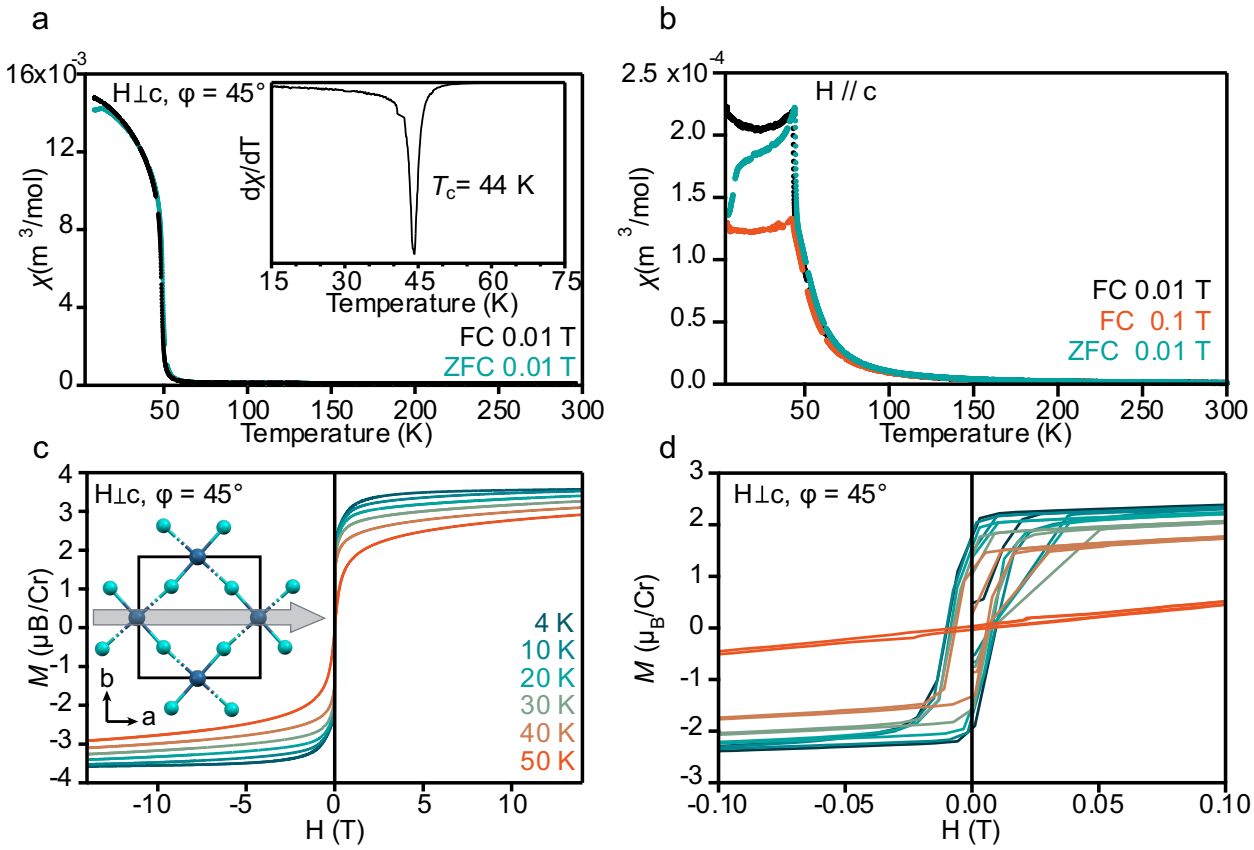

Figure 3.5. Magnetic data for a $(PEA)_2CrCl_4$ single crystal. (a) Field-cooled (FC) and zero-field-cooled (ZFC) susceptibility, measured with $H = 0.01$ T applied in the *ab* plane ($H \perp c$), bisecting the angle defined by the molecular axes ($\varphi = 45°$). The inset shows the derivative of the FC data, yielding an ordering temperature of $T_C = 44$ K. (b) FC and ZFC susceptibility data were collected with an applied magnetic field oriented perpendicular to the crystallographic *ab* plane and parallel to the *c* axis (H // c). (c) Field-sweep magnetization data were measured from −14 to +14 T at different temperatures. The inset illustrates the in-plane magnetic-field ($H \perp c$, $\varphi = 45°$) orientation, coinciding with a magnetic easy axis. (d) An expanded view of the data from Figure 3.5c, showing magnetic hysteresis at low temperatures.

~50 K. The inset to Figure 3.5a plots the derivative of the FC data vs temperature, from which a value of T_C = 44 K is determined. Magnetic measurements with the field oriented perpendicular to the *ab* plane ($H \parallel c$) show a similar temperature dependence but much smaller χ (Figure 3.5b), and those with the magnetic field oriented along either molecular axis ($H \perp c$, φ = 0° or 90°) also show reduced χ relative to φ = 45° (see Appendix B). These data indicate in-plane magnetic ordering with easy axes bisecting the Cr^{2+} molecular axes, parallel to the *a* and *b* crystallographic axes, as illustrated in the inset of Figure 3.5c.

Figure 3.5c plots magnetic-field-sweep data for the same sample, collected from −14 to +14 T ($H \perp c$ and φ = 45°) at several temperatures. At 4 K, *M* saturates at 3.55 μ_B/Cr, consistent with the ferromagnetic alignment of Cr^{2+} spins. Increasing the temperature slowly decreases the magnetization at a given field, similar to that in Figure 3.5a. Figure 3.5d shows the low-field region of Figure 3.5c on an expanded scale. A magnetic hysteresis is observed at 4 K, characterized by a coercivity of ~12.5 mT and remanent magnetization of ~2 μ_B/ Cr. Both values decrease as the temperature is raised, and at 50 K, there is no longer any evident hysteresis (see Appendix B). We note that the 100 K X-ray diffraction data in Figure 3.2 indicate antiferrodistortive ordering well above the magnetic ordering temperature T_C, consistent with a Jahn−Teller energy much greater than the inter-ion magnetic-exchange energy.[30] This cooperative Jahn−Teller distortion and its associated orbital ordering presents near-linear superexchange pathways between neighboring Cr^{2+} ions that connect the half-filled z^2 orbital (molecular coordinate frame) on one site to the empty x^2-y^2 orbital on its neighbor, yielding ferromagnetic Cr−Cr coupling and ultimately long-range in-plane ferromagnetism within the inorganic sheets.[9] The antiferrodistortive ordering also orients the easy axis along φ = 45°.

High-temperature susceptibility data for A_2CrCl_4 compounds have previously been analyzed using the series expansion given in eq 1[20] for a Heisenberg quadratic-layer magnet with a Hamiltonian of $H = -JS_i \bullet S_j$, to estimate the nearest-neighbor magnetic-exchange constant, *J*.

$$\frac{Ng^2{\mu_B}^2}{\chi} = \frac{1}{2}kT + J(-4 + 9x - 9.072x^2 + 55.728x^3 - 160.704x^4 + 116.640x^5) \qquad (1)$$

Here, $x = \frac{J}{kT}$, *N* is Avogadro's number, *g* is the Landé factor, μ_B is the Bohr magneton, *k* is the Boltzmann constant, and *S* = 2 for high-spin d^4 Cr^{2+}. After correcting for diamagnetic contributions, the susceptibility data from 70 - 155 K were fit to eq 1 (see Appendix B), giving a value of *J* = +0.87 ± 0.01 meV (+7.0 ± 0.1 cm^{-1}) that is comparable to *J* values of other A_2CrCl_4 compounds (see Appendix E for compilation of literature results). Similarly, T_C in $(PEA)_2CrCl_4$ is comparable to those of other hybrid A_2CrX_4 compounds (see Appendix B). Thus, although the interlayer spacing increases dramatically going from, *e.g.*, $(MeNH_4)_2CrCl_4$ to $(PEA)_2CrCl_4$, both *J* and T_C are minimally affected by this structural parameter,[8, 11, 20, 24, 31, 32] confirming that interlayer magnetic exchange coupling is effectively negligible.[9, 25]

Less obvious from these or other literature data are the microscopic magneto-structural correlations that *are* operative in A_2CrCl_4 compounds. One distinction is that all-inorganic

A_2CrCl_4 compounds appear to show a small but significant increase in T_C relative to hybrid A_2CrCl_4 compounds (~56 K vs 46 ± 9 K, see Appendix B). The all-inorganic A_2CrCl_4 compounds also have 180° Cr−Cl−Cr bond angles, whereas hybrid A_2CrCl_4 compounds (including $(PEA)_2CrCl_4$) generally show smaller Cr−Cl−Cr angles of 165 ± 2° (see Appendix B).[8] The smaller T_C for the hybrid compounds can be attributed in part to this decrease in bond angle, which reduces orbital overlap in the dominant ferromagnetic d_{z^2}-$d_{x^2-y^2}$ superexchange pathway, but other factors are also important. In particular, hybrid A_2CrX_4 compounds show substantially greater Cr−Cl bond lengths along the tetragonal axis (2.9 ± 0.1 Å vs 2.76 Å in Rb_2CrCl_4), which further reduces the strength of the nearest-neighbor superexchange coupling. Tilting of the octahedra relative to the *ab* plane is also observed in the hybrid A_2CrCl_4 perovskites but not in the all-inorganic compounds (see Appendix B) and may reduce superexchange coupling strengths. Unfortunately, a more detailed comparison across literature samples is hindered by inconsistencies in magnetic measurement and analysis methods. Additionally, thorough structural data are lacking for most of the known A_2CrX_4 compounds. A careful systematic investigation of magnetic and structural data across multiple A_2CrCl_4 compounds is needed to further clarify magneto-structural correlations in this family.

Although hybrid A_2CrCl_4 compounds remain relatively underexplored, a great deal of recent research has focused on the development of analogous hybrid magnetic A_2CuCl_4 and A_2MnCl_4 compounds, in addition to the aforementioned hybrid semiconducting A_2PbCl_4 and A_2SnCl_4 compounds. The Cu^{2+} compounds are most similar to the Cr^{2+} compounds investigated here, exhibiting an analogous in-plane antiferrodistortive ordering of local Jahn−Teller elongation axes and showing intralayer ferromagnetic ordering with weak interlayer antiferromagnetic exchange.[31-34] A_2CuCl_4 compounds have significantly lower magnetic ordering temperatures (~10 K), however, and they are not transparent across the visible spectral region but instead absorb broadly due to several low-energy spin-allowed *d*-*d* and charge-transfer transitions. As d^9 compounds, their magnetic moments at saturation are *ca*. 1/4 as large as those of the A_2CrCl_4 compounds (S = 1/2 *vs* S = 2). In contrast, the Mn^{2+} hybrid perovskites are not subject to Jahn−Teller distortions and thus show no antiferrodistortive ordering, and they order antiferromagnetically below *ca*. 40−55 K.[35-37] Among the magnetic hybrid metal-halide perovskites, the A_2CrCl_4 compounds are thus distinctive in their relatively high magnetic ordering temperatures, their relatively large magnetic moments, and, as described below, their unique optical properties. Figure 3.6a shows overview electronic absorption spectra of a bulk single crystal of $(PEA)_2CrCl_4$ ($E \perp c$) collected at 6 and 300 K. The spectra are characterized by a broad charge-transfer band in the UV (~3.5 eV), two sharp spin-forbidden ("spin-flip") Cr^{2+} transitions in the visible ($^5B_{1g} \rightarrow {}^3B_{1g}(^3F)$ at ~2.3 eV and $^3B_{1g}(^3H)$ at ~2.0 eV), and a broad spin-allowed ligand-field transition in the near-infrared ($^5B_{1g} \rightarrow {}^5B_{2g}$ at ~1.5 eV).[38]

The most distinctive aspect of these spectra is the extremely strong temperature dependence of the two spin-flip transitions, whose integrated intensities both increase by over 2 orders of magnitude upon warming from 6 to 300 K. Figure 3.6b plots variable-temperature absorption data collected from 6 to 300 K in the region of the $^5B_{1g} \rightarrow {}^3B_{1g}(^3H)$ spin-flip

transition, and Figure 3.6c plots the total integrated absorbance vs temperature for this transition. Absorption in this window is barely detectable at 6 K but increases rapidly and broadens as the temperature is raised, before turning over at ~125 K. Whereas spin-flip transitions are generally strongly forbidden for Cr^{2+}, Day, Bellitto, Güdel, and others have shown that those transitions that involve the same *d* orbitals as participate in superexchange can couple to magnons effectively, providing a mechanism for conserving total spin angular momentum during the optical transition.[38, 39] In A_2CrCl_4 compounds, these are the $^5B_{1g} \rightarrow {}^3B_{1g}(^3F)$ (~2.3 eV) and $^3B_{1g}(^3H)$ (~2.0 eV) transitions.[38] Critically, only magnon transitions that *increase* spin angular momentum can offset the reduction in spin angular momentum of the optical excitation, and because of ferromagnetic ordering, such magnon transitions are only possible as hot bands at elevated temperatures. This constraint makes the optical spectrum strongly temperature dependent. Below T_C, the spin-flip absorbance shows a T^2 temperature dependence that reflects

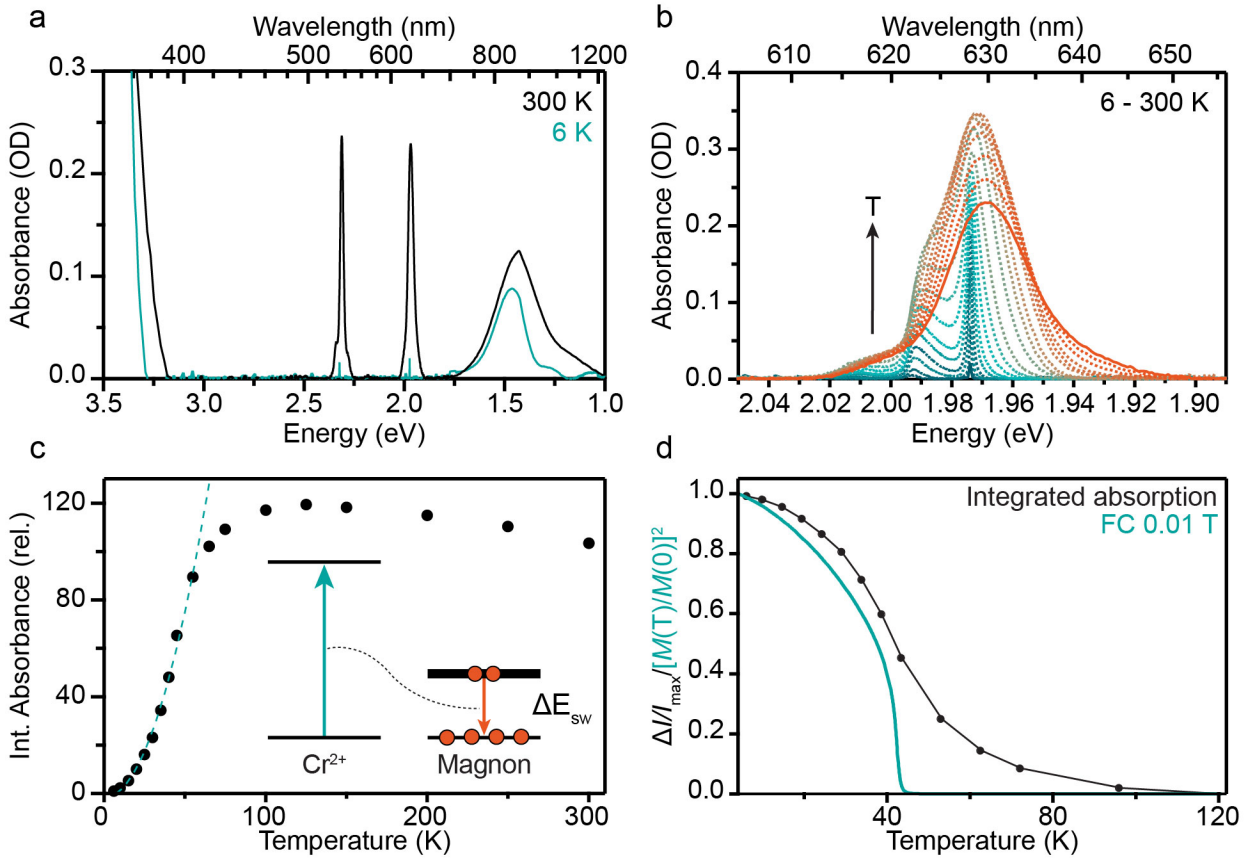

Figure 3.6. (a) Variable-temperature electronic absorption spectra of a $(PEA)_2CrCl_4$ bulk single crystal ($E \rightarrow\perp c$), collected at 6 (blue) and 300 K (black). (b) The $^5B_{1g} \rightarrow {}^3B_{1g}(^3H)$ region from (a) is plotted on an expanded scale, including spectra from several intermediate temperatures. (c) Total integrated absorbance of the $^5B_{1g} \rightarrow {}^3B_{1g}(^3H)$ transition from (b) plotted vs temperature. Inset: depiction of the simultaneous Cr^{2+} spin-flip excitation and annihilation of a thermally populated magnon. The dashed curve describes a T^2 temperature dependence. (d) Data from (c) (black) replotted as $\Delta I/I_{max}$, where $\Delta I = I_{max} - I(T)$. Also plotted are the field-cooled susceptibility data from Figure 3.5a (blue), represented here as $(M(T)/M(0))$.[2]

the thermal excitation of magnons (Figure 3.6c, dashed). This relationship holds until very low temperatures, and it also holds well above T_C.

To emphasize the latter, Figure 3.6d replots the absorption data from Figure 3.6c as $\Delta I/I_{max}$, where $\Delta I = I_{max} - I(T)$. Superimposing these data upon the infinite spin-correlation function, represented by $(M(T)/M(0))^2$ using the FC susceptibility data from Figure 3.5a,[40] highlights the correlation between hot exciton-magnon absorption intensity and the loss of long-range magnetic order. This comparison additionally highlights the continued growth of hot exciton-magnon absorption in the paramagnetic regime ($>T_C$), which requires intensity contributions from short-range spin correlations as well. On the low-temperature side, a deviation from simple T^2 scaling is expected to arise from the existence of an energy gap in the magnon density of states at the Brillouin zone center (Δ_0). Fitting the low-temperature data of Figure 3.6c to eq 2[39] (see Appendix B) yields a value of $\Delta_0 = 0.45 \pm 0.26$ meV (3.6 ± 2.1 cm^{-1}), consistent with the anisotropy gaps estimated for Rb_2CrCl_4 and $(MeNH_3)_2CrCl_4$.[41, 42] Lower-temperature absorption data are required to narrow the uncertainty in this estimate. Overall, the temperature dependence of the Cr^{2+} spin-flip excitations in $(PEA)_2CrCl_4$ thus provides a unique optical probe of zero-field magnetic correlations in a 2D ferromagnet.

$$I(T) \alpha\, T^2 \exp\left(\frac{\Delta_0}{kT}\right) \tag{2}$$

3.2.3 Conclusion

In summary, the 2D hybrid-perovskite compound $(PEA)_2CrCl_4$ was synthesized for the first time. Single-crystal X-ray diffraction shows a structure involving 2D inorganic sheets separated by organic PEA cation layers with a van der Waals gap between the organic layers. The inorganic sheets consist of networked $[CrCl_6]^{4-}$ distorted octahedra with alternating in-plane Jahn−Teller distortion axes. These $(PEA)_2CrCl_4$ crystals are substantially more stable in air than other known A_2CrX_4 compounds. The Cr^{2+} spins in each 2D layer of $(PEA)_2CrCl_4$ are ferromagnetically ordered with $T_C = 44$ K, having an in-plane easy axis. Mechanical exfoliation has also been demonstrated for the first time for any A_2CrX_4 compound, and monolayers with micrometer lateral dimensions have been achieved. These attributes make $(PEA)_2CrCl_4$ an attractive platform for the development of 2D perovskite chemistry that links structure, magnetism, and magneto-optics from bulk down to the monolayer limit. In the following section we continue our work on expanding the chemistry of these relatively underexplored ferromagnetic 2D perovskites, further exploring the chemical consequences of the sterically encumbering PEA^+ A-site cation.

3.3 Anion exchange and lateral heterostructure formation in ferromagnetic $(PEA)_2Cr(Cl,Br)_4$ two-dimensional perovskites

3.3.1 Introduction

Over recent decades, there have been profound advances in the chemistry of layered A_2MX_4 two-dimensional (2D) metal-halide perovskites (A = monovalent cation, M = divalent metal cation, X = Cl, Br, I).[43-45] While technically distinct from the "true" three-dimensional AMX_3 perovskite family,[46] these 2D Ruddlesden-Popper perovskite-like congeners share similar advantages including facile solution-phase syntheses,[44] wide compositional tunability,[47-49] and attractive optoelectronic functionality,[50-52] but additionally bring atomically precise reduced dimensionality of their inorganic metal-halide networks along one axis.[53] In an adjacent field, the recent discovery of Ising-like 2D ferromagnetism in monolayer CrI_3[54] and $Cr_2Ge_2Te_6$[55] has led to increased focus on magnetic 2D materials for application in next-generation spin-based electronics.[56-58] Several magnetic 2D metal-halide perovskite compositions are now also under active investigation. Recent studies have mostly focused on A_2MnX_4 compounds, which are antiferromagnetic,[59, 60] and A_2CuX_4 compounds, which are weakly ferromagnetic with small magnetic moments ($S_{Cu} = 1/2$, $T_C \sim 10$ K).[61, 62] In contrast, A_2CrX_4 compounds show more robust ferromagnetism ($S_{Cr} = 2$, $T_C \sim 40 - 60$ K[63]) and rich physical properties that were investigated deeply in the 1970s and 1980s,[64-66] yet A_2CrX_4 perovskites have been largely excluded from the recent 2D perovskite renaissance.

Here, we leverage post-synthetic anion exchange to achieve compositional tunability of A_2CrCl_4 compounds, previously undemonstrated for this family of materials. Informed by well-developed $CsPbX_3$ anion-exchange chemistry,[67-70] we use vapor-phase trimethylsilyl-bromide (TMS-Br) as a reactive anion-exchange reagent. We demonstrate that exfoliated single-crystal PEA_2CrCl_4 (PEA^+ = phenethylammonium) and MA_2CrCl_4 (MA^+ = methylammonium) undergo anion exchange under these conditions, and furthermore demonstrate full conversion of PEA_2CrCl_4 to the previously unreported PEA_2CrBr_4 composition in polycrystalline thin films. Using magnetic circular dichroism (MCD) spectroscopy, we demonstrate ferromagnetism in spin-coated polycrystalline PEA_2CrCl_4 films and their anion-exchanged PEA_2CrBr_4 products. We further demonstrate that the steric occlusion provided by the bulky PEA^+ cations, which we previously showed greatly suppresses aerobic decomposition of PEA_2CrCl_4,[71] may be leveraged to also suppress interlayer diffusion of halides or TMS-Br, allowing formation of abrupt lateral PEA_2CrCl_4/PEA_2CrBr_4 magneto-heterointerfaces that have no analog among prior A_2MX_4 compounds.

We contextualize our PEA_2CrCl_4 results within the broader 2D metal-halide perovskite class by comparing PEA_2CrCl_4 anion exchange with results obtained for PEA_2MnCl_4 and PEA_2PbCl_4 crystals, finding significantly slower 2D anion diffusion in PEA_2CrCl_4. In addition to advancing our understanding of the fundamental chemistry of A_2CrX_4 compounds, the post-synthetic composition control presented here enables the development of novel magnetic and phononic interfaces with potential ramifications for efforts to harness spin effects in layered perovskites.

3.3.2 Results and discussion

Initial anion-exchange experiments were performed on polycrystalline films of PEA_2CrCl_4 that were prepared by adapting previously reported spin-coating methods for synthesizing lead-halide perovskite thin films[44, 72] (see section 3.4 Methods). Spin-coated A_2CrCl_4 has not been described previously. Figure 3.7a shows an SEM image of a representative PEA_2CrCl_4 film, which reveals ~2 μm apparent lateral grain sizes. Such films were reacted with vapor-phase TMS-Br to probe for lattice anion exchange. Figure 3.7b shows an SEM image of a representative film collected after reaction with TMS-Br at 175 °C for 60 min. The film appears to be smoother and to have slightly larger grains following this procedure, likely due to grain boundary fusion and annealing under these reaction conditions. SEM-EDS analysis confirms complete conversion to PEA_2CrBr_4 with no residual chloride contribution (see Appendix C).

Figure 3.7c shows powder X-ray diffraction (pXRD) data from these two films, compared to XRD data from an oriented PEA_2CrCl_4 single crystal collected on the same powder diffractometer. The PEA_2CrCl_4 thin film data show only the (0, 0, l) reflections, indicating preferential orientation of the grains along the crystallographic basal plane. The anion-exchanged film shows similar but shifted (0, 0, l) reflections, consistent with incorporation of bromide into the lattice. The crystallographic *c*-axis unit-cell parameters extracted by fitting the positions of these reflections are 38.75 ± 0.05 Å for the PEA_2CrCl_4 film and 38.13 ± 0.03 Å for the

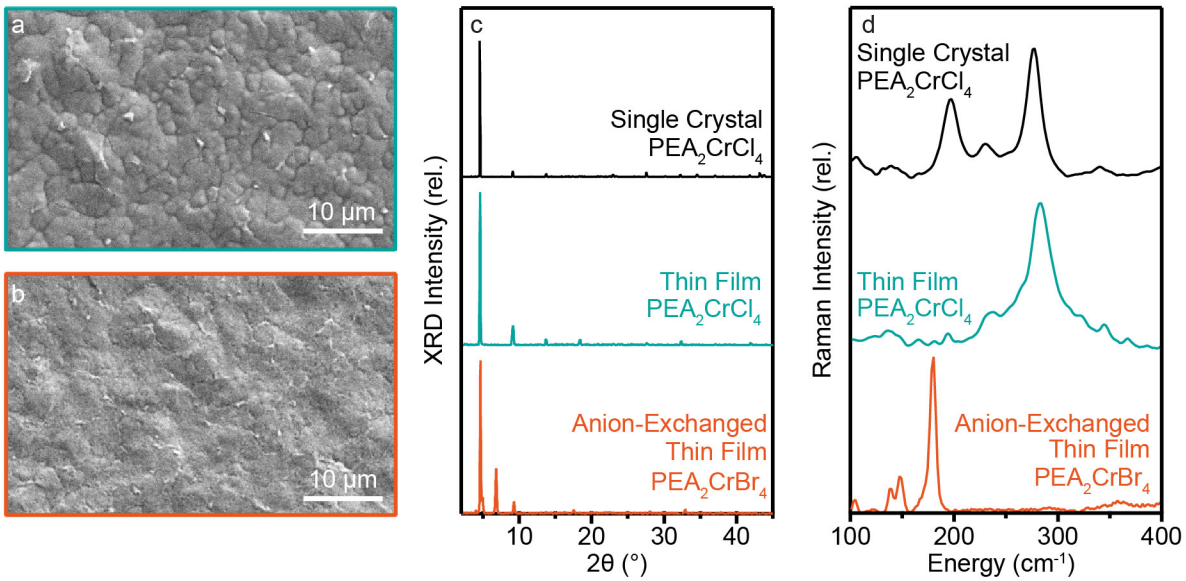

Figure 3.7. SEM images of (a) a PEA_2CrCl_4 polycrystalline film and (b) a PEA_2CrBr_4 polycrystalline film achieved by complete anion exchange. (c) Powder XRD data for a bulk PEA_2CrCl_4 oriented single crystal (black), and the same PEA_2CrCl_4 (teal) and PEA_2CrBr_4 (orange) thin films as shown in (a,b). All peaks in the PEA_2CrCl_4 thin film diffractogram are identifiable as reflections from PEA_2CrCl_4. (d) Raman spectra of a bulk PEA_2CrCl_4 single crystal (black), the same PEA_2CrCl_4 thin film shown in (a,c) (teal), and an anion-exchanged PEA_2CrBr_4 thin film prepared on a quartz substrate (orange). The B_{2g} peak centered at 285 cm^{-1} in the PEA_2CrCl_4 thin film shifts to 183 cm^{-1} in the PEA_2CrBr_4 film after complete anion exchange.

PEA_2CrBr_4 film (see Appendix C). These data are consistent with the *c*-axis contraction observed upon going from the chloride to bromide compositions of the analogous lead-halide[73, 74] and copper-halide[75] layered perovskites. The pXRD data of the anion-exchanged film also show an additional peak centered around $2\theta = 7°$, possibly related to decomposition of excess PEA-Cl (see Appendix C). Figure 3.7d plots the Raman spectra of a PEA_2CrCl_4 single crystal, a PEA_2CrCl_4 thin film, and an anion-exchanged thin film. The PEA_2CrCl_4 single crystal and polycrystalline film both show a prominent vibration centered around 280 cm^{-1} (278 and 285 cm^{-1}, respectively), assigned as an in-plane metal-chloride B_{2g} stretching mode in similar chromium-chloride and copper-chloride layered perovskites.[76, 77] We attribute the increase in intensity of the thin-film B_{2g} mode relative to the lower-energy features to crystallite orientation effects, consistent with reported polarized Raman studies of the aforementioned related compounds.[76, 77] This B_{2g} vibration shifts to 183 cm^{-1} and narrows in the anion-exchanged film, consistent with chloride substitution by the heavier bromide anion and film annealing during the anion exchange process, respectively.

Figure 3.8a plots room-temperature absorption spectra of these PEA_2CrCl_4 and PEA_2CrBr_4 thin films. Both compositions show the two narrow Cr^{2+} $^5B_{1g} \rightarrow {}^3B_{1g}$ spin-flip

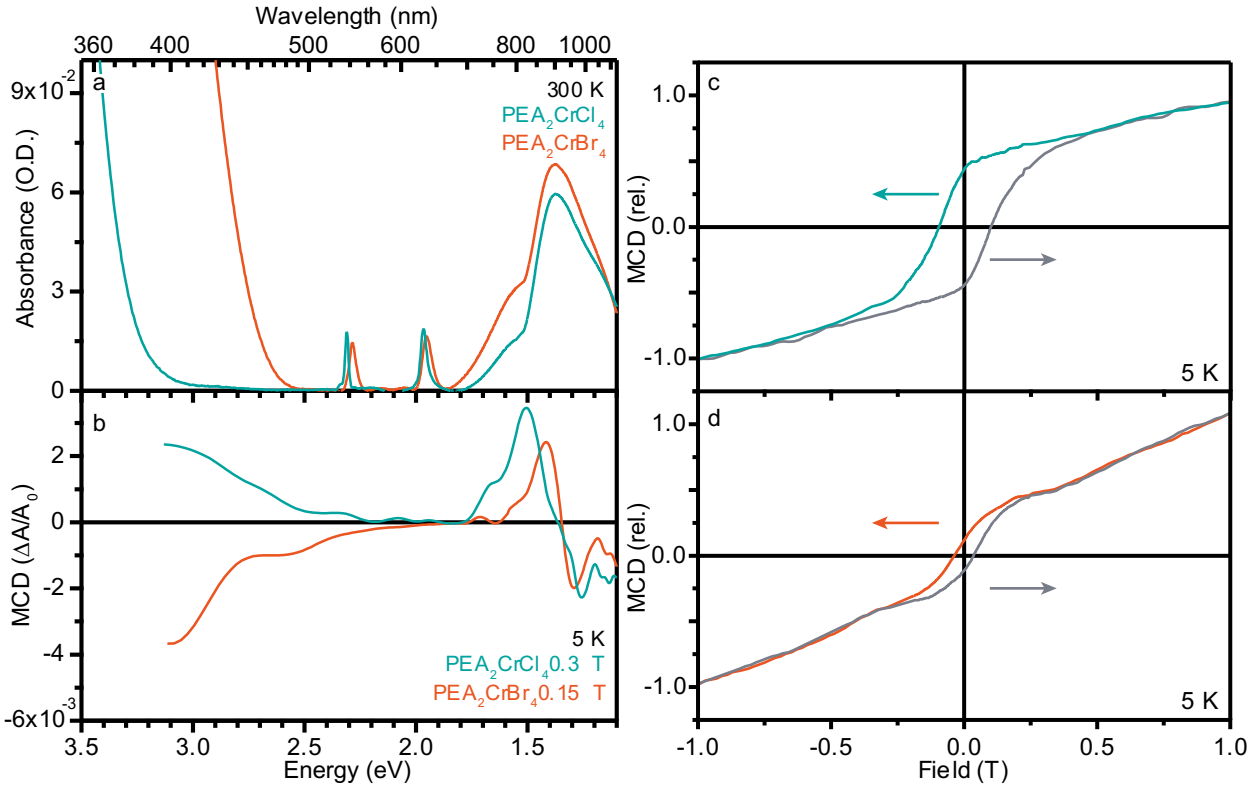

Figure 3.8. (a) Room-temperature absorption spectra and (b) 5 K MCD spectra of the PEA_2CrCl_4 (teal) and PEA_2CrBr_4 (orange) thin films. (c,d) 5 K field-sweep data collected while monitoring the MCD intensity of the NIR Cr^{2+} spin-allowed transitions of the same PEA_2CrCl_4 (teal) and PEA_2CrBr_4 (orange) thin films shown in (a,b), revealing magnetic hystereses in both samples. The arrows indicate the field-sweep direction of each trace.

transitions (using notation for an idealized D_{4h} point symmetry[78]) in the visible that are characteristic of this class of layered Cr^{2+} compounds.[63, 71] These spin-flip transitions are centered around 2.31 and 1.97 eV in the chloride thin film and each redshifts by ~20 meV in the bromide film (~2.29 and 1.95 eV). These transitions, formally forbidden by spin selection rules, gain allowedness through coupling with the annihilation of thermally populated "hot" magnons in the lattice.[64, 65] The higher-energy transitions, with onsets around 3.2 eV in the PEA_2CrCl_4 film and 2.6 eV in the PEA_2CrBr_4 film, are attributed to ligand-to-metal charge-transfer transitions. Both samples also show a broad, asymmetric absorption band in the near-IR, attributed to overlapping spin-allowed Cr^{2+} *d-d* transitions. In addition to low-symmetry-split components of the parent $^5E_g \rightarrow {}^5T_{2g}$ (O_h) transition, a $^5B_{1g} \rightarrow {}^5B_{2g}$ (D_{4h}) transition within the Jahn-Teller-split ^5E_g (O_h) ground state is also expected on the low-energy side of this *d-d* band, broadening its overall bandshape.[78, 79] Figure 3.8b plots 5 K MCD spectra of both samples. The PEA_2CrCl_4 film shows a prominent feature in the near-IR, centered around 1.5 eV, as well as weaker overlapping features to lower energy. The main feature redshifts to 1.4 eV in the PEA_2CrBr_4 film, consistent with the weaker ligand-field strength in the bromide lattice. The Cr^{2+} spin-flip transitions are not observed in these spectra because of their negligible intensity at cryogenic temperatures.[71]

To probe the magnetism of the PEA_2CrCl_4 and anion-exchanged PEA_2CrBr_4 thin films, we performed continuous magnetic field sweeps while monitoring the 5 K MCD intensities of the spin-allowed *d-d* transitions in the near-IR, sweeping in both the “positive” and “negative” field directions. These data reveal rapid magnetization at low fields and clear magnetic hystereses in both samples, with coercivities of ~195 mT (PEA_2CrCl_4) and ~65 mT (PEA_2CrBr_4), respectively, consistent with ferromagnetic ordering. We recently reported on the ferromagnetism of single-crystalline PEA_2CrCl_4.[71] Evidently, ferromagnetism is retained in the PEA_2CrCl_4 polycrystalline film – and notably – also after anion exchange to the PEA_2CrBr_4 composition. To higher (lower) fields of the hystereses, both samples show gradually increasing (decreasing) MCD intensities with increasing field, rather than saturation; a similar result is obtained in the magnetization of single-crystal PEA_2CrCl_4 and is attributable to spin canting.[71] Interestingly, the coercivity found for the PEA_2CrCl_4 film is more than 15 times greater than the largest observed in single-crystal PEA_2CrCl_4 (~12.5 mT).[71] These thin films are characterized by having a distribution of crystallite orientations, but we rule out crystallite orientation as the source of this enhanced coercivity by comparing the thin-film data to single-crystal vibrating sample magnetometry (VSM) field-sweep data collected with the field oriented along different crystallographic directions (see Appendix C). In each direction, the single crystal shows a *smaller* coercivity than seen here for the polycrystalline film. The enhanced coercivity in the PEA_2CrCl_4 polycrystalline film indicates an increased barrier to magnetization reversal, which could conceivably stem from partial elimination of magnetic domains in such microcrystallites due to their small sizes, similar to what was found for CrI_3 nanocrystals relative to bulk.[80] The observation of a smaller coercivity in the anion-exchanged bromide film characterized by larger apparent grain sizes is consistent with this interpretation, but further experiments dedicated to

systematic variation of more uniform crystallite sizes would be required to properly test this hypothesis.

To understand the mechanism of anion exchange in these materials, we performed partial anion-exchange reactions on exfoliated single-crystal flakes of bulk single-crystalline PEA_2CrCl_4, again using vapor-phase TMS-Br (see section 3.4 Methods). Figure 3.9a-c shows SEM-EDS images collected after reacting different PEA_2CrCl_4 flakes at 175 °C for 10, 60, and 180 min. The resulting partially exchanged flakes show well-defined lateral junctions between bromide-rich regions along their edges and chloride-rich regions in their interiors. Figure 3.9d highlights the abruptness of these heterointerfaces by plotting the bromide and chloride signals obtained from an SEM-EDS line scan taken across the entire width of a single flake following a 30-min exchange reaction. This heterostructure formation does not come from any inherent immiscibility between PEA_2CrCl_4 and PEA_2CrBr_4, given the homogeneous bromide distributions we find in mixed-halide single crystals synthesized directly from solution (see Appendix C).

We investigate the origin of the observed heterostructure formation by monitoring ion-migration dynamics, tracking the time-evolution of the bromide-rich region when crystals are heated in the presence of excess vaporous TMS-Br. Figure 3.9e plots bromide SEM-EDS line scans (scaled by the total halide signal) collected on flakes reacted for 10, 30, 60, and 180 min at 175 °C, highlighting lateral diffusion of bromide ions from the crystallite edges into their

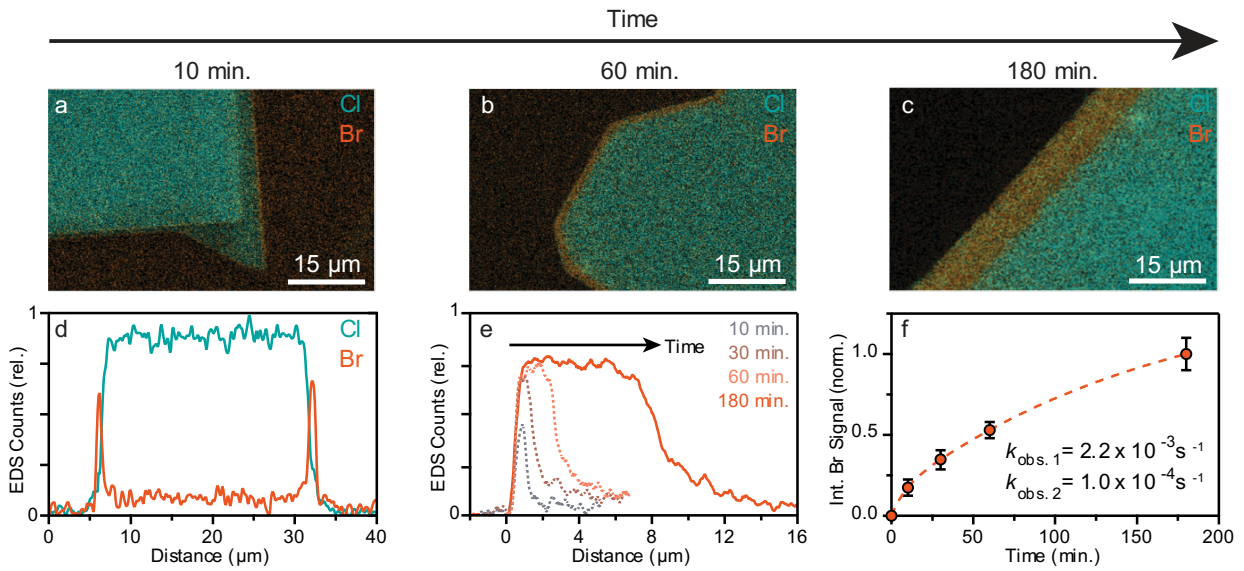

Figure 3.9. (a-c) SEM-EDS images collected after partial anion-exchange reactions of exfoliated flakes of PEA_2CrCl_4 using excess TMS-Br, plotting the chloride signal in teal and the bromide signal in orange. (d) Chloride and bromide SEM-EDS line scans taken across the width of a single flake following a 30-min anion-exchange reaction at 175 °C. (e) SEM-EDS line scans plotting the bromide signal after reacting exfoliated flakes of PEA_2CrCl_4 with TMS-Br at 175 °C for 10, 30, 60, and 180 min. Each trace was scaled relative to the total halide signal. (f) Plot of the total integrated bromide signal as a function of reaction time. The plateaus of the shorter timepoint reactions in (e) were extrapolated to 16 μm to account for varying flake sizes. The data were fit using a double-exponential function (dashed) to get the rate constants shown.

centers. Figure 3.9f quantifies these data by plotting the total integrated bromide signal as a function of reaction time, representing the relative surface flux of bromide. The experimental curve is not a simple exponential, but a double-exponential function gives a good fit using two effective rate constants separated by an order of magnitude, $k_{obs.\ 1}$ = 2.2x10^{-3} s^{-1} and $k_{obs.\ 2}$ = 1.0x10^{-4} s^{-1}. We interpret this result by proposing that these abrupt heterointerfaces form because of very different rates for the three dominant anion-exchange processes active in these crystals, illustrated in Figure 3.10: (i) $k_{v\text{-}s}$, describing the rate constant for the vapor-solid reaction between TMS-Br and edge sites in PEA_2CrCl_4, (ii) k_{2D}, describing "two-dimensional" intralayer solid-state diffusion of bromide, and (iii) k_{3D}, describing the combined contributions of "three-dimensional" interlayer bromide diffusion and the bulk anion-exchange reactivity arising from interlayer TMS-Br diffusion. The data in Figure 3.9d show that bromide accumulates at the crystal edges upon exposure to TMS-Br, indicating that the edge-localized vapor-solid reaction occurs substantially faster than any other process under these conditions; we thus attribute the fast and slow kinetics in Figure 3.9f to $k_{v\text{-}s}$ and k_{2D}, respectively. Moreover, this result also suggests that the bulky phenethylammonium cations strongly inhibit interlayer anion and TMS-Br diffusion (k_{3D}), similar to observations in the analogous lead-halide perovskites,[81-83] confining anion exchange to 2D solid-state diffusion within individual inorganic sheets. Edge-site reactivity that is an order of magnitude faster than intralayer bromide diffusion thus leads to

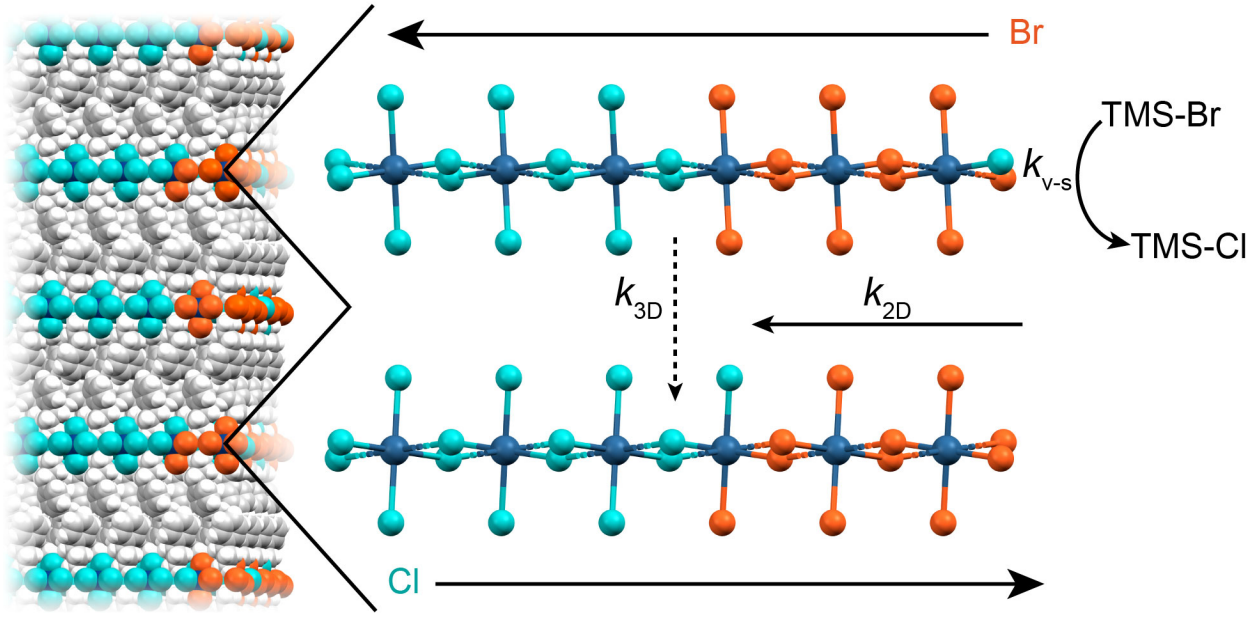

Figure 3.10. Illustration of the proposed anion-exchange mechanism in $PEA_2Cr(Cl{\rightarrow}Br)_4$. The exchange is initiated by the reaction of vaporous TMS-Br with the sterically uninhibited $[CrCl_6]^{4-}$ units at the edges of the flake. The rate of this reaction is dictated by the vapor-solid exchange rate constant, labeled $k_{v\text{-}s}$. Vertical "three-dimensional" diffusion of bromide between the layers (including as TMS-Br) is impeded by the bulky PEA^+ layer, illustrated by the dashed arrow labeled k_{3D}. Bromide instead diffuses laterally through a "two-dimensional" intralayer exchange reaction, labeled k_{2D}.

accumulation of bromide at the flake's edge, and hence to the abrupt lateral PEA_2CrCl_4/PEA_2CrBr_4 heterostructures observed in Figure 3.9a-c.

To test the association of the fast and slow kinetics in Figure 3.9f with $k_{v\text{-}s}$ and k_{2D}, respectively, we can use the SEM-EDS data in Figure 3.9e to quantify the fractional bromide content at the edge of the flake and the width of bromide region as a function of reaction time (see Appendix C). Although these parameters have different units and are thus not directly comparable, it is illustrative to highlight that fitting the time evolution of each to a single-exponential function yields effective rate constants that mirror the two kinetic components found in Figure 3.9f (see Appendix C). This comparison provides strong support for the conclusion that $k_{obs.\,1} \propto k_{v\text{-}s}$ and $k_{obs.\,2} \propto k_{2D}$. As a further control, measurements were also performed on partially anion-exchanged flakes in the absence of excess TMS-Br. These data showed loss of the abrupt lateral heterointerface and formation of a more diffuse bromide concentration gradient upon heating (see Appendix C), emphasizing the importance of the imbalance between vapor-solid and 2D-diffusion reaction rates for heterostructure formation. This result also establishes that the effective rate constants reported here ($k_{v\text{-}s}$ and k_{2D}) are phenomenological parameters applicable only in the limit of the surface reaction being pseudo-zeroth order in TMS-Br (see Appendix C).

It is also noteworthy that the fractional bromide concentrations all plateau at a uniform stoichiometry of ~75%, *i.e.*, $PEA_2Cr(Cl_{0.25}Br_{0.75})_4$ (see Appendix C). Even after extended reaction times (18 hours), these exfoliated single crystals show a laterally homogeneous composition yet still incomplete anion exchange, having a fractional bromide content of 93 ± 4 % (see Appendix C). These observations suggest a particular stability of a fractionally exchanged composition near $PEA_2Cr(Cl_{0.25}Br_{0.75})_4$. In bulk single crystals of $Rb_2CrCl_2Br_2$ and $Rb_2CrCl_2I_2$ grown from the melt, heavier halides have been observed to preferentially occupy the out-of-plane positions,[84] but full out-of-plane anion exchange here would correspond to a Br content of only 50%, *i.e.*, $PEA_2Cr(Cl_{0.50}Br_{0.50})_4$. If a similar site preference exists in $PEA_2Cr(Cl_{0.25}Br_{0.75})_4$, then the data here would indicate that on average one additional in-plane bridging Cl per Cr is also substituted by Br at this metastable intermediate composition, such that each lattice Cr^{2+} ion has an average local coordination of ca. $[CrCl_2Br_4]^{4-}$. In any case, exchange of the final Cl is clearly less favorable than the preceding exchanges.

To test our assertion that sterics of the phenethylammonium cation play a critical role in directing the formation of lateral heterointerfaces, we also studied analogous vapor-phase anion-exchange reactions on exfoliated flakes of a composition with a less sterically inhibiting A-site cation, MA_2CrCl_4 (MA^+ = methylammonium, see section 3.4 Methods). Figure 3.11a,b show SEM-EDS images of the bromide and chloride signals after reacting an exfoliated MA_2CrCl_4 crystal with excess TMS-Br at 175 °C for 30 min. These images show that the bromide content is evenly distributed across the entire width of the crystal, as confirmed by the SEM-EDS line scans shown in Figure 3.11c. Given that the inorganic $[CrCl_4]^{2-}$ sheets themselves are nearly identical between PEA_2CrCl_4 and MA_2CrCl_4,[71, 85] it is reasonable to conclude that this difference in anion-exchange reactivity is due to their different organic A-site cations; specifically, these data imply that interlayer anion diffusion (k_{3D}, including possible TMS-Br interlayer diffusion) is

much faster in MA_2CrCl_4 than in PEA_2CrCl_4 and is now competitive with the edge reactivity. The dashed line in Figure 3.11c shows that the fractional Br content is constant throughout the flake. Figure 3.11d tracks the progression of anion exchange in MA_2CrCl_4 by plotting this fractional bromide content as a function of reaction time, showing a nearly constant increase consistent with the high activity of the excess TMS-Br.

Figure 3.11e shows Raman spectra of a series of partially exchanged $MA_2Cr(Cl,Br)_4$ samples. MA_2CrCl_4 shows a prominent vibration centered at ~275 cm^{-1}, assigned as a B_{2g} mode similar to PEA_2CrCl_4. This feature decreases in intensity with increasing reaction time, concomitant with the growth of a new peak centered at ~175 cm^{-1} assigned to the same B_{2g} vibration in the bromide-exchanged composition. We note the lack of intermediates observed in the evolution of this peak, which could reflect the same kind of "quantized" layer-by-layer anion diffusion as described in analogous lead-halide perovskites.[81] The similarity of this vibration to that observed in the fully exchanged PEA_2CrBr_4 sample of Figure 3.7d is consistent with full exchange of individual layers at intermediate compositions.

To complement the above diffusion data collected for reactions performed at 175 °C, parallel measurements were performed as a function of reaction temperature. Figure 3.12a plots the bromide signals obtained from SEM-EDS line scans collected after 30-min partial anion-exchange reactions on exfoliated flakes of PEA_2CrCl_4 held at 100, 125, 150, and 175 °C, again using excess TMS-Br. The width of the surface-exchanged region increases with increasing

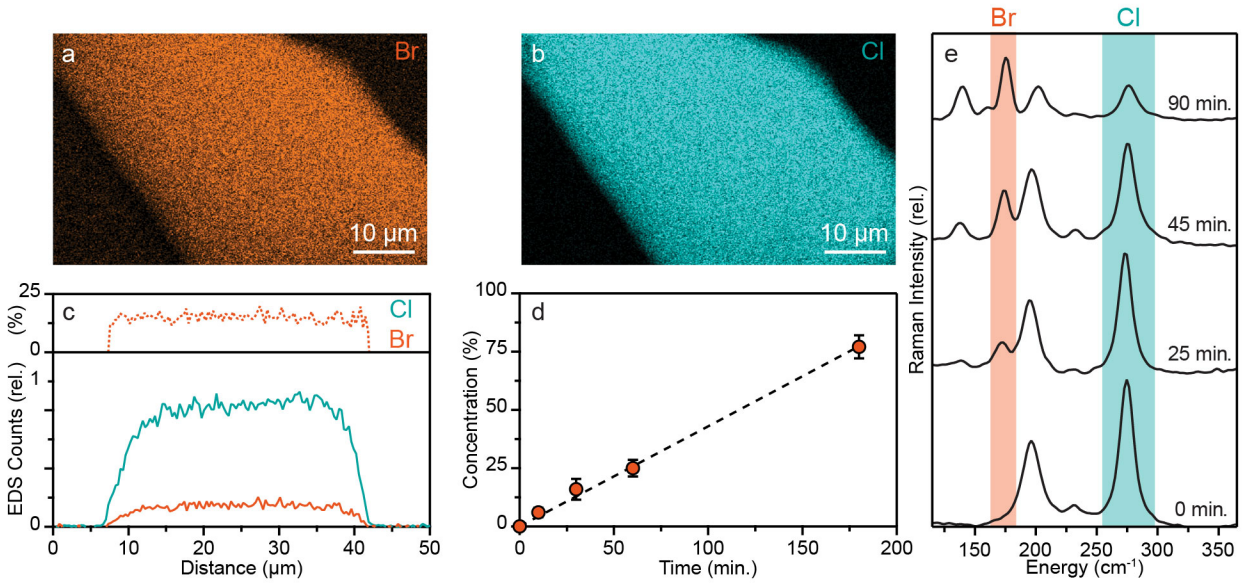

Figure 3.11. SEM-EDS images plotting (a) bromide and (b) chloride signals collected after partially anion exchanging an exfoliated flake of MA_2CrCl_4 by reacting with TMS-Br at 175 °C for 30 min. (c) Chloride and bromide SEM-EDS line scans taken across the entire width of the crystal shown in panels (a,b) (solid traces) and the fractional bromide content (*i.e.*, %Br = 100%*[Br]/([Cl] + [Br])) (dashed trace). These data indicate a laterally uniform fractional bromide content of 15 ± 2%. (d) Plot of the fractional bromide content as a function of reaction time. The dashed line shows a linear fit to guide the eye. (e) Raman spectra collected as a function of anion-exchange reaction time at 175 °C.

of the bromide-rich regions in each compound after 30 min reactions at different temperatures. All three compounds show increased diffusion at higher temperatures, with PEA_2PbCl_4 showing the most rapid diffusion and PEA_2CrCl_4 the slowest. At 175 °C, the partially exchanged PEA_2PbCl_4 flake showed a homogenous distribution of bromide across its entire width. The 175 °C data point displayed in Figure 3.12c for this sample therefore represents only the lower limit of the bromide region's width, limited by the flake size. This result suggests that $k_{2D} \approx k_{v\text{-}s}$ in PEA_2PbCl_4 under these conditions (see Appendix C). Remarkably, the homogeneous fractional bromide content in the 175 °C Pb^{2+} sample also plateaued at ~75%, the same value at which the Cr^{2+} data in Figure 3.9f plateau, possibly indicating a similar metastability of the ca. $PEA_2Pb(Cl_{0.25}Br_{0.75})_4$ composition. A recent study of mixed-halide $(BA)_2MAPb_2(Br_xI_{1-x})_7$ perovskites have also identified a preferential out-of-plane occupation of the heavier iodide

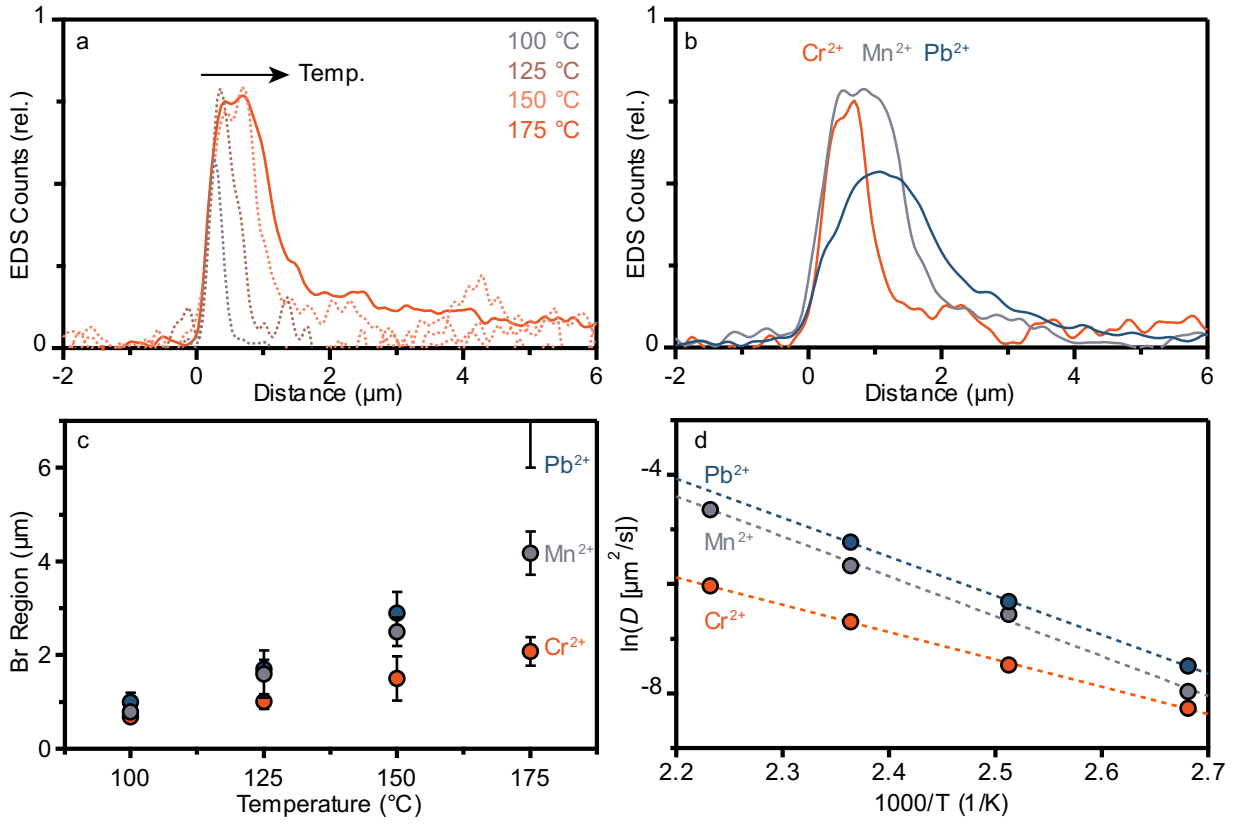

Figure 3.12. (a) SEM-EDS line scans plotting the bromide signal collected after reacting exfoliated flakes of PEA_2CrCl_4 with excess TMS-Br for 30 min at reaction temperatures of 100, 125, 150 and 175 °C. (b) Comparison of SEM-EDS line scans plotting the bromide signal collected after reacting exfoliated flakes of PEA_2CrCl_4 (orange), PEA_2MnCl_4 (gray), and PEA_2PbCl_4 (blue) with TMS-Br for 30 min at 150 °C. (c) Comparison of the bromide-exchange widths as a function of reaction temperature for PEA_2CrCl_4 (orange), PEA_2MnCl_4 (gray), and PEA_2PbCl_4 (blue). (d) Arrhenius plots based on the data in panel (c). The experimental diffusion coefficients (D) at each temperature are provided in Table C1. Fitting these data yields values of E_a = 0.4, 0.6, and 0.6 eV and D_0 = 1.7x10^2 μm^2/s, 1.1x10^5 μm^2/s, and 1.1x10^5 μm^2/s, for the Cr^{2+}, Mn^{2+}, and Pb^{2+} compounds, respectively.

ligands,[86] consistent with our observations here.

The data in Figure 3.12c were then used to quantify the bromide diffusivity in these three compounds, based on a simplified one-dimensional Fickian diffusion model in which the intralayer bromide diffusion coefficient is defined as $D = L^2/\tau$, where L is the width of the bromide-rich region as determined by SEM-EDS analysis (see Appendix C) and τ is the reaction time. The diffusion coefficients (D) obtained from analysis of the PEA_2CrCl_4, PEA_2MnCl_4, and PEA_2PbCl_4 results shown in Figure 3.12c are provided in Table C1. Although there are no published data for the specific PEA_2PbCl_4 reaction studied here, our values for the bromide diffusion coefficients in PEA_2PbCl_4 are similar to those found in other PEA_2PbX_4 lattices.[82, 87] Figure 3.12d shows Arrhenius plots of these diffusion coefficients for PEA_2CrCl_4, PEA_2MnCl_4, and PEA_2PbCl_4 results shown in Figure 3.12c. Fitting these data gives values of $E_a \approx 0.4$, 0.6, and 0.6 eV for the activation energy and $D_0 = 1.7\text{x}10^2$ $\mu m^2/s$, $1.1\text{x}10^5$ $\mu m^2/s$, and $1.1\text{x}10^5$ $\mu m^2/s$ for the Br limiting diffusivity (also described as the high-temperature diffusion limit) for the Cr^{2+}, Mn^{2+}, and Pb^{2+} compounds, respectively. Whereas there is only a small spread in E_a values among these three compounds, D_0 in PEA_2CrCl_4 is $\sim 10^3$x smaller than in the other two compounds. Among these three compounds, only PEA_2CrCl_4 displays an antiferrodistortive ordering of Jahn-Teller distortion axes[71] (found to persist even at 300 °C in Rb_2CrCl_4[88]), and this contrast in diffusivity most likely stems from this cooperative structural property.

It is not obvious *a priori* that PEA_2CrCl_4, PEA_2MnCl_4, and PEA_2PbCl_4 should show such similar post-synthetic anion exchange chemistries given the qualitative differences between these B-site cations including ionic radii, their open- *versus* closed-shell valencies, the propensity of octahedral Cr^{2+} to undergo a Jahn-Teller distortion, and the correlated antiferrodistortive ordering of PEA_2CrCl_4. Despite these differences, the general trends among all three compositions, and in particular the ability to form lateral heterostructures under these reaction conditions, are arguably still more similar than they are different. Indeed, the results presented here demonstrate that the organic cation is most important in directing (or not allowing) formation of abrupt lateral Cl/Br heterointerfaces, especially at lower reaction temperatures where thermally activated anion diffusion is suppressed.

3.3.3 Conclusion

Post-synthetic vapor-phase anion exchange has been demonstrated in layered Cr^{2+} two-dimensional perovskites, with MCD field-sweep measurements revealing ferromagnetic ordering in solution-processed films of PEA_2CrCl_4 and anion-exchanged PEA_2CrBr_4 films. Partial anion exchange on exfoliated flakes of PEA_2CrCl_4 yields lateral magneto-heterostructures of PEA_2CrCl_4/PEA_2CrBr_4, dictated by a kinetic imbalance between edge-site reactivity and intralayer halide diffusivity. Analogous anion-exchange reactions on exfoliated flakes of MA_2CrCl_4 illustrate the effect of the A-site cation on interlayer anion diffusion, and consequently the overall anion-exchange behavior. These results, along with direct comparisons to PEA_2MnCl_4 and PEA_2PbCl_4, highlight the versatility of the 2D perovskite synthetic toolbox. In addition to gaining a better understanding of the chemistry of magnetic Cr^{2+}-based 2D

perovskites, the results presented here demonstrate the ability to leverage post-synthetic anion exchange to achieve ferromagnetic heterostructures that cannot be made *via* traditional crystallization approaches.

It is interesting to consider how lateral heterostructures in A_2CrX_4 compounds – whose robust ferromagnetism distinguishes them among 2D metal-halide perovskites – may give rise to exotic spin-physics such as exchange biases, frustrated magnetism, and complex magnonic landscapes derived from sculpted spin-wave impedances. PEA_2CrCl_4/PEA_2CrBr_4 lateral interfaces such as those described here likely generate unique spin behavior arising from competing bromide- and chloride-mediated magnetic interactions at these interfaces; the Cr^{2+}-halide covalency has a strong influence on the strength of the ferromagnetic superexchange coupling, the Cr^{2+} single-ion anisotropies, and hence the ferromagnetic ordering temperature.[84, 89] It is also motivating to envision future studies exploring PEA_2CrX_4 post-synthetic anion exchange involving the more covalent iodide anion, especially given that no A_2CrI_4 material has ever been synthesized. Overall, these results highlight the utility of extending chemistries developed recently for Pb^{2+}-based 2D metal-halide perovskites to the rich but underexplored ferromagnetic Cr^{2+}-halide 2D perovskites in order to access entirely new low-dimensional magnetic materials.

3.4 Methods

An air-stable and exfoliable ferromagnetic two-dimensional perovskite, (phenethylammonium)$_2$CrCl$_4$

Synthesis. (phenethylammonium)$_2$CrCl$_4$ ((PEA)$_2$CrCl$_4$) crystals were grown in inert atmosphere by dissolving $CrCl_2$ powder (1.14 mmol) and PEA-Cl (2.39 mmol) in 50:50 methanol:ethanol (20 mL) through vigorous shaking, and placing this solution in a larger container containing diethyl ether (~50 mL). Slow vapor diffusion of the ether into the alcohol solution at room temperature yields large (>1 cm^2), thin, pale green, faceted crystals over ~18 h. Individual crystals were isolated by removing them from the mother liquor and allowing them to dry under inert atmosphere. (methylammonium)$_2$CrCl$_4$ ((MeNH$_3$)$_2$CrCl$_4$) crystals were grown by the same method using CH_3NH_3Cl in place of PEA-Cl.

Physical Measurements. Single-crystal x-ray diffraction data were collected at 100 K on a Bruker APEX II single-crystal diffractometer using Mo-radiation and a Miracol x-ray optical collimator. A crystal measuring 0.50 x 0.25 x 0.05 mm^3 was mounted on a loop with oil. The crystal-to-detector distance was 47 mm and the exposure time was 20 sec per frame for all sets. The scan width was 0.75^o. The data were integrated and scaled using SAINT (version 7.34A), SADABS (version 2007/4) within the APEX2 (version 2.1-4) software package by Bruker. Additional x-ray diffraction data were measured on single crystals using a Bruker D8 Discover powder diffractometer with a high-efficiency IμS microfocus x-ray source for Cu Kα radiation operating at 50,000 mW (50 kV, 1 mA). Optical microscope images were collected using a Cannon EOS 7000 camera equipped with Olympus optical objectives (LMPlanFL N, 5x/0.15/0/FN26.5; LMPlanFL N, 20x/0.40/0/FN26.5; SLMPlan N, 50x/0.35/0/FN26.5) housed in the UW MEM-C Shared Facilities. Height analysis of exfoliated flakes was performed using a Bruker Dimension Edge Atomic Force Microscope (MEM-C Shared Facilities) operating in contact mode. Variable-temperature electronic absorption spectra were collected on a single crystal cooled in a helium flow cryostat, using an Aligent Cary 5000 spectrometer. Magnetic measurements were collected on a single crystal using a Quantum Design Physical Property Measurement System (PPMS-14T) vibrating sample magnetometer.

Anion exchange and lateral heterostructure formation in ferromagnetic (PEA)$_2$Cr(Cl,Br)$_4$ two-dimensional perovskites

Chemicals. All chemicals were used as received, without further purification. Single crystal syntheses used anhydrous $CrCl_2$ (97% Alfa Aesar), $MnCl_2$ x 4 H_2O (98%, Sigma Aldrich), $PbCl_2$ (98%, Sigma Aldrich), phenethylammonium chloride (PEA-Cl, 98% Sigma Aldrich), phenethylammonium bromide (PEA-Br, 98% Sigma Aldrich), methylammonium chloride (MA-Cl, 99.99% Great Cell Solar Materials), anhydrous ethanol (HPLC-grade, 90% denatured, Fisher), anhydrous methanol (99.9%, Fisher), and anhydrous diethyl ether (≥99.0%, Sigma-Aldrich), methanol, and isopropyl alcohol. Thin film syntheses used anhydrous N,N-dimethylformamide (DMF, 99.8%, Alfa Aesar) and acetone (HPLC-grade, Sigma-Aldrich).

Anion exchange reactions were performed using trimethylsilyl bromide (TMS-Br, 97% Sigma-Aldrich) and methylammonium bromide (MA-Br, 99.99% Great Cell Solar Materials).

Preparation of PEA_2CrCl_4 thin films. PEA_2CrCl_4 thin films were prepared by adapting previously reported methods of preparing lead-halide thin films.[44, 72] In a nitrogen-filled glovebox a 1 M PEA_2CrCl_4 precursor solution was prepared by combining 5 mmol of anhydrous $CrCl_2$ and 10 mmol of PEA-Cl in 5 mL of DMF. Substrates were either 1 cm x 1 cm silicon wafers or 1 cm diameter quartz disks. Substrates were cleaned by sonicating in a detergent/water mixture for 10 min, followed by a 10-min sonication in DI water, followed by a 10-min sonication in acetone. Substrates were then further cleaned by a UV-ozone cleaner for 23 min. All thin film syntheses were prepared under inert conditions using a spin coater loaded in a nitrogen-filled glovebox. Substrates were pre-heated on a 100 °C hotplate for 10 min. Then, 50 µL of the 1 M precursor solution was deposited onto the hot substrate followed by a 5 sec 500 rpm spin, followed by a 30 sec 5000 rpm spin. The thin films were then annealed on a 100 °C hotplate for 30 min. All sample analysis was performed under inert conditions to avoid ambient degradation, which these thin films are more susceptible to than the bulk single crystals.

Preparation of PEA_2CrCl_4 single crystals. PEA_2CrCl_4 single crystals were prepared according to a literature procedure.[71] In a nitrogen-filled glovebox, 0.3 mmol of $CrCl_2$ was combined with 0.6 mmol of PEA-Cl in a 20 mL scintillation vial and dissolved in 5 mL of a 1:1 mixture of methanol:ethanol. The 20 mL vial was placed in a larger reaction jar, which was filled with 35 mL of diethyl ether. The reaction jar was sealed and left at room temperature overnight, yielding plate-like single crystals.

Preparation of MA_2CrCl_4 single crystals. MA_2CrCl_4 single crystals were prepared by modifying a literature procedure.[71] In a nitrogen-filled glovebox, 0.3 mmol of $CrCl_2$ was combined with 0.6 mmol of MA-Cl in a 20 mL scintillation vial and dissolved in 5 mL of a 1:1 mixture of methanol:ethanol. The 20 mL vial was placed in a larger reaction jar, which was filled with 35 mL of diethyl ether. The reaction jar was sealed and left at room temperature overnight, yielding plate-like single crystals.

Preparation of $PEA_2Cr(Cl_{1-x}Br_x)_4$ single crystals. $PEA_2Cr(Cl_{1-x}Br_x)_4$ single crystals were prepared by adapting a literature procedure.[71] In a nitrogen-filled glovebox, 0.3 mmol of $CrCl_2$ was combined with 0.6 mmol of PEA-Br in a 20 mL scintillation vial and dissolved in 5 mL of a 1:1 mixture of methanol:ethanol. The 20 mL vial was placed in a larger reaction jar, which was filled with 35 mL of diethyl ether. The reaction jar was sealed and left at room temperature overnight, yielding plate-like single crystals.

Preparation of PEA_2MnCl_4 single crystals. PEA_2MnCl_4 single crystals were prepared according to a literature procedure.[90] Under ambient conditions 0.3 mmol of $MnCl_2$ x 4 H_2O was combined with 0.6 mmol of PEA-Cl in a 15 mL falcon tube and dissolved in 5 mL of a 2:1 methanol:isopropyl alcohol solution. The tube was sealed with a rubber septum, and a vent needle was pierced through the septum before placing the tube in a 35 °C sand bath. The tube was left for a week, upon which pale pink PEA_2MnCl_4 crystals precipitated. Single crystals were exfoliated in the same manner as the chromium analogs prior to anion exchange reactions.

Preparation of PEA_2PbCl_4 microplates. PEA_2PbCl_4 microplates were prepared by adapting a literature procedure.[82] Under ambient conditions 2.25 mmol of $PbCl_2$ was combined with 5 mmol of PEA-Cl and dissolved in 1.5 mL of DMF to make a 1.5 M precursor solution. The solution was heated in a 70 °C sand bath. After several minutes of heating, small amounts of additional DMF were added to the solution until the precursors had fully dissolved and the solution turned clear. The heat was turned off and the solution slowly cooled to room

temperature over the course of approximately two hours, after which many colorless plate-like crystals had formed. The microplates were exfoliated in the same manner as the chromium analogs prior to anion exchange reactions.

Anion exchange reactions. All anion-exchange reactions were performed in a nitrogen-filled glovebox. Thin film-anion exchange reactions were performed directly on the as-prepared thin film. Exfoliated single crystal samples prepared for SEM-EDS analysis (PEA_2CrCl_4, MA_2CrCl_4, PEA_2MnCl_4, and PEA_2PbCl_4) were exfoliated onto an ozone-cleaned silicon wafer using the Scotch tape method, yielding a typical flake thickness of ~350 nm as probed by atomic force microscopy (AFM) prior to the anion exchange reactions. Partially anion exchanged MA_2CrCl_4 samples used for Raman analysis were reacted as bulk single crystals (not exfoliated). Anion exchange reactions were performed by placing the sample in a 20 mL glass vial. 0.3 mL of TMS-Br was added to a ½-dram vial, which was left open then placed in the 20 mL vial. The 20 mL vial was then sealed and placed on a hot plate set between 100 – 175 °C for varying reaction times.

X-ray diffraction. Powder X-ray diffraction measurements were performed using a Bruker D8 Discover Microfocus X-ray diffractometer equipped with a copper X-ray source (1.5406 Å). All samples were encapsulated on a glass microscope slide under inert conditions using a grease seal and Kapton film to avoid ambient degradation.

Electron microscopy and elemental analysis. Electron images were collected using a ThermoFisher Scientific Apreo variable-pressure scanning electron microscope (SEM). Elemental analysis was performed using an Oxford energy dispersive spectroscopy (EDS) detector. SEM images were typically collected using 5 keV and 14 pA. SEM-EDS measurements were typically performed at 20 keV and 0.2-0.8 nA. SEM-EDS error bars were determined by analyzing ≥3 flakes per reaction over separately prepared substrates.

Raman spectroscopy. Raman measurements were performed using a Renishaw inVia confocal Raman microscope equipped with a 532 nm laser. Samples were analyzed as either bulk single crystals or spin-coated thin films. All samples were encapsulated on a glass microscope slide under inert conditions using a grease seal and glass cover slip to avoid ambient degradation.

Absorption and magnetic circular dichroism spectroscopy. The films were prepared as a mull suspension using polydimethylsiloxane in order to increase the population of crystallite grains oriented along the magnetic easy axis. Room temperature absorption spectra were collected using an Agilent Cary 5000. Magnetic circular dichroism (MCD) measurements were performed using an Aviv 40DS spectropolarimeter with a superconducting magneto-optical cryostat (Cryo-Industries SMC-1659 OVT) oriented in the Faraday configuration. The samples were measured to be <5% depolarizing, checked by matching the circular dichroism signal of a nickel tartrate standard placed before and after the sample along the optical path.

3.5 References

1. Saparov, B. M., D. B. Organic-Inorganic Perovskites: Structural Versatility for Functional Materials Design. *Chem. Rev.* **2016,** *116*, 4558-4496.
2. Smith, M. D. C., E. J.; Jaffe, A.; Karunadasa, H. I. The Diversity of Layered Halide Perovskites. *Annu. Rev. Mater. Res.* **2018,** *48*, 111-138.
3. Smith, M. D. C., B. A.; Karunadasa, H. I. Tuning the Luminescence of Layered Halide Perovskites. *Chem. Rev.* **2019,** *119*, 3104-3139.
4. Kulkarni, S. A. M., S. G.; Mathews, N.; Boix, P. P. Perovskite Nanoparticles: Synthesis, Properties, and Novel Applications in Photovoltaics and LEDs. *Small Methods* **2019,** *3*, 1800231-1800246.
5. Blancon, J. C. E., J.; Stoumpous, C. C.; Kanatzidis, M. G.; Mohite, A. D. Semiconductor physics of organic-inorganic 2D halide perovskites. *Nat. Nanotechnol.* **2020,** *15*, 969-985.
6. Ke, W. S., C. C.; Kanatzidis, M. G. "Unleaded" Perovskites: Status Quo and Future Prospects of Tin-Based Perovskite Solar Cells. *Adv. Mater.* **2019,** *31*, 1803230-1803260.
7. Pitaro, M. T., E. K.; Shao, S.; Loi, M. A. Tin Halide Perovskites: From Fundamental Properties to Solar Cells. *Adv. Mater.* **2022,** *34*, 2105844-2105890.
8. Day, P. Correlation of Structures and Properties of Ferromagnetic Tetrahalogenochromate(II) Salts. *J. Magn. Magn. Mater.* **1986,** *54-57*, 1442-1446.
9. Bellitto, C. D., P. Organic-intercalated Halogenochromates(II): Low-dimensional Magnets. *J. Mater. Chem.* **1992,** *2*, 265-271.
10. Bellitto, C. B., E. M.; Righini, G Organic–inorganic hybrids: From magnetic perovskite metal(II) halides to multifunctional metal(II) phosphonates. *Coord. Chem. Rev.* **2015,** *289-290*, 123-136.
11. Day, P. New Transparent Ferromagnets. *Acc. Chem. Res.* **1979,** *12*, 236-243.
12. Sen, D. J., G.; Kaushal, N; Mukherjee, A.; Saha-Dasgupta, T Intrinsic ferromagnetism in atomically thin two-dimensional organic-inorganic van der Waals crystals. *Phys. Rev. B* **2020,** *102*, 054411-054416.
13. Ai, Y. S., R.; Liao, W.; Song, X.; Tang, Y.; Wang, B.; Wang, Z.; Gao, S.; Xiong, R Unprecedented Ferroelectricity and Ferromagnetism in a Cr^{2+}-Based Two-Dimensional Hybrid Perovskite. *Angew. Chem. Int. Ed.* **2022,** *61*, e202206034.
14. Berhe, T. A. S., W.; Chen, C.; Pan, C.; Cheng, J.; Chen, H.; Tsai, M.; Chen, L.; Dubale, A. A.; Hwang, B Organometal halide perovskite solar cells: degredation and stability. *Energy Environ. Sci.* **2016,** *9*, 323-357.
15. Saidaminov, M. I. M., O.; Bakr, O. M Low-Dimensional-Networked Metal Halide Perovskites: The Next Big Thing. *ACS Energy Lett.* **2017,** *2*, 889-896.
16. Seitz, M. M., A. J.; Alcazar-Cano, N.; Melendez, M.; Lubbers, T. J.; Walraven, S. W.; Pakdel, S.; Prada, E.; Delgado-Buscalioni, R.; Prins, F. Exciton diffusion in two-dimensional metal-halide perovskites. *Nat. Commun.* **2020,** *11*, 1-8.
17. Leung, T. L. A., I.; Syed, A. A.; Ng, A. M. C.; Popovic, J.; Djurisic, A. B. Stability of 2D and quasi-2D perovskite materials and devices. *Commun. Mater.* **2022,** *3*, 1-10.
18. Kore, B. P. G., J. M. Water-resistant 2D lead(II) iodide perovskites: correlation between optical properties and phase transitions. *Mater. Adv.* **2020,** *1*, 2395-2400.
19. Hutchings, M. T. G., A. K.; Day, P.; Leech, D. H. Neutron Diffraction Study of the Crystal and Magnetic Structure of the Ionic Ferromagnet Cs_2CrCl_4. *Solid State Commun.* **1974,** *15*, 313-316.
20. Bellitto, C. D., P. Magnetic Susceptibility and Optical Spectra of the Organic-intercalated

Two-dimensional Ferromagnets Bis(monomethylammonium)- and Bis(monoethylammonium) Tetrachlorochromate (II). *J. C. S. Chem. Comm.* **1978**, 1207-1210.
21. Janke, E. H., M. T.; Day, P.; Walker, P. J Neutron diffraction study of the crystal and magnetic structure of Rb_2CrCl_4: a two-dimensional ionic ferromagnet. *J. Phys. C: Solid State Phys.* **1983,** *16*, 5959-5969.
22. Barbar, M. A. L., M. F. C.; Larkworthy, L. F.; Newell, G. P.; Povey, D. C.; Proctor, K. J.; Summers, L. J. The Crystal Structures of Propane-1,3-diammonium Tetrachlorochromate(II), a Sheet Ferromagnet, and Bis(dimethylammonium) Tetrachlorochromate(II), an Antiferromagnetic Compound Containing Isolated $[Cr_3Cl_{12}]^{6-}$ Units. *J. C. S. Chem. Comm.* **1981**, 1046-1047.
23. Day, P.; Gregson, A. K.; Leech, D. H. Optical Properties of Ferromagnetic K_2CrCl_4. *Physical Review Letters* **1973,** *30*, 3.
24. Stead, M. J. D., P. Preparation, Characterization, and Magnetic Properties of Organic-intercalated Two-dimensional Ionic Ferromagnets $(C_nH_{2n+1}NH_3)_2CrCl_4$ (N = 3, 5, or 12). *J. Chem. Soc. Dalton Trans.* **1982**, 1081-1083.
25. Briat, B. B., S. T. ; Canit, J. C. ; Day, P.; F .R. S.; Thorne, J. R. G Spin dynamics and absorption-band profiles for the planar two-dimensional easy-plane ionic ferromagnet Rb_2CrCl_4. *Proc. R. Soc. Lond. A* **1988,** *415*, 277-302.
26. Woodward, P. M. Octahedral Tilting in Perovskites. I. Geometrical Considerations. *Acta Cryst.* **1997,** *B53*, 32-43.
27. Alaei, A. C., A.; Yuan, Y.; Yang, Y.; Lee, S. S. Polymorphism in metal halide perovskites. *Mater. Adv.* **2021,** *2*, 47-63.
28. McNulty, J. A. L., P. Structural chemistry of layered lead halide perovskites containing single octahedral layers. *IUCrJ* **2021,** *8*, 485-513.
29. Bechtel, J. S. V. d. V., A. Octahedral tilting instabilities in inorganic halide perovskites. *Phys. Rev. Mater.* **2018,** *2*, 025401.
30. Polinger, V., *Orbital Ordering Versus the Traditional Approach in the Cooperative Jahn–Teller Effect: A Comparative Study*. Springer Berlin Heidelberg: Berlin, Heidelberg, 2009; p 685-725.
31. Witteveen, H. T. Magnetic Measurements on Polycrystalline Samples of the Layer-Type Compounds Rb_2CuCl_4, Rb_2CuCl_3Br and $Rb_2CuCl_2Br_2$. *Physica* **1974,** *71*, 204-236.
32. Kassou, S. B., A. A Cu based layered multifunctional material: $(C_8H_{12}N)_2CuCl_4$ Optical and electronic properties. *Matter. Res. Express* **2018,** *5*, 076305.
33. Aguado, F. R., F.; Valiente, R.; Senas, A.; Goncharenko, I. Three-dimensional magnetic ordering in the Rb_2CuCl_4 layer perovskite - structural correlations. *J. Phys.: Condens. Matter* **2004,** *16*, 1927-1938.
34. Han, C. B., A. J.; Slawin, A. M. Z.; Bode, B. E.; Fusco, E.; Lee, S. L.; Tang, C. C.; Lightfoot, P. Structural features in some layered hybrid copper chloride perovskites, $ACuCl_4$ or A_2CuCl_4. *Inorg. Chem.* **2021,** *60*, 11014-11024.
35. Rauh, H. E., W. A. C.; Regnault, L. P.; Rossat-Mignod, J.; Kullmann, W.; Geick, R. Magnetic phase diagram of Rb_2MnCl_4, a quasi-two-dimensional uniaxial antiferromagnet. *J. Phys. C: Solid State Phys.* **1986,** *19*, 4503-4510.
36. Watanabe, N. K., N.; Ban, T.; Tsujikawa, I. Optical absorption spectra in the quasi-two-dimensional antiferromagnets $[NH_3(CH_2)_nNH_3]MnCl_4$ (n=2,3,4,5): I. Experimental. *J. Phys. C: Solid State Phys.* **1988,** *21*, 4795-4808.
37. Septiany, L. T., D.; Chislov, M.; Baas, J.; Blake, G. R. Polar Structure and Two-Dimensional Heisenberg Antiferromagnetic Properties of Arylamine-Based Manganese Chloride

Layered Organic-Inorganic Perovskites. *Inorg. Chem.* **2021,** *60*, 15151-15158.
38. Bellitto, C. B., H.; Gudel, H. U. Optical Spectroscopy of One- and Two-Dimensional Ionic Magnets of Cr^{2+}: $CsCrCl_3$, $(CH_3)_4NCrCl_3$, $(CH_3)_4NCrBr_3$, $CrCl_2$, $(C_2H_5NH_3)_2CrCI_4$, and $(C_2H_5NH_3)_2CrBr_4$. *Inorg. Chem.* **1987,** *26*, 2347-2351.
39. Day, P. J., E.; Wood, T. E.; Woodwark, D. Optical estimation of the zone-centre magnon gap in Rb_2CrCl_4: a two-dimensional easy-plane ionic ferromagnet. *J. Phys. C: Solid State Phys.* **1979,** *12*, L329-334.
40. Bramwell, S. T. D., P.; Hutchings, M. T.; Thorne, J. R. G.; Visser, D. Neutron Scattering and Optical Study of the Magnetic Properties of the Two-Dimensional Ionic Ferromagnets Rb_2CrCl_3Br and $Rb_2CrCl_2Br_2$. *Inorg. Chem.* **1986,** *25*, 417-421.
41. Janke, E. W., T. E.; Ironside, C.; Day, P. Optical and magneto-optical study of the transparent ionic ferromagnet Rb_2CrCl_4. *J. Phys. C: Solid State Phys.* **1982,** *15*, 3809-3820.
42. Bellitto, C. W., T. E.; Day, P. Low-Temperature Optical and Magneto-Optical Study of the Organic-Intercalated Two-Dimensional Ferromagnet $(CH_3NH_3)_2CrCl_4$. *Inorg. Chem.* **1985,** *24*, 558-562.
43. Smith, M. D.; Connor, B. A.; Karunadasa, H. I. Tuning the Luminescence of Layered Halide Perovskites. *Chem. Rev.* **2019,** *119*, 3104-3139.
44. Li, X.; Hoffman, J. M.; Kanatzidis, M. G. The 2D Halide Perovskite Rulebook: How the Spacer Influences Everything from the Structure to Optoelectronic Device Efficiency. *Chem. Rev.* **2021,** *121*, 2230-2291.
45. Mao, L.; Stoumpos, C. C.; Kanatzidis, M. G. Two-Dimensional Hybrid Halide Perovskites: Principles and Promises. *J. Am. Chem. Soc.* **2019,** *141*, 1171-1190.
46. Akkerman, Q. A.; Manna, L. What Defines a Halide Perovskite? *ACS Energy Lett.* **2020,** *5*, 604-610.
47. Mao, L.; Teicher, S. M. L.; Stoumpos, C. C.; Kennard, R. M.; DeCrescent, R. A.; Wu, G.; Schuller, J. A.; Chabinyc, M. L.; Cheetham, A. K.; Seshadri, R. Chemical and Structural Diversity of Hybrid Layered Double Perovskite Halides. *J. Am. Chem. Soc.* **2019,** *141*, 19099-19109.
48. Mao, L.; Chen, J.; Vishnoi, P.; Cheetham, A. K. The Renaissance of Functional Hybrid Transition-Metal Halides. *Acc. Mater. Res.* **2022,** *3*, 439-448.
49. Smith, I. C.; Smith, M. D.; Jaffe, A.; Lin, Y.; Karunadasa, H. I. Between the Sheets: Postsynthetic Transformations in Hybrid Perovskites. *Chem. Mater.* **2017,** *29*, 1868-1884.
50. Zhang, F.; Lu, H.; Tong, J.; Berry, J. J.; Beard, M. C.; Zhu, K. Advances in Two-Dimensional Organic–Inorganic Hybrid Perovskites. *Energy Environ. Sci.* **2020,** *13*, 1154-1186.
51. Chen, Y.; Sun, Y.; Peng, J.; Tang, J.; Zheng, K.; Liang, Z. 2D Ruddlesden–Popper Perovskites for Optoelectronics. *Adv. Mater.* **2018,** *30*, 1703487.
52. Grancini, G.; Nazeeruddin, M. K. Dimensional Tailoring of Hybrid Perovskites for Photovoltaics. *Nat. Rev. Mater.* **2019,** *4*, 4-22.
53. Smith, M. D.; Crace, E. J.; Jaffe, A.; Karunadasa, H. I. The Diversity of Layered Halide Perovskites. *Annu. Rev. Mater. Res.* **2018,** *48*, 111-136.
54. Huang, B.; Clark, G.; Navarro-Moratalla, E.; Klein, D. R.; Cheng, R.; Seyler, K. L.; Zhong, D.; Schmidgall, E.; McGuire, M. A.; Cobden, D. H.; Yao, W.; Xiao, D.; Jarillo-Herrero, P.; Xu, X. Layer-Dependent Ferromagnetism in a van der Waals Crystal Down to the Monolayer Limit. *Nature* **2017,** *546*, 270-273.
55. Gong, C.; Li, L.; Li, Z.; Ji, H.; Stern, A.; Xia, Y.; Cao, T.; Bao, W.; Wang, C.; Wang, Y.; Qiu, Z. Q.; Cava, R. J.; Louie, S. G.; Xia, J.; Zhang, X. Discovery of Intrinsic

Ferromagnetism in Two-Dimensional van der Waals Crystals. *Nature* **2017,** *546*, 265-269.
56. Gish, J. T.; Lebedev, D.; Song, T. W.; Sangwan, V. K.; Hersam, M. C. Van der Waals Opto-Spintronics. *Nat. Electron.* **2024,** *7*, 336-347.
57. Song, T.; Cai, X.; Tu, M. W.-Y.; Zhang, X.; Huang, B.; Wilson, N. P.; Seyler, K. L.; Zhu, L.; Taniguchi, T.; Watanabe, K.; McGuire, M. A.; Cobden, D. H.; Xiao, D.; Yao, W.; Xu, X. Giant Tunneling Magnetoresistance in Spin-Filter van der Waals Heterostructures. *Science* **2018,** *360*, 1214-1218.
58. Wang, Q. H.; Bedoya-Pinto, A.; Blei, M.; Dismukes, A. H.; Hamo, A.; Jenkins, S.; Koperski, M.; Liu, Y.; Sun, Q.-C.; Telford, E. J.; Kim, H. H.; Augustin, M.; Vool, U.; Yin, J.-X.; Li, L. H.; Falin, A.; Dean, C. R.; Casanova, F.; Evans, R. F. L.; Chshiev, M.*, et al.* The Magnetic Genome of Two-Dimensional van der Waals Materials. *ACS Nano* **2022,** *16*, 6960-7079.
59. Huang, B.; Zhang, J.-Y.; Huang, R.-K.; Chen, M.-K.; Xue, W.; Zhang, W.-X.; Zeng, M.-H.; Chen, X.-M. Spin-Reorientation-Induced Magnetodielectric Coupling Effects in Two Layered Perovskite Magnets. *Chem. Sci.* **2018,** *9*, 7413-7418.
60. van Amstel, W. D.; de Jongh, L. J. Magnetic Measurements on $(CH_3NH_3)_2MnCl_4$, a Quasi Two-Dimensional Heisenberg Antiferromagnet. *Solid State Commun.* **1972,** *11*, 1423-1429.
61. de Jongh, L. J.; Botterman, A. C.; de Boer, F. R.; Miedema, A. R. Transition Temperature of the Two-Dimensional Heisenberg Ferromagnet with S=½. *J. Appl. Phys.* **1969,** *40*, 1363-1365.
62. Polyakov, A. O.; Arkenbout, A. H.; Baas, J.; Blake, G. R.; Meetsma, A.; Caretta, A.; van Loosdrecht, P. H. M.; Palstra, T. T. M. Coexisting Ferromagnetic and Ferroelectric Order in a $CuCl_4$-based Organic–Inorganic Hybrid. *Chem. Mater.* **2012,** *24*, 133-139.
63. Day, P. New Transparent Ferromagnets. *Acc. Chem. Res.* **1979,** *12*, 236-243.
64. Day, P. Correlation of Structures and Properties of Ferromagnetic Tetrahalogenochromate(II) Salts. *J. Magn. Magn. Mater.* **1986,** *54-57*, 1442-1446.
65. Briat, B.; Bramwell, S. T.; Canit, J. C.; Day, P.; Thorne, J. R. G. Spin Dynamics and Absorption-Band Profiles for the Planar Two-Dimensional Easy-Plane Ionic Ferromagnet Rb_2CrCl_4. *Proc. R. Soc. London, Ser. A* **1997,** *415*, 277-302.
66. Bellitto, C.; Day, P. Organic-Intercalated Halogenochromates(II): Low-Dimensional Magnets. *J. Mater. Chem.* **1992,** *2*, 265-271.
67. Creutz, S. E.; Crites, E. N.; De Siena, M. C.; Gamelin, D. R. Anion Exchange in Cesium Lead Halide Perovskite Nanocrystals and Thin Films Using Trimethylsilyl Halide Reagents. *Chem. Mater.* **2018,** *30*, 4887-4891.
68. De Siena, M. C.; Sommer, D. E.; Creutz, S. E.; Dunham, S. T.; Gamelin, D. R. Spinodal Decomposition During Anion Exchange in Colloidal Mn^{2+}-Doped $CsPbX_3$ (X = Cl, Br) Perovskite Nanocrystals. *Chem. Mater.* **2019,** *31*, 7711-7722.
69. Milstein, T. J.; Kluherz, K. T.; Kroupa, D. M.; Erickson, C. S.; De Yoreo, J. J.; Gamelin, D. R. Anion Exchange and the Quantum-Cutting Energy Threshold in Ytterbium-Doped $CsPb(Cl_{1-x}Br_x)_3$ Perovskite Nanocrystals. *Nano Lett.* **2019,** *19*, 1931-1937.
70. Roh, J. Y. D.; Sommer, D. E.; Milstein, T. J.; Dunham, S. T.; Gamelin, D. R. Evolution of Yb^{3+} Speciation in Cl^-/Br^-- and Yb^{3+}/Gd^{3+}-Alloyed Quantum-Cutting Lead-Halide Perovskite Nanocrystals. *Chem. Mater.* **2023,** *35*, 8057-8064.
71. Smith, R. T.; Walsh, K. M.; Jiang, Q.; Chu, J.-H.; Gamelin, D. R. An Air-Stable and Exfoliable Ferromagnetic Two-Dimensional Perovskite, $(Phenethylammonium)_2CrCl_4$. *Chem.*

Mater. **2024,** *36*, 1571-1578.
72. Dubey, A.; Adhikari, N.; Mabrouk, S.; Wu, F.; Chen, K.; Yang, S.; Qiao, Q. A Strategic Review on Processing Routes Towards Highly Efficient Perovskite Solar Cells. *J. Mater. Chem. A* **2018,** *6*, 2406-2431.
73. Mitzi, D. B. A Layered Solution Crystal Growth Technique and the Crystal Structure of $(C_6H_5C_2H_4NH_3)_2PbCl_4$. *J. Solid State Chem.* **1999,** *145*, 694-704.
74. Shibuya, K.; Koshimizu, M.; Nishikido, F.; Saito, H.; Kishimoto, S. Poly[bis(phenethylammonium) [dibromidoplumbate(II)]-di-mu-bromido]]. *Acta Cryst. E* **2009,** *65*, m1323-m1324.
75. Willett, R. Structures of the Antiferrodistortive Layer Perovskites Bis(phenethylammonium) Tetrahalocuprate(II), Halo = Cl^-, Br^-. *Acta Cryst. C* **1990,** *46*, 565-568.
76. Abdalian, A. T.; Dugautier, C.; Moch, P. Magnon and Phonon Raman Scattering of the Planar Ferromagnet Rb_2CrCl_4. *J. Phys. C: Solid State Phys.* **1987,** *20*, 2465.
77. Iqbal, Z.; Arend, H.; Wachter, P. Raman Scattering from Layer-Type Magnets: $(CH_2)_n(NH_3)_2CuCl_4$, n=2, 3 and 5. *J. Phys. C: Solid State Phys.* **1980,** *13*, 4757.
78. Bellitto, C.; Brunner, H.; Güdel, H. Optical Spectroscopy of One- and Two-Dimensional Ionic Magnets of Cr^{2+}: $CsCrCl_3$, $(CH_3)_4NCrCl_3$, $(CH_3)_4NCrBr_3$, $CrCl_2$, $(C_2H_5NH_3)_2CrCl_4$, and $(C_2H_5NH_3)_2CrBr_4$. *Inorg. Chem.* **1987,** *26*, 2750-2754.
79. Münninghoff, G.; Treutmann, W.; Hellner, E.; Heger, G.; Reinen, D. Structure and Jahn-Teller Effect in Mixed Crystals $Rb_2Cr_{1-x}Mn_xCl_4$: A Single-Crystal Neutron Diffraction Study and Spectroscopic Results. *J. Solid State Chem.* **1980,** *34*, 289-299.
80. De Siena, M. C.; Creutz, S. E.; Regan, A.; Malinowski, P.; Jiang, Q.; Kluherz, K. T.; Zhu, G.; Lin, Z.; De Yoreo, J. J.; Xu, X.; Chu, J.-H.; Gamelin, D. R. Two-Dimensional van der Waals Nanoplatelets with Robust Ferromagnetism. *Nano Lett.* **2020,** *20*, 2100-2106.
81. Akriti; Shi, E.; Shiring, S. B.; Yang, J.; Atencio-Martinez, C. L.; Yuan, B.; Hu, X.; Gao, Y.; Finkenauer, B. P.; Pistone, A. J.; Yu, Y.; Liao, P.; Savoie, B. M.; Dou, L. Layer-By-Layer Anionic Diffusion in Two-Dimensional Halide Perovskite Vertical Heterostructures. *Nat. Nanotechnol.* **2021,** *16*, 584-591.
82. He, C.; Li, J.; Bao, Y.; Li, J.; Wang, H.; Zhang, M.; Li, H.; Tang, H.; Sun, Z.; Zhang, Q.; Fang, Y.; Xu, J.; Yang, Y. Robust Heterostructures in Two-Dimensional Perovskites by Threshold-Dominating Anion Exchange. *Small* **2022,** *18*, 2203036.
83. Roy, C. R.; Pan, D.; Wang, Y.; Hautzinger, M. P.; Zhao, Y.; Wright, J. C.; Zhu, Z.; Jin, S. Anion Exchange of Ruddlesden–Popper Lead Halide Perovskites Produces Stable Lateral Heterostructures. *J. Am. Chem. Soc.* **2021,** *143*, 5212-5221.
84. Fyne, P. J.; Day, P. Powder Neutron Diffraction Study of the Crystal and Magnetic Structures of Ferromagnetic Mixed Anion Salts $Rb_2CrCl_{4-x}X_x$. *Mater. Res. Bull.* **1985,** *20*, 197-201.
85. Bellitto, C.; Wood, T. E.; Day, P. Low-Temperature Optical and Magneto-Optical Study of the Organic-Intercalated Two-Dimensional Ferromagnet Methylammonium Tetrachlorochromate(II). *Inorg. Chem.* **1985,** *24*, 558-562.
86. Toso, S.; Gushchina, I.; Oliver, A. G.; Manna, L.; Kuno, M. Are Mixed-Halide Ruddlesden–Popper Perovskites Really Mixed? *ACS Energy Lett.* **2022,** *7*, 4242-4247.
87. Akriti; Zhang, S.; Lin, Z.-Y.; Shi, E.; Finkenauer, B. P.; Gao, Y.; Pistone, A. J.; Ma, K.; Savoie, B. M.; Dou, L. Quantifying Anionic Diffusion in 2D Halide Perovskite Lateral Heterostructures. *Adv. Mater.* **2021,** *33*, 2105183.

88. Janke, E.; Hutchings, M. T.; Day, P.; Walker, P. J. Neutron Diffraction Study of the Crystal and Magnetic Structure of Rb_2CrCl_4: A Two-Dimensional Ionic Ferromagnet. *J. Phys. C: Solid State Phys.* **1983,** *16*, 5959.
89. Bramwell, S. T.; Day, P.; Hutchings, M. T.; Thorne, J. R. G.; Visser, D. Neutron Scattering and Optical Study of the Magnetic Properties of the Two-Dimensional Ionic Ferromagnets Rb_2CrCl_3Br and $Rb_2CrCl_2Br_2$. *lnorg. Chem.* **1986,** *25*, 417-421.
90. Park, G.; Oh, I.-H.; Park, J. M. S.; Park, S.-H.; Hong, C. S.; Lee, K.-S. Investigation of Magnetic Phase Transition on the Layered Inorganic-Organic Hybrid Perovskites $(C_6H_5CH_2CH_2NH_3)_2MnCl_4$ by Single-Crystal Neutron Diffraction. *Physica B: Condensed Matter* **2018,** *551*, 89-93.

Chapter 4. Magnetically Pinned Spin-Bearing Yb^{3+} Optical Impurity Dopants in the van der Waals Ferromagnet CrI_3

In Chapter 4, the broadband luminescence of the well-studied ferromagnet CrI_3 is transformed into sharp-line luminescence by incorporating Yb^{3+} as a spin-bearing optical impurity dopant. Critically, the magnetization of the Yb^{3+} dopant is pinned to that of the ferromagnetic host. This chapter establishes design rules for eliciting spin-correlated optical functionalities in doped 2D ferromagnets through donor-acceptor spectral matching and ligand covalency considerations.

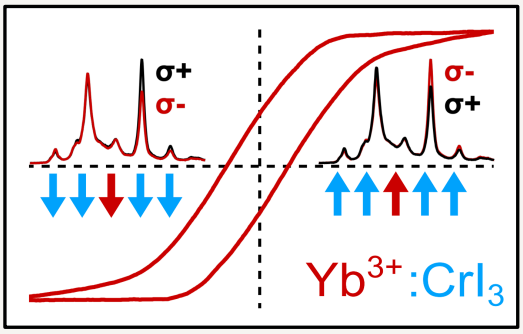

4.1 Overview

Section 4.2 describes how the two-dimensional (2D) van der Waals ferromagnet CrI_3 has been doped with the magnetic optical impurity Yb^{3+} to yield materials that display sharp multi-line Yb^{3+} photoluminescence (PL) controlled by the magnetism of CrI_3. Magneto-PL shows that Yb^{3+} magnetization is pinned to the magnetization of CrI_3. An effective internal field of ~10 T at Yb^{3+} is estimated, attributed to strong in-plane Yb^{3+}-Cr^{3+} superexchange coupling. The anomalously low energy of Yb^{3+} PL in CrI_3 reflects relatively high Yb^{3+}-I^- covalency, contributing to Yb^{3+}-Cr^{3+} superexchange coupling. The Yb^{3+} PL energy and linewidth both reveal the effects of spontaneous zero-field CrI_3 magnetic ordering *within* 2D layers below T_C, despite the absence of net magnetization in multilayer samples. Section 4.3 reports photoluminescence data analysis and angular overlap model (AOM) calculations of the complete Yb^{3+}:CrX_3 (X = Cl, Br, I) family to understand Yb^{3+}-X covalency in these materials, which is critically consequential to the Yb^{3+}-Cr^{3+} superexchange coupling and thusly the observed magnetic pinning of Yb^{3+} by CrI_3. These analyses and calculations show that Yb^{3+} in Yb^{3+}:CrI_3 has a lower spin-orbit splitting energy than reported for *any* Yb^{3+} in any other compound. We attribute these observations to exceptionally high covalency of the Yb^{3+} *f* orbitals in Yb^{3+}:CrI_3 stemming primarily from the shallow valence-shell ionization potentials of the iodide anions. Overall, these results illustrate the use of spin-bearing optical impurities as "designer defects" to introduce spin-correlated optical functionalities to 2D magnets.

4.2 Magnetic amplification at Yb^{3+} "designer defects" in the van der Waals ferromagnet CrI_3

4.2.1 Introduction

Defects have the power to transform the physical properties of crystals, imparting new and potentially useful functionalities from conductivity to quantum photon emission.[1-6] In magnetic materials, defects can strongly affect spin-wave propagation, magnetic domain-wall propagation, skyrmion dynamics, and magnetic vortex pinning.[7-9] Recently, the layered van der Waals ferromagnet CrI_3 has emerged as a promising platform for exploring strongly correlated spin physics, magnetic proximity effects, and next-generation spin-based device architectures in the two-dimensional (2D) limit,[10-14] but the potential to expand CrI_3 functionality through introduction of defects remains untapped. Here, we report that doping CrI_3 with Yb^{3+} as a "designer point defect" transforms its normally broad and featureless *d-d* photoluminescence (PL) into narrow-line sensitized *f-f* emission, without compromising its attractive magnetic properties. We further show that Yb^{3+} in CrI_3 experiences a large internal effective field that makes it extremely sensitive to small external magnetic fields. Using this property, we demonstrate magnetically saturated circular polarization of Yb^{3+} emission at anomalously small applied fields. Strikingly, the internal effective field also transmits magnetic information to Yb^{3+} even in the absence of any applied field, making Yb^{3+} a unique embedded luminescent probe of spontaneous zero-field magnetic ordering within the 2D monolayers of bulk CrI_3. These discoveries establish optical impurity doping as an effective strategy for expanding the functionality of 2D magnets, with potential ramifications for both basic science and future spin-photonic technologies.

CrI_3 has become a model system for exploring magnetic exchange in 2D van der Waals structures,[10-14] stimulated by recent discoveries of Ising-like hard ferromagnetism in exfoliated monolayer CrI_3 and layer- and stacking-dependent magnetism in multi-layer CrI_3.[15, 16] Layering CrI_3 with non-magnetic 2D materials introduces magnetic functionality to the non-magnetic material *via* inter-layer exchange coupling, allowing magnetic manipulation of properties such as WSe_2 valley polarization and valley Zeeman splittings.[17] Extension from few to many (bulk) layers preserves the strong Ising-like intralayer ferromagnetic ordering, but facile motion of domain walls unblocks demagnetization.[18] Despite its rich magnetic properties, CrI_3 itself has not garnered much attention as an optical material. Bulk CrI_3 has been investigated for its very large Kerr and Faraday rotation strengths in relation to optical isolators and associated technologies.[19, 20] PL of bulk CrI_3 has apparently not been reported, and few-layer CrI_3 shows[17] only the very broad *d-d* PL characteristic of weak-field pseudo-octahedral Cr^{3+}.[21] Circular polarization of this *d-d* PL was used to probe the magnetism of few-layer CrI_3,[17] but the emission's breadth limits its further utility for fundamental studies or in spin-photonics, stimulating efforts to narrow the band *via* cavity coupling.[22] Doping CrI_3 with optically active impurities has also not been reported, either in bulk or exfoliated samples.

4.2.2 Results and discussion

To investigate *intra*layer "proximity" effects resulting from magnetic exchange coupling, we have prepared CrI_3 doped with luminescent and spin-bearing Yb^{3+} ions. Large-diameter single-crystal flakes of CrI_3 were prepared by chemical vapor transport. Yb^{3+} was introduced by adding Yb(0) to the precursor mix. The Yb^{3+} concentration in the resulting Yb^{3+}:CrI_3 crystals is controllable, and samples with up to ~5% Yb^{3+} (cation mole fraction, $[Yb^{3+}]/([Cr^{3+}]+[Yb^{3+}])$) are described here. Further experimental details are provided in section 4.4. Figure 4.1a shows a photograph of representative Yb^{3+}:CrI_3 flakes in their growth tube. The flakes are between 5 and 10 mm across, with typical thicknesses of 5-20 μm (see Appendix C). Figure 4.1b plots XRD data collected on undoped and 4.9% Yb^{3+}-doped CrI_3 single-crystal flakes using a powder diffractometer. Only (00*l*) peaks are observed, corresponding to the interlayer lattice spacing and reflecting the flake's alignment. Figure 4.1c highlights the shifts to smaller angles of the 001 peak upon doping. From fitting the XRD peak positions of the undoped and doped samples, the interlayer lattice parameter was found to increase 0.24% from 6.996 ± 0.002 to 7.013 ± 0.002 Å, attributed to the larger ionic radius of Yb^{3+} than Cr^{3+} (87 *vs* 62 pm, respectively) (see Appendix C). These data suggest that the local strain of doping is relieved by distorting the lattice along its softest dimension, as expected. Substitutional incorporation of Yb^{3+} at the Cr^{3+} site is verified by single-crystal XRD measurements (see Appendix C), which also show the increased interlayer spacing. The single-crystal data show no detectable electron density between layers, ruling out Yb^{3+} intercalation.

Figure 4.2a plots the PL spectra of CrI_3 and Yb^{3+}:CrI_3 single flakes measured at several

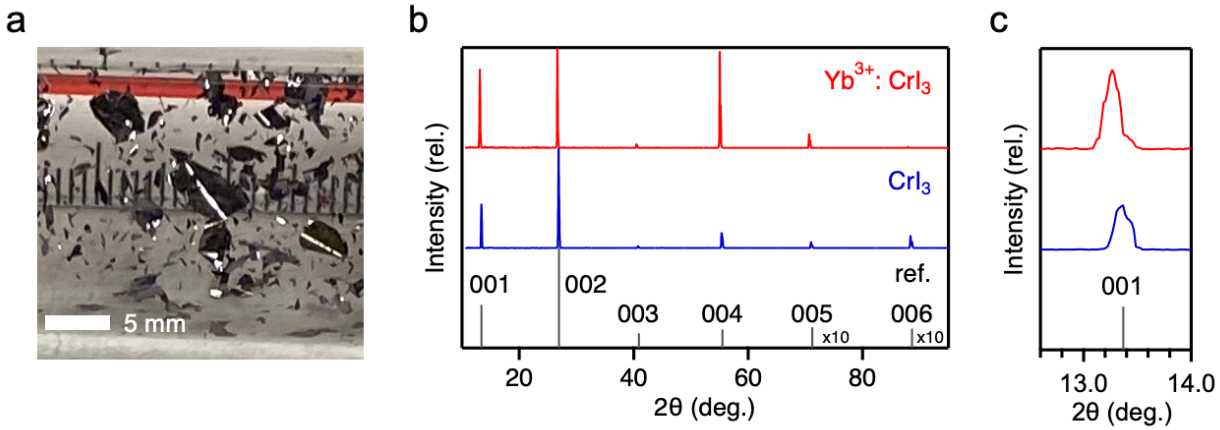

Figure 4.1 (a) Photograph of 4.9% Yb^{3+}:CrI_3 crystals prepared by chemical vapor transport. The scale bar shows 5 mm. All experiments were performed on individual single-crystal flakes from such a reaction tube. (b) XRD data collected on undoped and Yb^{3+}-doped CrI_3 single crystals using a powder diffractometer. Only (00*l*) peaks are observed, indicating an oriented sample. Reference peaks for *c*-oriented CrI_3 diffraction are included (black, ICSD Coll. Code 251654). (c) Magnified view of the 001 reflection for the same samples, displaying an increase in the interlayer lattice spacing upon Yb^{3+} doping. The displayed XRD data was corrected for instrumental error due to sample height and x-ray alignment (see Appendix C).

temperatures between 4 and 200 K. The CrI_3 spectrum broadens and decreases in intensity with increasing temperature, eventually reaching only 7.5% of its 4 K intensity at 200 K (see Appendix C). Although the broadening to higher energies is expected from thermal hot bands, the broadening to lower energies is abnormal and suggests an additional feature. Upon introduction of Yb^{3+}, the broad featureless *d-d* emission of Cr^{3+} disappears and is replaced by a series of sharp *f-f* transitions of Yb^{3+} around 1.15 eV. Assignment of the PL fine structure is discussed later. In some samples, Yb^{3+} doping also reveals another broad emission band centered at ~0.95 eV, which is responsible for the red tail of the CrI_3 PL here and in some literature spectra. This feature has been traced to Ni^{2+} impurities (<0.4%) found in some Cr(0) precursors, and it can be mostly eliminated by using 5N Cr(0) precursors (Figure 4.2a, bottom). The Yb^{3+} PL is not influenced by this Ni^{2+} impurity (see Appendix C).

Figure 4.2b illustrates the photophysics of Yb^{3+}:CrI_3 schematically. The lowest-energy excited state of CrI_3 is the Cr^{3+} $^4T_{2g}$ ligand-field state, involving excitation of a t_{2g} electron into a σ-antibonding e_g orbital (in idealized O_h symmetry). The resulting change in equilibrium geometry is described by the single-configurational-coordinate (SCC) diagram of Figure 4.2b, which illustrates the totally symmetric distortion coordinate. This $^4T_{2g}$ excited state also distorts along a symmetry-breaking Jahn-Teller coordinate (not illustrated).[21] These distortions lead to extensive vibronic progressions in the absorption and PL spectra associated with this transition,

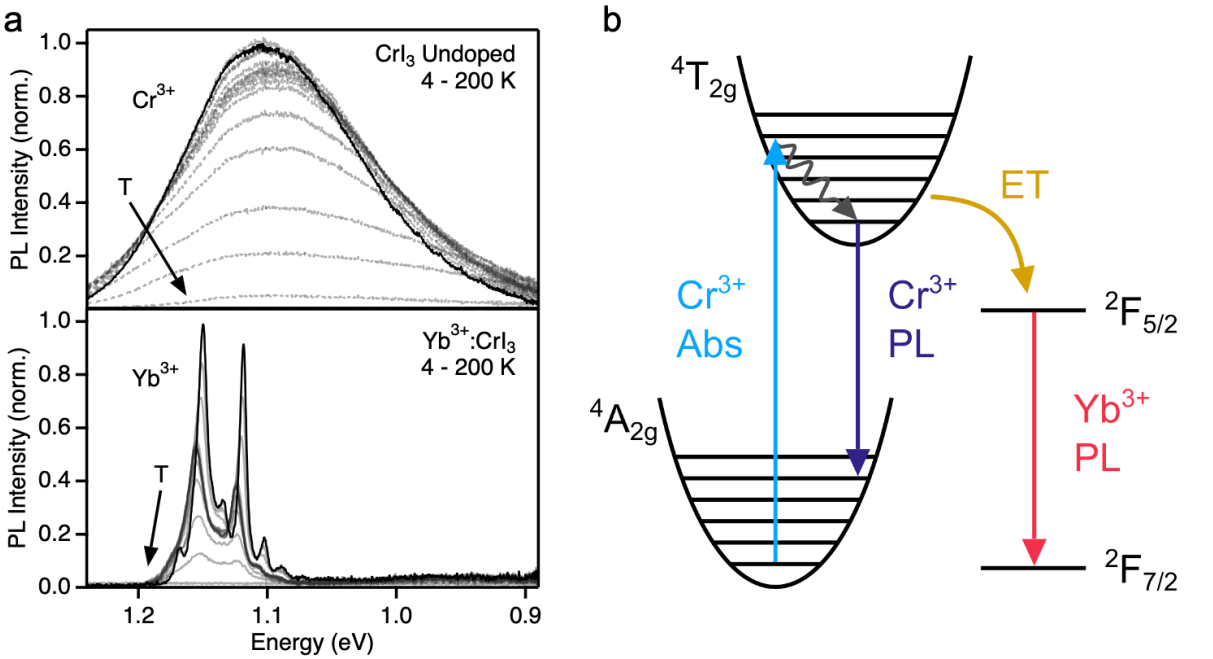

Figure 4.2 (a) Variable-temperature PL spectra of CrI_3 (top) and 4.9% Yb^{3+}:CrI_3 (bottom), measured from 4 to 200 K under 1.88 eV CW excitation at 4 mW/cm^2. (b) Single-configurational-coordinate diagram (A_{1g} coordinate) describing vibronic broadening of the absorption and luminescence bands associated with transitions between the $^4A_{2g}$ and $^4T_{2g}$ ligand-field states of pseudo-octahedral Cr^{3+}. In Yb^{3+}-doped CrI_3, energy transfer from the Cr^{3+} $^4T_{2g}$ excited state to Yb^{3+} yields sensitized $^2F_{5/2} \rightarrow {}^2F_{7/2}$ *f-f* luminescence.

and cause a large PL Stokes shift. Doping CrI_3 with Yb^{3+} introduces a set of $^2F_{5/2}$ states just below the Cr^{3+} $^4T_{2g}$ excited state, favorably positioned for efficient $Cr^{3+} \rightarrow Yb^{3+}$ energy transfer. At 4.9% Yb^{3+} doping, the Cr^{3+} $^4T_{2g}$ PL is entirely quenched and strong Yb^{3+} $^2F_{5/2}$ emission is observed in its place (Figure 4.2a). Because both Cr^{3+} and Yb^{3+} states are localized at single ions, energy migration within the CrI_3 lattice is required for this complete quenching. In undoped CrI_3, energy migration among equivalent Cr^{3+} sites may occur but is not readily apparent. In Yb^{3+}:CrI_3, this energy migration is interrupted when energy is captured by Yb^{3+} dopants. In 4.9% Yb^{3+}:CrI_3, the average Cr^{3+} ion has only ~14% probability of having a neighboring Yb^{3+}, and ~50% probability of having at least one Yb^{3+} within its first two cation shells. Energy must therefore migrate over at least a few lattice sites within the $^4T_{2g}$ lifetime to fully quench the Cr^{3+} emission as observed in Figure 4.2a.

Figure 4.3a shows the anticipated electronic structure of Yb^{3+} in CrI_3. In the free ion, spin-orbit coupling splits the ^2F term into $^2F_{5/2}$ (excited) and $^2F_{7/2}$ (ground) states by an amount $\Delta E = 7/2\zeta$, where $\zeta = 361.8$ meV is the free-ion spin-orbit coupling constant.[23] In crystals, each of these states is further split by the crystal field. Figure 4.3b shows circularly polarized PL spectra of 4.9% Yb^{3+}:CrI_3 measured in a 0.5 T field applied parallel to the crystal's *c* axis (*vide infra*). Three zero-phonon electronic origins are observed and assigned to the $\Gamma_8 \rightarrow \Gamma_6$, Γ_8, and Γ_7 transitions anticipated from Figure 4.3a using idealized O_h notation. The actual cation site symmetry in CrI_3 is lower (Figure 4.3a, right),[24] but the expected low-symmetry splitting of the Γ_8 origin is not clearly identifiable. Analysis of these PL energies within the Angular Overlap Model (AOM)[25] reproduces the $^2F_{7/2}$ splittings well, predicting a $^2F_{5/2}$ splitting of ~34 meV and splittings of the two Γ_8 levels by <0.5 meV each (see Appendix C). Additional satellite features are observed ~127 cm^{-1} (15.7 meV) below the Γ_8 and Γ_7 electronic origins and assigned as phonon sidebands. Raman spectra show a totally symmetric lattice breathing mode of CrI_3 at this energy ($\nu = 127$ cm^{-1}).[26]

A striking aspect of this Yb^{3+}:CrI_3 PL is its very low energy relative to other Yb^{3+} PL. This energy is primarily determined by spin-orbit coupling (Figure 4.3a). Yb^{3+} spin-orbit coupling can be reduced from that in the free ion by covalent expansion of the *f*-electron wavefunctions (nephelauxetic effect),[27, 28] but *f*-orbital covalency in trivalent lanthanides is typically very small and this effect is usually considered negligible at ambient pressure. A survey of Yb^{3+}-doped crystals shows that the energy gap between Yb^{3+} $^2F_{5/2}$ and $^2F_{7/2}$ barycenters remains very near the free-ion value of ΔE ~ 1.266 eV across doped oxide, fluoride, chloride, bromide, sulfide, and phosphide lattices (see Appendix C).[29-33] We note that we have been unable to find *any* reports of PL from other Yb^{3+}-doped iodide crystals, perhaps because Yb^{3+} is easily reduced to Yb^{2+} under common iodide crystal-growth conditions. Yb^{3+}:CrI_3 deviates from this typical behavior substantially: ΔE is only ~1.163 eV, or ~9% smaller than in the free ion, representing the smallest spin-orbit coupling yet reported for Yb^{3+}. Covalency in Yb^{3+}:CrI_3 is certainly enhanced by the large ionic radius and polarizability of the iodides, but this consideration alone likely cannot explain the anomaly. The atomic spin-orbit coupling of I is also much greater than those of other common ligands for Yb^{3+}, and should contribute to the

spectroscopic spin-orbit splitting *via* covalency. Furthermore, the large ionic radius of Yb^{3+} compared to Cr^{3+} means that Yb^{3+} experiences an internal pressure imposed by the surrounding lattice, which may also increase covalency. Importantly, Yb^{3+}-I^- covalency is essential for strong Yb^{3+}-Cr^{3+} superexchange coupling.

From Figure 4.3a, all features show circularly polarized PL, with the $\Gamma_8 \rightarrow \Gamma_7$ origin showing the greatest polarization ratio ($\rho = (\sigma^- - \sigma^+)/(\sigma^- + \sigma^+) = 19\%$). ρ is independent of

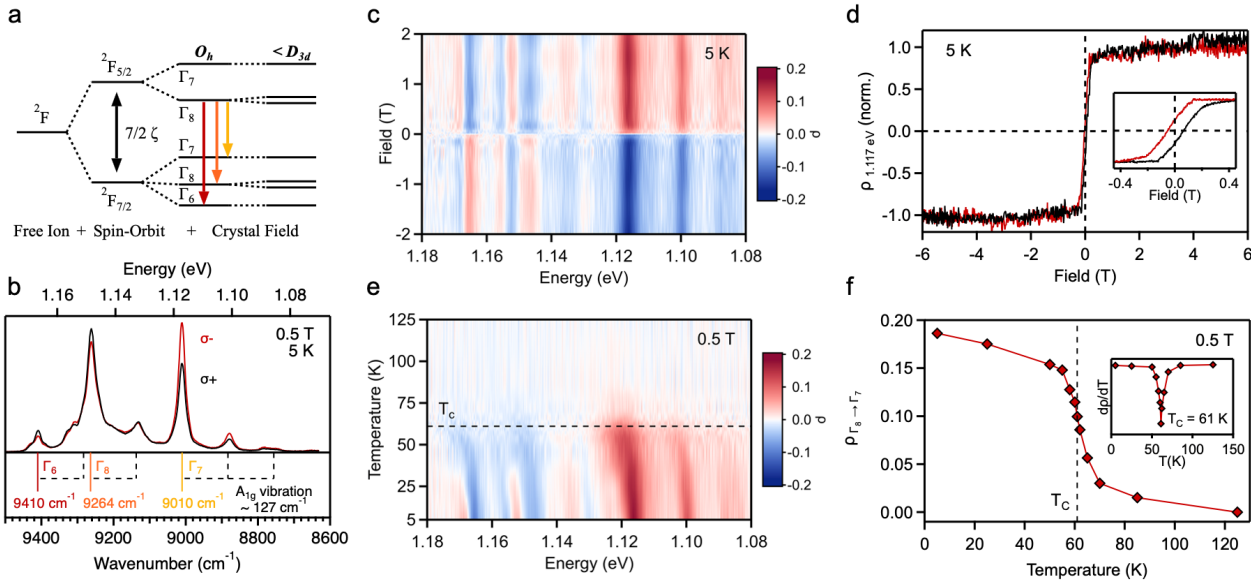

Figure 4.3. (a) Splitting of the Yb^{3+} free-ion ^2F term due to spin-orbit (ζ) and crystal-field (O_h, $<D_{3d}$) interactions. The colored down arrows indicate the three crystal-field transitions anticipated in the low-temperature PL spectrum in the idealized O_h site symmetry. The actual site symmetry is reduced to $<D_{3d}$, *e.g.*, to C_2, splitting each Γ_8 level into two Kramers doublets. (b) Magnetic circularly polarized luminescence (MCPL) spectra of 4.9% Yb^{3+}:CrI_3 measured at 5 K with an applied magnetic field of 0.5 T. The σ^- (red) and σ^+ (black) spectra were collected using unpolarized 1.88 eV CW excitation at 40 mW/cm^2 and have different amplitudes. The three electronic origins in idealized O_h symmetry are indicated below the spectra, assigned to the $\Gamma_8 \rightarrow \Gamma_6$, Γ_8, and Γ_7 transitions illustrated in panel (a). The dashed black lines indicate vibronic sidebands with a characteristic energy spacing of ~127 cm^{-1} (15.7 meV), consistent with the A_{1g} lattice mode of CrI_3. (c) False-color plot of the MCPL polarization ratio, $\rho = (\sigma^- - \sigma^+)/(\sigma^- + \sigma^+)$, for the full Yb^{3+} PL spectrum, measured from -2 to +2 T at 5 K. (d) ρ of the $\Gamma_8 \rightarrow \Gamma_7$ electronic origin (1.117 eV) plotted as a function of magnetic field from -6 to 6 T. The black (red) trace corresponds to the positive (negative) field sweep direction. Inset: Expanded plot of ρ between -0.4 and +0.4 T, showing a coercive field of ~55 mT. For both field-sweep measurements, the sample was excited with linearly polarized 1.96 eV excitation, but with different powers (see section 4.4 Methods). (e) False-color plot of the polarization ratio *vs* temperature, measured at 0.5 T. The dashed black line indicates the Curie temperature of bulk CrI_3 (T_C = 61 K). (f) Plot of the $\Gamma_8 \rightarrow \Gamma_7$ polarization ratio at the peak maximum measured at 0.5 T as a function of temperature. The red curve is a guide to the eye. Inset: Derivative of ρ as a function of temperature. The extracted Curie temperature is 61 K, indistinguishable from that of the undoped crystal.

excitation power but its maximum value varies somewhat between samples (see Appendix C). Figure 4.3c plots ρ across the entire PL spectrum as a function of magnetic field. All Yb^{3+} transitions are influenced by the applied field in the same way, consistent with all PL arising from the same excited state (Γ_8). Figure 4.3d plots ρ for the $\Gamma_8 \rightarrow \Gamma_7$ peak as a function of applied field. ρ increases rapidly at very low fields and saturates at only ~0.2 T. Increasing the field from 0.2 to 6.0 T does not change ρ further, consistent with complete magnetization of Yb^{3+} by 0.2 T. On an expanded scale, these data show a hysteresis with coercivity of ~55 mT, comparable to that found in magnetic measurements of bulk CrI_3.[18, 34] We note that these ρ values are generally small compared to those in cubic Yb^{3+}:InP (~70% at 10 T, 4.2 K),[33] possibly suggesting an in-plane or canted Yb^{3+} anisotropy. Figure 4.3e summarizes the temperature dependence of ρ, measured at 0.5 T, and Figure 4.3f highlights the temperature dependence for $\Gamma_8 \rightarrow \Gamma_7$ individually. All spectral features behave similarly, showing a pronounced drop in polarization at the Curie temperature of bulk CrI_3 (~61 K, see Figure 4.3f, inset). These magneto-optical data agree well with magnetic susceptibility data (see Appendix C), and both indicate that Yb^{3+} doping causes no significant change in the magnetic characteristics of CrI_3 in these samples. This MCPL field and temperature dependence is highly unusual for Yb^{3+}, which generally shows simple paramagnetism of a pseudo-spin 1/2. For example, our AOM crystal-field analysis (see Appendix C) predicts $g_{avg} \sim 2.7$ for the lowest $^2F_{7/2}$ Kramers doublet. Overall, the anomalous magnetism seen in the Yb^{3+} MCPL reflects *magnetic* integration of Yb^{3+} with ferromagnetic CrI_3.

Magnetic ordering was originally explained by Weiss in terms of a huge internal "molecular field"[35] exerted upon individual ions by their surrounding magnetic matrix, and this model provides a useful heuristic for estimating the effective field experienced by Yb^{3+} within CrI_3. In this model, the effective field is given by the sum of external and molecular fields, as in eq 1.

$$H_{eff} = H_{ext} + H_{mol} \tag{1}$$

In Figure 4.3c,d, CrI_3 reaches magnetic saturation at very small H_{ext} (<0.2 T). At such low fields, $H_{ext} << H_{mol}$, and hence $H_{eff} \sim H_{mol}$. In the molecular-field model, H_{mol} in CrI_3 is given by eq 2,

$$H_{mol} = \frac{2zJ\langle S\rangle}{g\mu_B} \tag{2}$$

where, J is the nearest-neighbor exchange coupling constant, $z = 3$ in CrI_3, g is the Landé g factor (2.00 for Cr^{3+} in CrI_3), μ_B is the Bohr magneton, and $\langle S\rangle$ is the spin expectation value for Cr^{3+} in CrI_3, whose absolute value equals 3/2 at saturation. T_C in this model is determined by J according to eq 3,

$$T_C = \frac{2zJS(S+1)}{3k_B} \tag{3}$$

where $S = 3/2$ for Cr^{3+}, and k_B is the Boltzmann constant. From $T_C = 61$ K, eq

3 yields a value of J = 0.70 meV in CrI_3. Entering this J value into eq 2 yields H_{mol} = ~54 T in CrI_3. H_{mol} is dominated by superexchange coupling, since dipolar contributions cannot account for the high T_C of CrI_3.[36] For Yb^{3+} in CrI_3, J is reduced by the shielding of the 4*f* orbitals. Cr^{3+}(*d*)-Yb^{3+}(*f*) superexchange coupling has received relatively little experimental or theoretical attention,[37-39] but relevant experimental data are found in inelastic neutron scattering analyses of $Cs_3Yb_{1.8}Cr_{0.2}Br_9$, where Yb^{3+}-Cr^{3+} exchange splittings are ~1/4 those for Cr^{3+}-Cr^{3+}.[37] This scaling factor is approximate because of the different lattice structure, but $Cs_3Yb_{1.8}Cr_{0.2}Br_9$ is the most similar halide-bridged Yb^{3+}-Cr^{3+} system for which reliable exchange-coupling strengths could be found. This rough scaling reduces H_{mol} to ~14 T. Accounting for the larger g value of Yb^{3+} (~2.7, see Appendix C), our best estimate is H_{mol} ~ 10 T for Yb^{3+} ions within CrI_3. Future spectroscopic measurements (*e.g.*, inelastic neutron scattering, Mössbauer, *etc.*) and calculations will be needed to refine this estimate, but the central conclusion drawn from both the experimental data and this analysis is clear: Yb^{3+} magnetization in Yb^{3+}:CrI_3 is effectively pinned to the magnetic ordering of the CrI_3 lattice through strong Yb^{3+}-Cr^{3+} superexchange coupling. The large H_{mol} in Yb^{3+}:CrI_3 is attributable in large part to the Yb^{3+}-I^- covalency discussed above. For comparison, exchange fields of 1.7 and ~1.1 T are reported for Yb^{3+} in ferrimagnetic hexagonal $YbFeO_3$[40] and distorted orthorhombic $YbCrO_3$.[41] At these values, Yb^{3+} magnetization is not pinned to the ordered TM^{3+} spin sublattices.

A further remarkable aspect of Yb^{3+}:CrI_3 is that the effects of H_{mol} are evident even at zero magnetic field (H_{ext} = 0). Figure 4.4a plots zero-field Yb^{3+} PL spectra as a function of temperature from 4 to 200 K. Viewing the data starting from high temperature, the peak positions appear nearly constant until roughly T_C. Below T_C, the peaks all shift to lower energy together. This redshift is also evident in Figure 4.3e. Figure 4.4b highlights the temperature dependence of the $\Gamma_8 \rightarrow \Gamma_7$ transition energy. From 120 K to ~T_C, the transition energy increases gradually by only ~2 meV. Such temperature dependence has been variously modeled in terms of Raman scattering of non-resonant phonons or direct absorption/emission of phonons resonant with a crystal-field splitting.[42, 43] For example, both models reproduce the $^2F_{7/2} \rightarrow {}^2F_{5/2}$ transition energies of Yb^{3+}:YAG well, whereas the resonant phonon model reproduces absorption linewidths marginally better.[43] As such, we apply the resonant phonon model here. The PL energies above T_C are thus described by eq 4,[42, 43]

$$E(T) = E_0 + \frac{\alpha_s}{e^{\Delta/k_B T} - 1} \qquad T > T_C \qquad (4)$$

where E_0 is the energy at 0 K, α_s describes the electron-phonon interaction strength, and Δ is the energy of the activating phonon mode, fixed at Δ = 127 cm^{-1} (15.7 meV, Figure 4.3b).

The solid curve in the high-temperature portion of Figure 4.4b (>T_C) shows a fit to the high-temperature data using eq 4, floating E_0 and α_s and yielding best-fit values of 1.1242 eV and -6.3 meV, respectively. Eq 4 plateaus at E_0 in the limit of 0 K (dashed line < T_C in Figure 4.4b), but the experimental peak energy shows a discontinuity at T_C, dropping sharply and decreasing with decreasing temperature until reaching ~7 meV below E_0 in the low-temperature limit. With its link to T_C and its characteristic curvature, this trend in Yb^{3+} PL energy is associated with the

spontaneous magnetization of individual CrI_3 monolayers, even though there is no net magnetization in these samples.

Spontaneous ferromagnetic ordering is classified as a second-order phase transition and, within the theory of universal scaling laws, is characterized by the order parameter β shown in eq 5 describing the magnetization temperature dependence.[44]

$$M(T) = M_0\left(-\frac{T-T_c}{T_c}\right)^{\beta} \tag{5}$$

M_0 is the saturation moment per magnetic ion and equals 3.1 μ_B for CrI_3.[18] The precise value of β depends on the underlying spin physics, but it is commonly around 1/3.[12] Previous examination of bulk CrI_3 found a critical exponent of β = 0.284, between that expected from the 3D Ising model (β = 0.325) and that of the tri-critical mean-field model (β = 0.250).[34] Accordingly, the data in Figure 4.4b below T_C were simulated using eq 6 (sum of eq 4 and eq 5, with eq 4 parameters fixed by the high-temperature data). The scaling parameter (γ) in eq 6 relates magnetization to PL energy shift. The data are reproduced well using fixed values of β = 1/3,

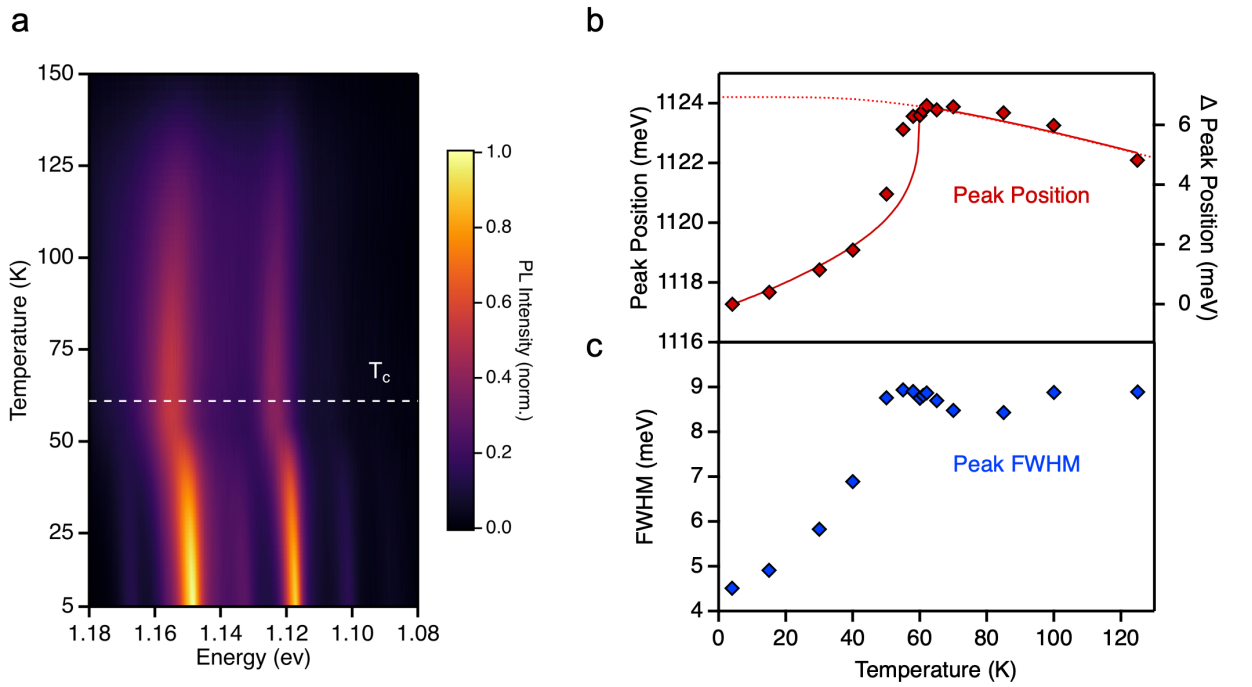

Figure 4.4. (a) False-color plot of the Yb^{3+} PL intensities *vs* temperature measured for 4.9% Yb^{3+}:CrI_3 from 4 to 150 K at zero external magnetic field. The horizontal dashed line indicates T_C = 61 K. (b) Peak position of the $\Gamma_8 \rightarrow \Gamma_7$ transition plotted *vs* temperature. The solid red curve shows the behavior predicted from the combination of resonant phonon interactions (eq 4) and spontaneous magnetization (below T_C, eq 6). The dashed red curve shows the behavior predicted from eq 4 alone below T_C. The solid curve was obtained using eqs 4 and 6 with fixed parameters of Δ = 127 cm^{-1} (15.7 meV), T_C = 60 K, and β = 1/3, adjusting only the amplitude scaling. (c) Plot of the $\Gamma_8 \rightarrow \Gamma_7$ PL linewidth *vs* temperature, from the same VTPL measurements.

T_C = 60 K, and Δ = 127 cm^{-1} (15.7 meV), with γ as the only adjustable parameter. Relating eqs 5 and 6, these results indicate an Yb^{3+} PL energy shift of -2.2 meV/μ_B during spontaneous CrI_3 intralayer magnetization. We stress that the zero-field PL data in Figure 4.4 are not magnetic data, but highlight the strong influence of CrI_3 spontaneous magnetization on the Yb^{3+} PL. Because T_C in these samples is indistinguishable from that of bulk CrI_3 (Figure 4.3f, also see Appendix C), we tentatively attribute the small apparent broadening of the PL energy discontinuity around T_C in Figure 4.4b to additional PL hot bands that are not spectrally resolved.

$$E(T) = E_0 + \frac{\alpha_s}{e^{\Delta/k_B T}-1} + \gamma\left(-\frac{T-T_c}{T_c}\right)^{\beta} \qquad T < T_C \qquad (6)$$

Figure 4.4c plots the temperature dependence of the $\Gamma_8 \rightarrow \Gamma_7$ linewidth (full-width-at-half-maximum, FWHM). These data show similar trends as observed in the peak energies of Figure 4.4b. Below T_C, the FWHM decreases from ~9 meV to ~4.5 meV in the low-temperature limit, attributed to the reduction in spin disorder around Yb^{3+}. These data thus also reflect spontaneous magnetic ordering in monolayers of CrI_3. Although distinct low-energy shoulders are not resolved in these data, we hypothesize that the energy and linewidth changes below T_C both ultimately stem from loss of hot-magnon sideband intensity as CrI_3 monolayers order magnetically.[45] It will be an interesting future direction to explore magnon coupling to *f-f* transitions in these and related doped 2D magnetic materials.

4.2.3 Conclusion

In summary, doping Yb^{3+} into the 2D van der Waals ferromagnet CrI_3 transforms this material's PL from broad-band to sharp multi-line, while retaining its key magnetic functionality. The *f-f* PL of Yb^{3+}:CrI_3 is anomalously low in energy, reflecting relatively covalent Yb^{3+}-I^- bonding. Yb^{3+} magnetization is pinned to CrI_3 by strong superexchange interactions, which contribute an effective internal field of ~10 T that is greater than the field required for magnetic saturation of paramagnetic Yb^{3+} and much greater than the field required for full CrI_3 magnetization at low temperature (~0.2 T). Flipping the magnetization of CrI_3 with a small external field thus also flips the Yb^{3+} magnetization and inverts its PL circular polarization. Magnetic pinning is maintained up to the T_C of CrI_3, but is rapidly lost above T_C. We further showed that the Yb^{3+} PL energy and linewidth both sense this internal field even at zero applied field, mapping spontaneous *intra*layer magnetic ordering below T_C despite the absence of net magnetization. Because each Yb^{3+} ion is a local lattice defect within an individual CrI_3 monolayer, we expect these induced functionalities to persist down to the monolayer, prompting future studies on exfoliated Yb^{3+}:CrI_3 and associated stacked van der Waals heterostructures and layered devices. These results demonstrate the power of designer defects to add functionality to 2D magnetic materials, enrich their fundamental physics, and create new materials of potential utility for future spin-photonics applications.

4.3 Luminescence and covalency in ytterbium-doped CrX_3 (X = Cl, Br, I) van der Waals compounds

4.3.1 Introduction

The recent demonstration of single-layer ferromagnetism in CrI_3[15] has sparked renewed interest in the CrX_3 (X = Cl, Br, I) family of layered 2D van der Waals materials.[46-48] Although the absorption spectrum of CrI_3 was reported as early as 1965,[49] its photoluminescence (PL) went largely unexplored for decades, and apparently no PL spectra were reported until that of monolayer CrI_3 in 2018.[50] This spectrum shows just a broad nondescript band at the low edge of the visible range, characteristic of Cr^{3+} *d-d* luminescence in a weak ligand field.[51] Reports on the optical properties of $CrCl_3$ and $CrBr_3$ have followed a similar trajectory, with a handful of absorption[52-54] and reflectivity[55, 56] studies dating from the 1960s to 1980s, until the recent pursuit of exfoliable magnetic materials led to a resurgence of interest in their properties.[57, 58] The historical lack of attention given to CrX_3 PL likely results from their poor or non-existent emission at room-temperature.

Optical doping of CrX_3 compounds has also received little or no attention. Recently, our group communicated the first such results,[59] showing that successful doping of Yb^{3+} ions into bulk CrI_3 yields sharp sensitized Yb^{3+} *f-f* emission in the near-IR. Magneto-PL measurements demonstrated that the Yb^{3+} impurities are strongly magnetically coupled to the CrI_3 host lattice but do not interfere with its ferromagnetic ordering. As a consequence, Yb^{3+} magnetic saturation occurs at external magnetic fields roughly 100x smaller than necessary for Yb^{3+} in diamagnetic lattices. Such intimate magnetic integration of a lanthanide with a ferromagnet implies strong electronic coupling, but remarkably, the electronic structures of Yb^{3+}-doped iodide crystals have received essentially no prior attention, warranting a broader systematic investigation.

Here, we expand upon these initial results by demonstrating successful Yb^{3+} doping of the two magnetic congeners, $CrCl_3$ and $CrBr_3$, establishing the first complete series of lanthanide-doped CrX_3 (X = Cl, Br, I) van der Waals compounds. We show that Yb^{3+}:$CrCl_3$ and Yb^{3+}:$CrBr_3$ share many of the basic properties of Yb^{3+}:CrI_3 but both display higher-energy *f-f* PL with narrower PL line widths and longer PL decay times. Systematic trends across this series of compounds are analyzed in terms of increasing Yb^{3+}-X^- covalency linked to the reduced anion electronegativities and concomitantly decreasing energies of $X^- \rightarrow Yb^{3+}$ ligand-to-metal charge-transfer (LMCT) excited states in the heavier halides. In addition to illustrating the use of lanthanide dopants to alter the photonic properties of CrX_3 van der Waals ferromagnets, these results highlight the uniquely strong effects of *f*-orbital covalency in Yb^{3+}:CrI_3 relative to other known Yb^{3+} compounds.

4.3.2 Results and discussion

Figure 4.5a depicts a top-down view of a CrX_3 monolayer, showing its honeycomb network lattice structure. In this study, we aimed to replace Cr^{3+} ions with Yb^{3+} impurity ions (cyan) randomly throughout the lattice. To this end, CrX_3 and Yb^{3+}-doped CrX_3 crystals were grown (see section 4.4 Methods) by chemical vapor transport using elemental Cr(0), I_2, and Yb(0) as precursors for CrI_3-based compositions,[59] and using $CrCl_3$, $CrBr_3$, and Yb(0) as precursors for the other halide compositions. Heating these precursors in sealed quartz tubes under a temperature gradient for several days yielded large single-crystal flakes as products. Individual flakes were selected from such samples and used for all of the experiments described here. Figure 4.5b shows a photograph of representative as-grown flakes of Yb^{3+}-doped CrX_3 (X = Cl, Br, I). Figure 4.5c shows room-temperature X-ray diffraction patterns of individual oriented CrX_3 flakes and their Yb^{3+}-doped counterparts taken on a powder diffractometer. Only (00*l*) reflections are observed, consistent with the flakes being single crystals with their out-of-plane axes aligned with the crystallographic *c* axis. At room temperature, CrI_3 and $CrCl_3$ adopt a

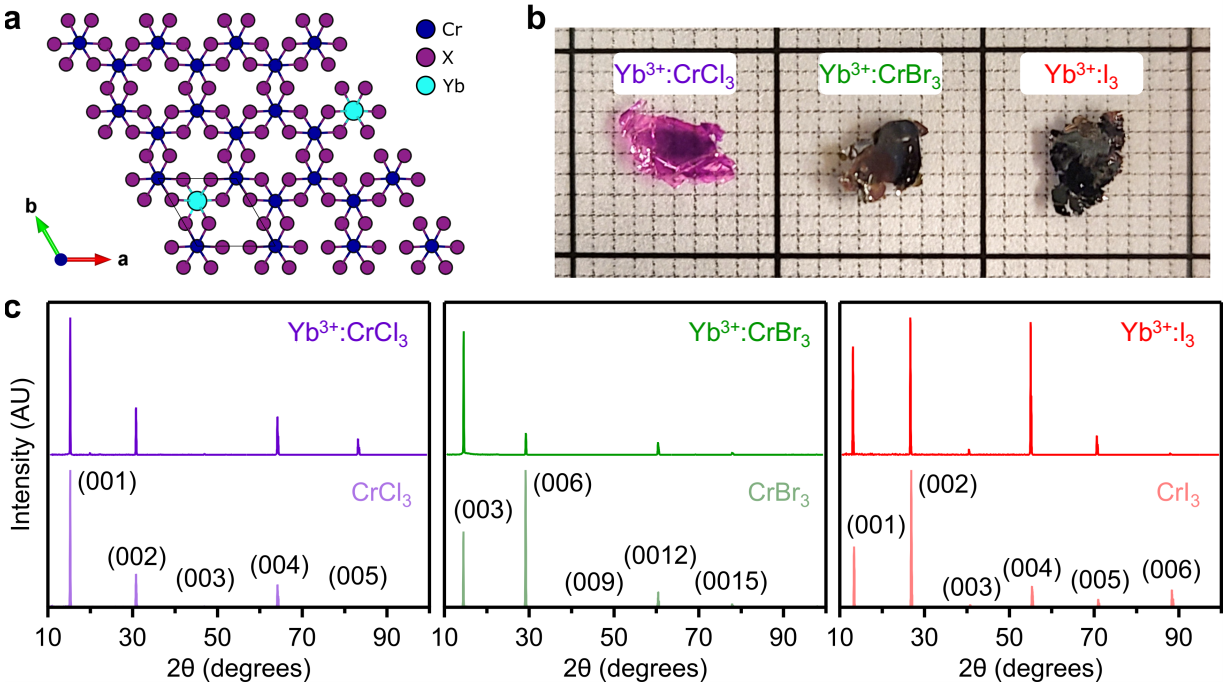

Figure 4.5. (a) Top-down view of a layer of CrX_3 (X = Cl, Br, I), with Yb^{3+} dopant ions (cyan) substitutionally replacing Cr^{3+} ions (blue) at random sites in the lattice, based on the X-ray crystal structure of Yb^{3+}:CrI_3.[59] (b) Photograph of representative as-grown single-crystal flakes of CrX_3 doped with Yb^{3+} on graph paper (minor grid size 1x1 mm^2). (c) Room-temperature X-ray diffraction patterns of oriented $CrCl_3$, $CrBr_3$, and CrI_3 single crystals together with their Yb^{3+}-doped counterparts, collected on a powder diffractometer. Due to sample orientation, only (00*l*) peaks are observed. For monoclinic (C12/m1) $CrCl_3$ and CrI_3, $l = n$, for rhombohedral ($R\bar{3}h$) $CrBr_3$ $l = 3n$. At low temperatures, all three materials adopt the $R\bar{3}h$ structure. Cation-relative Yb^{3+} doping concentrations are 2.0, 0.4, and 4.9%, respectively.

monoclinic C12/m1 structure, while $CrBr_3$ has an R$\bar{3}$h space group, which differs from C12/m1 only in the offset between layers. At cryogenic temperatures, all three materials exist in the R$\bar{3}$h phase.[60-62] The Yb^{3+}-doped materials all show small but nonzero shifts in 2θ, consistent with expansion of the unit cells along the soft *c* axis relative to the undoped parent compound. Yb^{3+} doping concentrations for all measurements detailed in this work are 2.0, 0.4, and 4.9% for X = Cl, Br, and I, respectively, as determined by ICP-MS. EDX data on Yb^{3+}:$CrBr_3$ indicate even distribution of Yb throughout the material (see Appendix E).

The ionic radius of Yb^{3+} with six-fold coordination is about 41% larger than that of Cr^{3+},[63] making the possibility of substitutional Yb^{3+} doping uncertain. The local structures of the Cr^{3+} and Yb^{3+} ions were therefore investigated using Extended X-ray Absorption Fine Structure (EXAFS) measurements. Figure 4.6 shows Fourier-transformed (real-space) EXAFS spectra collected at the Cr K- and Yb L_3-edges of Yb^{3+}:CrX_3, for X = Cl, Br, I. Both edges were measured for each sample at room temperature and the data were phase-corrected with their respective single-scattering paths using the Artemis package.[64] The *k*-space EXAFS data (see

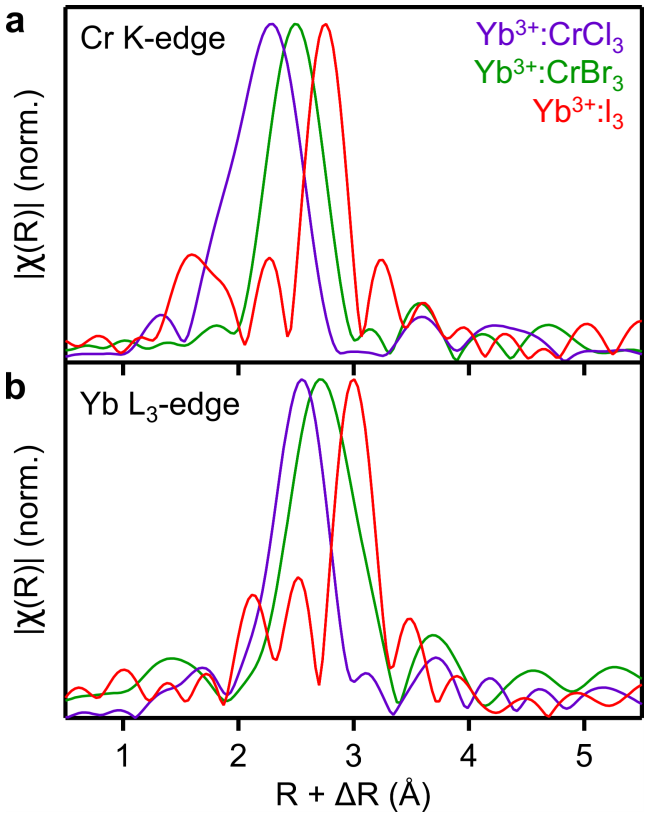

Figure 4.6. (a) Cr K-edge and (b) Yb L_3-edge Fourier-transformed (real-space) EXAFS data for Yb^{3+}:CrX_3 (X = Cl, Br, I) samples. Data are phase-corrected using the respective primary halide scattering paths from fits. Cr peaks are at 2.30, 2.49, and 2.76 Å for Cl, Br, and I data, respectively. Yb peaks are at 2.55, 2.70, and 3.01 Å for Cl, Br, and I data, respectively. Smaller features in the data are consistent with their respective calculated single-scattering paths.

Appendix E) show comparable signal-to-noise ratios for all of the samples described here, as well as a distinct increase in low-*k* features moving from Cl to Br to I. These features are consistent with the calculated scattering paths. For all spectra, the features are fit well (see Appendix E) by a single-scattering path of the nearest-neighbor halide and indicate octahedral coordination of the metal. Fitting parameters are summarized in Table E1. For both edges, the Yb^{3+}:CrI_3 data show additional minority features consistent with an iodide single-scattering path. Overall, these EXAFS data strongly support the presence of $[YbX_6]^{3-}$ octahedra, likely in the form of Yb^{3+} substitution at Cr^{3+} sites. Another possibility is the vacant octahedral interstitial site within the layer,[65] which is differentiated from substitutional sites by having six Cr^{3+} nearest-neighbors and threefold coordination of the bridging halides. Yb^{3+} in interstitial sites would require charge compensation, but little anti-site electron density is observed in the single-crystal X-ray structure of Yb^{3+}:CrI_3.[59] These two sites are expected to have similar EXAFS signatures.

Having established their structures, we now turn to the luminescence of these compounds. Figure 4.7a summarizes overview aspects of the relevant anticipated electronic states of Yb^{3+}-doped CrX_3, including the manifold of Cr^{3+} *d-d* excited states, the narrow set of Yb^{3+} *f-f* excited states just below the first Cr^{3+} *d-d* excited state, and the approximate positions of anticipated Cr^{3+} and Yb^{3+} ligand-to-metal charge-transfer (LMCT) excited states. Figure 4.7b shows normalized 4 K PL spectra of undoped and Yb^{3+}-doped CrX_3 (X = Cl, Br, I) single-crystal flakes. The undoped materials all show similarly broad Cr^{3+} *d-d* PL, with peak maxima at 1.43, 1.35, and 1.10 eV, that are consistent with the ligand-field luminescence of other weak-field Cr^{3+} ions. For example, $[CrCl_6]^{3-}$ in Cr^{3+}-doped Cs_2NaYCl_6 shows vibronically broadened PL centered at ~1.38 eV.[51] Figure 4.7b shows that the broad Cr^{3+} *d-d* PL is effectively quenched in each of the Yb^{3+}-doped CrX_3 compounds and is replaced by narrow Yb^{3+} *f-f* emission. The Yb^{3+} PL sensitization scheme is summarized by the arrows in Figure 4.7a: photoexcitation into the Cr^{3+}-based *d-d* or LMCT bands is followed by energy transfer to Yb^{3+}, from which *f-f* emission is observed. Particularly remarkable is the spectrum of 0.4% Yb^{3+}-doped $CrBr_3$, which shows little or no Cr^{3+} luminescence in its CW spectrum despite its relatively low Yb^{3+} concentration. The mean in-plane separation between Yb^{3+} ions in this material is roughly 11 cation sites, indicating that energy migration over these length scales within the Cr^{3+} lattice must be rapid even at 4 K, precluding substantial impedance from traps. CrX_3 compounds can host several native defects[65, 66] and energy trapping is likely to affect their native PL in some way, although it is unclear whether any of the observed CrX_3 PL is actually associated with traps. Were this PL from traps, we estimate an upper limit of ~100 meV trapping depth in CrI_3 from comparison of PL and absorption spectra, and even smaller upper limits in $CrBr_3$ and $CrCl_3$, consistent with retention of $[CrX_6]^{3-}$ coordination in each case. As such, trapping is not expected to alter the present analysis or conclusions in any significant way, but may have interesting consequences in energy-migration dynamics. Current work is investigating the energy migration dynamics that precede energy capture by Yb^{3+} dopants, and these findings will be described in a subsequent report; the present study focuses on characterizing the electronic structures of the Yb^{3+} ions themselves.

Figure 4.7c shows time-resolved PL (TRPL) data collected for the series of undoped CrX_3 samples measured at 4 K. The PL decay accelerates systematically down the halide series, and each decay curve is fit well to a single exponential function. We hypothesize that this acceleration is primarily due to increased radiative transition probabilities of the emissive *d-d* excited state associated with that state's increased charge-transfer character, as anticipated from the correspondingly decreasing energies of LMCT transitions down this series. The first LMCT absorption band in CrI_3 has been identified at $E_{CT} \approx 1.9$ eV and in $CrBr_3$ it occurs at $E_{CT} \approx 2.9$ eV,[67] but the one in $CrCl_3$ has not yet been reported. Using Jørgensen's optical electronegativity model[68] and $E_{CT} \approx 2.9$ eV for $CrBr_3$, we estimate the first LMCT band of $CrCl_3$ will occur at ~3.6 eV.

Covalency in a metal-ligand complex can be described perturbatively within the molecular-orbital (MO) model in terms of hybridization between the metal's valence orbitals ($|M\rangle$, *e.g.*, 3*d* or 4*f*) and symmetry-adapted linear combinations of ligand valence atomic orbitals ($|L_{\mathrm{SALC}}\rangle$), as in eq 1.

$$\Psi = N(|M\rangle - c|L_{SALC}\rangle) \tag{1}$$

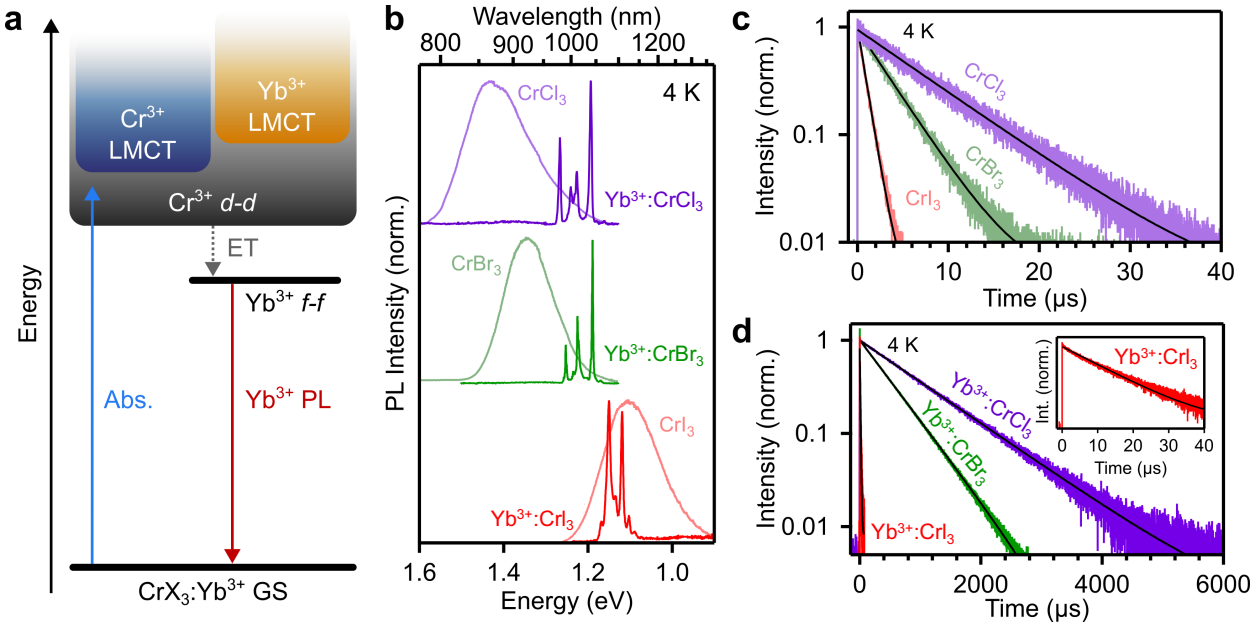

Figure 4.7 (a) State diagram illustrating absorption and subsequent energy transfer (ET) from the Cr^{3+} excited state to Yb^{3+}, resulting in Yb^{3+} PL. (b) Low-temperature PL spectra of CrX_3 (X = Cl, Br, I) (semi-transparent curves) showing broad $^4T_{2g} \rightarrow {}^4A_{2g}$ luminescence and of their Yb^{3+}-doped counterparts (dark curves) showing sharp $^2F_{5/2} \rightarrow {}^2F_{7/2}$ luminescence. The absence of lattice PL in the latter indicates efficient energy transfer from Cr^{3+} to Yb^{3+}. (c) 4 K time-resolved PL (TRPL) data for CrX_3 compounds. Decay times found from single-exponential fits (black) are 7.42(2), 3.38(4), and 0.84(1) μs for X = Cl, Br, I, respectively. (d) 4 K TRPL data for Yb^{3+}:CrX_3 compounds. Decay times found from single exponential fits (black) are 971.5(6), 501.2(1), and 8.63(1) μs for X = Cl, Br, I, respectively. Inset: enlarged view of the Yb^{3+}:CrI_3 decay curve. Yb^{3+} doping concentrations are 2.0, 0.4, and 4.9% for X = Cl, Br, and I, respectively.

N is a normalization constant. The covalency coefficient (c) is given by eq 2,

$$c = \frac{H_{ML}}{\Delta E_{ML}} \approx \frac{H_{ML}}{E_{CT}} \quad (2)$$

where ΔE_{ML} is the energy difference between metal and L_{SALC} orbitals in the absence of mixing, and H_{ML} is the off-diagonal matrix element describing the resonance energy associated with M-L_{SALC} mixing. The covalent admixture of ligand valence orbitals into the metal valence orbitals is given by c^2. H_{ML} is proportional to the M-L_{SALC} orbital overlap integral, S. The energy difference ΔE_{ML} relates to the difference between metal and ligand valence-shell ionization energies and is approximated by the energy of the complex's lowest-energy LMCT transition ($\Delta E_{ML} \approx E_{CT}$).

The radiative rate constants ($k_{rad} = \frac{1}{\tau_{rad}}$) controlling emission from the metal's valence-shell excited states (*e.g.*, *d-d*, *f-f*) are proportional to the corresponding excitation's oscillator strengths and are given by:[69]

$$k_{rad} = \frac{e^2 n \omega^2}{2\pi\varepsilon_0 m_0 c^3} f_M \quad (3)$$

Here, n is the refractive index of the material, ω is the intra-shell transition's angular frequency, f_M is its oscillator strength, and the other parameters are fundamental constants. The refractive indices are 1.8, 2.6, and 2.0 for $CrCl_3$, $CrBr_3$, and CrI_3, respectively.[70, 71]

Because the $^4T_{2g} \rightarrow {}^4A_{2g}$ *d-d* intra-shell transitions of pseudo-octahedral Cr^{3+} are formally electric-dipole forbidden due to parity, their radiative lifetimes are to first order determined by "intensity borrowing" from parity-allowed LMCT excited states. Microscopically, this process involves mixing of *d-d* and LMCT configurations and is therefore closely related to covalency. In this scenario, the anticipated trend in *d-d* oscillator strengths is described to first order as in eq 4, [72, 73] where f_{CT} is the allowed LMCT transition's oscillator strength and the bracketed term is very similar to the covalency coefficient, c, of eq 2, with H_{MLu} representing only the odd-parity matrix elements (static or dynamic). Because of energetic proximity, intensity borrowing is dominated by contributions from the metal's excited state (at energy E_{ES}) rather than its ground state (at energy $E_{GS} = 0$), and hence the energy denominator in eq 4 is reduced by E_{ES}.

$$f_M \approx \frac{E_{ES}}{E_{CT}} \left[\frac{H_{MLu}}{E_{CT} - E_{ES}}\right]^2 f_{CT} \quad (4)$$

Neglecting changes in f_{CT} and H_{MLu} across the CrX_3 series, eqs 3 and 4 predict relative radiative lifetimes of (1.00):(0.32):(0.10) for Cl:Br:I, in reasonable agreement with the experimental lifetime trend of (1.00):(0.46):(0.11) at 4 K. This simple analysis thus shows that the short PL decay time of the $^4T_{2g} \rightarrow {}^4A_{2g}$ transition observed in Figure 4.7c primarily results from the relatively low LMCT energy of CrI_3, which in turn favors high *d*-orbital covalency.

Figure 4.7d shows the 4 K decay dynamics of the narrow Yb^{3+} *f-f* luminescence in each of the doped CrX_3 compounds. Again, the PL decay accelerates systematically going down the halide series, and each curve fits well to a single-exponential function. The inset shows an enlarged view of the Yb^{3+}:CrI_3 PL decay curve. The absence of noticeable rise times in these PL

decay curves is consistent with the conclusion of rapid energy migration within the CrX_3 lattices. Whereas the Yb^{3+} PL decay times of ~970 and 500 μs for Yb^{3+}:$CrCl_3$ and Yb^{3+}:$CrBr_3$ are comparable to those reported for Yb^{3+} in other chloride and bromide lattices,[74, 75] the 8.6 μs Yb^{3+} decay time of Yb^{3+}:CrI_3 is extraordinarily short. Although some of this reduction may be due to nonradiative contributions even at 4 K, low-energy LMCT transitions in $[YbI_6]^{3-}$ are also expected to relax intra-shell parity forbiddenness and accelerate radiative decay, as discussed for Cr^{3+} above. The Yb^{3+} LMCT transition energies in these compounds are unknown, but the first LMCT excited states of $[YbX_6]^{3-}$ centers in other chloride, bromide, and iodide compounds have been reported at ~4.46 eV,[68, 76, 77] ~3.60 eV,[68, 76, 78] and ~2.21 eV,[68, 79] respectively, in each case formally generating $Yb^{2+}(4f^{14})X(np^5)X^-(np^6)$ final-state configurations.[77] The shifts in these transition energies are consistent with the differences in halide optical electronegativities. From these data the LMCT energy for Yb^{3+} in CrI_3 is placed ~0.3 eV higher in energy than the first LMCT transitions of CrI_3 itself (Figure 4.7a). Direct spectroscopic determination of E_{CT} for Yb^{3+} in Yb^{3+}:CrX_3 is thus complicated by the low concentration of Yb^{3+} and the overlapping Cr^{3+} LMCT bands in the same spectral region.

Applying the same analysis described above using these LMCT energies, and taking the highest *f-f* emission energy in each compound at 4 K as E_{ES}, eqs 3 and 4 predict relative Yb^{3+} radiative lifetimes across this Yb^{3+}:CrX_3 series to be (1.00):(0.31):(0.06) for Cl:Br:I, compared to the experimental results of (1.00):(0.52):(0.01) from Figure 4.7d. Again, we find reasonable agreement (see Appendix E) between experiment and expectations from the simple perturbation model of eq 4. Importantly, this analysis also indicates that *f*-orbital Yb^{3+}-X^- covalency (c^2) increases markedly across the Yb^{3+}:CrX_3 series in a ratio of roughly 1:2:10 for Cl:Br:I. The short lifetime of Yb^{3+} in CrI_3 is thus consistent with unusually high *f*-orbital covalency in this lattice. Although 4*f* covalency in lanthanides is often considered negligible, $[LnCl_6]^{3-}$ compounds typically have 4*f* covalencies approaching ~1%,[80, 81] suggesting that *f*-orbital covalency may reach as high as several percent in Yb^{3+}:CrI_3.

Figure 4.8a shows an enlarged view of the Yb^{3+}-doped CrX_3 PL spectra shown in Figure 4.7b. Yb^{3+}:$CrCl_3$ and Yb^{3+}:$CrBr_3$ show sharp multi-line spectra at energies that are typical for Cl and Br lattices. Although the spectra are dominated by only a few prominent peaks, careful inspection shows a multitude of nearby lines. We assign the most prominent peaks to electronic origins, as indicated by the colored lines in Figure 4.8a. The Yb^{3+}:CrI_3 spectrum occurs at much lower energy than the other two, and its main peaks are more obviously broadened by distinct shoulders. Sideband intensities are also relatively more intense in this spectrum. We again associate the three maxima in this spectrum with electronic origins. Note that the highest-energy maximum in the Yb^{3+}:CrI_3 PL spectrum has a higher-energy shoulder, making precise identification of the true electronic origin uncertain to within ~2.5 meV.

Figure 4.8b illustrates the splitting of the Yb^{3+} ^2F free-ion term upon introduction of spin-orbit and crystal-field terms of the molecular Hamiltonian. Using the angular overlap model (AOM) for analysis of these spectra, spin-orbit coupling and crystal-field parameters (see Appendix E) were adjusted to reproduce the experimental $^2F_{5/2} \rightarrow {}^2F_{7/2}$ transition energies of

each compound (colored lines in Figure 4.8a), from which the energies of the remaining $^2F_{5/2}$ crystal-field levels were extracted.[82] These energies are plotted in Figure 4.8b for each compound. Barycenters of the $^2F_{5/2}$ and $^2F_{7/2}$ states were then calculated from the crystal-field levels for each compound. The energy difference between $^2F_{5/2}$ and $^2F_{7/2}$ barycenters is denoted

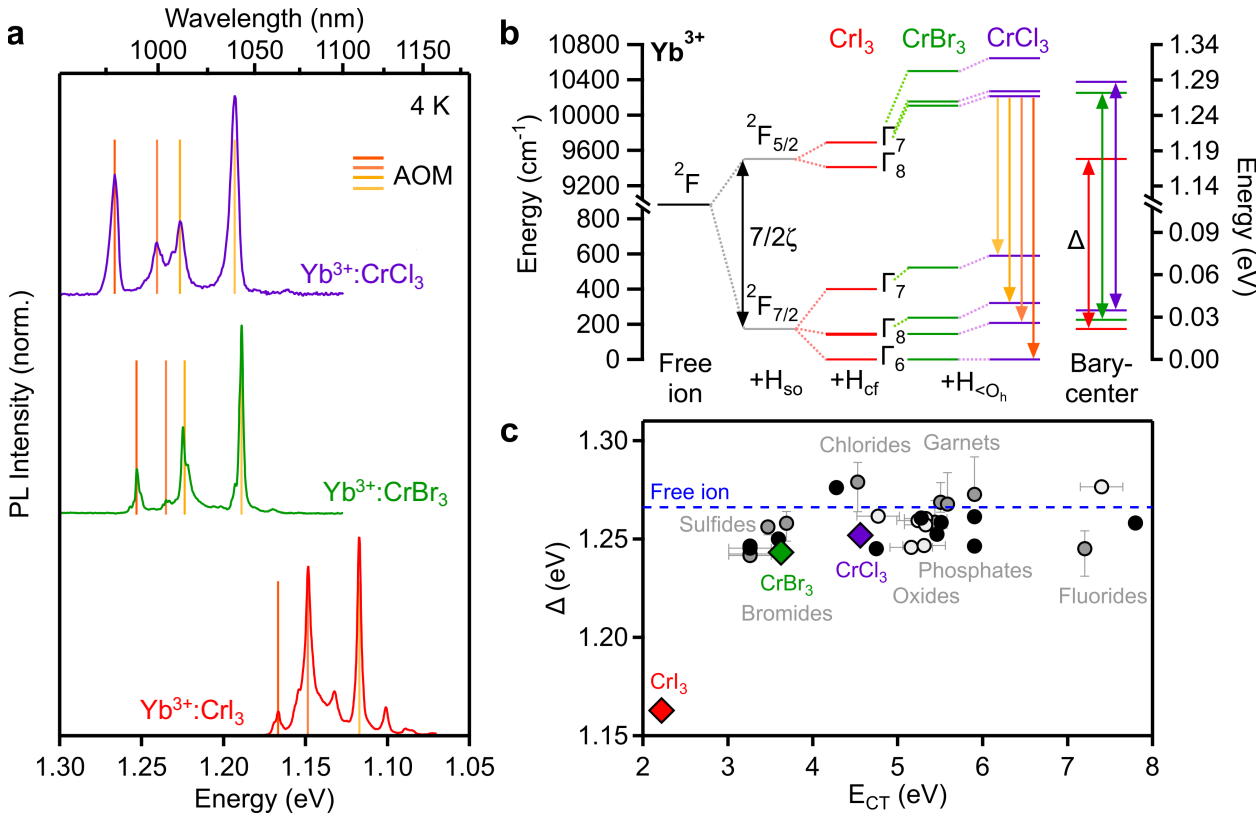

Figure 4.8. (a) Low-temperature PL data for Yb^{3+}-doped CrX_3 (X = Cl, Br, I). The colored vertical sticks indicate the electronic origin assignments used in angular overlap model (AOM) calculations. (b) *f*-shell spin-orbit and crystal-field splittings for Yb^{3+} ions in CrX_3 lattices, from panel (a) and calculated by AOM. The splitting of the ground- and excited-state Γ_8 levels indicate deviation from O_h Yb^{3+} site symmetry. This deviation is more pronounced for the smaller halides. The colored arrows represent the transitions observed in panel (a). The energy difference between $^2F_{5/2}$ and $^2F_{7/2}$ barycenters is denoted Δ. (c) Plot of the ligand-to-metal charge-transfer (LMCT) energies *vs* Δ for Yb^{3+} ions doped into a variety of lattices. Δ values for Yb^{3+}:CrX_3 are obtained from panel (a) and AOM calculations, and E_{CT} is taken from literature for other $[YbX_6]^{3-}$ species.[68] The black data points represent experimental values for E_{CT} and Δ, the gray data points use experimental values for E_{CT} and semi-experimental values for Δ, and the white data points use experimental values for Δ and values for E_{CT} calculated from Eu^{3+} charge-transfer energies in the same lattice, following the method of Li *et al.* (see section 4.4 Methods), Uncertainties estimated from consideration of multiple literature sources are approximately the size of the CrX_3 data points.

Δ. From Figure 4.8b, these values of Δ primarily reflect the magnitude of the spin-orbit coupling parameter, $\Delta \approx 7/2\zeta$. For example, the above AOM analysis yields Δ values that differ from $7/2\zeta$ by only 0.81, 0.59, and 0.31 meV (<0.1%) for Yb^{3+} in $CrCl_3$, $CrBr_3$, and CrI_3, respectively. Note that although the $^2F_{5/2}$ crystal-field energies in the Yb^{3+}:CrX_3 compounds are not obtained experimentally, they have relatively little influence on Δ, and essentially indistinguishable results are obtained from simply considering the mean PL energy of each spectrum in Figure 4.8a.

Inspired by the relationship between covalency and E_{CT} in eq 2, Figure 4.8c plots Δ *vs* E_{CT} for the three Yb^{3+}:CrX_3 compounds reported here. This plot also includes additional data points from a wide variety of literature sources for other Yb^{3+}-doped compounds (see Appendix E). Select compound classes are labeled in the figure. Previous studies have demonstrated that Δ is generally independent of ligand class,[83, 84] consistent with the high shielding and low covalency that typifies the 4*f* valence shell of trivalent lanthanide ions. This typical behavior is highlighted in Figure 4.8c, which shows Δ values nearly the same as the free-ion spin-orbit splitting energy for all but one notable exception: Yb^{3+}:CrI_3. Δ in this compound is substantially smaller than in any other known Yb^{3+} compound. From its value, ζ is reduced by 9% in Yb^{3+}:CrI_3 (330 meV) relative to the Yb^{3+} free ion (362 meV). Not coincidentally, Yb^{3+}:CrI_3 also has the smallest value of E_{CT}, ~1 eV smaller than for the next closest compounds in Figure 4.8c. Per eq 2, the data in Figure 4.8c thus support the conclusion that the anomalously small value of Δ in Yb^{3+}:CrI_3 is attributable to exceptionally high *f*-orbital covalency in this compound, which in turn arises from the shallow valence-shell ionization energy of the iodide ligands relative to other ligands in this figure. This interpretation supports the conclusion drawn from analysis of the PL decay times in Figure 4.7d.

In addition to the low LMCT energies (E_{CT} in eq 2), the large size discrepancy between Yb^{3+} and Cr^{3+} ($r_{Yb}/r_{Cr} = 1.41$) may also contribute to high covalency by effectively forcing the X^- ligands toward the Yb^{3+} dopant, thereby increasing orbital overlap (and hence increasing H_{ML} in eq 2). To assess the importance of this kind of "internal pressure", it is interesting to compare Δ in Yb^{3+}:$CrBr_3$ with that found in $NaYS_2$:Yb^{3+}.[85] Both lattices have octahedral coordination of Yb^{3+} and show similar values of E_{CT} (~3.26 eV). The ionic radii of Br^- (196 pm) and S^{2-} (184 pm) are also similar, but in the latter Yb^{3+} substitutes for Y^{3+}, which has a substantially larger ionic radius than Cr^{3+} (90 *vs* 62 pm). Nevertheless, Δ in $NaYS_2$:Yb^{3+} is very similar to that in Yb^{3+}:$CrBr_3$ (Figure 4.8c, also see Appendix E). This comparison suggests that E_{CT} is the dominant factor differentiating covalency in these compounds, not H_{ML}.

An additional consideration is the effect of anion spin-orbit coupling on Δ. The spin-orbit coupling constant of iodine, 581 meV (4690 cm^{-1}),[86] greatly exceeds even that of Yb^{3+} (362 meV (2918 cm^{-1}) in the Yb^{3+} free ion). Anion SOC is thus no longer negligible in Yb^{3+}:CrI_3 like in most of the compounds in Figure 4.8, and given the relatively high covalency in Yb^{3+}:CrI_3 this factor may influence the spectroscopic splitting, Δ. For example, sulfides have much smaller ligand SOC constants (36 meV (288 cm^{-1})). We note that a few examples of Yb^{3+}-doped tellurides have been reported,[87] which should have similar values for both E_{CT} and ligand SOC compared to Yb^{3+}:CrI_3. Direct comparison with Yb^{3+}:CrI_3 is precluded by the fact that these

tellurides all have tetrahedral coordination of Yb^{3+}, however. This low coordination number is expected to reduce the total *f*-orbital covalency, and indeed their Δ values are again similar to the free ion. Further investigation will be required to elucidate the impact of two-center SOC in such compounds.

Overall, these data contribute to the more general discussion of *f*-orbital covalency in lanthanides and actinides that has recently drawn broad attention, primarily in molecular contexts. [80, 88-91] The present data provide strong evidence for so-called "degeneracy-driven" covalency in the $[YbX_6]^{3-}$ units of Yb^{3+}:CrX_3 compounds across the Cl → Br → I composition series, based on systematic trends correlated with anion electronegativity and comparison to other lattices. Indeed, the entire Yb^{3+} data set in Figure 4.8c appears to follow a trend of the form $\Delta = 7/2\zeta_{\text{free ion}} - (\text{const.}/E_{CT})^2$, albeit with some scatter. We also note that the Yb^{3+} barycenter trend in Figure 4.8 upon going from Cl → I is far more pronounced than those typically observed for other lanthanide compounds of the same halides. For example, whereas $\Delta(I)/\Delta(Cl) \sim 92.8\%$ in Yb^{3+}:CrX_3, the average ratio of visible and NIR Δ values in $Cs_3Er_2X_9$ compounds[92] is $\Delta_{avg}(I)/\Delta_{avg}(Cl) \sim 99.9\%$. For the Er^{3+} multiplet closest in energy to the Yb^{3+} $^2F_{5/2}$ state ($^4I_{11/2}$) this ratio is $\Delta(I)/\Delta(Cl) \sim 100.0\%$. Yb^{3+} is the second most easily reduced trivalent lanthanide behind only Eu^{3+}, and hence it has comparatively low charge-transfer energies. Er^{3+} CT energies are expected ~1.8 eV higher in energy than those of Yb^{3+} with the same coordination,[76, 93] which translates to a reduction in ground-state covalency c^2 by a factor of ~3.3 in $[ErI_6]^{3-}$ relative to $[YbI_6]^{3-}$. This comparison thus supports the conclusion that ΔE_{ML} (or E_{CT}, eq 2) dominates over H_{ML} in enhancing the *f*-orbital covalency of Yb^{3+} in CrI_3.

Finally, and remarkably, we note that Yb^{3+} *f-f* PL has apparently not been reported for Yb^{3+} in any other iodide lattice. In fact, surprisingly few compounds involving $[YbI_6]^{3-}$ octahedra have been reported at all,[79, 94-96] and no *f-f* spectra have been reported for those compounds. Thus, at this moment no conclusions can be drawn about whether Yb^{3+}:CrI_3 typifies iodides or is in some way also distinct within this class. The scarcity of $[YbI_6]^{3-}$ *f-f* data is likely related to the same relative ease of Yb^{3+} reduction that leads to its enhanced covalency; $[EuI_6]^{3-}$ compounds appear to be even more rare, but both Yb^{2+} and Eu^{2+} iodides are well known.[97-99] Experiments are under way to develop other Yb^{3+}-doped iodides for deeper exploration of this rare motif, from which our preliminary results show that other iodides also fall well below the distribution represented by the other compounds in Figure 4.8c; these findings support the above analyses and will be reported separately.

4.3.3 Conclusion

In conclusion, we have demonstrated successful incorporation of Yb^{3+} dopants into $CrCl_3$, $CrBr_3$, and CrI_3 van der Waals lattices. EXAFS data show Yb-X bond lengths that are ~0.25 Å larger than their Cr-X counterparts, and data fitting shows structures consistent with Yb^{3+} substituting for Cr^{3+} despite its ~1.4x larger ionic radius. PL measurements demonstrate efficient energy transfer from Cr^{3+} to Yb^{3+}, resulting in complete quenching of the broad Cr^{3+} *d-d* luminescence and appearance of sharp Yb^{3+} *f-f* luminescence at modest Yb^{3+} doping levels.

TRPL measurements show an exceptionally short excited-state lifetime of only 8.6 μs for Yb^{3+} in Yb^{3+}:CrI_3 at 4 K. Energetically, the Yb^{3+}:CrI_3 PL spectrum is also significantly redshifted compared to those of Yb^{3+}:$CrBr_3$ and Yb^{3+}:$CrCl_3$. Data analysis and AOM calculations show that this shift is due to an anomalously small $^2F_{7/2}$-$^2F_{5/2}$ spin-orbit splitting in Yb^{3+}:CrI_3. Broader comparison to Yb^{3+} in a wide variety of other lattices shows that the low PL energy of Yb^{3+}:CrI_3 is in fact an outlier across *all* investigated materials. We propose that the low energy and short decay time of Yb^{3+}:CrI_3 PL are both attributable to anomalously high Yb-I *f*-orbital covalency, ultimately stemming from the shallow valence-shell ionization potentials of the iodide ligands. Beyond demonstrating Yb^{3+} doping as an effective approach to narrowing the emission of the entire family of CrX_3 2D van der Waals ferromagnets, these results provide rare fundamental insights into the electronic structure and luminescence of the remarkably underexplored $[YbI_6]^{3-}$ motif, revealing it to be an outlier among known Yb^{3+} compounds because of its exceptionally high *f*-orbital covalency. In addition to the above manifestations, this high covalency has important physical consequences for the promotion of strong Yb^{3+}-Cr^{3+} magnetic superexchange in Yb^{3+}:CrI_3.[59]

4.4 Methods

Magnetic Amplification at Yb^{3+} "Designer Defects" in the van der Waals Ferromagnet CrI_3

General Considerations. All sample preparation and manipulation was performed in a glovebox under an atmosphere of purified dinitrogen.

Chemicals. Chromium metal powder (200 mesh, 99.94%, lot X15E028) was purchased from Alfa Aesar. According to the manufacturer's certificate of analysis, the majority of the impurity in this sample lot was Ni at 343 ppm. A chromium chip (99.995%, lot MKCH4484) was also purchased from Sigma Aldrich as a higher-purity Cr source. The Cr chip was ground to a powder using a mortar and pestle and used in an analogous manner as the powder precursor. I_2 (≥99.99%) was purchased from Sigma Aldrich. Ytterbium metal powder 40 mesh (99.9%) was purchased from BeanTown chemical. All chemicals were used as received without further purification.

Synthesis of CrI_3 and Yb^{3+}-Doped CrI_3 Single Crystals. Single crystals of the doped and undoped CrI_3 were grown by chemical vapor transport in a manner similar to that described in previous literature reports.[100] For undoped CrI_3, Cr(0) metal and I_2 were loaded as a 1:3 stochiometric ratio into a quartz tube and sealed under an evacuated atmosphere. For Yb^{3+}-doped CrI_3, additional Yb(0) metal was loaded along with the other starting materials. The quartz tubes were 15 cm long with inner and outer diameters of 14 and 16 mm, respectively. Sealed tubes were placed in an open-ended horizontal tube furnace with the starting materials in the hot zone set at 650 ˚C and the other end at a temperature of ca. 500 ˚C. Samples were heated for 5 days and then allowed to slowly cool to room temperature. Once cooled, the tubes were brought into a glove box and cracked open to yield shiny dark plate-like crystals that had formed at the cold end of the quartz tube. Elemental analysis of the Yb^{3+}-doped samples was performed by inductively coupled plasma mass spectrometry (ICP-MS) using a PerkinElmer NexION 2000B. Samples were prepared by digesting single crystals in concentrated nitric acid with sonication and then further diluted in ultrapure H_2O. Yb^{3+} doping levels are reported as cation mole fraction, $[Yb^{3+}]/([Cr^{3+}]+[Yb^{3+}])$, in percentage, with an estimated uncertainty of ±0.1%. Crystal thickness was measured by mounting a representative flake to a glass slide using double-sided tape and imaging the flake with an optical microscope in a glovebox at various magnifications. The edge length was calculated in ImageJ[101] using known pixel resolutions.

X-ray Diffraction (XRD) Characterization. Samples were prepared for XRD on the powder diffractometer by placing single crystals onto silicon substrates and sealing under Kapton films to reduce exposure to air. Data were collected using a Bruker D8 Discover powder diffractometer with a high-efficiency IμS microfocus x-ray source for Cu Kα radiation (50 kV, 1 mA). For single-crystal XRD, a crystal measuring 0.10 x 0.05 x 0.01 mm^3 was mounted on a loop with oil. Data were collected at 263 K on a Bruker APEX II single-crystal X-ray diffractometer using Mo-radiation, equipped with a Miracol X-ray optical collimator. The data were integrated and scaled using SAINT, SADABS within the APEX2 software package by Bruker.[102] Solution by direct methods (SHELXT[103, 104] or SIR97[105, 106]) produced a complete

heavy-atom phasing model consistent with the proposed structure. The structure was completed by difference Fourier synthesis with SHELXL.[107, 108] Scattering factors are from Waasmair and Kirfel.[109] All atoms were refined anisotropically by full-matrix least-squares.

Including intrinsic disorder, a least squares refinement optimization of the data yields the lattice structure that we report. From the 983 reflections collected covering the indices, $-8 \leq h \leq 8$, $-14 \leq k \leq 14$, $-8 \leq l \leq 8$, 518 reflections were found that were symmetry independent and an R_1 value of 0.0521 was obtained, indicating a good fit. R_1 is calculated as:

$$R_1 = \frac{\sum\left||F_{obs}| - |F_{calc}|\right|}{\sum|F_{obs}|}$$

There is no detectable electron density between layers, indicating that Yb^{3+} does not intercalate between layers in CrI_3.

Variable-Temperature Photoluminescence (VTPL). Samples for VTPL measurements were prepared by placing a single crystal between two quartz disks and loading into a closed-cycle helium cryostat. PL spectra were collected by exciting the sample with a continuous-wave 660 nm (1.88 eV) diode at 4 mW/cm^2. Emission was collected and focused into a monochromator with a spectral bandwidth of 0.627 nm and detected by a Hamamatsu InGaAs/InP NIR photomultiplier tube, with signal recorded using a photon counter. Temperature was varied from 4 to 300 K, starting at low temperature. All spectra were corrected for instrument response.

Magnetic Circularly Polarized Luminescence (MCPL). Samples for MCPL measurements were prepared as single crystals placed between two quartz disks and loaded into a superconducting magneto-optical cryostat (Cryo-Industries SMC-1659 OVT) oriented in the Faraday configuration. For full-spectrum measurements at static fields, samples were excited with a 660 nm (1.88 eV) diode at approximately 40 mW/cm^2. For field-sweep measurements, samples were excited with a linearly polarized HeNe laser (632.8 nm/1.96 eV, 27 mW/cm^2 for -6 to +6 T scans, 55 mW/cm^2 for -0.4 to +0.4 T scans). No distinguishable difference was found in the either the PL spectra or variable-field data between the two excitation sources. For field-sweep measurements, the monochromator was centered at 1.117 eV with a 6 nm spectral bandwidth, and the signal was continuously monitored as the field was swept at a rate of 0.10 T/min and 0.45 T/min for the 0.4 T and 6 T scans, respectively. PL was collected along the magnetic-field axis and passed through a liquid-crystal variable retardation plate set at $\lambda/4$, followed by a linear polarizer to separate the left- and right-circularly polarized components. The PL was then focused into a fiber-optic cable and fed into a monochromator with a spectral bandwidth of 0.627 nm and detected by a Hamamatsu InGaAs/InP NIR photomultiplier, with signals recorded using a photon counter. Polarization ratios are defined as $\rho = (\sigma^- - \sigma^+)/(\sigma^- + \sigma^+) = (I_L - I_R)/(I_L + I_R) = \Delta I/I$, following the sign conventions outlined in Piepho and Schatz.[110]

Magnetic Measurements. Magnetic data on individual single-crystal flakes (Figure 3.1) were collected using a Quantum Design PPMS DynaCool vibrating sample magnetometer (VSM). A flake was affixed to the end of a quartz paddle with varnish (VGE 7031). The paddle was then snapped into the VSM brass sample holder with another quartz paddle placed

symmetrically above the sample. The weak background signal from the sample holder was removed in the data analysis. The sample was probed with the external field aligned perpendicular to the face of the crystal, and magnetization data were collected as a function of applied field and temperature. The masses of individual flakes are below 0.1 mg and could not be accurately measured, so the magnetic data are reported in units of emu.

Ligand-field calculations within the Angular Overlap Model (AOM). Yb^{3+} ligand(crystal)-field energies and *g* factors were calculated using the BonnMag package.[25] Crystallographic data[18] on CrI_3 were used to create an $[YbI_6]^{3-}$ unit with reduced symmetry (point group C_2). Crystallographic parameters were not adjusted for size differences between Cr^{3+} and Yb^{3+}. The electronic structure of Yb^{3+} was calculated using the spin-orbit coupling parameter ζ as well as AOM parameters e_σ and e_π to describe σ and π interactions with the I^- ligands, respectively. The value for e_π was taken to be isotropic. The Slater-Condon-Shortley (SCS) parameters F_2, F_4, and F_6 were taken to be 0, as is typically the case for Yb^{3+} ($4f^{13}$ configuration). The Stevens orbital reduction factor *k* was taken to be equal to 1.0. Increasing (decreasing) ζ while keeping all other parameters constant results in an increase (decrease) in all transition energies while retaining peak splitting energies. Adjusting e_σ or e_π alters the relative energies of the peaks but maintains the barycenters.

Luminescence and covalency in ytterbium-doped CrX_3 (X = Cl, Br, I) van der Waals compounds

General considerations. All sample preparations and manipulations were performed in a glovebox under an atmosphere of purified dinitrogen.

Chemicals. A chromium chip (99.995%, lot MKCH4484) was purchased from Sigma Aldrich as a high-purity Cr source. The Cr chip was ground to a powder using a mortar and pestle and used as the powder precursor for CrI_3. I_2 (≥99.99%) was purchased from Sigma Aldrich. Ytterbium metal powder 40 mesh (99.9%) was purchased from BeanTown chemical. Anhydrous chromium(III) bromide (99%, lot 28644600) was purchased from Strem Chemicals. Anhydrous chromium(III) chloride (99.9%, lot U02D017) was purchased from Alfa Aesar. All chemicals were used as received without further purification.

Synthesis of CrX_3 (X = Cl, Br, I) and Yb^{3+}-doped CrX_3 single crystals. The synthesis of single crystals of CrI_3 and Yb^{3+}:CrI_3 grown through chemical vapor transport is detailed in Pressler et al.[59] This procedure was slightly modified for undoped $CrBr_3$ and $CrCl_3$, for which as-bought chromium(III) bromide and chromium(III) chloride precursors were used instead of elemental precursors. For Yb^{3+}-doped CrX_3, additional Yb(0) metal was loaded along with the other starting materials. Evacuated and sealed quartz tubes loaded with precursor materials were placed in an open-ended horizontal tube furnace, with the precursors placed in the center of the furnace at 650˚C (CrI_3) or 750˚C ($CrBr_3$, $CrCl_3$). The other end of the quartz tubes was placed in the cold zone, at a temperature ca. 150˚C colder than the center of the furnace. The samples were kept at temperature for approximately 3 days and then slowly cooled to room temperature, yielding thin flakes up to 1 cm in length.

pXRD measurements. As-synthesized flakes were characterized by X-ray diffraction using a Bruker D8 Discover powder diffractometer with IμS microfocus X-ray source for Cu Kα radiation (50 kV, 1 mA). Samples were placed onto crystalline silicon substrates and packed in Kapton film under an air-free environment to avoid sample degradation in air.

ICP-MS measurements. Yb^{3+} doping was confirmed using inductively coupled plasma mass spectrometry (ICP-MS) using a PerkinElmer NexION 2000B. ICP-MS samples were digested in high-purity concentrated nitric acid, followed by dilution in ultrapure H_2O. Yb^{3+} doping levels are reported as a percentage relative to the total cation contents, $[Yb^{3+}]/([Cr^{3+}]+[Yb^{3+}])$. Yb^{3+} incorporation into the CrX_3 flakes was found to be inhomogeneous throughout the same synthesis batch. We estimate an uncertainty of ±0.3% in the Yb^{3+} concentration to account for flake-to-flake inhomogeneity.

XAS measurements. X-ray absorption near edge structure (XANES) and extended X-ray absorption fine structure (EXAFS) spectra were collected at beamline 20-BM at the Advanced Photon Source at Argonne National Laboratory. Yb L_3-edge (8944 eV) and Cr K-edge (5989 eV) data were collected in fluorescence mode for single crystals of each sample at room temperature under helium atmosphere with active purging. Samples were sealed in Kapton tape under inert atmosphere to prevent air exposure prior to loading in the beamline holder. A Si(111) double-crystal monochromator was used to select the incident energy with He/N_2 filled ion chambers to monitor the flux. The monochromator was calibrated using Cr foil. The pre-edge region was collected from 150 to 20 eV below the edge with a step size of 10 eV and a collection time of 0.4 s at each step. From 20 eV below the edge to 30 eV above the edge, data were collected in 0.50-eV steps for 0.4 s at each step. Post-edge data were collected to 9.6 keV (for Yb) or 7 keV (for Cr) and obtained with a 0.05-keV step size and a collection time of 0.4 s per step. Data normalization and energy calibration were performed using Athena software.[64] Data were normalized to low energy regions of interest. Fits to the EXAFS data from proposed defect structures were performed with Artemis software.[64] A window from 3 $Å^{-1}$ to 12 $Å^{-1}$ with a dk value of 1 $Å^{-1}$ was used for shell-by-shell fitting. R-space EXAFS data were corrected in Artemis using an X (X = Cl, Br, I, depending on lattice) single scattering path from the CrX_3 host lattice structure. For the sake of clarity, we use $R + \Delta R$ to denote the corrected radial distance axis in the EXAFS data.

Photoluminescence measurements. A single crystal of the material was placed between two quartz disks and loaded into a closed-cycle helium cryostat. Measurements were performed under high vacuum (10^{-6} Pa) at a sample temperature of approximately 4 K. Samples were excited using a continuous-wave 660 nm (1.88 eV) diode in the case of X = Br, I, and a 405 nm (3.06 eV) diode for X = Cl at an excitation power of approximately 4 mW/cm^2. Sample emission was focused into a monochromator with a spectral bandwidth of 0.627 nm ($(Yb^{3+}:)CrI_3$), 1.617 nm ($CrBr_3$, $(Yb^{3+}:)CrCl_3$) and 0.259 nm ($Yb^{3+}:CrBr_3$). Spectra were collected using a LN_2-cooled silicon CCD camera ($CrCl_3$, $CrBr_3$) and a Hamamatsu InGaAs/InP NIR photomultiplier tube ($Yb^{3+}:CrCl_3$, $Yb^{3+}:CrBr_3$, $(Yb^{3+}:)CrI_3$), with signal recorded using a photon counter. All spectra were corrected for instrument response.

Time-resolved photoluminescence measurements. Measurements were done under the same conditions as used for PL measurements. Samples were excited using an EKSPLA PL2230 532 nm Nd:YAG/YVO_4 pulsed laser excitation source at a pulse frequency of 50 Hz, a pulse duration of 20 ps and an excitation energy of ~7 nJ/cm^2 per pulse. Data was collected using a LN_2-cooled Hamamatsu InGaAs/InP NIR photomultiplier tube. Monitor wavelengths of 910, 920 and 1100 nm were used for $CrCl_3$, $CrBr_3$ and CrI_3 respectively. Monitor wavelengths of 1039, 1042.5 and 1080 nm were used for Yb^{3+}:$CrCl_3$, Yb^{3+}:$CrBr_3$ and Yb^{3+}:CrI_3, respectively. Undoped CrX_3 measurements were performed using a 5 ns bin width. Bin widths of 640, 320, and 5 ns were used for Yb^{3+}:$CrCl_3$, Yb^{3+}:$CrBr_3$ and Yb^{3+}:CrI_3, respectively.

Angular Overlap Model. Energy values for the Yb^{3+} crystal field energies were calculated using the BonnMag software package.[82] Atomic coordinates were determined from crystallographic data on CrX_3 (X = Cl, Br, I), which were used to create distorted $[YbX_6]^{3-}$ octahedra of C_2 symmetry. Size differences between Cr^{3+} and Yb^{3+} were not considered in these calculations. A Stevens orbital reduction factor k of 1.0 was used and Slater-Condon-Shortley (SCS) parameters were set to 0 for Yb^{3+} ($4f^{13}$). The spin-orbit coupling parameter ζ was adjusted along with orbital overlap parameters e_σ and e_π to reproduce experimentally assigned electronic origin transition energies in the photoluminescence spectra. Experimental data could be reproduced well with an isotropic value for e_π in Yb^{3+}:CrI_3, but Yb^{3+}:$CrBr_3$ and Yb^{3+}:$CrCl_3$ required anisotropic values of $e_{\pi,x}$ and $e_{\pi,y}$ to accurately reproduce the spectra. Increasing (decreasing) ζ while keeping all other parameters constant results in an increase (decrease) in all transition energies while retaining peak splitting energies. Adjusting e_σ or e_π alters the relative energies of the peaks but maintains the barycenters.

Calculation of Select E_{CT} Values in Figure 4.8. Values of E_{CT} for the corresponding experimental Δ values for the white data points in Figure 4.8 were calculated from Eu^{3+} charge-transfer energies in the same lattice, following the method of Li *et al*.[111]

4.5 References

1. Cox, P. A., *Electronic Structure and Chemistry of Solids*. Oxford University Press: Oxford, 1987.
2. Henderson, B.; Imbusch, G. F., *Optical Spectroscopy of Inorganic Solids*. Oxford University Press: Oxford, 1989.
3. Kittel, C., *Introduction to Solid State Physics*. 8 ed.; Wiley: New York, 2004.
4. Bassett, L. C.; Alkauskas, A.; Exarhos, A. L.; Fu, K.-M. C. Quantum defects by design. *Nanophotonics* **2019,** *8*, 1867-1888.
5. Tran, T. T.; Elbadawi, C.; Totonjian, D.; Lobo, C. J.; Grosso, G.; Moon, H.; Englund, D. R.; Ford, M. J.; Aharonovich, I.; Toth, M. Robust Multicolor Single Photon Emission from Point Defects in Hexagonal Boron Nitride. *ACS Nano* **2016,** *10*, 7331-7338.
6. Hong, J.; Jin, C.; Yuan, J.; Zhang, Z. Atomic Defects in Two-Dimensional Materials: From Single-Atom Spectroscopy to Functionalities in Opto-/Electronics, Nanomagnetism, and Catalysis. *Adv. Mater.* **2017,** *29*, 1606434.
7. Cowley, R. A.; Buyers, W. J. L. The Properties of Defects in Magnetic Insulators. *Rev. Mod. Phys.* **1972,** *44*, 406-450.
8. Wiesendanger, R. Nanoscale Magnetic Skyrmions in Metallic Films and Multilayers: A New Twist for Spintronics. *Nat. Rev. Mater.* **2016,** *1*, 16044.
9. Lima Fernandes, I.; Bouaziz, J.; Blügel, S.; Lounis, S. Universality of Defect-Skyrmion Interaction Profiles. *Nat. Commun.* **2018,** *9*, 4395.
10. Song, T.; Cai, X.; Tu, M. W.-Y.; Zhang, X.; Huang, B.; Wilson, N. P.; Seyler, K. L.; Zhu, L.; Taniguchi, T.; Watanabe, K.; McGuire, M. A.; Cobden, D. H.; Xiao, D.; Yao, W.; Xu, X. Giant Tunneling Magnetoresistance in Spin-Filter van der Waals Heterostructures. *Science* **2018,** *360*, 1214-1218.
11. Huang, B.; McGuire, M. A.; May, A. F.; Xiao, D.; Jarillo-Herrero, P.; Xu, X. Emergent phenomena and proximity effects in two-dimensional magnets and heterostructures. *Nat. Mater.* **2020,** *19*, 1276-1289.
12. Gibertini, M.; Koperski, M.; Morpurgo, A. F.; Novoselov, K. S. Magnetic 2D materials and heterostructures. *Nat. Nanotech.* **2019,** *14*, 408-419.
13. Gong, C.; Zhang, X. Two-dimensional magnetic crystals and emergent heterostructure devices. *Science* **2019,** *363*, eaav4450.
14. Wang, Q. H.; Bedoya-Pinto, A.; Blei, M.; Dismukes, A. H.; Hamo, A.; Jenkins, S.; Koperski, M.; Liu, Y.; Sun, Q.-C.; Telford, E. J.; Kim, H. H.; Augustin, M.; Vool, U.; Yin, J.-X.; Li, L. H.; Falin, A.; Dean, C. R.; Casanova, F.; Evans, R. F. L.; Chshiev, M.*, et al.* The Magnetic Genome of Two-Dimensional van der Waals Materials. *ACS Nano* **2022,** *16*, 6960-7079.
15. Huang, B.; Clark, G.; Navarro-Moratalla, E.; Klein, D. R.; Cheng, R.; Seyler, K. L.; Zhong, D.; Schmidgall, E.; McGuire, M. A.; Cobden, D. H.; Yao, W.; Xiao, D.; Jarillo-Herrero, P.; Xu, X. Layer-Dependent Ferromagnetism in a van der Waals Crystal Down to the Monolayer Limit. *Nature* **2017,** *546*, 270-273.
16. Sivadas, N.; Okamoto, S.; Xu, X.; Fennie, C. J.; Xiao, D. Stacking-Dependent Magnetism in Bilayer CrI_3. *Nano Lett.* **2018,** *18*, 7658-7664.
17. Seyler, K. L.; Zhong, D.; Huang, B.; Linpeng, X.; Wilson, N. P.; Taniguchi, T.; Watanabe, K.; Yao, W.; Xiao, D.; McGuire, M. A.; Fu, K.-M. C.; Xu, X. Valley Manipulation by Optically Tuning the Magnetic Proximity Effect in WSe_2/CrI_3 Heterostructures. *Nano Lett.* **2018,** *18*, 3823-3828.

18. McGuire, M. A.; Dixit, H.; Cooper, V. R.; Sales, B. C. Coupling of Crystal Structure and Magnetism in the Layered, Ferromagnetic Insulator CrI_3. *Chem. Mater.* **2015,** *27*, 612-620.
19. Dillon, J. F.; Kamimura, H.; Remeika, J. P. Magneto-Optical Properties of Ferromagnetic Chromium Trihalides. *J. Phys. Chem. Solids* **1966,** *27*, 1531-1549.
20. Suits, J. Faraday and Kerr Effects in Magnetic Compounds. *IEEE Trans. Mag.* **1972,** *8*, 95-105.
21. Güdel, H. U.; Snellgrove, T. R. Jahn-Teller Effect in the $^4T_{2g}$ State of Chromium(III) in Dicesium Sodium Indium(III) Hexachloride. *Inorg. Chem.* **1978,** *17*, 1617-1620.
22. Peng, B.; Chen, Z.; Li, Y.; Liu, Z.; Liang, D.; Deng, L. Multiwavelength Magnetic Coding of Helical Luminescence in Ferromagnetic 2D Layered CrI_3. *iScience* **2022,** *25*, 103623.
23. Wyart, J.-F.; Tchang-Brillet, W.-Ü. L.; Spector, N.; Palmeri, P.; Quinet, P.; Biémont, E. Extended Analysis of the Spectrum of Triply-ionized Ytterbium (Yb IV) and Transition Probabilities. *Phys. Scripta* **2001,** *63*, 113-121.
24. Georgescu, A. B.; Millis, A. J.; Rondinelli, J. M. Trigonal Symmetry Breaking and Its Electronic Effects in the Two-Dimensional Dihalides MX_2 and Trihalides MX_3. *Phys. Rev. B* **2022,** *105*, 245153.
25. Bronova, A.; Bredow, T.; Glaum, R.; Riley, M. J.; Urland, W. BonnMag: Computer program for ligand-field analysis of f^n systems within the angular overlap model. *J. Comp. Chem.* **2018,** *39*, 176-186.
26. Zhang, Y.; Wu, X.; Lyu, B.; Wu, M.; Zhao, S.; Chen, J.; Jia, M.; Zhang, C.; Wang, L.; Wang, X.; Chen, Y.; Mei, J.; Taniguchi, T.; Watanabe, K.; Yan, H.; Liu, Q.; Huang, L.; Zhao, Y.; Huang, M. Magnetic Order-Induced Polarization Anomaly of Raman Scattering in 2D Magnet CrI_3. *Nano Lett.* **2020,** *20*, 729-734.
27. Al-Mobarak, R.; Warren, K. D. The Effect of Covalency on the Spin—Orbit Coupling Constant. *Chem. Phys. Lett.* **1973,** *21*, 513-516.
28. Bungenstock, C.; Tröster, T.; Holzapfel, W. B. Effect of Pressure on Free-Ion and Crystal-Field Parameters of Pr^{3+} in LOCl (L = La, Pr, Gd). *Phys. Rev. B* **2000,** *62*, 7945-7955.
29. Schwartz, R. W. Electronic Structure of the Octahedral Hexachloroytterbate Ion. *Inorg. Chem.* **1977,** *16*, 1694-1698.
30. Kanellakopulos, B.; Amberger, H. D.; Rosenbauer, G. G.; Fischer, R. D. Zur Elektronenstruktur hochsymmetrischer Verbindungen der Lanthanoiden und Actinoiden—V: Paramagnetische Suszeptibilität und elektronisches Raman-Spektrum von $Cs_2NaYb(III)Cl_6$. *J. Inorg. Nuc. Chem.* **1977,** *39*, 607-611.
31. Tsujii, N.; Imanaka, Y.; Takamasu, T.; Kitazawa, H.; Kido, G. Photoluminescence of Yb^{3+}-Doped $CuInS_2$ Crystals in Magnetic Fields. *J. Appl. Phys.* **2001,** *89*, 2706-2710.
32. Haumesser, P.-H.; Gaumé, R.; Viana, B.; Antic-Fidancev, E.; Vivien, D. Spectroscopic and Crystal-Field Analysis of New Yb-doped Laser Materials. *J. Phys.: Cond. Mat.* **2001,** *13*, 5427-5447.
33. de Maat-Gersdorf, I. Spectroscopic Analysis of Erbium-Doped Silicon and Ytterbium Doped Indium Phosphide. University of Amsterdam, 2001.
34. Liu, Y.; Petrovic, C. Three-Dimensional Magnetic Critical Behavior in CrI_3. *Phys. Rev. B* **2018,** *97*, 014420.
35. Coey, J. M. D., *Magnetism and Magnetic Materials*. Cambridge University Press 2010.
36. Lado, J. L.; Fernández-Rossier, J. On the Origin of Magnetic Anisotropy in Two Dimensional CrI_3. *2d Mater.* **2017,** *4*, 035002.
37. Aebersold, M. A.; Güdel, H. U.; Hauser, A.; Furrer, A.; Blank, H.; Kahn, R. Exchange

Interactions in Mixed Yb^{3+}-Cr^{3+} and Yb^{3+}-Ho^{3+} Dimers: An Inelastic-Neutron-Scattering Investigation of $Cs_3Yb_{1.8}Cr_{0.2}Br_9$ and $Cs_3Yb_{1.8}Ho_{0.2}Br_9$. *Phys. Rev. B* **1993,** *48*, 12723-12731.
38. Mironov, V. S.; Chibotaru, L. F.; Ceulemans, A. Exchange Interaction in the $YbCrBr_9^{3-}$ Mixed Dimer: The Origin of a Strong Yb^{3+}-Cr^{3+} Exchange Anisotropy. *Phys. Rev. B* **2003,** *67*, 014424.
39. Atanasov, M.; Daul, C.; Güdel, H. U., Modelling of Anisotropic Exchange Coupling in Rare-Earth -Transition-Metal Pairs: Applications to Yb^{3+}-Mn^{2+} and Yb^{3+}-Cr^{3+} Halide Clusters and Implications to the Light Up-Conversion. In *Comp. Chem.: Rev. Current Trends*, World Scientific: 2005; Vol. 9, pp 153-194.
40. Cao, S.; Sinha, K.; Zhang, X.; Zhang, X.; Wang, X.; Yin, Y.; N'Diaye, A. T.; Wang, J.; Keavney, D. J.; Paudel, T. R.; Liu, Y.; Cheng, X.; Tsymbal, E. Y.; Dowben, P. A.; Xu, X. Electronic Structure and Direct Observation of Ferrimagnetism in Multiferroic Hexagonal $YbFeO_3$. *Phys. Rev. B* **2017,** *95*, 224428.
41. Dalal, B.; Sarkar, B.; Dev Ashok, V.; De, S. K. Evolution of Magnetic Properties and Exchange Interactions in Ru Doped $YbCrO_3$. *J. Phys.: Cond. Mat.* **2016,** *28*, 426001.
42. Imbusch, G. F.; Yen, W. M.; Schawlow, A. L.; McCumber, D. E.; Sturge, M. D. Temperature Dependence of the Width and Position of the $^2E \rightarrow {}^4A_2$ Fluorescence Lines of Cr^{3+} and V^{2+} in MgO. *Phys. Rev.* **1964,** *133*, A1029-A1034.
43. Böttger, T.; Thiel, C. W.; Cone, R. L.; Sun, Y.; Faraon, A. Optical Spectroscopy and Decoherence Studies of Yb^{3+}:YAG at 968 nm. *Phys. Rev. B* **2016,** *94*, 045134.
44. Fisher, M. E. The Theory of Equilibrium Critical Phenomena. *Rep. Prog. Phys.* **1967,** *30*, 615-730.
45. Bermudez, V. M.; McClure, D. S. Spectroscopic studies of the two-dimensional magnetic insulators chromium trichloride and chromium tribromide—II. *J. Phys. Chem. Solids* **1979,** *40*, 149-173.
46. Burch, K. S.; Mandrus, D.; Park, J.-G. Magnetism in Two-Dimensional van der Waals Materials. *Nature* **2018,** *563*, 47-52.
47. Duong, D. L.; Yun, S. J.; Lee, Y. H. Van der Waals Layered Materials: Opportunities and Challenges. *ACS Nano* **2017,** *11*, 11803-11830.
48. Liu, Y.; Huang, Y.; Duan, X. Van der Waals Integration Before and Beyond Two-Dimensional Materials. *Nature* **2019,** *567*, 323-333.
49. Dillon, J. F.; Olson, C. E. Magnetization, Resonance, and Optical Properties of the Ferromagnet CrI_3. *J. Appl. Phys.* **1965,** *36*, 1259-1260.
50. Seyler, K. L.; Zhong, D.; Klein, D. R.; Gao, S.; Zhang, X.; Huang, B.; Navarro-Moratalla, E.; Yang, L.; Cobden, D. H.; McGuire, M. A.; Yao, W.; Xiao, D.; Jarillo-Herrero, P.; Xu, X. Ligand-Field Helical Luminescence in a 2D Ferromagnetic Insulator. *Nat. Phys.* **2018,** *14*, 277-281.
51. Güdel, H. U.; Snellgrove, T. R. Jahn-Teller Effect in the 4T2g State of Chromium(III) in Dicesium Sodium Indium(III) Hexachloride. *Inorganic Chemistry* **1978,** *17*, 1617-1620.
52. Dillon, J. F.; Kamimura, H.; Remeika, J. P. Magnetic Rotation of Visible Light by Ferromagnetic $CrBr_3$. *Phys. Rev. Lett.* **1962,** *9*, 161-163.
53. Dillon, J. F.; Kamimura, H.; Remeika, J. P. Magneto-Optical Properties of Ferromagnetic Chromium Trihalides. *J. Phys. Chem. Solids* **1966,** *27*, 1531-1549.
54. Limido, C.; Pedroli, G.; Spinolo, G. Specific Magnetic Rotation in the Crystal Field Bands of $CrCl_3$. *Solid State Commun.* **1972,** *11*, 1385-1388.
55. Nosenzo, L.; Samoggia, G.; Pollini, I. Effect of Magnetic Ordering on the Optical

Properties of Transition-Metal Halides: $NiCl_2$, $NiBr_2$, $CrCl_3$, and $CrBr_3$. *Phys. Rev. B* **1984,** *29*, 3607-3616.
56. Borghesi, A.; Guizzetti, G.; Samoggia, G.; Reguzzoni, E. Magneto-Optical Effects in the Paramagnetic and Ferromagnetic Phases of $CrBr_3$. *Phys. Rev. Lett.* **1981,** *47*, 538-541.
57. Zhang, Z.; Shang, J.; Jiang, C.; Rasmita, A.; Gao, W.; Yu, T. Direct Photoluminescence Probing of Ferromagnetism in Monolayer Two-Dimensional $CrBr_3$. *Nano Lett.* **2019,** *19*, 3138-3142.
58. Cai, X.; Song, T.; Wilson, N. P.; Clark, G.; He, M.; Zhang, X.; Taniguchi, T.; Watanabe, K.; Yao, W.; Xiao, D.; McGuire, M. A.; Cobden, D. H.; Xu, X. Atomically Thin $CrCl_3$: An In-Plane Layered Antiferromagnetic Insulator. *Nano Lett.* **2019,** *19*, 3993-3998.
59. Pressler, K.; Snoeren, T. J.; Walsh, K. M.; Gamelin, D. R. Magnetic Amplification at Yb^{3+} "Designer Defects" in the van der Waals Ferromagnet CrI_3. *Nano Lett.* **2023,** *23*, 1320-1326.
60. Morosin, B.; Narath, A. X-Ray Diffraction and Nuclear Quadrupole Resonance Studies of Chromium Trichloride. *J. Chem. Phys.* **1964,** *40*, 1958-1967.
61. Kozlenko, D. P.; Lis, O. N.; Kichanov, S. E.; Lukin, E. V.; Belozerova, N. M.; Savenko, B. N. Spin-Induced Negative Thermal Expansion and Spin–Phonon Coupling in van der Waals Material $CrBr_3$. *npj Quantum Mater.* **2021,** *6*, 19.
62. McGuire, M. A.; Dixit, H.; Cooper, V. R.; Sales, B. C. Coupling of Crystal Structure and Magnetism in the Layered, Ferromagnetic Insulator CrI_3. *Chem. Mater.* **2015,** *27*, 612-620.
63. Shannon, R. Revised Effective Ionic Radii and Systematic Studies of Interatomic Distances in Halides and Chalcogenides. *Acta Crystallogr. A* **1976,** *32*, 751-767.
64. Ravel, B.; Newville, M. ATHENA, ARTEMIS, HEPHAESTUS: Data Analysis for X-Ray Absorption Spectroscopy Using IFEFFIT. *J. Synch. Rad.* **2005,** *12*, 537-541.
65. Pizzochero, M. Atomic-Scale Defects in the Two-Dimensional Ferromagnet CrI_3 from First Principles. *J. Phys. D: Appl. Phys.* **2020,** *53*, 244003.
66. Zhang, J.; Guo, Y.; Li, P.; Wang, J.; Zhou, S.; Zhao, J.; Guo, D.; Zhong, D. Imaging Vacancy Defects in Single-Layer Chromium Triiodide. *J. Phys. Chem. Lett.* **2021,** *12*, 2199-2205.
67. De Siena, M. C.; Creutz, S. E.; Regan, A.; Malinowski, P.; Jiang, Q.; Kluherz, K. T.; Zhu, G.; Lin, Z.; De Yoreo, J. J.; Xu, X.; Chu, J.-H.; Gamelin, D. R. Two-Dimensional van der Waals Nanoplatelets with Robust Ferromagnetism. *Nano Lett.* **2020,** *20*, 2100-2106.
68. Jørgensen, C. K., Electron Transfer Spectra. In *Progress in Inorganic Chemistry*, 1970; Vol. 12, pp 101-158.
69. 't Hooft, G. W.; Van der Poel, W. A. J. A.; Molenkamp, L. W.; Foxon, C. T. Giant Oscillator Strength of Free Excitons in GaAs. *Phys. Rev. B* **1987,** *35*, 8281-8284.
70. Bermudez, V. M.; McClure, D. S. Spectroscopic Studies of the Two-Dimensional Magnetic Insulators Chromium Trichloride and Chromium Tribromide—I. *J. Phys. Chem. Solids* **1979,** *40*, 129-147.
71. Tomarchio, L.; Macis, S.; Mosesso, L.; Nguyen, L. T.; Grilli, A.; Guidi, M. C.; Cava, R. J.; Lupi, S. Low Energy Electrodynamics of CrI_3 Layered Ferromagnet. *Sci. Rep.* **2021,** *11*, 23405.
72. Ballhausen, C. J., *Introduction to Ligand Field Theory*. McGraw-Hill: New York (State), 1962.
73. Solomon, E. I. Inorganic Spectroscopy: An Overview. *Comments Inorg. Chem.* **1984,** *3*, 225-320.

74. Mir, W. J.; Mahor, Y.; Lohar, A.; Jagadeeswararao, M.; Das, S.; Mahamuni, S.; Nag, A. Postsynthesis Doping of Mn and Yb into $CsPbX_3$ (X = Cl, Br, or I) Perovskite Nanocrystals for Downconversion Emission. *Chem. Mater.* **2018,** *30*, 8170-8178.
75. Chen, N.; Cai, T.; Li, W.; Hills-Kimball, K.; Yang, H.; Que, M.; Nagaoka, Y.; Liu, Z.; Yang, D.; Dong, A.; Xu, C.-Y.; Zia, R.; Chen, O. Yb- and Mn-Doped Lead-Free Double Perovskite Cs_2AgBiX_6 (X = Cl^-, Br^-) Nanocrystals. *ACS Appl. Mater. Interfaces* **2019,** *11*, 16855-16863.
76. Dorenbos, P.; Josef, A.; De Haas, J. T. M.; Krämer, K. W. Vacuum Referred Binding Energies of the Lanthanides in Chloride, Bromide, and Iodide Compounds. *J. Lumin.* **2019,** *208*, 463-467.
77. Ryan, J. L.; Jørgensen, C. K. Absorption Spectra of Octahedral Lanthanide Hexahalides. *J. Phys. Chem.* **1966,** *70*, 2845-2857.
78. Gafurov, M. R.; Iskhakova, A. I.; Kurkin, I. N.; Kurzin, S. P.; Boris, Z. M.; Sergey, I. N.; Orlinskii, S. B.; Rakhmatullin, R. M.; Gil'man, S. S.; Valery, F. T.; Demirbilek, R.; Heber, J. Spectra and Relaxation of Electronic Excitations in $CsCdBr_3:Yb^{3+}$ and $CsCdBr_3:Nd^{3+}$ Monocrystals. *Proc.SPIE* **2002,** *4766*, 279-291.
79. Ryan, J. L. Weak or Unstable Iodo Complexes. I. Hexaiodo Complexes of the Lanthanides. *Inorg. Chem.* **1969,** *8*, 2053-2058.
80. Löble, M. W.; Keith, J. M.; Altman, A. B.; Stieber, S. C. E.; Batista, E. R.; Boland, K. S.; Conradson, S. D.; Clark, D. L.; Lezama Pacheco, J.; Kozimor, S. A.; Martin, R. L.; Minasian, S. G.; Olson, A. C.; Scott, B. L.; Shuh, D. K.; Tyliszczak, T.; Wilkerson, M. P.; Zehnder, R. A. Covalency in Lanthanides. An X-ray Absorption Spectroscopy and Density Functional Theory Study of $LnCl_6^{x-}$ (x = 3, 2). *J. Am. Chem. Soc.* **2015,** *137*, 2506-2523.
81. Atanasov, M.; Daul, C.; Güdel, H. U.; Wesolowski, T. A.; Zbiri, M. Ground States, Excited States, and Metal−Ligand Bonding in Rare Earth Hexachloro Complexes: A DFT-Based Ligand Field Study. *Inorg. Chem.* **2005,** *44*, 2954-2963.
82. Bronova, A.; Bredow, T.; Glaum, R.; Riley, M. J.; Urland, W. BonnMag: Computer Program for Ligand-Field Analysis of f^n Systems Within the Angular Overlap Model. *J. Comp. Chem.* **2018,** *39*, 176-186.
83. Antic-Fidancev, E. Simple Way to Test the Validity of $^{2S+1}L_J$ Barycenters of Rare Earth Ions (e.g. $4f^2$, $4f^3$ and $4f^6$ Configurations). *J. Alloys Compd.* **2000,** *300-301*, 2-10.
84. Haumesser, P.-H.; Gaumé, R.; Viana, B.; Antic-Fidancev, E.; Vivien, D. Spectroscopic and Crystal-Field Analysis of New Yb-Doped Laser Materials. *J. Phys. Condens. Matter* **2001,** *13*, 5427.
85. Hansen, P.-A.; Kumar, S.; Meijerink, A. Strong Self-Sensitized Green and NIR Emission in $NaYS_2$ Doped with Pr^{3+} and Yb^{3+} by Inducing Laporte Allowed and Charge Transfer Transitions. *J. Lumin.* **2021,** *235*, 118012.
86. Martin, W. C. Table of Spin-Orbit Energies for *p*-Electrons in Neutral Atomic (core)*np* Configurations. *J. Res. Natl. Inst. Stand. Technol. A Phys. Chem.* **1971,** *75A*, 109-111.
87. Bryant, F. J. Ion Implanation in Group II–VI Compounds. *Prog. Cryst. Growth Charact.* **1983,** *6*, 191-263.
88. Neidig, M. L.; Clark, D. L.; Martin, R. L. Covalency in f-Element Complexes. *Coord. Chem. Rev.* **2013,** *257*, 394-406.
89. Kerridge, A. Quantification of f-Element Covalency Through Analysis of the Electron Density: Insights from Simulation. *Chem. Comm.* **2017,** *53*, 6685-6695.
90. Vitova, T.; Pidchenko, I.; Fellhauer, D.; Bagus, P. S.; Joly, Y.; Pruessmann, T.; Bahl,

S.; Gonzalez-Robles, E.; Rothe, J.; Altmaier, M.; Denecke, M. A.; Geckeis, H. The Role of the 5*f* Valence Orbitals of Early Actinides in Chemical Bonding. *Nat. Commun.* **2017,** *8*, 16053.
91. Vitova, T.; Roesky, P. W.; Dehnen, S. Open Questions on Bonding Involving Lanthanide Atoms. *Commun. Chem.* **2022,** *5*, 12.
92. Hehlen, M. P.; Krämer, K.; Güdel, H. U.; McFarlane, R. A.; Schwartz, R. N. Upconversion in Er^{3+}-Dimer Systems: Trends Within the Series $Cs_3Er_2X_9$ (*X*=Cl,Br,I). *Phys. Rev. B* **1994,** *49*, 12475-12484.
93. Dorenbos, P. Systematic Behaviour in Trivalent Lanthanide Charge Transfer Energies. *J. Phys. Condens. Matter* **2003,** *15*, 8417.
94. Asprey, L. B.; Keenan, T. K.; Kruse, F. H. Preparation and Crystal Data for Lanthanide and Actinide Triiodides. *Inorg. Chem.* **1964,** *3*, 1137-1141.
95. Arumugam, G. M.; Xu, C.; Karunakaran, S. K.; Shi, Z.; Zhu, C.; Wei, M.; Feifei, Q. Efficient Red Up-Conversion Emission from Er^{3+}-Yb^{3+} Co-Doped Rubidium Lead Iodide Perovskite Nanowires with Surface Plasmons. *Appl. Phys. Lett.* **2018,** *112*, 054104.
96. Shi, J.; Li, F.; Yuan, J.; Ling, X.; Zhou, S.; Qian, Y.; Ma, W. Efficient and Stable $CsPbI_3$ Perovskite Quantum Dots Enabled by In Situ Ytterbium Doping for Photovoltaic Applications. *J. Mater. Chem. A* **2019,** *7*, 20936-20944.
97. Meyer, G., The Divalent State in Solid Rare Earth Metal Halides. In *The Rare Earth Elements: Fundamentals and Applications*, 2012; p 161.
98. Rubio, O. J. Doubly-Valent Rare-Earth Ions in Halide Crystals. *J. Phys. Chem. Solids* **1991,** *52*, 101-174.
99. Dorenbos, P. Energy of the First $4f^7 \rightarrow 4f^6 5d$ Transition of Eu^{2+} in Inorganic Compounds. *J. Lumin.* **2003,** *104*, 239-260.
100. Seyler, K. L.; Zhong, D.; Klein, D. R.; Gao, S.; Zhang, X.; Huang, B.; Navarro-Moratalla, E.; Yang, L.; Cobden, D. H.; McGuire, M. A.; Yao, W.; Xiao, D.; Jarillo-Herrero, P.; Xu, X. Ligand-field helical luminescence in a 2D ferromagnetic insulator. *Nat. Physics* **2018,** *14*, 277-281.
101. Abramoff, M. D.; Magalhaes, P. J.; Ram, S. J. Image Processing with ImageJ. *Biophot. Int.* **2004,** *11*, 35-42.
102. Bruker APEX2 (Version 2.1-4), SAINT (version 7.34A), SADABS (version 2007/4),. **2007**.
103. Sheldrick, G. M. A short history of SHELX. *Acta Cryst.* **2007,** *A64*, 112-122.
104. Sheldrick, G. M. SHELXT - Integrated space-group and crystal-structure determination. *Acta Cryst.* **2015,** *A71*, 3-8.
105. Altomare, A.; Cascarano, G. L.; Giacovazzo, C.; Guagliardi, A. Completion and refinement of crystal structures with SIR92. *J. Appl. Cryst.* **1993,** *26*, 343-350.
106. Altomare, A.; Burla, C.; Camalli, M.; Cascarano, G. L.; Giacovazzo, C.; Guagliardi, A.; Moliterni, A. G. G.; Polidori, G.; Spagna, R.; Burla, C.; Camalli, M.; Cascarano, G. L.; Giacovazzo, C.; Guagliardi, A.; Moliterni, A. G. G.; Polidori, G.; Spagna, R. SIR97: a new tool for crystal structure determination and refinement. *J. Appl. Crystallogr.* **1999**, 115-119.
107. Sheldrick, G. M. SHELXL-97, Program for the Refinement of Crystal Structures. **1997**.
108. Sheldrick, G. M. Crystal structure refinement with SHELXL. *Acta Cryst.* **2015,** *C71*, 3-8.
109. Waasmaier, D.; Kirfel, A. New Analytical Scattering Factor Functions for Free Atoms and Ions. *Acta Crysta.* **1995,** *A51*.
110. Schatz, P. N.; Piepho, S. B., *Group Theory in Spectroscopy: With Applications to Magnetic Circular Dichroism*. Wiley: New York, 1983.

111. Li, L.; Zhou, S.; Zhang, S. Relationship Between Charge Transfer Energies of Yb^{3+} and Sm^{3+} and Crystal Environmental Factor. *J. Lumin.* **2009,** *129*, 187-191.

Appendices

Appendix A: Supplementary Information for Chapter 2

Ferromagnetism and Spin-Polarized Luminescence in Lead-Free $CsEuCl_3$ Perovskite Nanocrystals and Thin Films

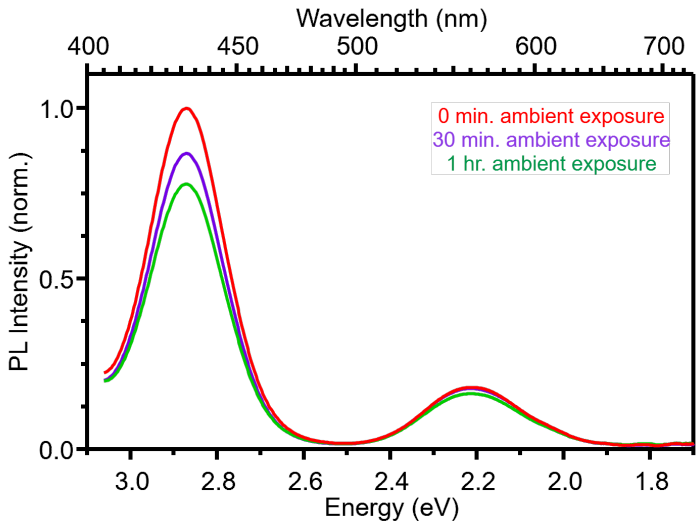

Figure A1. Photoluminescence spectra of $CsEuCl_3$ nanocrystals in solution before exposure to air (red) and after 30 min. and 1 hr. of ambient air exposure (purple and green traces, respectively). The low-energy (~2.2 eV) PL intensity does not increase when the nanocrystals are exposed to air, ruling out the possibility that it arises from aerobic degradation of $CsEuCl_3$.

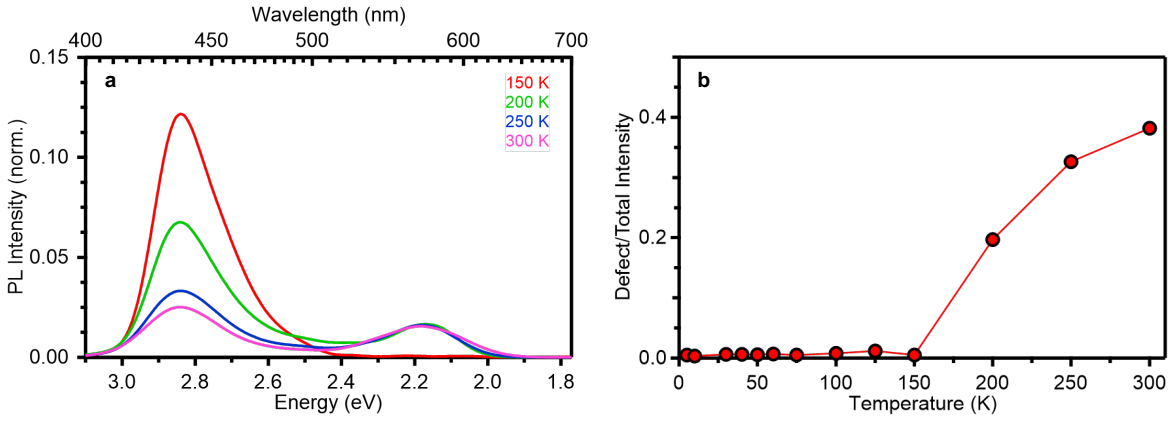

Figure A2. (a) Selected zoomed-in spectra from the temperature-dependent PL study of the $CsEuCl_3$ nanocrystals from Figure 2.2b, demonstrating the appearance of a low-energy PL feature at temperatures at and above ~200 K. **(b)** Scatter plot of the low-energy defect/total PL intensity as a function of temperature for all spectra presented in Figure 2.2b.

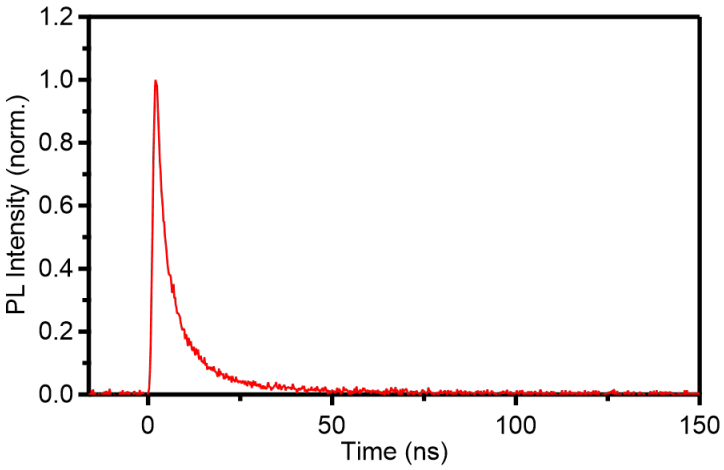

Figure A3. Room-temperature PL decay curve for the low-energy PL feature centered around 2.2 eV, collected using 375 nm pulsed laser excitation. The data were fit with a bi-exponential decay function, yielding an average lifetime of ~5 ns.

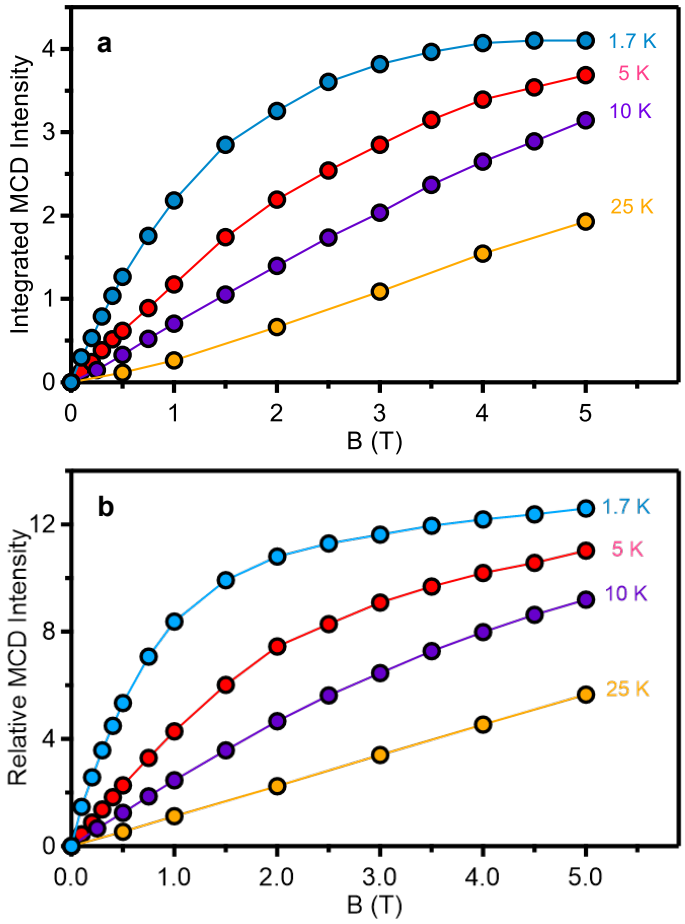

Figure A4. MCD data for **(a)** $CsEuCl_3$ nanocrystals and **(b)** a $CsEuCl_3$ thin film, taken from Figure 2.3c,d and replotted as a function of magnetic field.

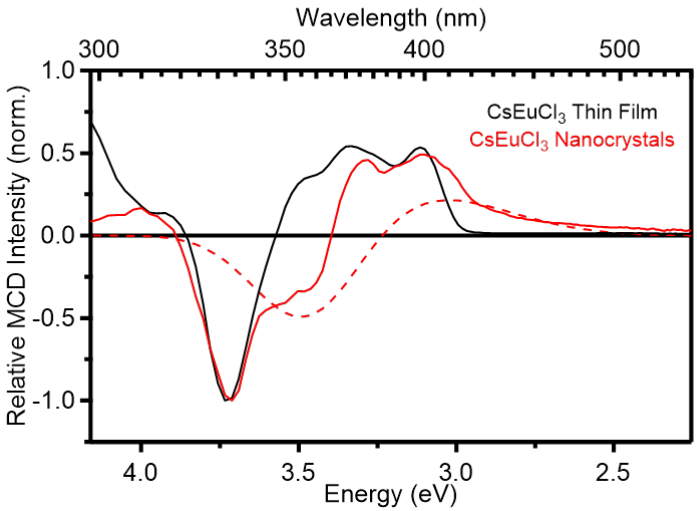

Figure A5. Comparison of 5 K, 5 T MCD spectra of the $CsEuCl_3$ thin film (black) and nanocrystal (red) samples. The dotted red trace shows the best-fit difference (sum of two Gaussians) between the nanocrystal and thin-film spectra, indicating a secondary Eu^{2+} species in the $CsEuCl_3$ nanocrystals that contributes broad MCD intensity, tentatively assigned as surface Eu^{2+}. The experimental spectra have been normalized to the feature centered around ~3.71 eV for ease of comparison.

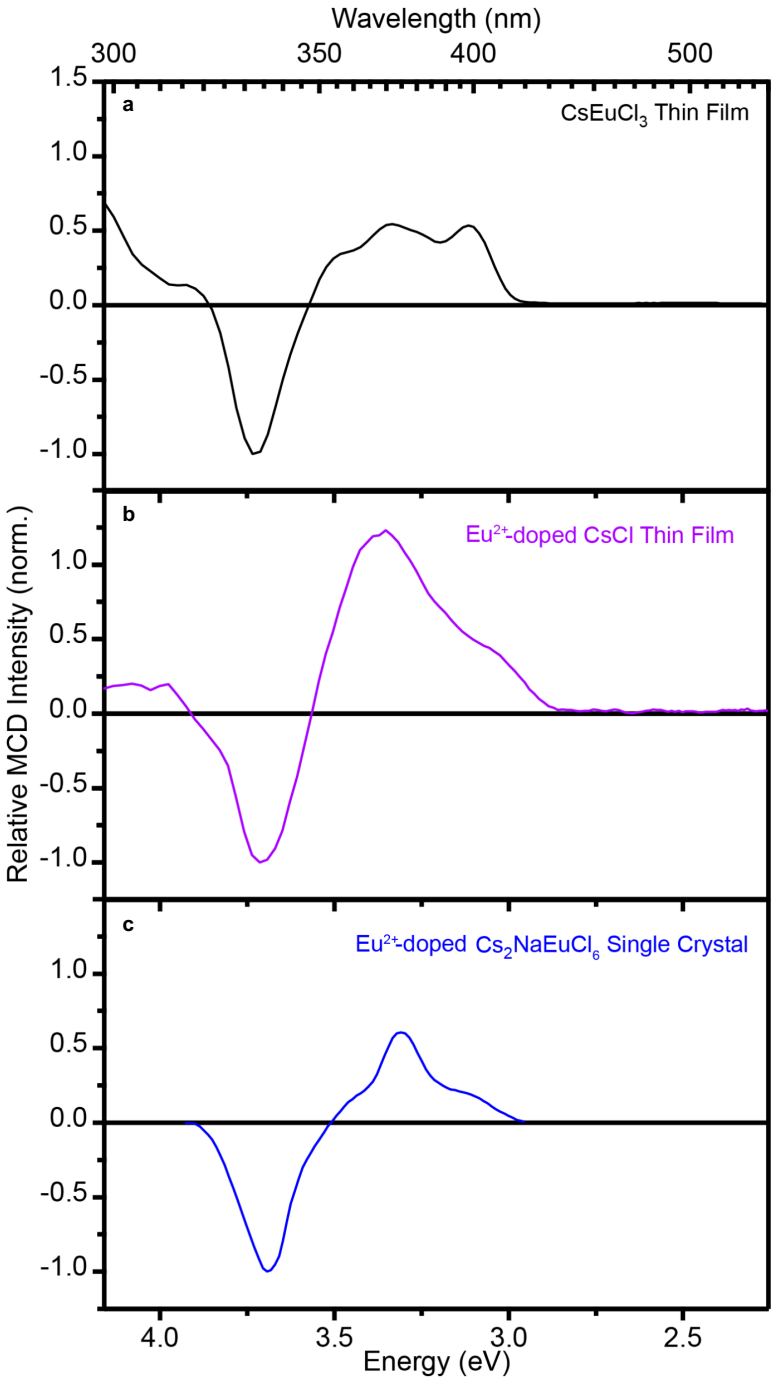

Figure A6. Comparison of 5 K, 5 T MCD spectra of **(a)** $CsEuCl_3$ thin film, **(b)** Eu^{2+}-doped CsCl thin film, and **(c)** Eu^{2+}-doped $Cs_2NaEuCl_6$ single crystal. The Eu^{2+}-doped $Cs_2NaEuCl_6$ single crystal data are adapted from Chapter 2 ref. 29. Spectra have been normalized to the feature centered around ~3.71 eV for ease of comparison.

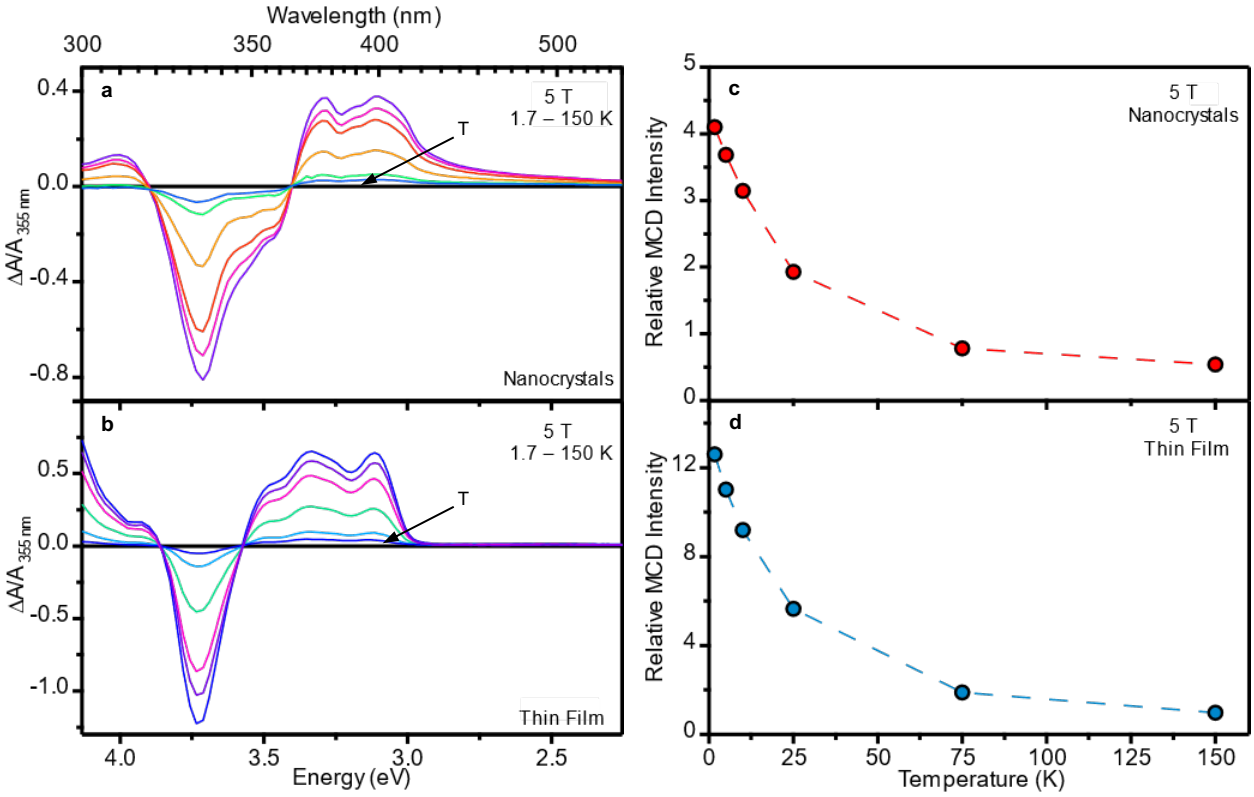

Figure A7. Variable-temperature MCD spectra collected at 5 T for **(a)** $CsEuCl_3$ nanocrystals and **(b)** a $CsEuCl_3$ thin film. **(c,d)** Scatter plots of 5 T MCD intensity *vs* temperature, from the data in panels (a,b).

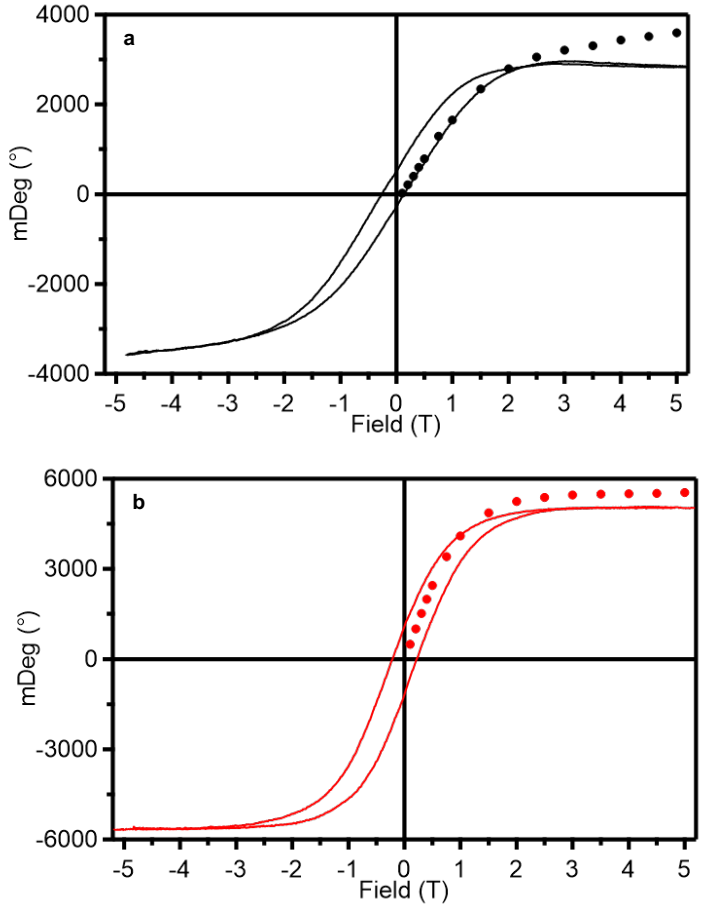

Figure A8. (a) 1.7 K MCD hysteresis data for the $CsEuCl_3$ nanocrystals from a continuous field-sweep measurement (solid, from Figure 4), superimposed upon the 1.7 K variable-field MCD intensities for the same sample collected from variable-field spectral measurements (circles, taken from the spectra in Figure 2.3a). **(b)** 1.7 K MCD hysteresis data for the $CsEuCl_3$ thin film from a continuous field-sweep measurement (solid, from Figure 4), superimposed upon the 1.7 K variable-field MCD intensities for the same sample collected from variable-field spectral measurements (circles, from the spectra in Figure 2.3b). The continuous field-sweep measurements were performed by centering the monochromator at 334 nm with a spectral bandwidth of 4 nm. The variable-field MCD measurements were also performed with a 4 nm spectral bandwidth, and the intensities at 334 nm are plotted in panels (a,b).

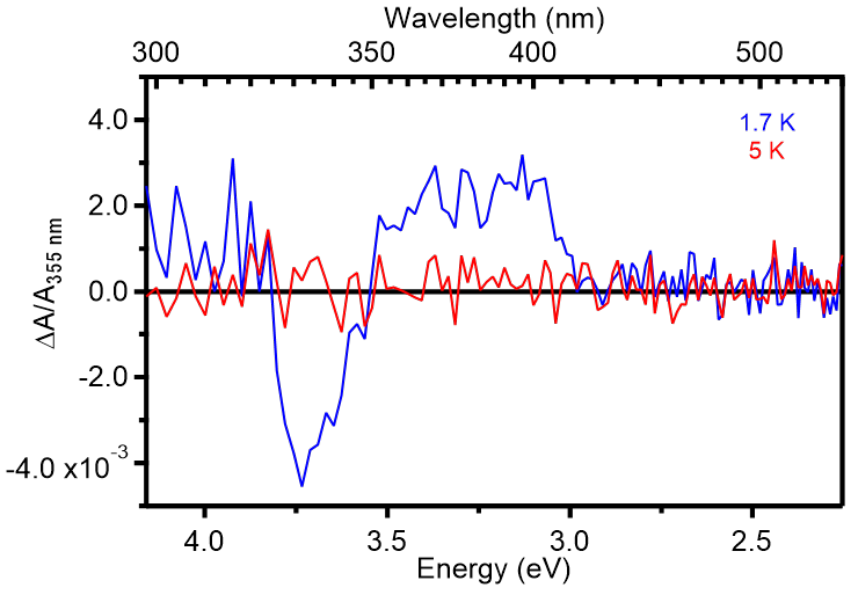

Figure A9. Zero-field MCD spectra of the $CsEuCl_3$ thin film collected at 1.7 K (blue) and 5 K (red). The 1.7 K scan was collected immediately after magnetization and shows an MCD signal as a result of remanent magnetization in the ferromagnetic $CsEuCl_3$. The 5 K spectrum shows no remanent MCD intensity, indicating that T_C is between 1.7 and 5 K.

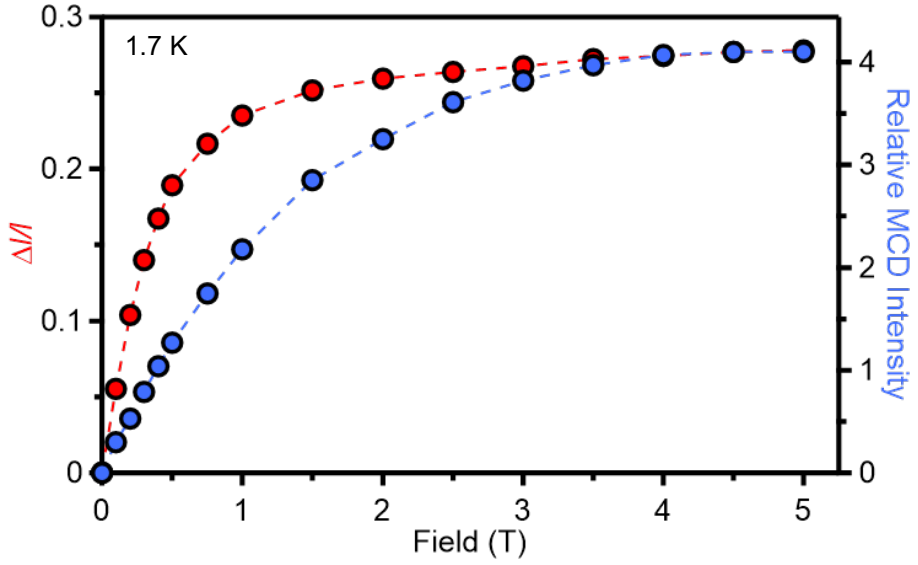

Figure A10. Comparison of $CsEuCl_3$ nanocrystal MCPL (red) and MCD (blue) saturation magnetization plotted as a function of magnetic field. Both data sets were collected at 1.7 K.

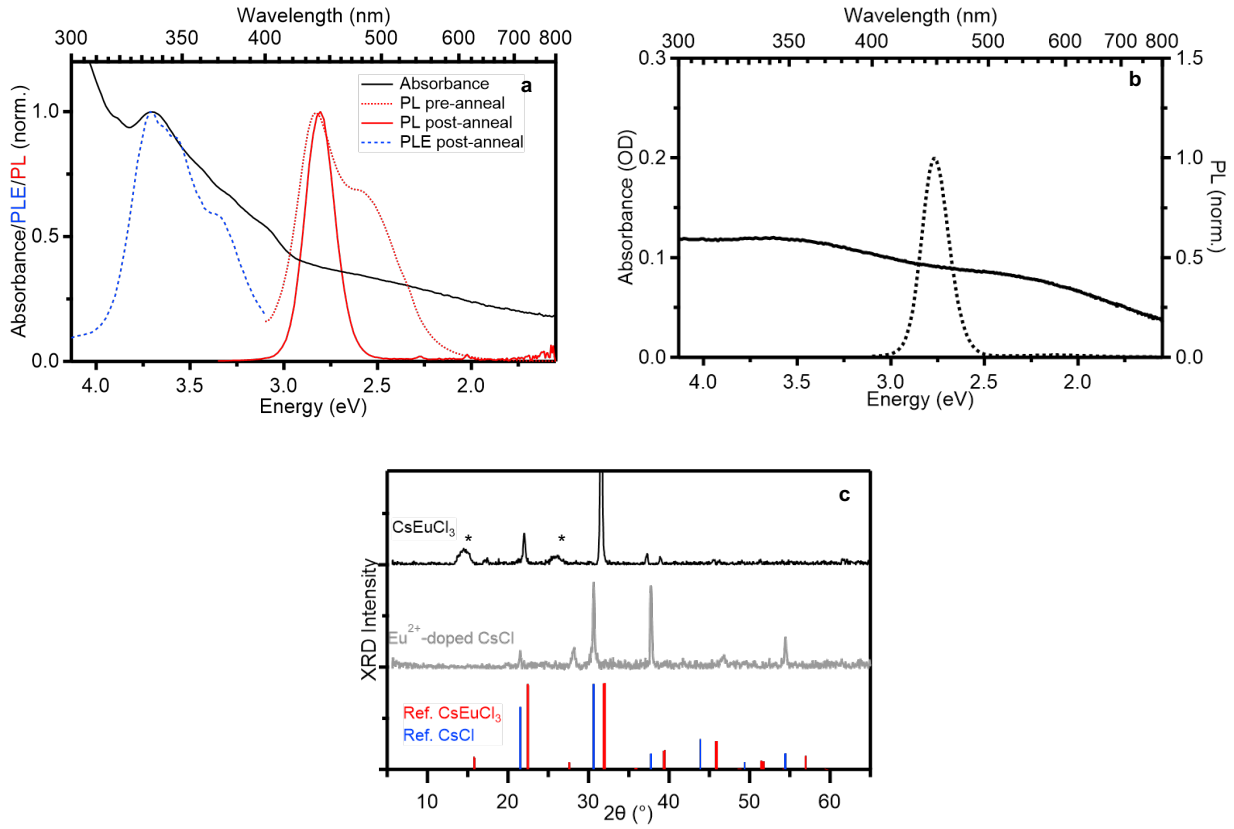

Figure A11. (a) Room-temperature absorption (solid black), PL before and after annealing at 300 °C for 30 min (red dotted and red solid, respectively), and PLE (blue dashed) spectra of a $CsEuCl_3$ thin film. Whereas the film's absorption spectrum shows considerable background due to either scattering, interference fringes, *etc.*, the PLE spectrum of the same film shows clean features attributable to $CsEuCl_3$. **(b)** Room-temperature absorption (solid) and PL (dashed) spectra of Eu^{2+}-doped CsCl thin film. **(c)** Powder XRD data for $CsEuCl_3$ and Eu^{2+}-doped CsCl thin films, plotted along with $CsEuCl_3$ (tetragonal, ICSD Coll. Code 201316) and CsCl (ICSD Coll. Code 257256) reference diffraction patterns. The asterisks denote additional peaks that arise as a consequence of the Kapton tape used for air-free data collection.

Appendix B: Supplementary Information for Chapter 3.2

An Air-Stable and Exfoliable Ferromagnetic Two-Dimensional Perovskite, (Phenethylammonium)$_2$CrCl$_4$

Adapted with permission from Smith, R. T.; Walsh, K. M.; Jiang, Q.; Chu, J.-H..; Gamelin, D. R. *Chem. Mater.* **2024**, *36*, 1571-1578. Copyright 2024 American Chemical Society. Note: The originally published manuscript included an error in the labeling of the magnetic easy axis which has been corrected in this dissertation. The as-published manuscript has been corrected with an erratum.

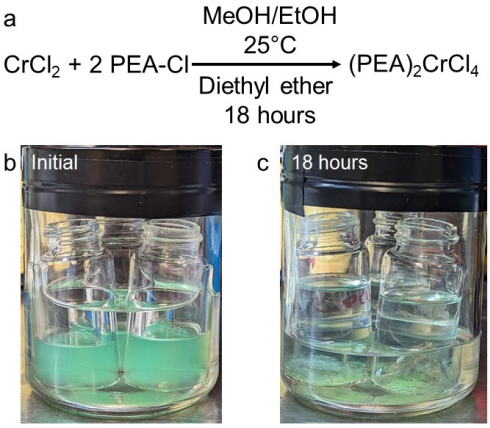

Figure B1. (a) Reaction scheme for synthesis and crystallization of (PEA)$_2$CrCl$_4$. **(b)** Image of reaction vessel with the solubilized $CrCl_2$ and PEA-Cl in vials that sit within a larger chamber containing diethyl ether for slow vapor diffusion. **(c)** Image of the same reaction vessel after 18 hours. Large, transparent crystals are visible in the scintillation vials.

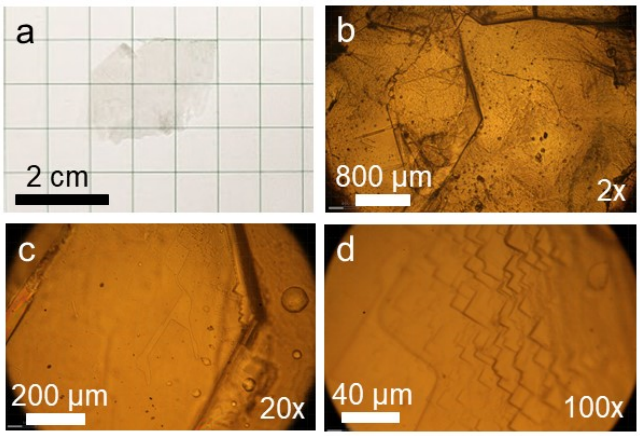

Figure B2. Optical images of a (PEA)$_2$CrCl$_4$ crystal. **(a)** Photograph of the crystal with no magnification. **(b-d)** Optical microscopy images of the crystal with different magnifications.

Table B1. Crystal data and structure refinement.

Identification code	shelx	
Empirical formula	$C_{16}H_{24}Cl_4CrN_2$	
Formula weight	438.17	
Temperature	100(2) K	
Wavelength	0.71073 Å	
Crystal system	Orthorhombic	
Space group	P b c a	
Unit cell dimensions	a = 38.378(5) Å	a = 90°.
	b = 7.2444(10) Å	b = 90°.
	c = 7.2691(11) Å	g = 90°.
Volume	2021.0(5) $Å^3$	
Z	4	
Density (calculated)	1.440 Mg/m^3	
Absorption coefficient	1.095 mm^{-1}	
F(000)	904	
Crystal size	0.500 x 0.250 x 0.050 mm^3	
Theta range for data collection	1.061 to 28.426°.	
Index ranges	$-51 \le h \le 51$, $-9 \le k \le 9$, $-9 \le l \le 9$	
Reflections collected	17411	
Independent reflections	2492 [R(int) = 0.0478]	
Completeness to theta = 25.000°	98.3 %	
Refinement method	Full-matrix least-squares on F^2	
Data / restraints / parameters	2492 / 0 / 107	
Goodness-of-fit on F^2	1.036	
Final R indices [I > 2sigma(I)]	R1 = 0.0667, wR2 = 0.1458	
R indices (all data)	R1 = 0.0679, wR2 = 0.1463	
Largest diff. peak and hole	0.804 and -1.146 $e.Å^{-3}$	

Table B2. Atomic coordinates ($x10^4$) and equivalent isotropic displacement parameters ($Å^2 x\ 10^3$). U(eq) is defined as one third of the trace of the orthogonalized U^{ij} tensor.

	x	y	z	U(eq)
C(1)	6566(1)	5152(6)	5217(6)	15(1)
C(2)	6696(1)	6338(7)	3859(7)	21(1)
C(3)	7033(1)	6153(8)	3204(8)	23(1)
C(4)	7247(1)	4779(8)	3875(8)	23(1)
C(5)	7120(1)	3581(7)	5202(8)	23(1)
C(6)	6781(1)	3767(7)	5842(7)	18(1)
C(7)	6198(1)	5407(7)	5888(7)	16(1)
C(8)	5932(1)	4561(6)	4576(6)	15(1)
Cl(1)	5070(1)	2823(1)	2438(1)	11(1)
Cl(2)	5621(1)	5410(1)	-167(1)	12(1)
Cr(1)	5000	5000	0	8(1)
N(1)	5572(1)	5107(5)	5152(6)	14(1)

Table B3. Literature A_2CrCl_4 structural and magnetic data.

Compound	Interlayer spacing (Å)	Cr-Cl-Cr angle (°)	Cr-Cl elongated in-plane bond (Å)	Cr-Cl short in-plane bond (Å)	Cr-Cl out-of-plane bond (Å)	Tilt angle θ_a (degrees)	Tilt angle θ_b (degrees)	T_C (K) susceptibility	T_C (K) neutron scattering	J (meV)
Rb_2CrCl_4[1-3]	7.88	180	2.76	2.39	2.41	0.0	0.0	57	52.4	1.24
*Cs_2CrCl_4[4]	8.22	180	2.61	2.61	2.40			55		
$(MeNH_3)_2CrCl_4$[2, 5-7]	9.44	166.5	2.82	2.41	2.41			50	42	1.12
$(EtNH_3)_2CrCl_4$[2, 5, 7]	10.7							50	41	0.87
$(C_3H_7NH_3)_2CrCl_4$[8]	12.35							44	39.5	0.81
$(C_5H_{11}NH_3)_2CrCl_4$[8]	17.81							61		0.81
$(C_{12}H_{25}NH_3)_2CrCl_4$[8]	30.60							48		0.81
$(PMA)_2CrCl_4$[9]	15.72							37		0.91
$(DFCBA)_2CrCl_4$[10]	13.07	162.83	2.955, 3.077	2.375, 2.418	2.378, 2.413			32.6		0.62
$(dienH_3)(CrCl_4)Cl$[11]	12.03	162.25	2.79	2.39	2.41					
$[H_3N(CH_2)_3NH_3)CrCl_4$[2, 12]	9.27	165.3	2.87	2.39						0.91
$(PEA)_2CrCl_4$ (this study)	19.19	166.63	2.779	2.387	2.405	+5.98	±5.04	44		0.87

* Denotes data collected before the antiferrodistortive Jahn-Teller ordering was recognized.
All J values for $H = -JS_i \bullet S_j$ Hamiltonian.

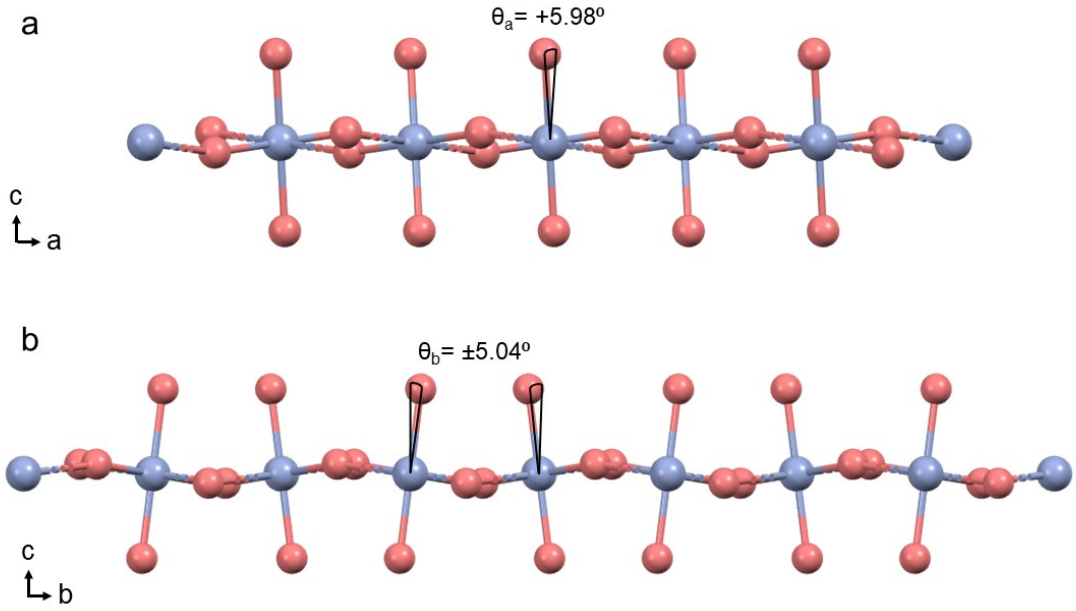

Figure B3. Octahedral tilting in $(PEA)_2CrCl_4$. **(a)** An edge-on view of an individual inorganic sheet (*ab* plane) viewed down the *b* axis, showing uniform tilting of octahedra along the *a* direction with a tilt angle of $\theta_a = +5.98°$. The tilt direction alternates in alternating layers. **(b)** An edge-on view of an individual inorganic sheet (*ab* plane) viewed down the *a* axis, showing alternating tilting of octahedra along the *b* direction, with tilt angles of $\theta_b = \pm 5.04°$

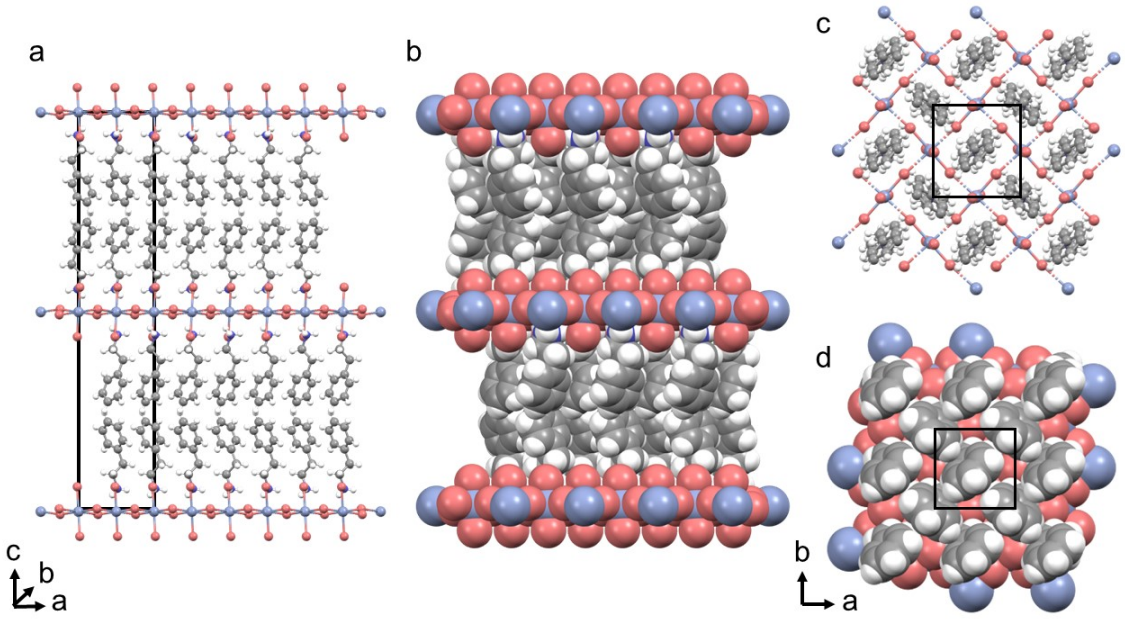

Figure B4. Space filling representation of a $(PEA)_2CrCl_4$ crystal demonstrating the PEA coverage of the inorganic layer. **(a** and **c)** Ball-and-stick representations of the edge and top for comparison with the space-filling representations **(b** and **d)**. The black lines represent the unit cell.

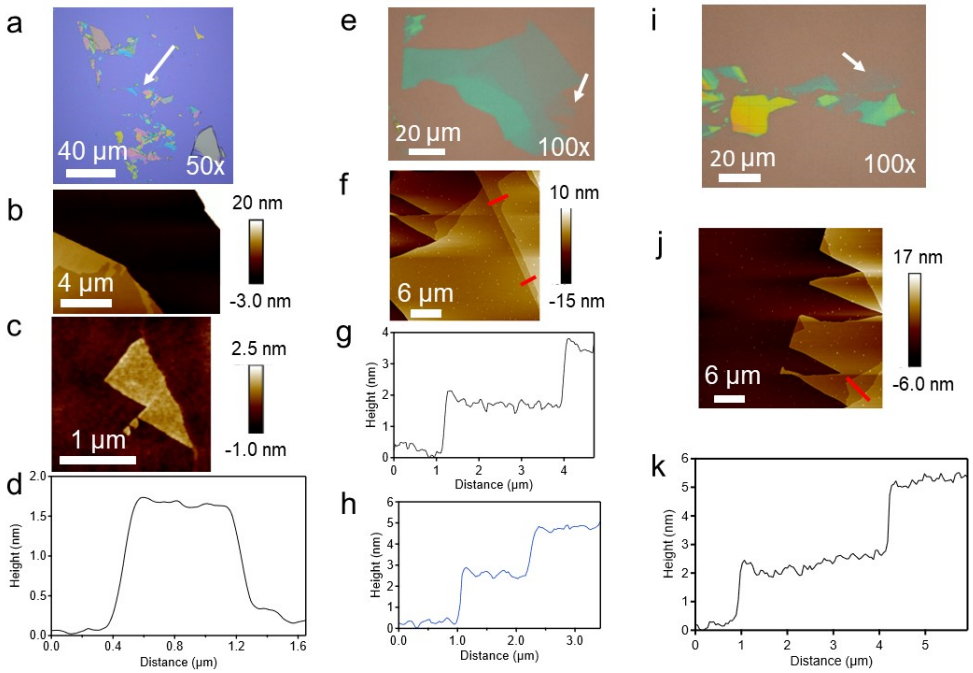

Figure B5. Optical images, AFM data, and flake-height plots for several exfoliated flakes of $(PEA)_2CrCl_4$ crystals. **(a, e,** and **i)** Optical microscope images of exfoliated $(PEA)_2CrCl_4$ on SiO_2 wafers, with arrows indicating the regions scanned by AFM. **(b, c, f,** and **j)** AFM images of the exfoliated flakes with colored lines depicting the regions sampled for height analysis. **(d, g, h,** and **k)** Plots of sample height *vs* position as depicted by the lines in the AFM images above. These data, in combination with data for many other exfoliated flakes, indicate a flake height of 2.0 ± 0.1 nm, consistent with the height of a single $(PEA)_2CrCl_4$ monolayer anticipated from the single-crystal XRD structure (~1.9 nm, Figure 3.2 of section 3.2).

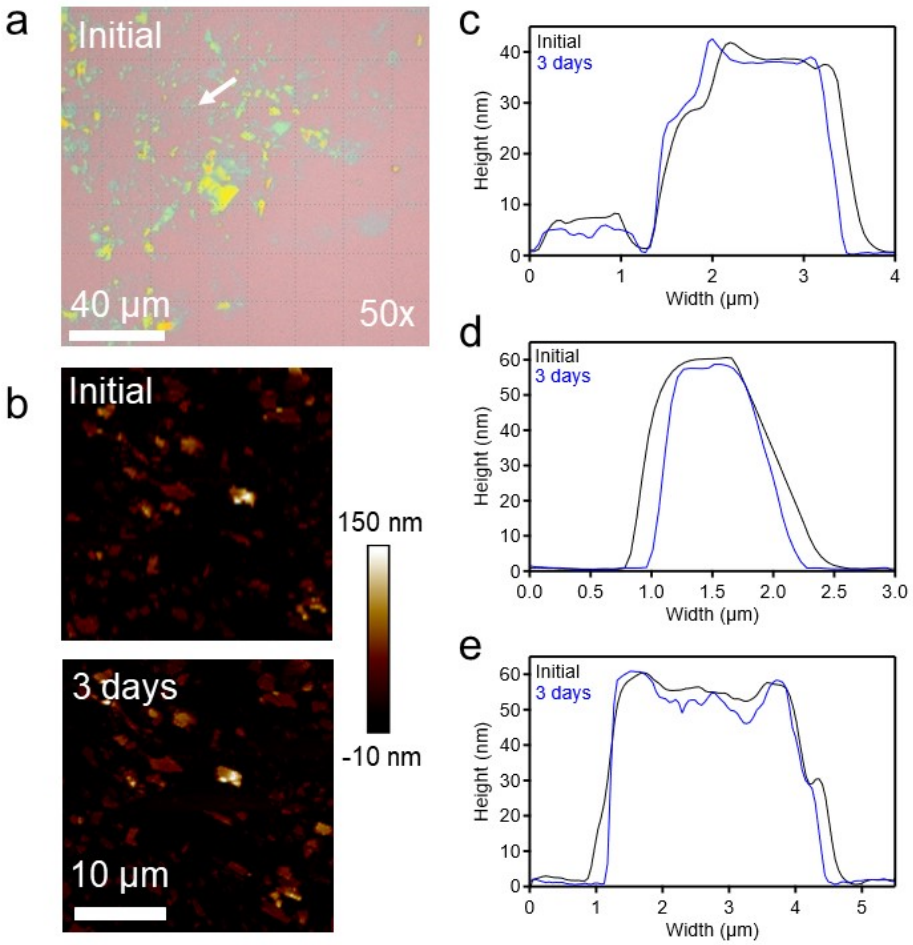

Figure B6. Optical image, AFM data, and flake-height plots for exfoliated flakes of $(PEA)_2CrCl_4$ crystals before and after air exposure. **(a)** Optical microscope image of exfoliated $(PEA)_2CrCl_4$ on a SiO_2 wafer with an arrow indicating the region scanned by AFM. **(b)** AFM images of the exfoliated flakes before air exposure and after 3 days of continuous air exposure. The flakes show retention of their general shapes, sizes, and faceting after exposure to air. **(c, d,** and **e)** Plots of sample height *vs* position for three different exfoliated flakes. The black traces were collected before air exposure and the blue traces were collected after three days in air. All three plots show retention of the flake profiles.

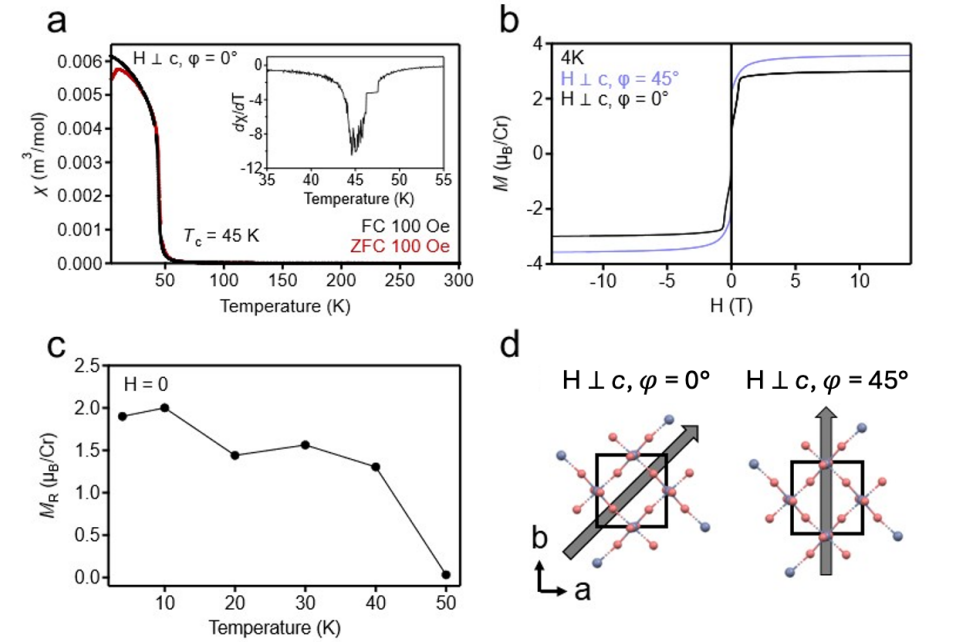

Figure B7. Magnetic data for a $(PEA)_2CrCl_4$ single crystal. **(a)** Field-cooled (FC) and zero-field-cooled (ZFC) magnetization sweeps collected with an applied magnetic field oriented in the crystallographic *ab* plane and with an angle of 0º with respect to the Cr^{2+} molecular axis. The inset shows the derivative of the FC data, yielding an ordering temperature of T_C = 45 K. **(b)** Magnetic hysteresis loop measured from -14 to +14 T at 4 K for two different in-plane applied magnetic field orientations with angles of 45º and 0º with respect to the molecular axes. **(c)** The remanent magnetization (M_R) per Cr^{2+}, obtained from the 0 T data of Figure 3.5d, plotted *vs* sample temperature and showing loss of the hysteresis above T_C. **(d)** A depiction of the applied magnetic field directions used in panels (a) and (b).

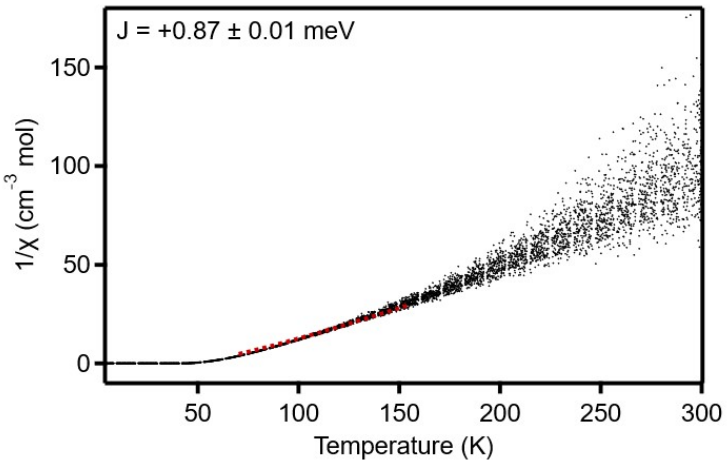

Figure B8. Best fit of the high-temperature susceptibility data (70 - 150 K) to eq 1^5 of section 3.2 ($H = -JS_i \bullet S_j$ with $S_i = S_j = 2$ for high-spin d^4 Cr^{2+}), yielding a pairwise magnetic exchange coupling constant of $J = +0.87 \pm 0.01$ meV ($+7.0 \pm 0.1$ cm^{-1}).

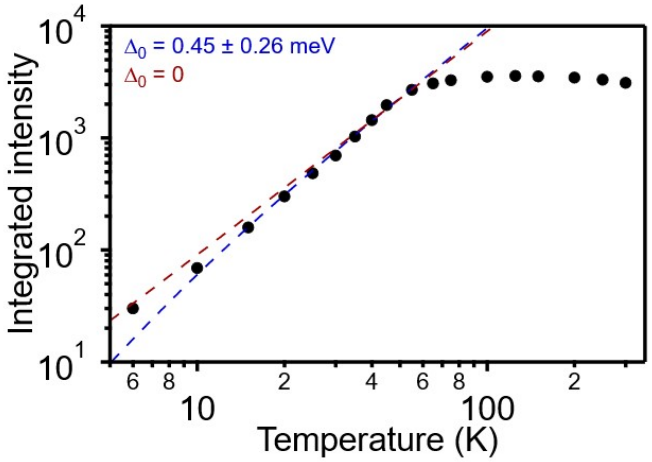

Figure B9. Fit of the integrated absorbance of the $^5B_{1g} \rightarrow {}^3B_{1g}(^3H)$ transition from Figure 3.6c to eq 2^{13} of section 3.2. The blue curve shows the best fit allowing a non-zero energy gap in the magnon density of states at the Brillouin zone center, yielding a value of $\Delta_0 = 0.45 \pm 0.26$ meV (3.6 ± 2.1 cm^{-1}). For reference, the red curve shows the best fit when Δ_0 is fixed at 0. Additional data at lower temperatures would be required to refine the estimate of Δ_0.

References:

1. Janke, E. H., M. T.; Day, P.; Walker, P. J Neutron diffraction study of the crystal and magnetic structure of Rb_2CrCl_4: a two-dimensional ionic ferromagnet. *J. Phys. C: Solid State Phys.* **1983,** *16*, 5959-5969.
2. Day, P. Correlation of Structures and Properties of Ferromagnetic Tetrahalogenochromate(II) Salts. *J. Magn. Magn. Mater.* **1986,** *54-57*, 1442-1446.
3. Hutchings, M. T. A.-N., J.; Lindgard, P. A.; Walker, P. J. Neutron scattering investigation of the temperature dependence of long-wavelength spin waves in ferromagnetic Rb_2CrCl_4. *J. Phys. C: Solid State Phys.* **1981,** *14*, 5227-5245.
4. Hutchings, M. T. G., A. K.; Day, P.; Leech, D. H. Neutron Diffraction Study of the Crystal and Magnetic Structure of the Ionic Ferromagnet Cs_2CrCl_4. *Solid State Commun.* **1974,** *15*, 313-316.
5. Bellitto, C. D., P. Magnetic Susceptibility and Optical Spectra of the Organic-intercalated Two-dimensional Ferromagnets Bis(monomethylammonium)- and Bis(monoethylammonium) Tetrachlorochromate (II). *J. C. S. Chem. Comm.* **1978**, 1207-1210.
6. Bellitto, C. W., T. E.; Day, P. Low-Temperature Optical and Magneto-Optical Study of the Organic-Intercalated Two-Dimensional Ferromagnet $(CH_3NH_3)_2CrCl_4$. *Inorg. Chem.* **1985,** *24*, 558-562.
7. Bellitto, C. F., M. J.; Wood, T. E.; Day, P. Optical absorption intensity and short-range spin correlation in the ionic ferromagnets A_2CrCl_4 (A = Rb, CH_3NH_3, $CH_3CH_2NH_3$). *J. Phys. C: Solid State Phys.* **1980,** *13*, L627-630.
8. Stead, M. J. D., P. Preparation, Characterization, and Magnetic Properties of Organic-intercalated Two-dimensional Ionic Ferromagnets $(C_nH_{2n+1}NH_3)_2CrCl_4$ (N = 3, 5, or 12). *J. Chem. Soc. Dalton Trans.* **1982**, 1081-1083.
9. Bellitto, C. D., P.; Wood, T. E. Magnetic Susceptibility and Optical Study of the Organic-intercalated Two-dimensional Ionic Ferromagnet Bis(benzylammonium) Tetrachlorochromate (II). *J. Chem. Soc. Dalton Trans.* **1986**, 847-861.
10. Ai, Y. S., R.; Liao, W.; Song, X.; Tang, Y.; Wang, B.; Wang, Z.; Gao, S.; Xiong, R Unprecedented Ferroelectricity and Ferromagnetism in a Cr^{2+}-Based Two-Dimensional Hybrid Perovskite. *Angew. Chem. Int. Ed.* **2022,** *61*, e202206034.
11. Barbar, M. A. L., M. F. C.; Larkworthy, L. F.; Newell, G. P.; Povey, D. C. Research Communication: 3-Azoniapentane-1,5-diammonium pentachlorochromate (II), $C_4H_{16}Cl_5CrN_3$. *J. Cryst. Mol. Struct.* **1978,** *8*, 43-47.
12. Barbar, M. A. L., M. F. C.; Larkworthy, L. F.; Newell, G. P.; Povey, D. C.; Proctor, K. J.; Summers, L. J. The Crystal Structures of Propane-1,3-diammonium Tetrachlorochromate(II), a Sheet Ferromagnet, and Bis(dimethylammonium) Tetrachlorochromate(II), an Antiferromagnetic Compound Containing Isolated $[Cr_3Cl_{12}]^{6-}$ Units. *J. C. S. Chem. Comm.* **1981**, 1046-1047.
13. Bramwell, S. T. D., P.; Hutchings, M. T.; Thorne, J. R. G.; Visser, D. Neutron Scattering and Optical Study of the Magnetic Properties of the Two-Dimensional Ionic Ferromagnets Rb_2CrCl_3Br and $Rb_2CrCl_2Br_2$. *Inorg. Chem.* **1986,** *25*, 417-421.

Appendix C: Supplementary Information for Chapter 3.3

Anion Exchange and Lateral Heterostructure Formation in Ferromagnetic $PEA_2Cr(Cl,Br)_4$ Two-Dimensional Perovskites

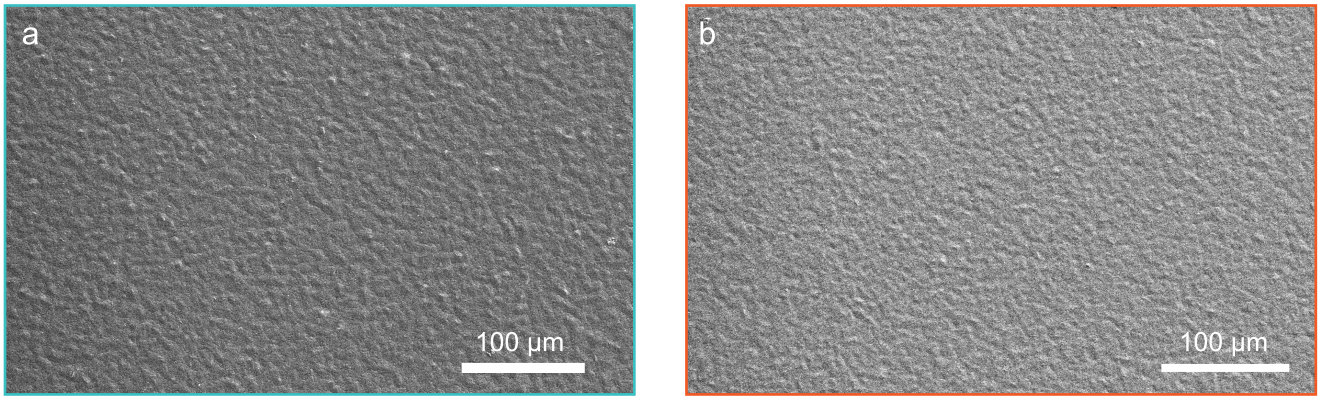

Figure C1. Low-magnification SEM images of the same (a) PEA_2CrCl_4 and (b) anion-exchanged PEA_2CrBr_4 polycrystalline films shown in Chapter 4.3.

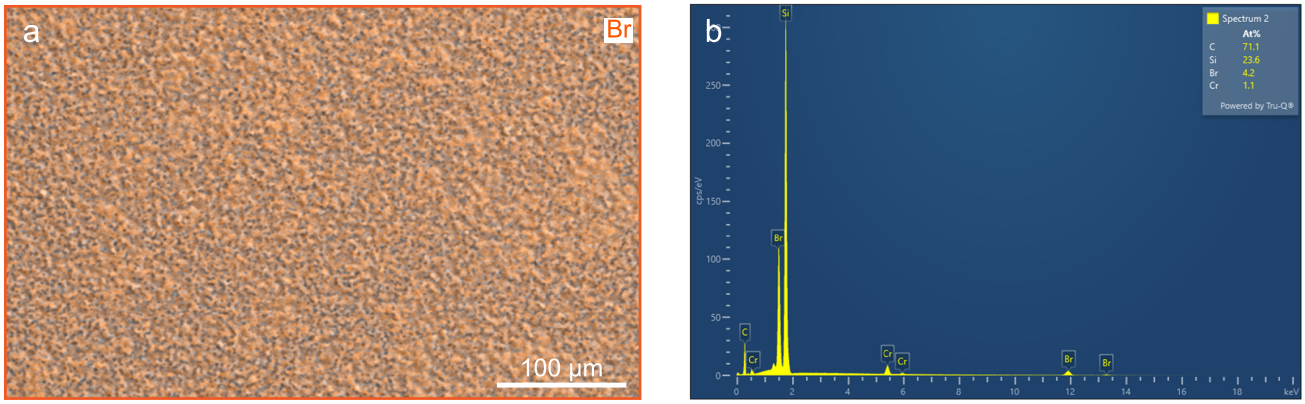

Figure C2. (a) Layered SEM-EDS image collected of the same PEA_2CrBr_4 film shown in the main text, overlaying the bromide signal in orange showing homogeneous bromide distribution. (b) SEM-EDS spectrum of the film shown in (a), demonstrating complete bromide conversion and no residual chloride signal.

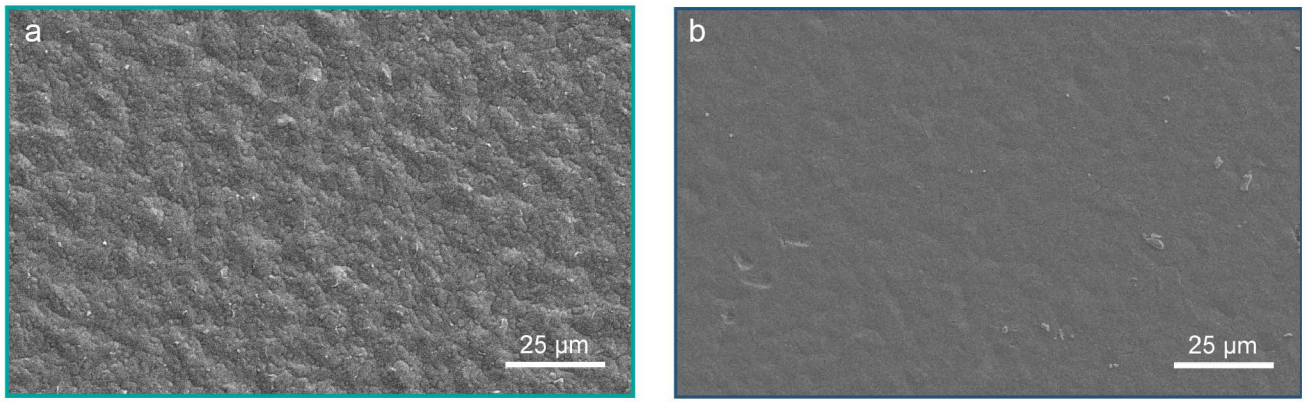

Figure C3. SEM images of (a) an as-synthesized PEA_2CrCl_4 polycrystalline film and (b) a PEA_2CrCl_4 polycrystalline film after heating at 175 °C for 1 hour in the presence of TMS-Cl.

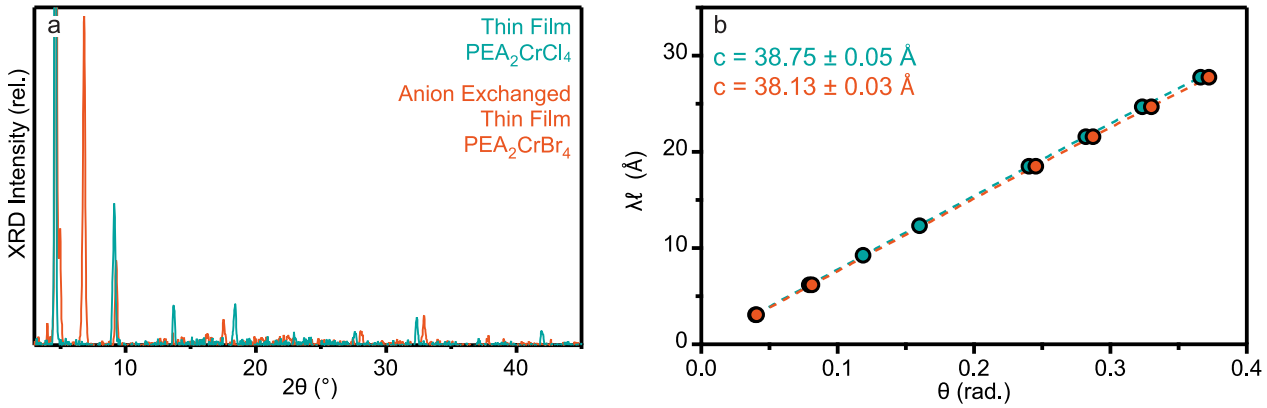

Figure C4. (a) Zoomed-in pXRD plot of the as-synthesized PEA_2CrCl_4 and anion-exchanged PEA_2CrBr_4 thin films, replotted from Figure 1c in the main text. (b) Scatter plot showing the fit (dashed lines) for extracting the crystallographic *c*-axis unit cell parameters of the PEA_2CrCl_4 (teal) and anion-exchanged PEA_2CrBr_4 (orange) polycrystalline films shown in Chapter 4.3. The (0, 0, l) peaks were identified in the powder X-ray diffraction patterns, and their respective Miller indices were multiplied by the X-ray wavelength (Cu, 1.5406 Å). Plotting the resultant values against the peak position allows extraction of the *c*-axis unit cell parameter based on Bragg's law for an orthorhombic space group.[1]

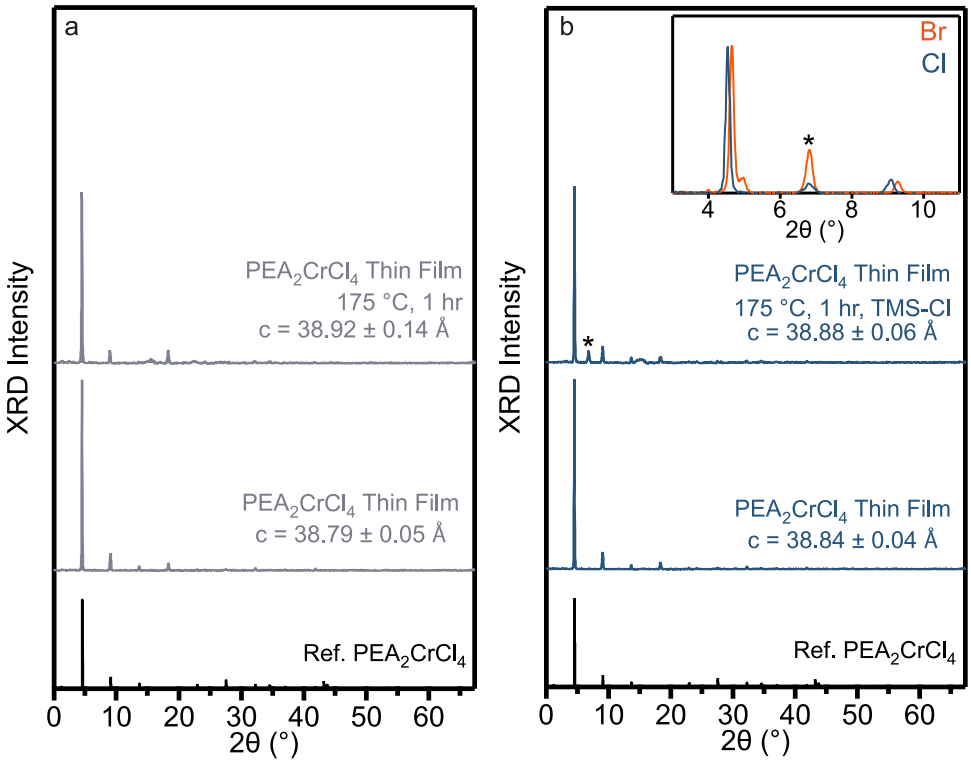

Figure C5. (a) pXRD data of an as-synthesized PEA_2CrCl_4 polycrystalline film, and the same film after 1 hour of heating at 175 °C. (b) pXRD data of an as-synthesized PEA_2CrCl_4 polycrystalline film, and the same film after 1 hour of heating at 175 °C in the presence of TMS-Cl. The same film is also shown in Figure D3b. The inset compares the chloride film after heating in the presence of TMS-Cl to the anion-exchanged bromide film shown in Chapter 4.3. The asterisk indicates an additional peak that is possibly related to decomposition of excess PEA-Cl present in the film. The *c*-axis unit cell parameters extracted for each film are listed.

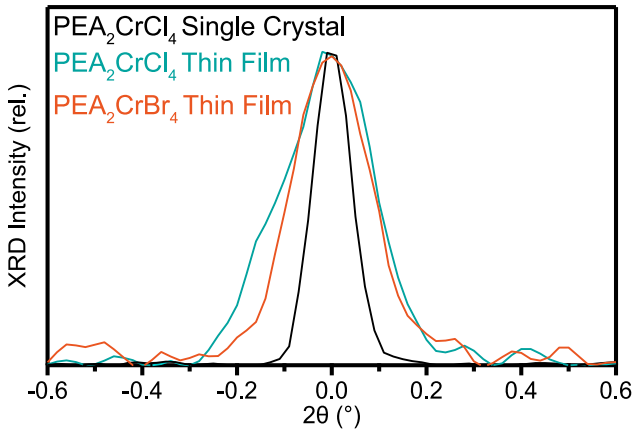

Figure C6. Comparison of the (0, 0, 4) X-ray diffraction peaks of the oriented PEA_2CrCl_4 single crystal (black), PEA_2CrCl_4 polycrystalline film (teal), and anion-exchanged PEA_2CrBr_4 polycrystalline film (orange) shown in Chapter 4.3. The peaks are offset to be centered around 0° to illustrate the wider diffraction peaks present in the films, related to smaller crystallite sizes. The vertical crystallite size of the films as calculated by Scherrer analysis is ~40 nm.

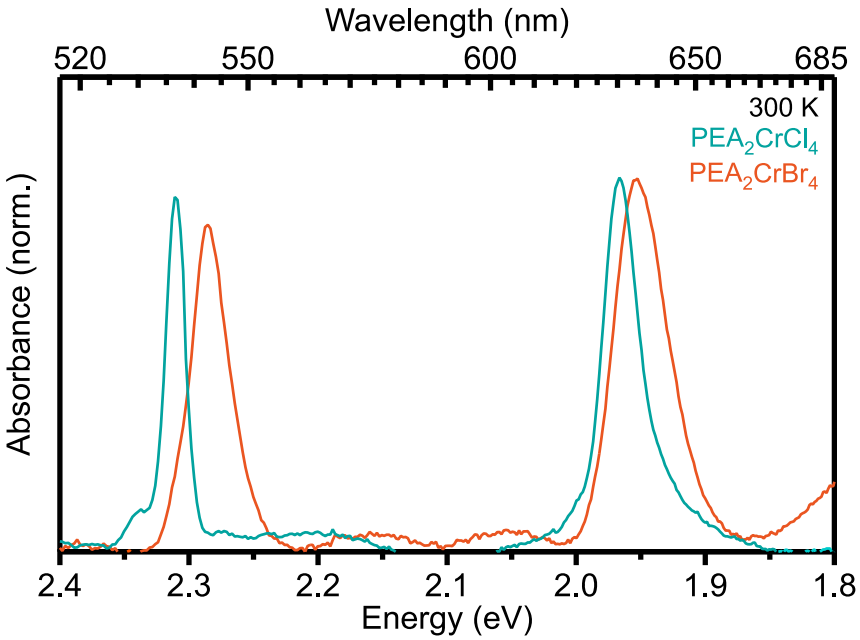

Figure C7. Room-temperature absorption spectra of PEA_2CrCl_4 (teal) and PEA_2CrBr_4 (orange) polycrystalline films zoomed in and replotted from Chapter 4.3.

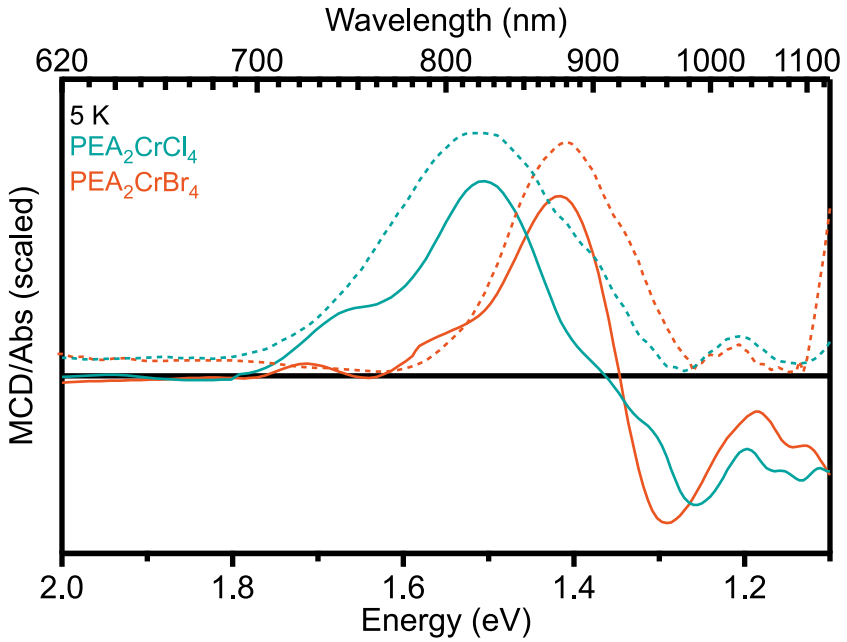

Figure C8. 5 K MCD spectra (solid traces) and 5 K absorption spectra (dashed traces) of PEA_2CrCl_4 (teal) and PEA_2CrBr_4 (orange) polycrystalline films shown in Chapter 4.3.

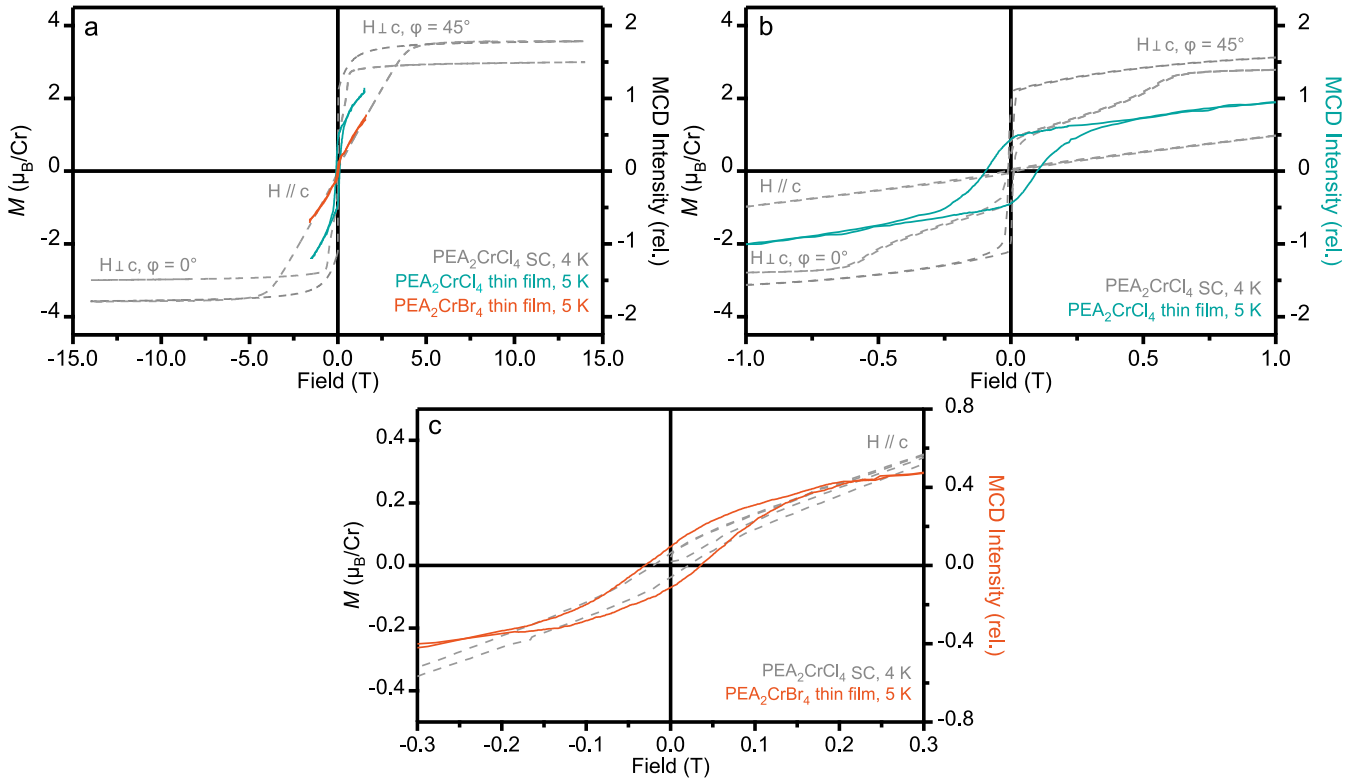

Figure C9. Previously reported[2] VSM data of a bulk PEA_2CrCl_4 single crystal collected along different crystallographic orientations with respect to the Cr^{2+} molecular axes (gray dashed traces) and MCD hystereses of the PEA_2CrCl_4 polycrystalline film (teal solid traces) and anion-exchanged PEA_2CrBr_4 polycrystalline film shown in Chapter 4.3. The hysteresis of the chloride film is characterized by a coercive field of ~195 mT and that of the bromide is ~67 mT.

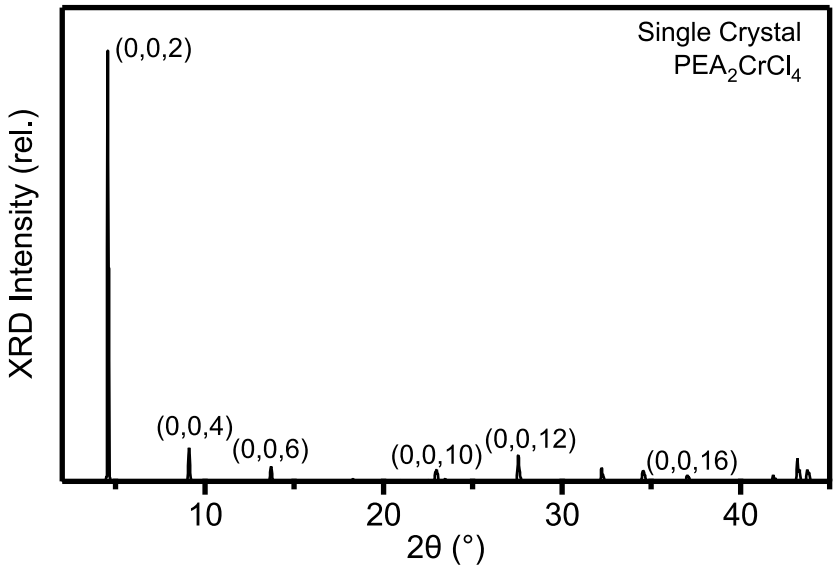

Figure C10. X-ray diffraction pattern of an oriented single crystal of PEA_2CrCl_4 collected on a powder diffractometer. The (0, 0, l) peaks were identified based on the reported single-crystal structure[2] (CCDC 2245076).

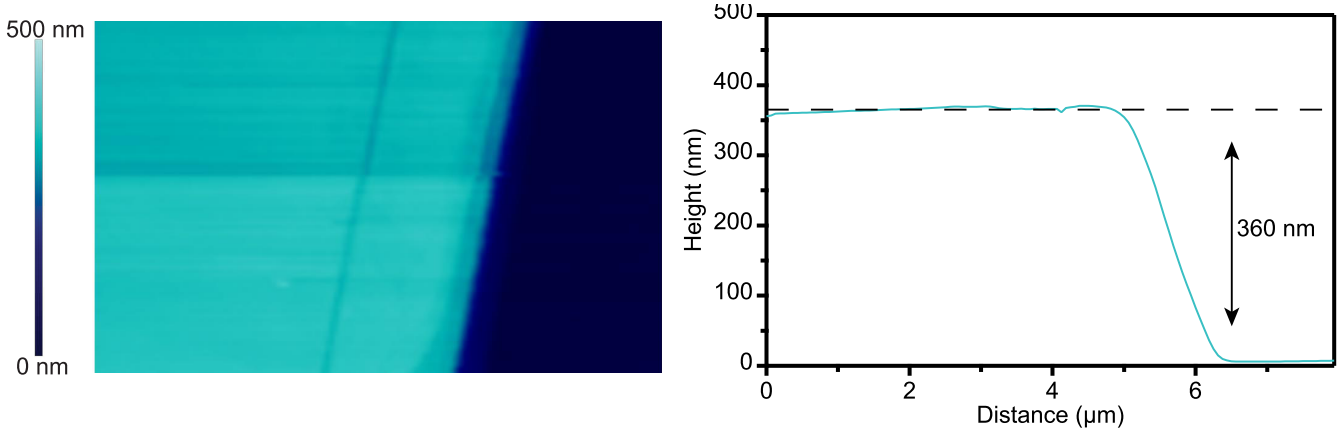

Figure C11. AFM height profile analysis of a representative exfoliated flake of single-crystalline PEA_2CrCl_4.

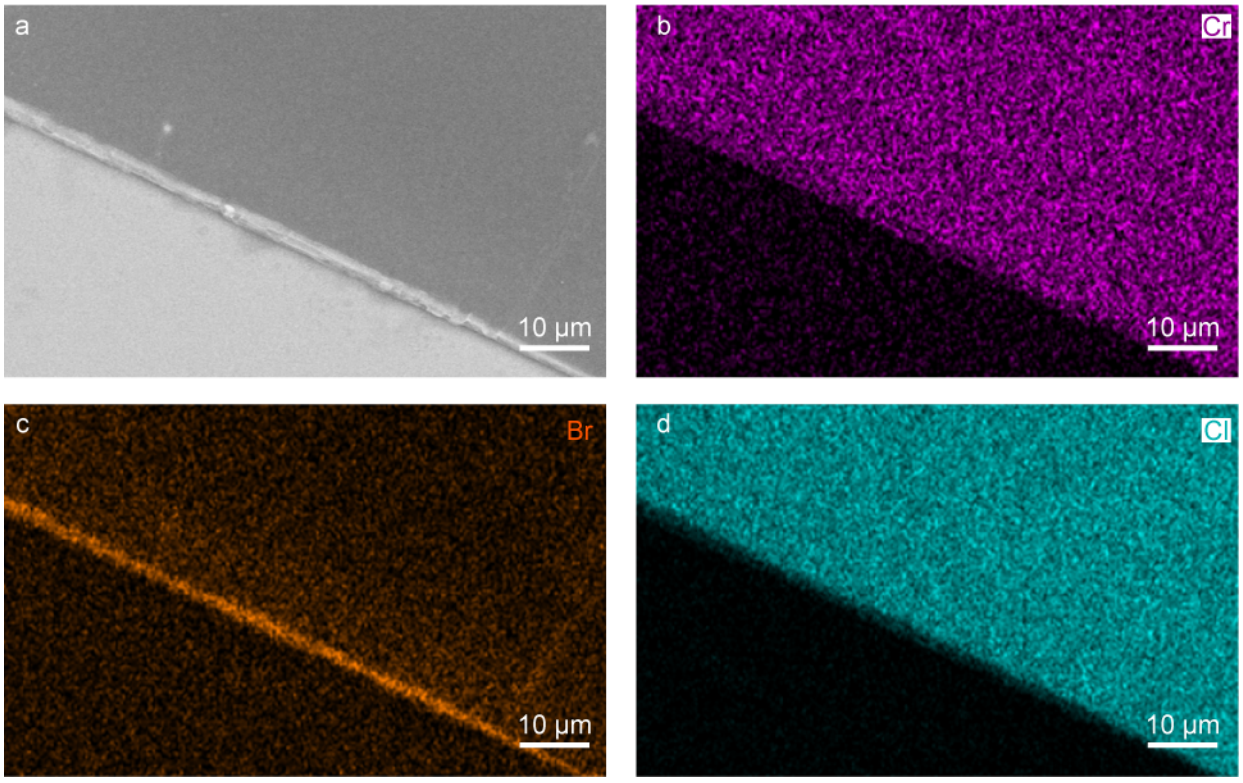

Figure C12. (a) SEM image collected after reacting an exfoliated single-crystalline flake of PEA_2CrCl_4 with TMS-Br at 175 °C for 30 minutes. The difference in contrast along the edge of the crystal is correlated to the difference in composition between the bromide and chloride regions. SEM-EDS images of the same crystal shown in (a) plotting the (b) chromium, (c) bromide, and (d) chloride signals.

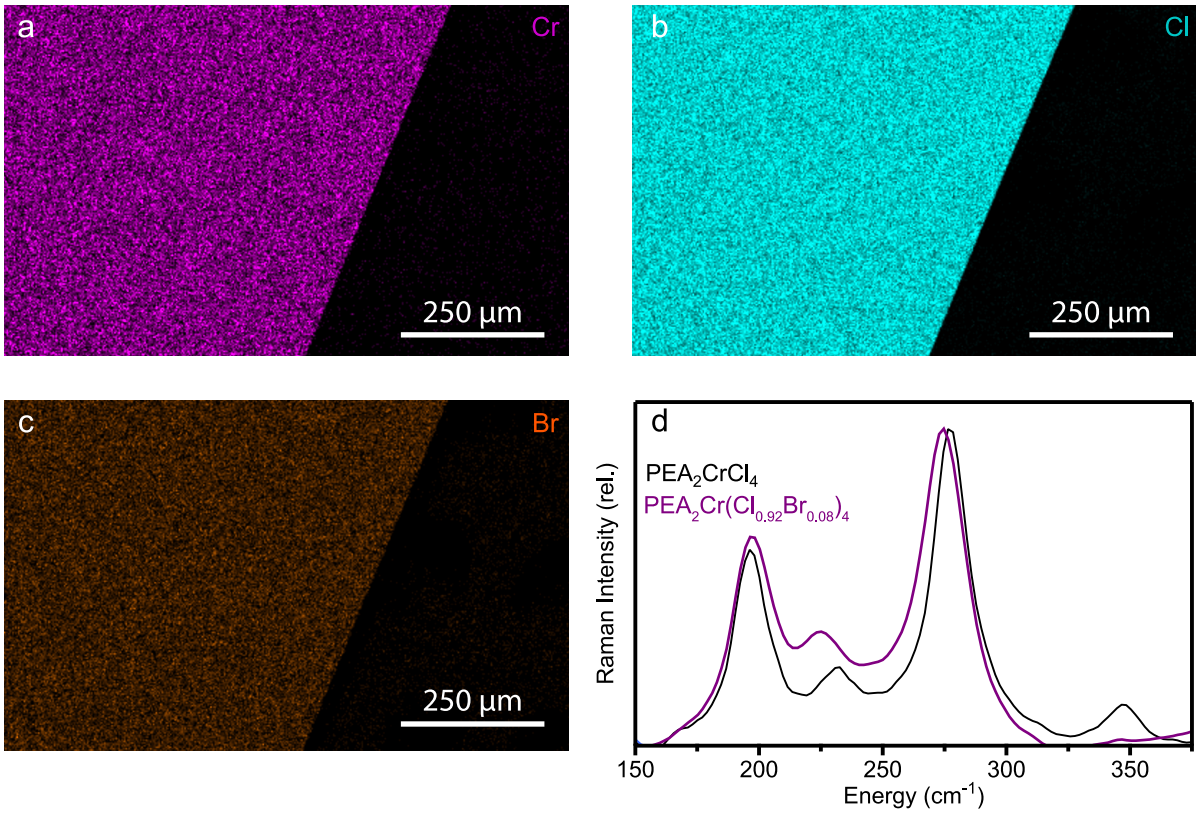

Figure C13. SEM-EDS images of directly synthesized $PEA_2Cr(Cl_{0.92}Br_{0.08})_4$ plotting the (a) chromium, (b) chloride, and (c) bromide signals. (d) Raman spectra of PEA_2CrCl_4 (black) and $PEA_2Cr(Cl_{0.92}Br_{0.08})_4$ (purple).

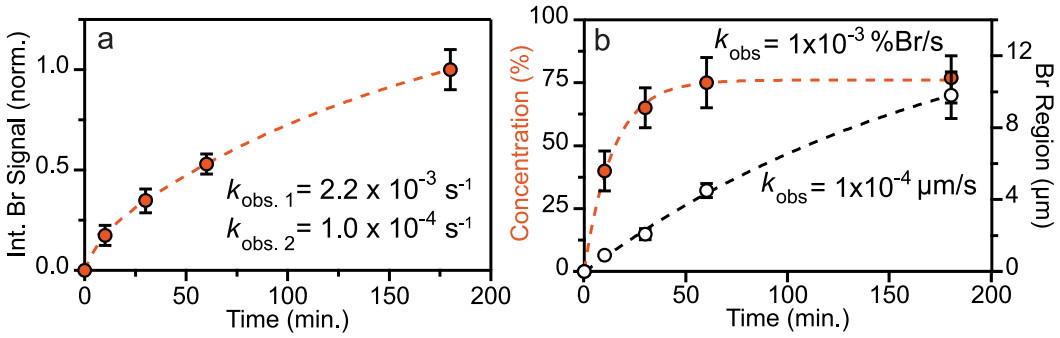

Figure C14. (a) Plot of the total integrated bromide signal extracted from SEM-EDS line scans collected after reacting exfoliated flakes of PEA_2CrCl_4 with TMS-Br at 175 °C for 10, 30, 60, and 180 min replotted from Chapter 4.3. The data were fit using a double-exponential function (dashed line) to yield the two rate constants shown. (b) Plot of the fractional bromide content (*i.e.*, %Br = 100%*[Br]/([Cl] + [Br])) in the bromide-rich region (orange circles, left axis) and the width of the bromide-rich region (white circles, right axis) as a function of reaction time. These data were fit using phenomenological single-exponential functions to get the rate constants shown. Although the differing units do not allow direct comparison of the extracted rate constants, these results agree well with the independent results obtained in panel (a).

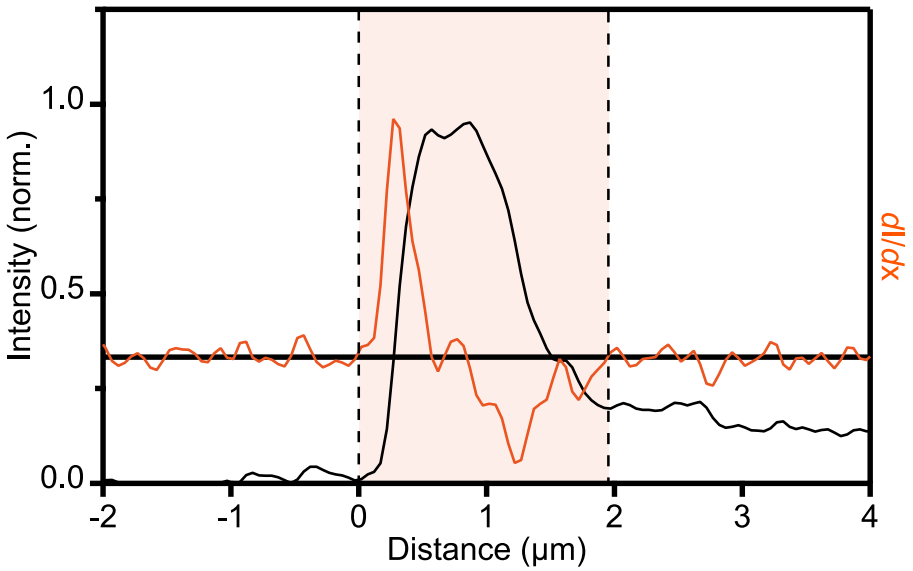

Figure C15. Representative example of determining the width of the bromide-rich region in partially exchanged exfoliated crystalline flakes of PEA_2CrCl_4 based on SEM-EDS line scans. The black trace plots the line-scan data. The orange trace plots the derivative of the line scan. The bromide region width is defined as the distance between the zero points in the derivative curve, between the edge of the crystal and where the bromide signal reaches a plateau.

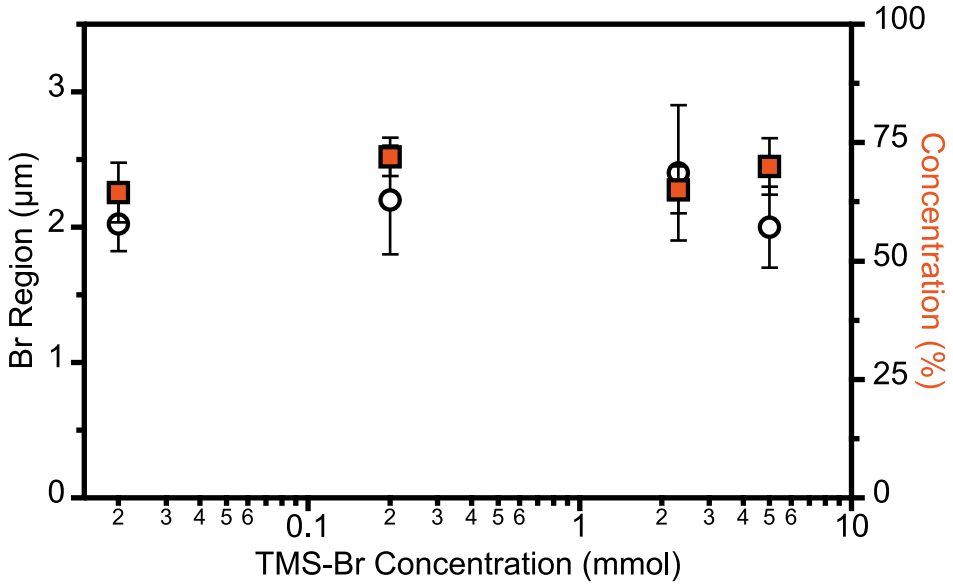

Figure C16. Scatter plot of the bromide region width after reacting an exfoliated crystalline flake of PEA_2CrCl_4 for 30 min at 175 °C with varying TMS-Br concentrations (white circles, left axis) and the fractional bromide concentration within the bromide-exchange region (orange squares, right axis).

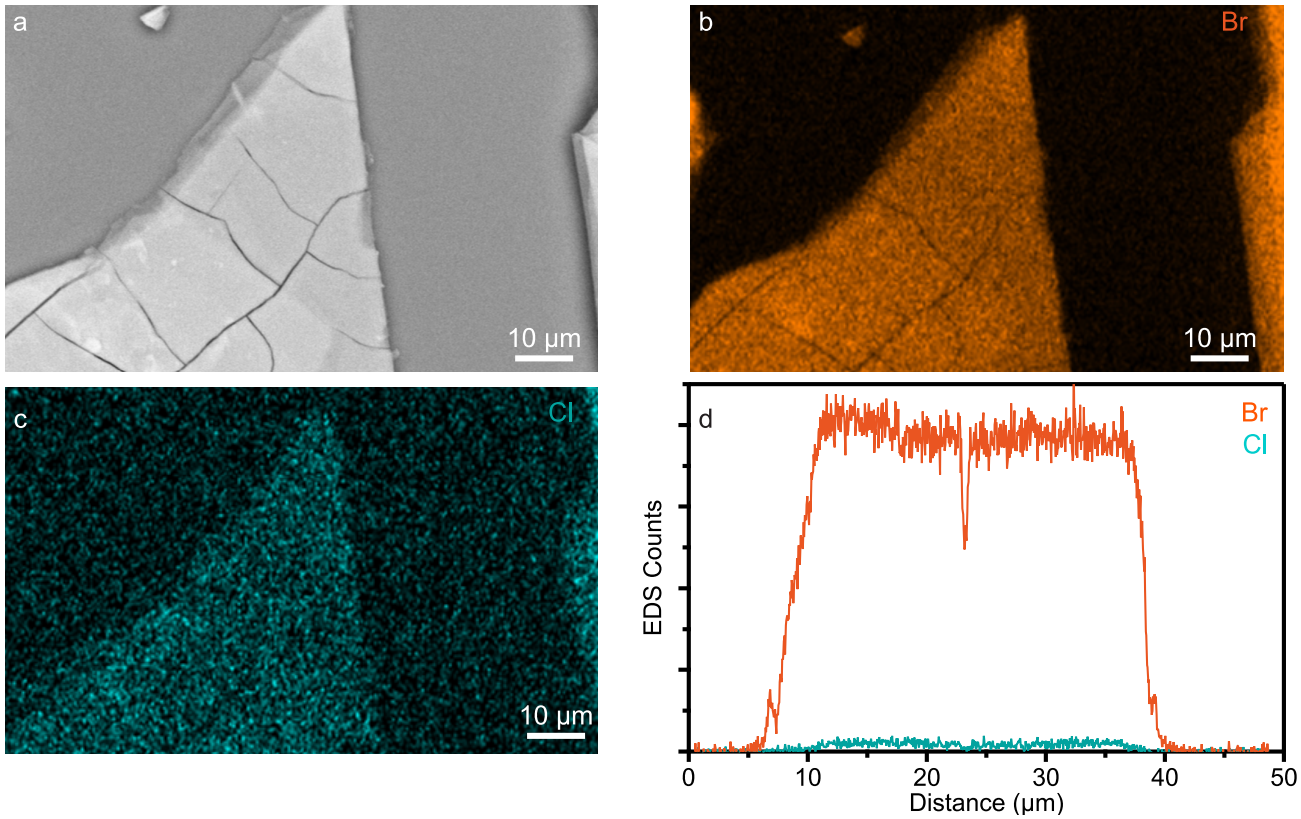

Figure C17. (a) SEM image collected after reacting an exfoliated flake of PEA_2CrCl_4 with TMS-Br at 175 °C for 18 hours. SEM-EDS images of the same crystal shown in (a), plotting the (b) bromide and (c) chloride signals. (d) SEM-EDS line scans taken across the width of the flake showing that the bromide region propagated all the way to the edge of the flake. The dip around 25 μm corresponds with a crack in the flake. Averaging across several flakes, the bromide concentration after 18 hours was 93 ± 4 %.

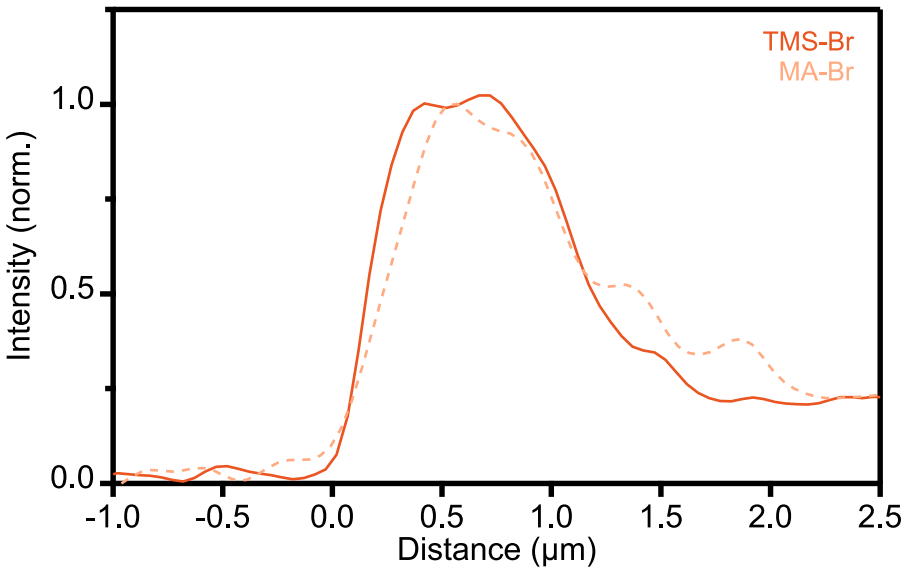

Figure C18. SEM-EDS line scans plotting the bromide signal after reacting PEA_2CrCl_4 with TMS-Br for 30 min at 175 °C (solid line) as compared to reacting with MA-Br for 30 min at 175 °C (dashed line). Averaging over several flakes, the width of the bromide-rich region after reacting with TMS-Br was 2.1 ± 0.3 μm while that of the MA-Br reaction was 1.9 ± 0.2 μm.

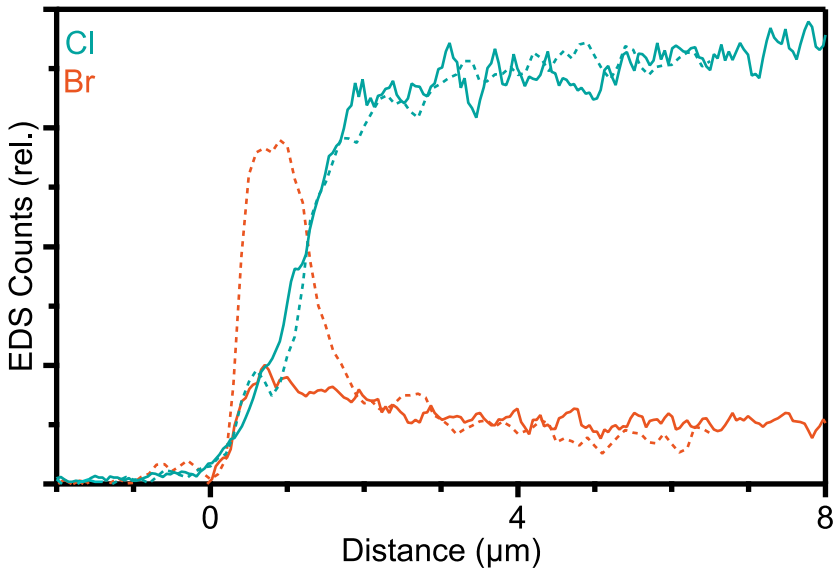

Figure C19. (Dashed lines) SEM-EDS line scans plotting the bromide (orange) and chloride (teal) signals after reacting an exfoliated flake of PEA_2CrCl_4 with TMS-Br at 175 °C for 30 min. Traces were scaled relative to the total halide signal. (Solid lines) SEM-EDS line scans plotting the bromide (orange) and chloride (teal) signals after reacting a separate exfoliated flake of PEA_2CrCl_4 with TMS-Br at 175 °C for 30 min, followed by removal of TMS-Br and heating for an additional hour. Traces were scaled relative to the total halide signal.

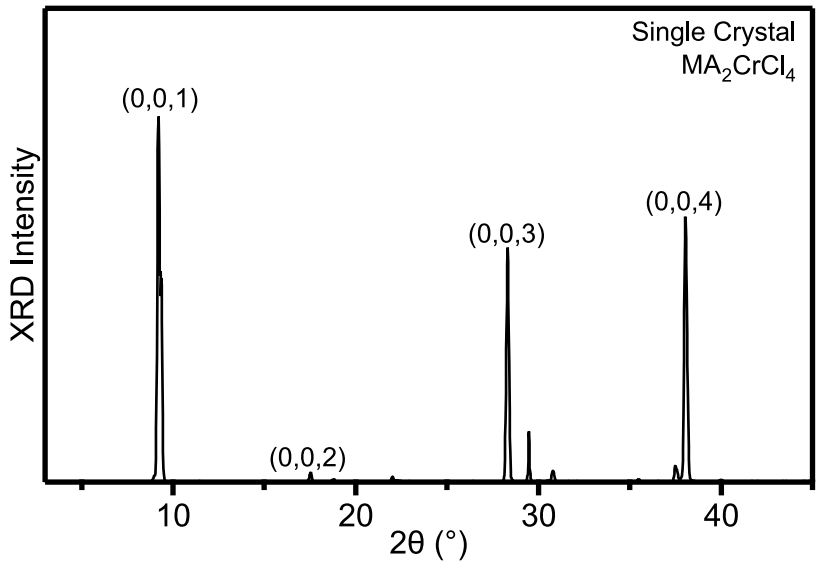

Figure C20. X-ray diffraction pattern of an oriented single crystal of MA_2CrCl_4 collected on a powder diffractometer. (0, 0, l) peaks were identified based on previous literature reports.[3, 4]

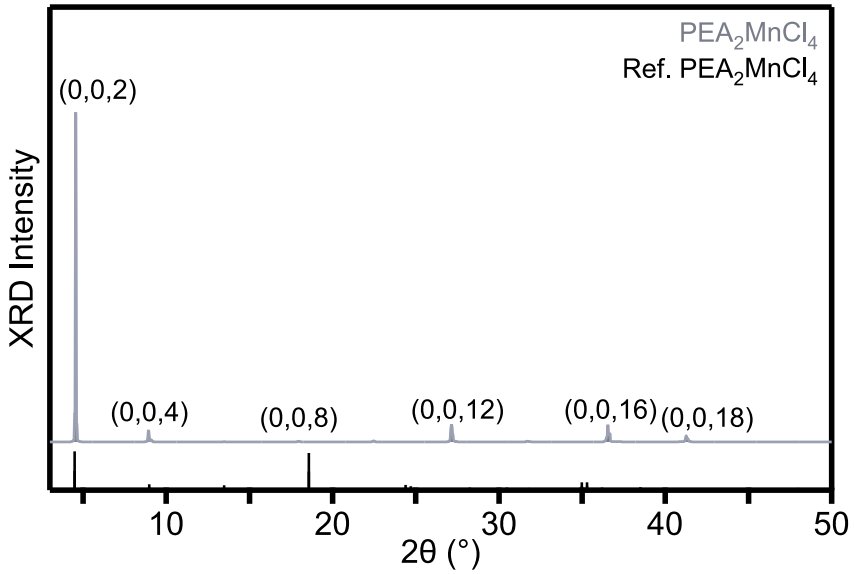

Figure C21. X-ray diffraction pattern of an oriented single crystal of PEA_2MnCl_4 collected on a powder diffractometer. The reference pattern was generated based on the reported single crystal structure[5] (CCDC 258590).

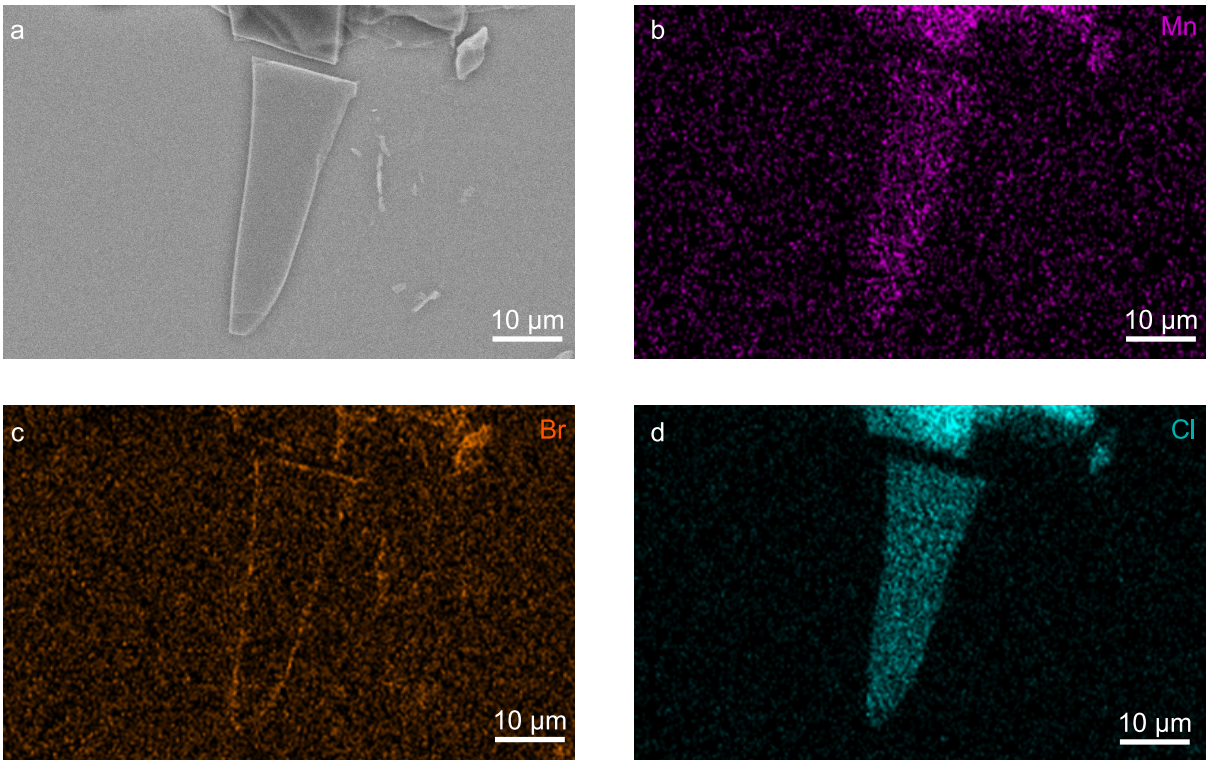

Figure C22. (a) SEM image collected after reacting an exfoliated crystalline flake of PEA_2MnCl_4 with TMS-Br at 100 °C for 30 min. SEM-EDS images of the same crystal shown in (a), plotting the (b) manganese, (c) bromide, and (d) chloride signals.

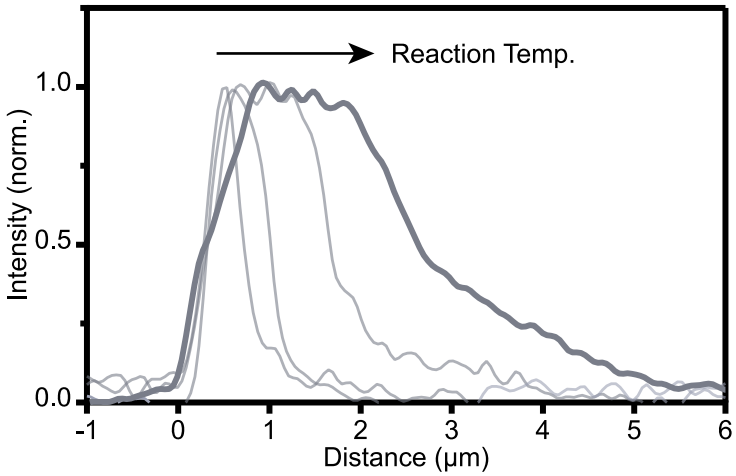

Figure C23. Representative SEM-EDS line scans plotting the bromide signal after reacting an exfoliated crystalline flake of PEA_2MnCl_4 with TMS-Br for 30 min at 100, 125, 150, and 175 °C.

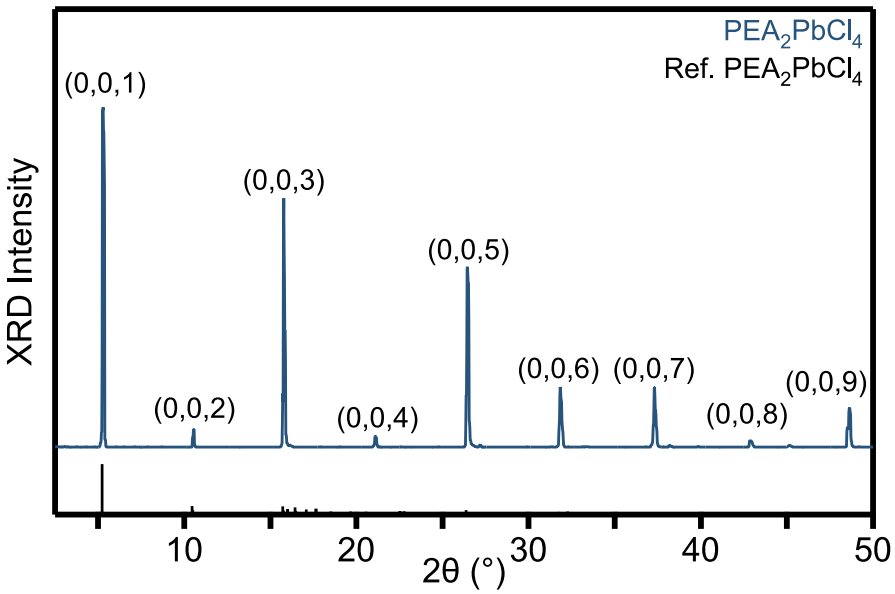

Figure C24. X-ray diffraction pattern of microcrystals of PEA_2PbCl_4 collected on a powder diffractometer. The reference pattern was generated based on the reported single crystal structure[6] (CCDC 1209430).

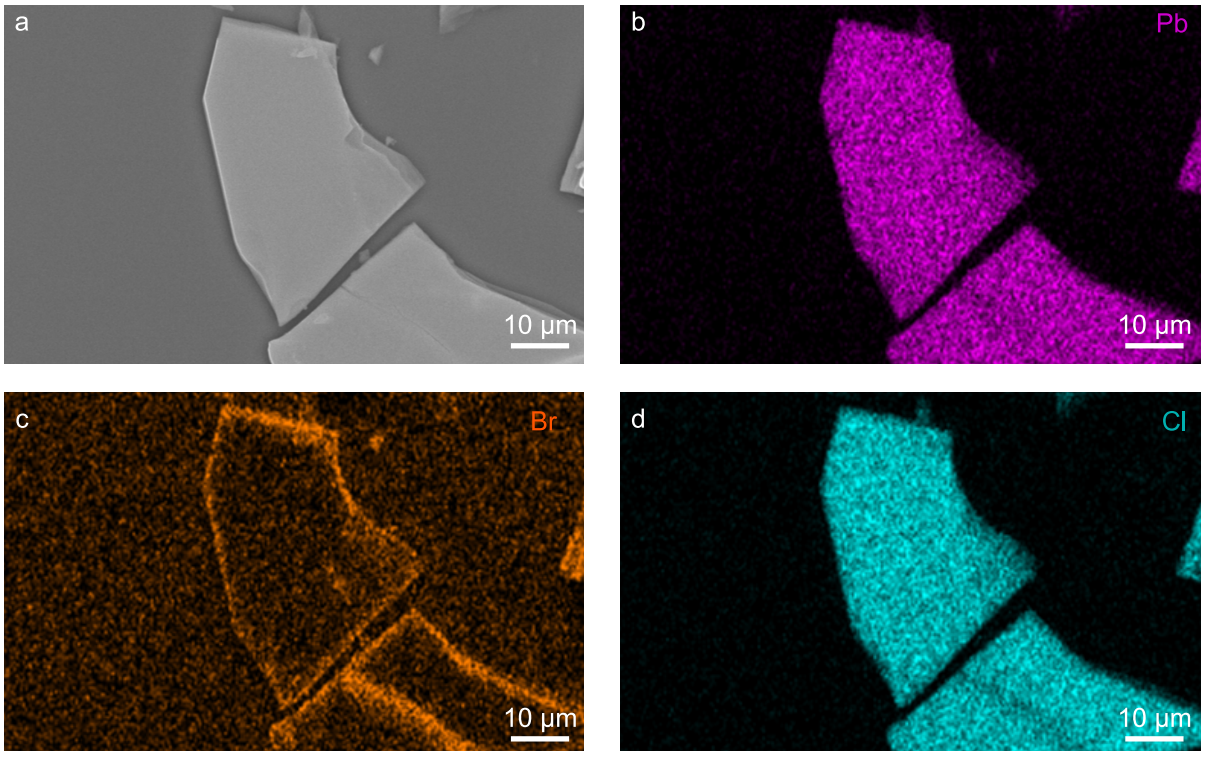

Figure C25. (a) SEM image collected after reacting an exfoliated crystalline flake of PEA_2PbCl_4 with TMS-Br at 125 °C for 30 min. SEM-EDS images of the same crystal shown in (a), plotting the (b) lead, (c) bromide, and (d) chloride signals.

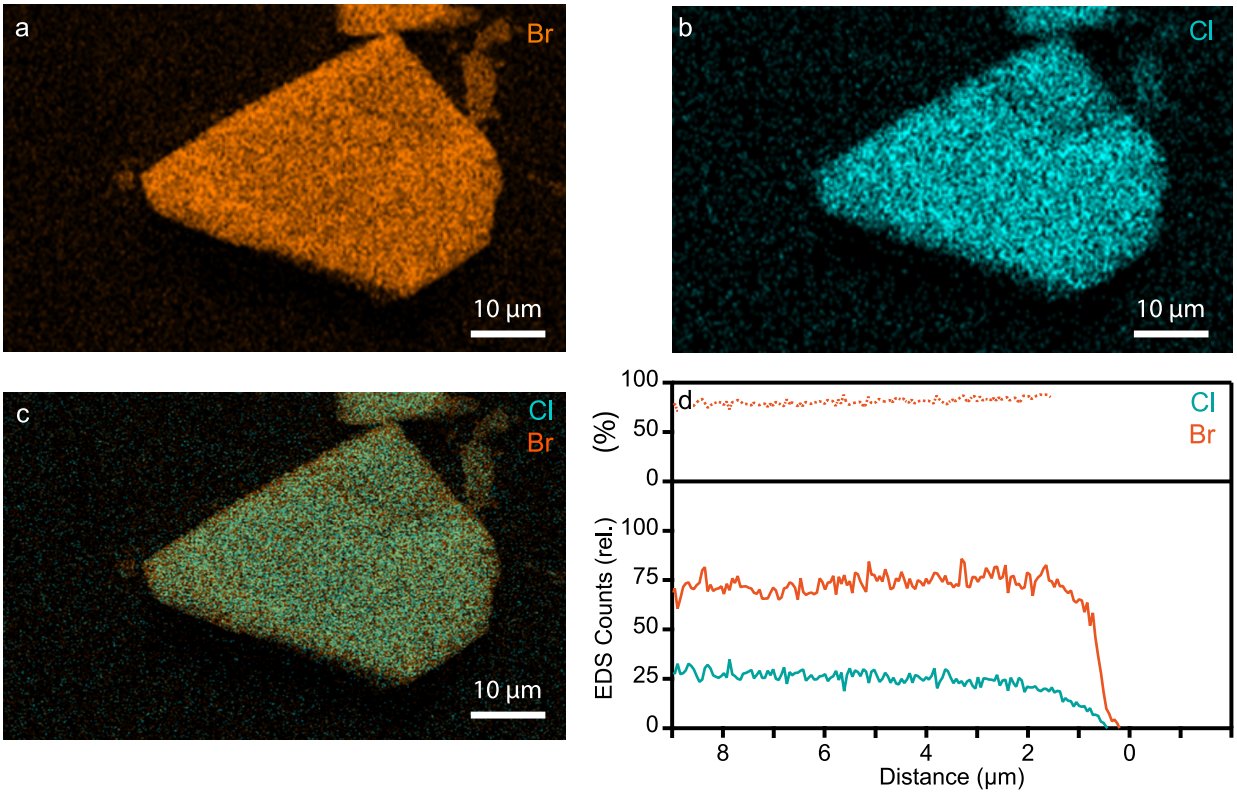

Figure C26. Representative SEM-EDS images collected after reacting an exfoliated crystalline flake of PEA_2PbCl_4 with TMS-Br for 30 min at 175 °C plotting the (a) bromide, (b) chloride, and (c) layered chloride plus bromide signals. (d) SEM-EDS line scans taken across the width of the flake shown in (a-c), indicating the bromide has diffused across the entire width of the flake. The solid traces show the bromide and chloride signals scaled relative to the total halide signal, while the dashed trace is the fractional bromide concentration (%Br = 100%*[Br]/([Cl] + [Br])).

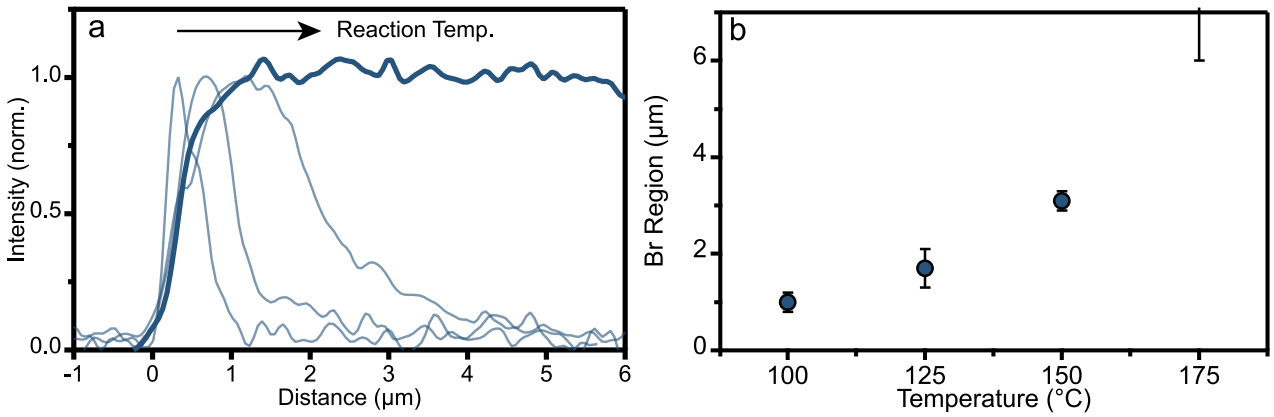

Figure C27. (a) Representative SEM-EDS line scans plotting the bromide signal after reacting an exfoliated crystalline flake of PEA_2PbCl_4 with TMS-Br for 30 min at 100, 125, 150, and 175 °C. (b) Scatter plot of the width of the bromide-rich region as a function of reaction temperature. The 175 °C data point represents the lower limit of the bromide-rich region given that the bromide diffused across the entire width of the flake.

Table C1. The experimental diffusion coefficients (*D*) plotted in Figure 6d with units of $\mu m^2/s$, determined from reactions of exfoliated flakes with excess TMS-Br for 30 min at each temperature.

T (K)	PEA_2CrCl_4	PEA_2PbCl_4	PEA_2MnCl_4
373	$2.57x10^{-4}$	$5.56x10^{-4}$	$3.47x10^{-4}$
398	$5.67x10^{-4}$	$1.61x10^{-3}$	$1.42x10^{-3}$
423	$1.25x10^{-3}$	$4.67x10^{-3}$	$3.47x10^{-3}$
448	$2.40x10^{-3}$	N/a (> $5.56x10^{-2}$)	$9.71x10^{-3}$

References:

1. Jesche, A.; Fix, M.; Kreyssig, A.; Meier, W. R.; Canfield, P. C. X-Ray Diffraction on Large Single Crystals Using a Powder Diffractometer. *Philos. Mag.* **2016,** *96*, 2115-2124.
2. Smith, R. T.; Walsh, K. M.; Jiang, Q.; Chu, J.-H.; Gamelin, D. R. An Air-Stable and Exfoliable Ferromagnetic Two-Dimensional Perovskite, $(Phenethylammonium)_2CrCl_4$. *Chem. Mater.* **2024,** *36*, 1571-1578.
3. Bellitto, C.; Day, P. Magnetic Susceptibility and Optical Spectra of the Organic-Intercalated Two-Dimensional Ferromagnets Bis(monomethylammonium)- and Bis(monoethylammonium) tetrachlorochromate(II). *J. Chem. Soc., Dalton Trans.* **1978**, 1207-1212.
4. Bellitto, C.; Wood, T. E.; Day, P. Low-Temperature Optical and Magneto-Optical Study of the Organic-Intercalated Two-Dimensional Ferromagnet Methylammonium Tetrachlorochromate(II). *lnorg. Chem.* **1985,** *24*, 558-562.
5. Park, S.-H.; Oh, I.-H.; Park, S.; Park, Y.; Kim, J. H.; Huh, Y.-D. Canted Antiferromagnetism and Spin Reorientation Transition in Layered Inorganic–Organic Perovskite $(C_6H_5CH_2CH_2NH_3)_2MnCl_4$. *Dalton Trans.* **2012,** *41*, 1237-1242.
6. Mitzi, D. B. A Layered Solution Crystal Growth Technique and the Crystal Structure of $(C_6H_5C_2H_4NH_3)_2PbCl_4$. *J. Solid State Chem.* **1999,** *145*, 694-704.

Appendix D: Supplementary Information for Chapter 4.2

Magnetic Amplification at Yb^{3+} "Designer Defects" in the van der Waals Ferromagnet CrI_3

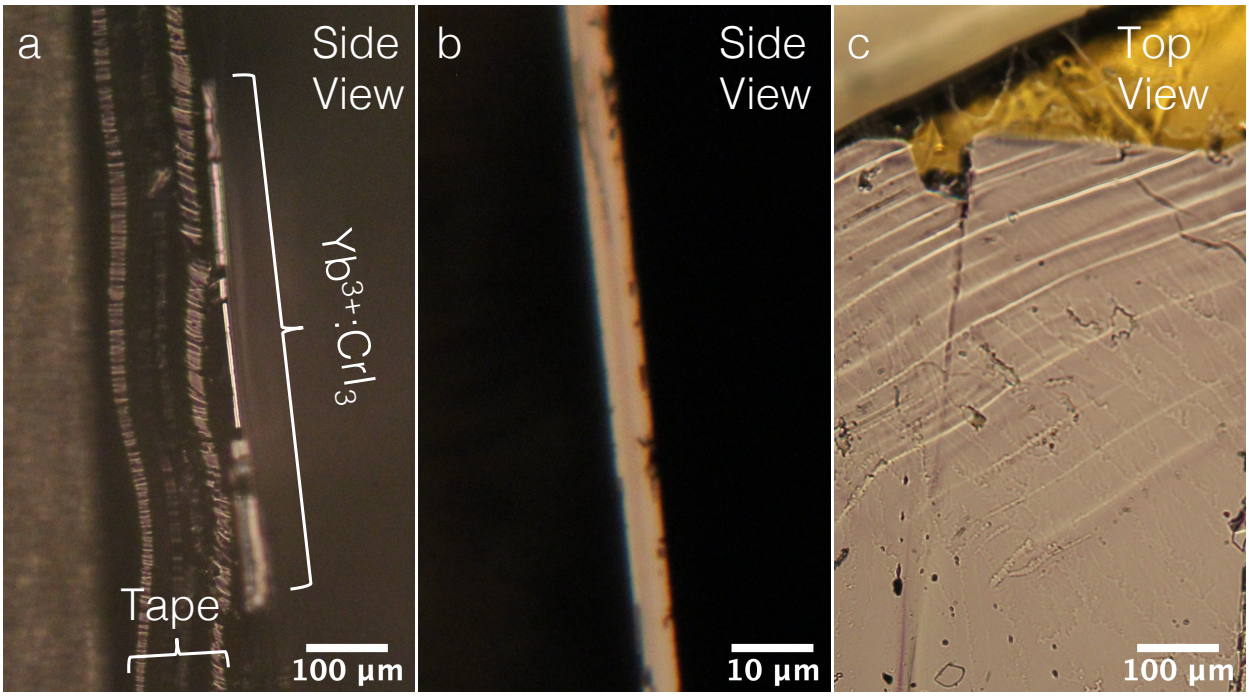

Figure D1. Images of an individual Yb^{3+}:CrI_3 single-crystal flake under an optical microscope at various magnification levels, viewing the flake's **(a,b)** edge, and **(c)** face. The flake thickness is estimated to be 5.1 ± 0.3 µm.

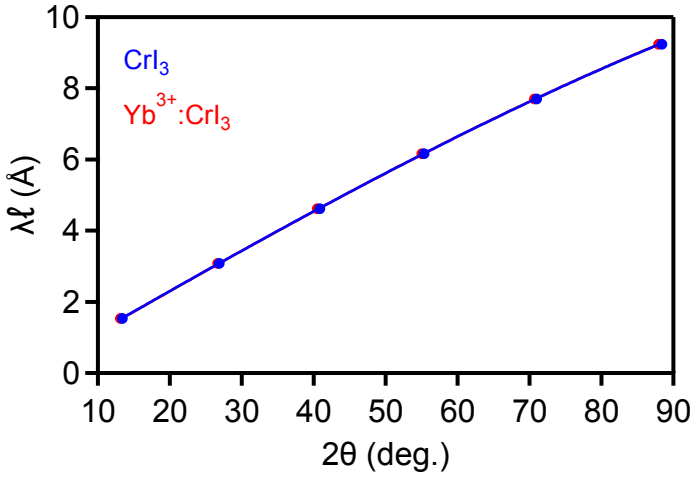

Figure D2. Analysis of XRD reflections collected using a powder diffractometer for 4.9% Yb^{3+}-doped and undoped CrI_3 single-crystal flakes (same data as shown in Figure 4.1bc). Using the

method described by Jesche,[1] the lattice parameter *c* for oriented single crystals with a monoclinic space group can be extracted from XRD data from a powder diffractometer using the following equation:

$$2c \cdot \sin\beta \cdot \sin\left(\theta - S\frac{\cos\theta}{2}\right) = \lambda\ell$$

Here, β is the obtuse angle in the monoclinic unit cell (108.507° for CrI_3), λ is the x-ray wavelength (Cu, 1.5406 Å), ℓ is the Miller index of each reflection in the XRD pattern and $S\frac{\cos\theta}{2}$ is a correction factor related to the displacement of the X-ray focal plane relative to the sample surface. Plotting 2θ values of the peak maxima *vs* $\lambda\ell$, the data can be fit using the equation above. For fitting, β and θ were taken in radians. By this method, the *c* lattice parameters were found to be 6.996 ± 0.002 and 7.013 ± 0.002 Å for the undoped and doped samples, respectively. From the lattice parameter *c*, the position of the (00ℓ) powder diffractometer XRD peaks for a monoclinic single crystal can be calculated using the following equation:

$$2\theta = 2\sin^{-1}\left(\frac{\lambda}{2\sin\beta}\frac{\ell}{c}\right)$$

The zero-shift in 2θ was determined by adding an offset to the experimental 2θ values and adjusting the offset to minimize the difference between experimental and calculated peak positions across all peaks in the XRD pattern. This offset accounts for the measurement discrepancy due to the thickness of the single crystals displacing the x-ray focal plane. For CrI_3, a zero-shift of -0.015° was found, contrasted to a zero-shift of +0.164° for Yb^{3+}-doped CrI_3. The displacement-corrected XRD patterns are shown in Figure 4.1c in section 4.2.

Table D1. Single-crystal X-ray diffraction data for 2.5% Yb^{3+}:CrI_3 measured at 263 K, compared to literature data for CrI_3.

	Yb^{3+}:CrI_3	**CrI_3 (250 K, ref. [2])**
Space group	*C2/m*	*C2/m*
a	6.86 Å	6.87 Å
b	11.89 Å	11.89 Å
c	6.99 Å	6.98 Å
α	90.0°	90.0°
β	108.7°	108.5°
γ	90.0°	90.0°
$[(Yb/Cr) – Cr]_{avg}$	3.96 Å	3.96 Å
$[(Yb/Cr) – I]_{avg}$	2.72 Å	2.72 Å
$[(Yb/Cr) – I – (Yb/Cr)]_{avg}$	93.3°	93.6°
$[I – (Yb/Cr) – I]_{avg}$	86.8°	86.9°

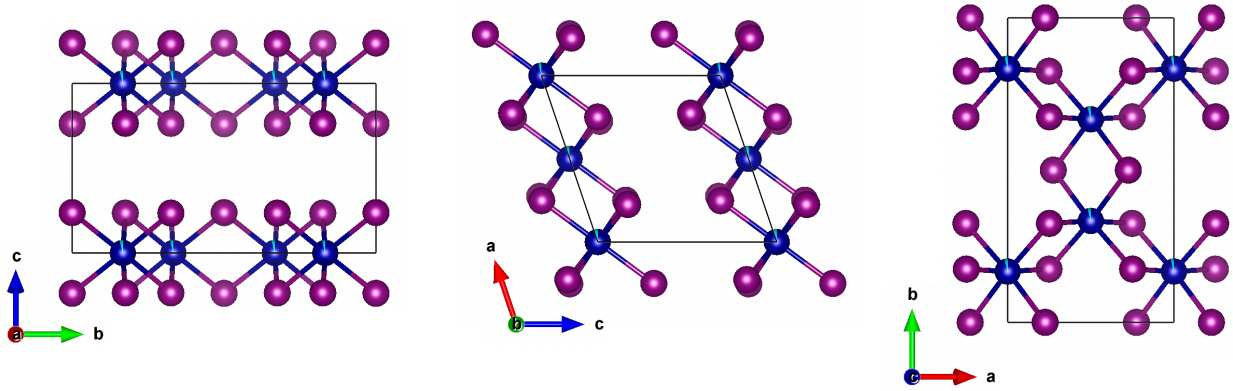

Figure D3. Visualization of the experimental room-temperature single-crystal XRD structure as viewed along the *a*, *b*, and *c* principal axes (left to right). Yb^{3+} (cyan) is found to substitute for Cr^{3+} (blue) in the edge-sharing octahedra formed by I^- (purple) anions. No excess electron density is observed between layers. Intralayer disorder is observed. The structure refines to the expected high-temperature *C2/m* monoclinic symmetry. Some intralayer disorder was observed (not shown).

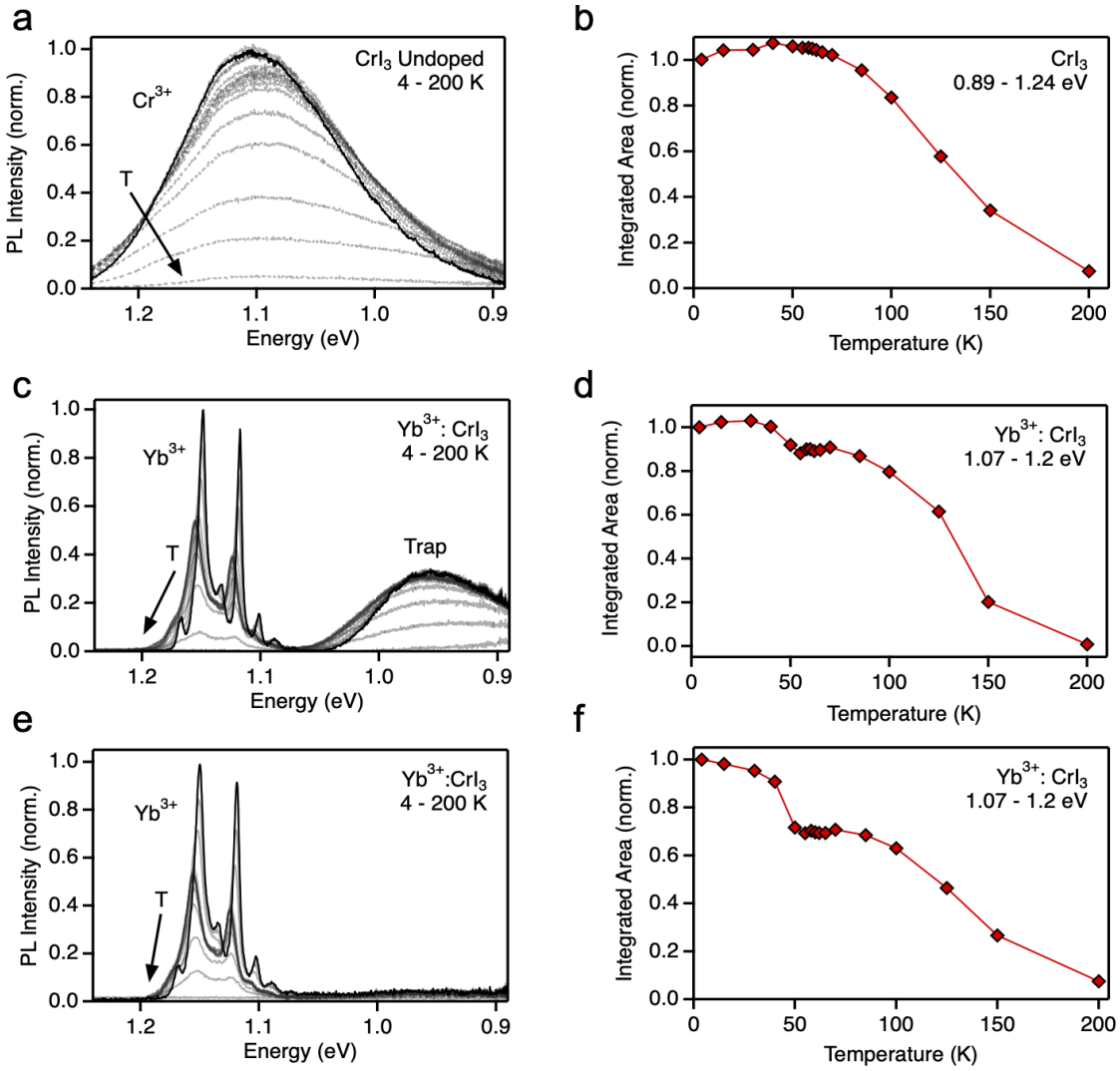

Figure D4. (a) Variable-temperature PL spectra of CrI_3 measured from 4 to 200 K under 1.88 eV CW excitation (from Figure 4.2 of section 4.2). (b) Scatter plot depicting total integrated area of the CrI_3 PL from panel (a). The 200 K intensity is 7.5% that of the 4 K value. (c) Variable-temperature PL spectra of 4.9% Yb^{3+}:CrI_3 measured from 4 to 200 K under 1.88 eV CW excitation (from Figure 3.2 of the main text). (d) Scatter plot depicting total integrated area of the Yb^{3+} PL from panel (c). The 200 K intensity is 0.8% that of the 4 K value. (e) Variable-temperature PL spectra of 5.0% Yb^{3+}:CrI_3 measured from 4 to 200 K under 1.88 eV CW excitation (from Figure 4.2 of section 4.2). (f) Scatter plot depicting total integrated area of the Yb^{3+} PL from panel (e). The 200 K intensity is 7.5% that of the 4 K value. Note that a second, broad "trap" PL band is observed at ~0.98 eV in samples made from Cr metal powder precursor (99.94%, panel (c)) but not in samples made from Cr chip precursor (99.995%, panel (e)). Ni is the primary impurity in the powder precursor (see section 4.4 Methods), and Ni is detected in this CrI_3 sample at 0.4% cation mole fraction. Ni^{2+} $^3A_{2g} \rightarrow {}^3T_{2g}$ absorption in NiI_2 and Ni^{2+}:CdI_2 is centered around 0.93 eV,[3] and the broad "trap" PL band in panel (c) is thus tentatively attributed to Ni^{2+} impurities in CrI_3.

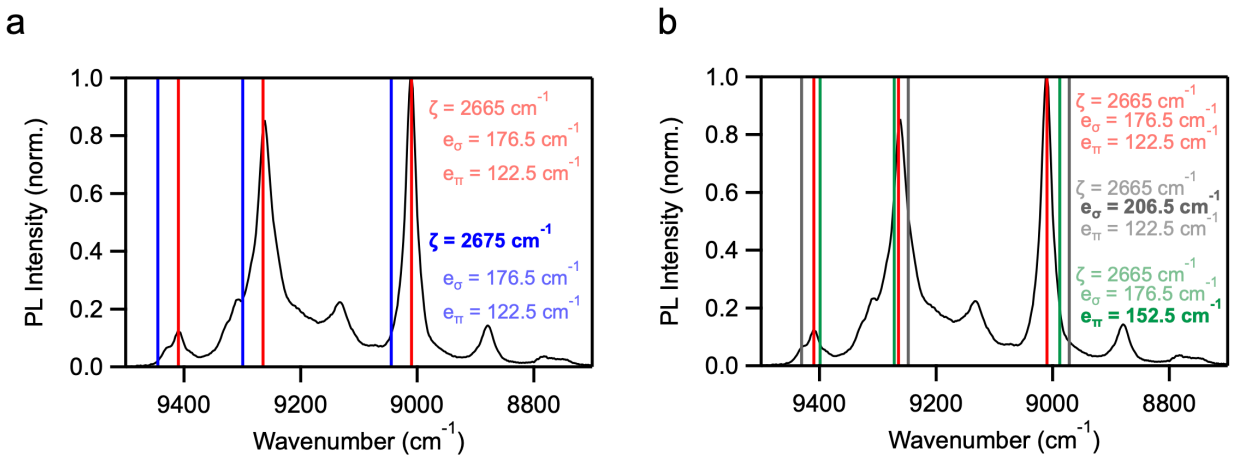

Figure D5. Comparison of the 5 K experimental data and calculated (AOM) *f-f* PL transition energies for 4.9% Yb^{3+}:CrI_3. A best fit to the experimental PL data resulted in the following values: $\zeta = 2665$ cm^{-1} (330.4 meV), $e_\sigma = 176.5$ cm^{-1} (21.9 meV), $e_\pi = 122.5$ cm^{-1} (15.2 meV). The calculated transition energies using these parameters are shown as the vertical red lines in both panels. (a) Comparison of calculated transition energies obtained by changing from $\zeta = 2665$ cm^{-1} (red) to $\zeta = 2675$ cm^{-1} (blue), with all other parameters constant to the best-fit (red). (b) Comparison of calculated transition energies obtained by individually changing the values of e_σ and e_π. The gray traces show the effect of changing from $e_\sigma = 176.5$ cm^{-1} (red) to $e_\sigma = 206.5$ cm^{-1} with all other parameters constant to the best fit (red). The green traces show the effect of changing from $e_\pi = 122.5$ cm^{-1} (red) to $e_\pi = 152.5$ cm^{-1} with all other parameters constant to the best fit (red). From the best-fit parameters, g is anisotropic ($g_1 = 2.672$, $g_2 = 2.686$, $g_3 = 2.642$) and an average ground-state g value of ~2.7 is predicted.

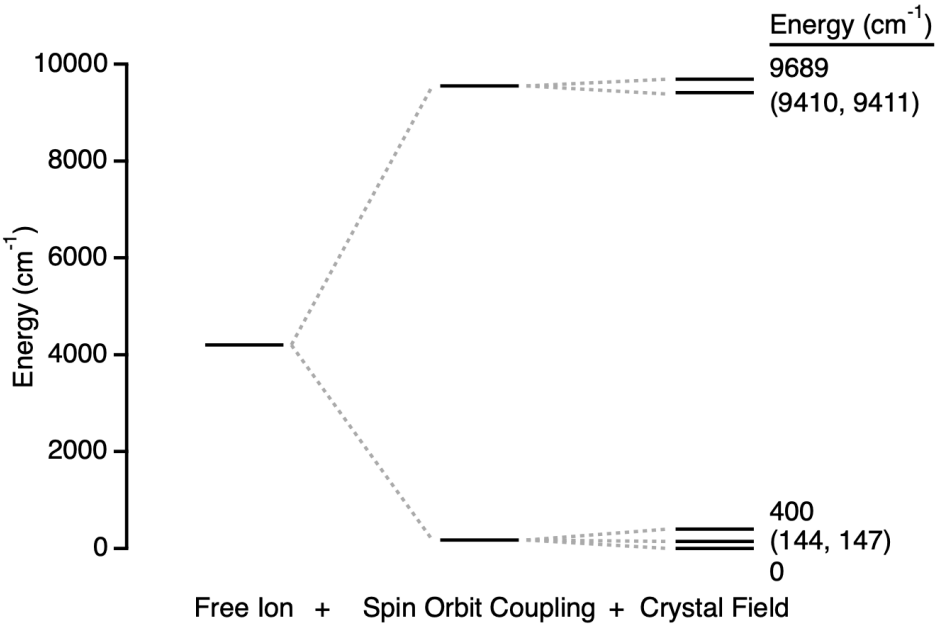

Figure D6. The Yb^{3+} valence energy level diagram described by the best-fit parameters of Fig. B5. The energies of the crystal field states in eV are: 0.0000, (0.0179, 0.0182), 0.0496, (1.1667, 1.1668), 1.2013 eV.

Table D2. Energies (cm^{-1}) of the valence electronic states, $^2F_{5/2}$ and $^2F_{7/2}$ barycenter energies,[a] and ΔE(Barycenter) for Yb^{3+} ions in several host crystals, and for the free ion. These data were used to generate Fig. B7 (after converting to eV). Many of these entries are compiled in ref. [4].

Host Lattice	0	1	2	3	$^2F_{7/2}$ Barycenter	0'	1'	2'	$^2F_{5/2}$ Barycenter	ΔE(Bary)	ref.
$Ca_2Ga_2SiO_7$ (CGS)	0.0	300	490	970	440	10250	10570	11010	10610	10170	[5]
$SrLaGa_3O_7$ (SLG)	0.0	220	386	910	379	10190	10450	11025	10555	10176	[5]
$Ca_4GdO(BO_3)_3$ (GdCOB) (site I, Gd)	0.0	423	668	1003	524	10246	10706	11089	10680	10157	[6]
GdCOB (site II, Ca)	0.0	437	694	1003	534	10261	10737	11150	10716	10183	[6]
GdCOB (site III, Ca)	0.0	417	688	1003	527	10240	10682	11026	10649	10122	[6]
$Ca_4YO(BO_3)_3$ (YCOB)	0.0	427	556	1023	502	10242	10537	11109	10629	10128	[7]
Sc_2O_3	0.0	474	634	1076	546	10250	10640	11198	10696	10150	[8]
$Ca_5(PO_4)_3F$ (CFAP)	0.0	409	597	1099	526	10178	10496	11069	10581	10055	[9]
$Sr_5(PO_4)_3F$ (SFAP)	0.0	362	618	1190	543	10150	10512	11108	10590	10048	[10]
$Sr_5(VO_4)_3F$ (SVAP)	0.0	321	562	1078	490	10141	10740	11050	10644	10153	[11]
$Y_3Al_5O_{12}$ (YAG)	0.0	584	635	783	501	10328	10752	10917	10666	10165	[12]
$BaCaBO_3F$ (BCBF)	0.0	303	533	902	435	10204	10570	11000	10591	10157	[13]
$LiNbO_3$	0.0	352	448	788	397	10204	10471	11090	10588	10191	[14]
$KGd(WO_4)_2$ (KGW)	0.0	163	385	535	271	10188	10471	10682	10447	10176	[15]
$KY(WO_4)_2$ (KYW)	0.0	169	407	568	286	10187	10476	10695	10453	10167	[15]
$CaWO_4$	0.0	220	366	492	270	10278	10366	10665	10436	10167	[16]
$YAlO_3$	0.0	209	341	590	285	10220	10410	10730	10453	10168	[16]
$LiYF_4$	0.0	216	371	479	267	10288	10409	10547	10415	10148	[16]
$YAl_3(BO3)_4$ (YAB)	0.0	94	185	581	215	10194	10277	10672	10381	10166	[17]
$Cs_2NaYbCl_6$	0	225	225	573	256	10243	10243	10708	10398	10142	[18, 19]
$Cs_3Yb_2Br_9$	0.0	144	201	421	192	10277	10301	10578	10385	10194	[20]
$CsCdBr_3$	0.0	114	140	441	174	10119	10146	10590	10285	10111	[20]
$CuInS_2$	0.0	32	87	182	75	10033	10060	---	10095[a]	10020	[21]
InP	0	35.5	35.5	97.5	42	10018	10064	10064	10049	10007	[22]
Free ion	---	---	---	---	0.0	---	---	---	10213	10213	[23]
CrI_3	0.0	146	146	400	173	9410		---	9551[a]	9379	this work

[a]For the entire data set of complete entries, the ratio of $^2F_{5/2}$:$^2F_{7/2}$ CF splitting energies, (E($^2F_{5/2}$ Barycenter) - $E_{0'}$)/(E($^2F_{7/2}$ Barycenter)) is 0.82 ± 0.14. The $^2F_{5/2}$ barycenter energies for Yb^{3+}:CrI_3 and Yb^{3+}:$CuInS_2$ were thus set equal to the $^2F_{7/2}$ barycenter energies for the same compounds. The resulting uncertainties in ΔE(Bary) are estimated to be < ~1%, close to or smaller than the data points in Fig. B7. For comparison, the Yb^{3+}:CrI_3 AOM calculations above yield: $^2F_{7/2}$ barycenter = 173 cm^{-1} (21 meV), $^2F_{5/2}$ barycenter = 9503 cm^{-1} (1.178 eV), ΔE(Bary) = 9330 cm^{-1} (1.157 eV), within this uncertainty range.

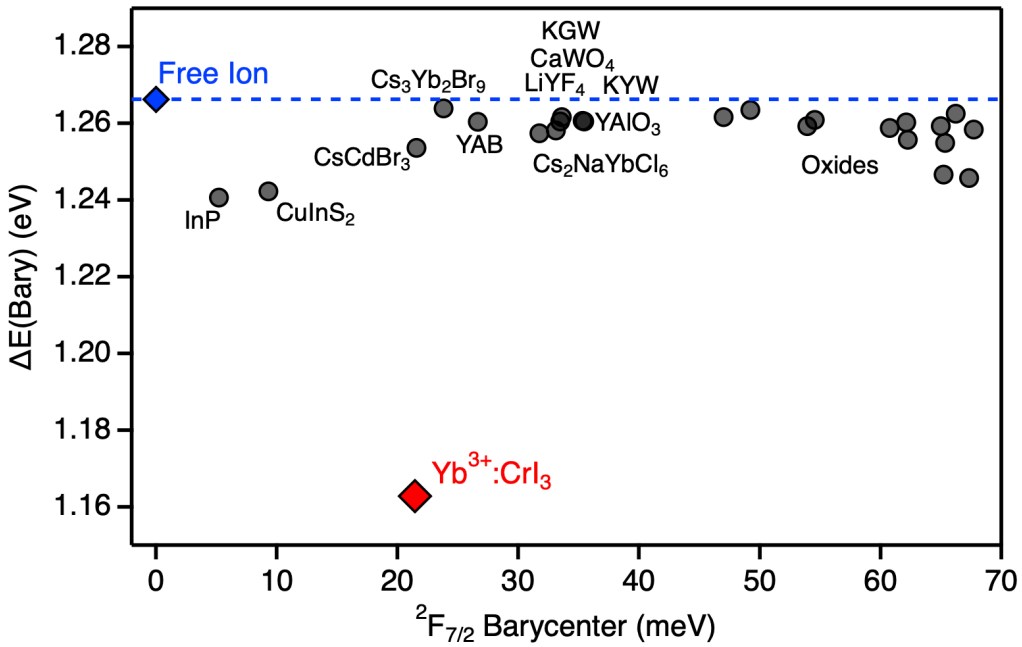

Figure D7. Plot of the difference between experimental Yb^{3+} $^2F_{5/2}$ and $^2F_{7/2}$ barycenter energies (ΔE(Bary)) for the compounds listed in Table B2, and for the free ion, *vs* the barycenter energy for the $^2F_{7/2}$ ground multiplet. The compounds associated with select data points are labeled. The dashed blue line shows the value of the free ion.

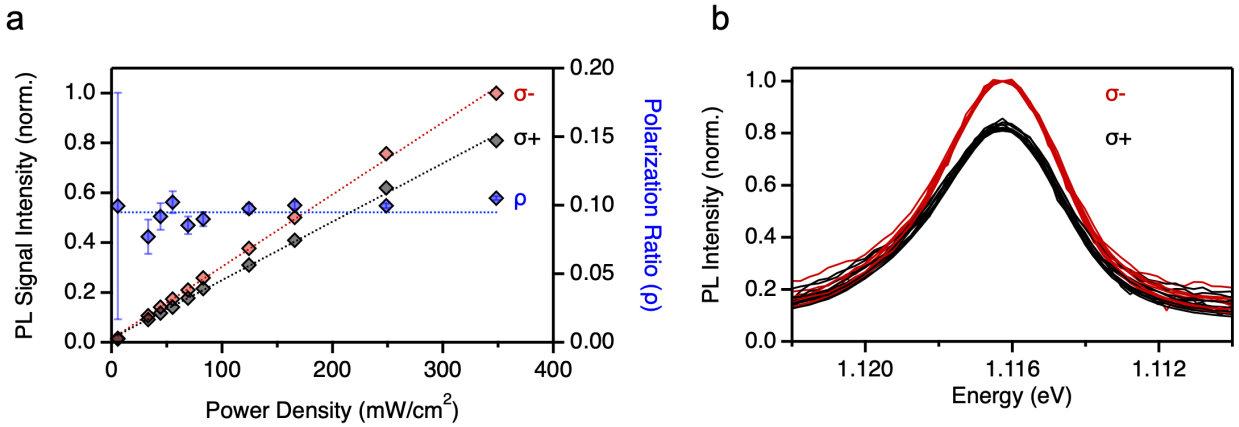

Figure D8. (a) Power dependence of σ^- (red) and σ^+ (black) PL peak intensities and circular polarization (ρ, blue) of the $\Gamma_8 \rightarrow \Gamma_7$ transition. The data were collected at 0.5 T and 5 K and the sample was excited with linearly polarized light at 1.96 eV. The PL intensities show a linear increase with power, resulting in a constant polarization ratio. The error bars represent uncertainty estimated from the linear fit of the polarization intensities. (b) The σ^- (red) and σ^+ (black) component of the $\Gamma_8 \rightarrow \Gamma_7$ transition normalized across all powers. The traces overlay each other well, showing no detectable power dependence.

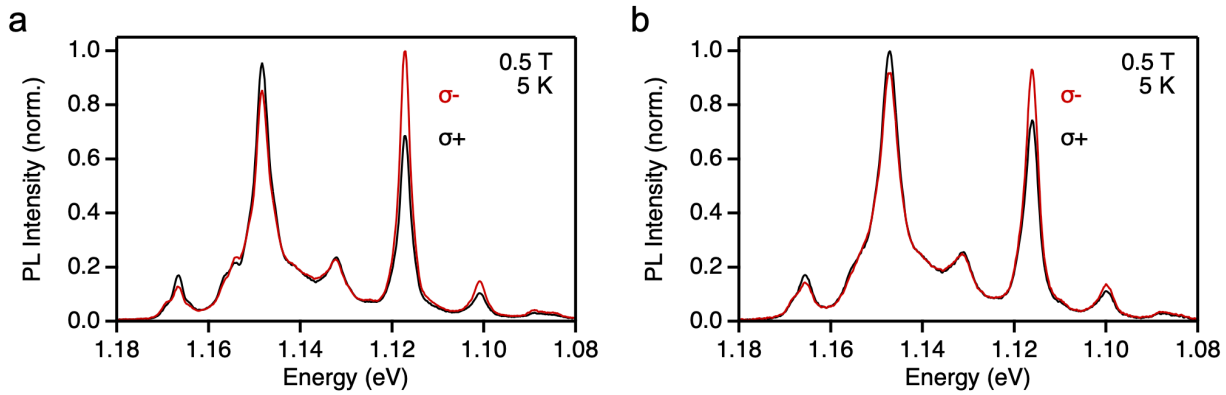

Figure D9. Comparison of full MCPL spectra across two different samples, measured at 0.5 T, 5 K. (a) The sample used in Figure 4.3b,c,e,f of section 4.2. (b) The sample used in Figure 4.3d of section 4.2. The two samples show very similar spectra, with slight differences in polarization magnitude.

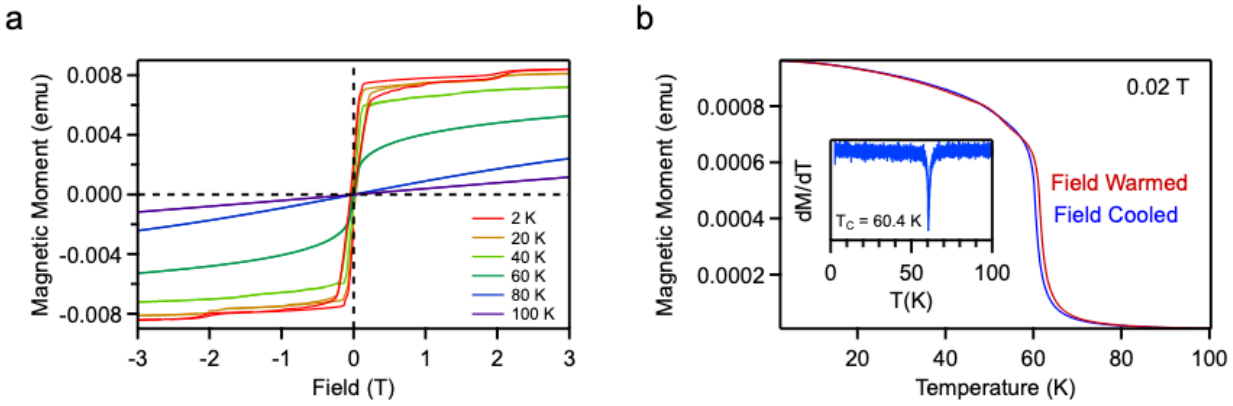

Figure D10. Magnetic data for a single-crystal flake of 5% Yb^{3+}:CrI_3, measured by VSM. The sample was probed with the external field aligned perpendicular to the face of the crystal. (a) Plots of magnetization vs external field measured at various temperatures. The data are similar to those collected on undoped CrI_3 bulk crystals (*e.g.*, Fig. B11). At 2 K, a coercive field of ~44 mT was found. (b) Plot of magnetization *vs* temperature measured in the field-cooled and field-warmed directions. The inset shows the derivative of the field-cooled data as a function of temperature, where the Curie temperature is found to be 60.4 K. These data show that Yb^{3+} doping has no significant effect on the magnetism of CrI_3 in these samples.

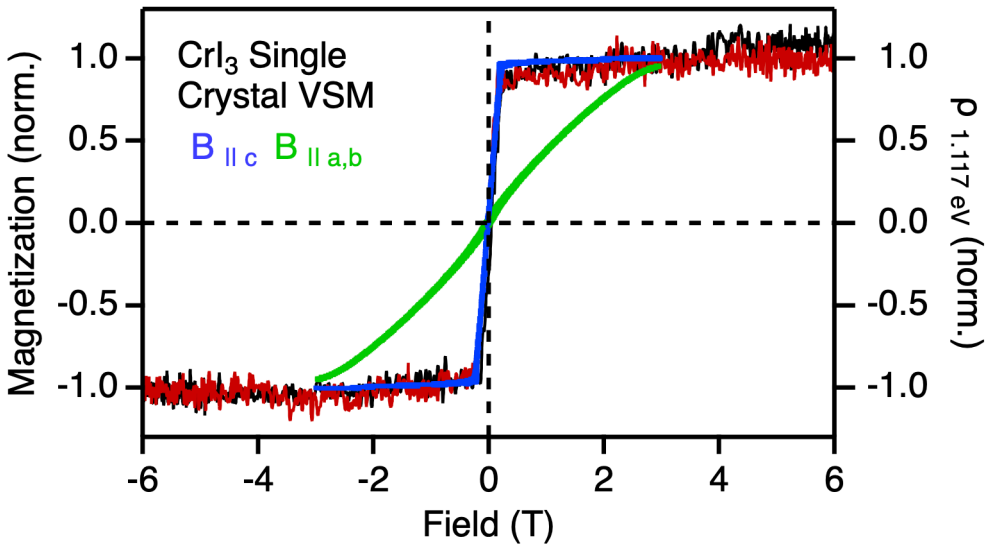

Figure D11. The same polarization data as featured in Figure 4.3d of section 4.2, overlayed with CrI_3 magnetization data measured from -3 to +3 T with the field oriented parallel to the crystallographic *c* axis (blue) by single-crystal vibrating sample magnetometry (VSM).[24] For comparison, the magnetization perpendicular to *c* (green) is also shown. The Yb^{3+} MCPL polarization ρ is superimposable with the CrI_3 magnetization measured in the same configuration.

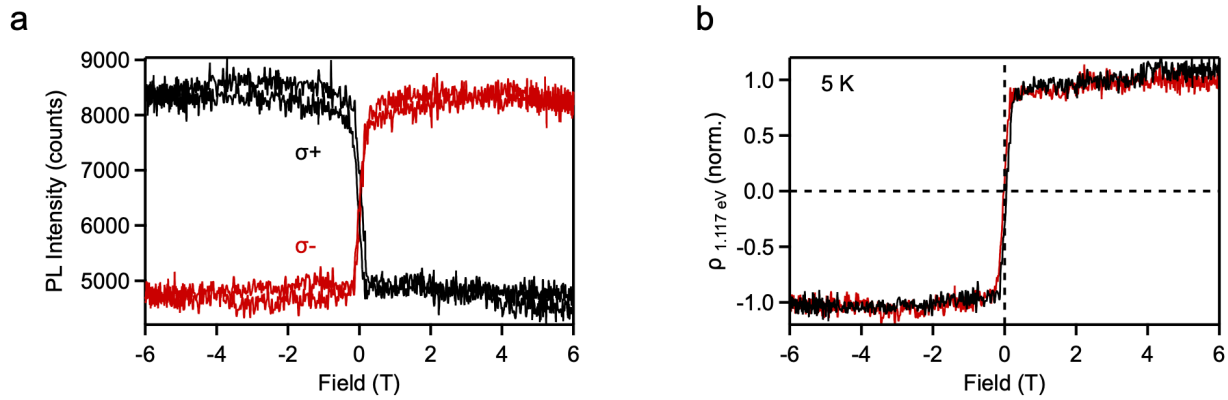

Figure D12. (a) Individual circularly polarized MCPL components measured during continuous field sweeps from -6 to +6 T and back at 5 K. (b) The same data, displayed as the polarization ratio (ρ, normalized). Panel (b) is shown as Figure 4.3d of section 4.2. Data measured using 14 mW/cm^2 excitation.

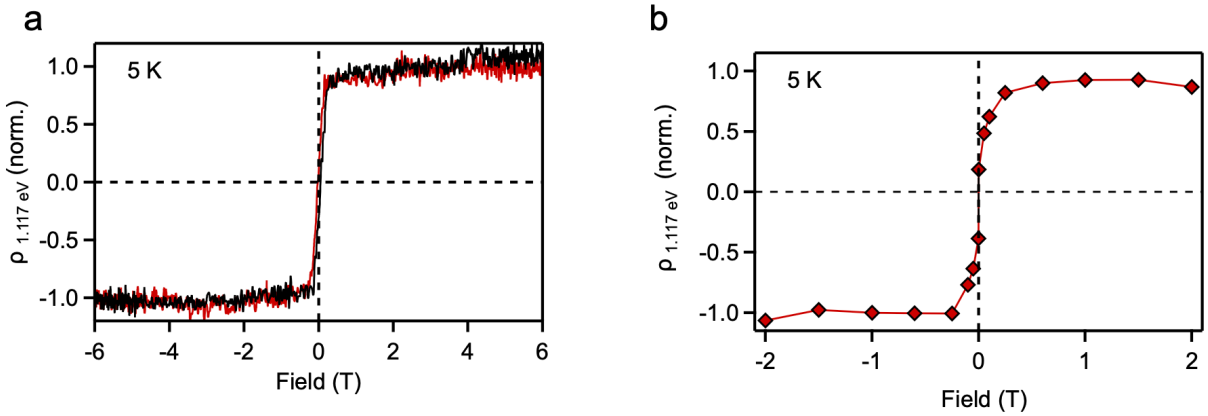

Figure D13. Comparison of field-dependent polarization ratios (ρ, normalized) measured with (a) linearly polarized and (b) unpolarized excitation at 5 K. In panel (b), no data were collected above 2 T. Panel (a) is shown as Figure 4.3d of the main text.

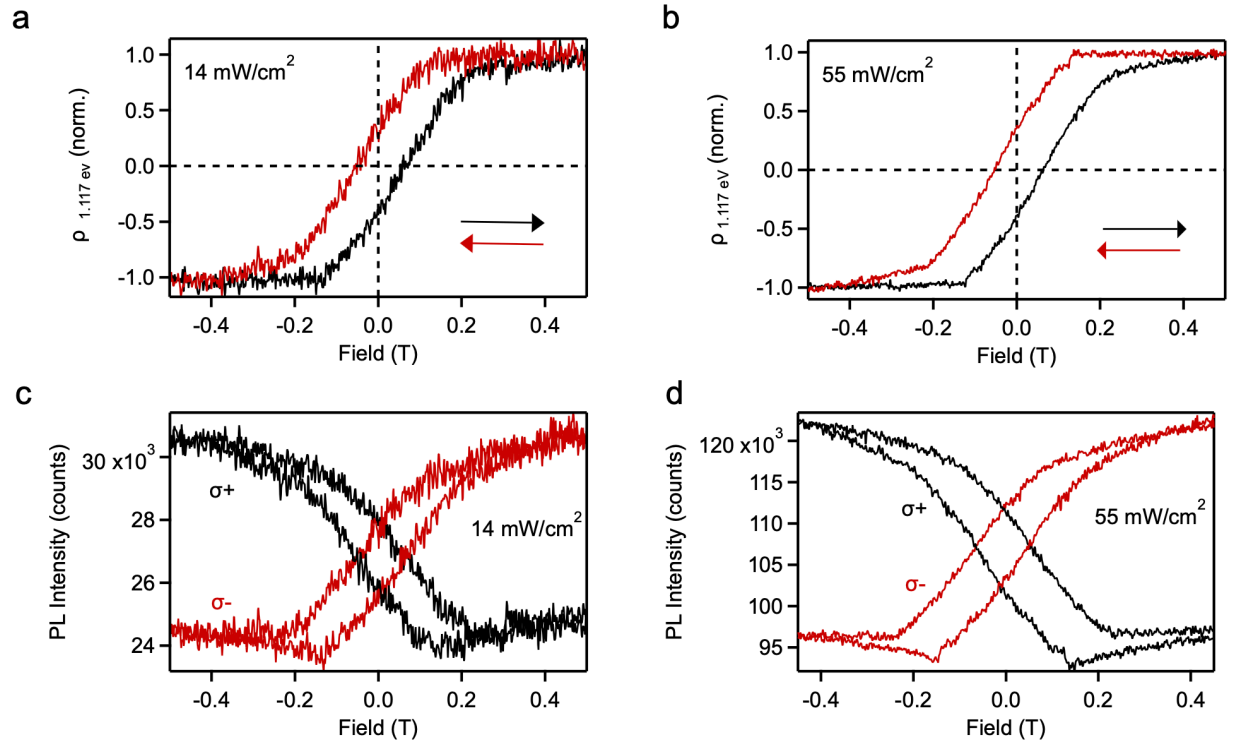

Figure D14. (a,b) Effect of excitation power on the polarization ratio (ρ, normalized). Magnetic hystereses measured under (a) low- and (b) higher-power excitation (14 *vs* 55 mW/cm^2, 5 K) show no difference. The black (red) trace corresponds to the sweep from negative (positive) to positive (negative) fields. (c, d) The separate circularly polarized PL components from the same (c) low- and (d) high-power measurements.

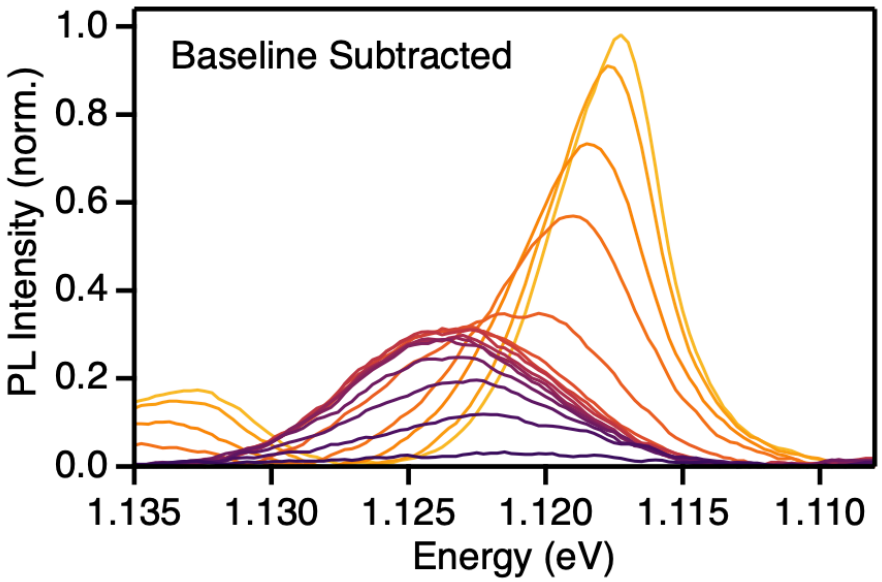

Figure D15. Temperature dependence of the $\Gamma_8 \rightarrow \Gamma_7$ PL feature of 4.9% Yb^{3+}:CrI_3 measured from 4 to 200 K under no external magnetic field (from **Figure 4.4** of section 4.2, T = 4, 15, 30, 40, 50, 55, 58, 60, 62, 65, 70, 85, 100, 125, 150 K). A linear baseline was subtracted from each spectrum here to facilitate viewing and determination of the peak's FWHM.

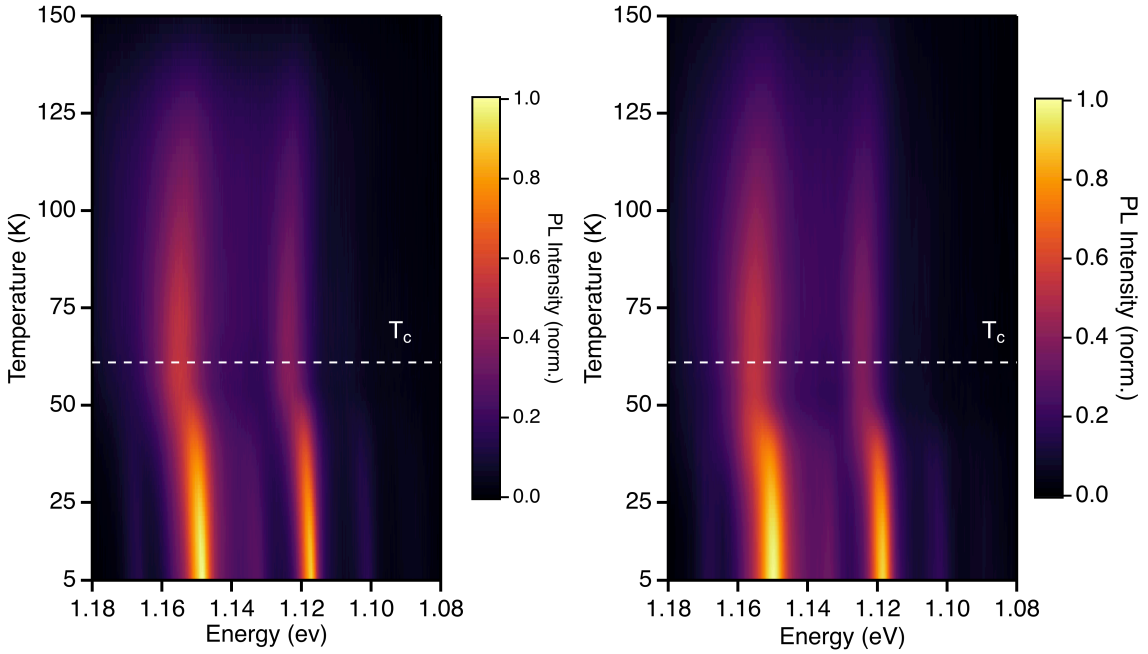

Figure D16. (a,b) False-color plots of the Yb^{3+} PL intensities *vs* temperature measured for the two samples shown in Fig. B4c,e, respectively, from 4 to 150 K at zero external magnetic field. The horizontal dashed line indicates T_C = 61 K. The two samples show the same temperature dependence, but the features are slightly better resolved in panel (a). Panel (a) is shown as **Figure 4.4** of section 4.2.

References:

1. Jesche, A. F., M.; Kreyssig, A.; Meier, W. R.; Canfield, P. C. X-Ray Diffraction on large single crystals using a powder diffractometer. *Philos, Mag. (Abingdon)* **2016,** *96*, 2115-2124.
2. McGuire, M. A.; Dixit, H.; Cooper, V. R.; Sales, B. C. Coupling of Crystal Structure and Magnetism in the Layered, Ferromagnetic Insulator CrI_3. *Chem. Mater.* **2015,** *27*, 612-620.
3. Kuindersma, S. R.; Boudewijn, P. R.; Haas, C. Near-Infrared d–d Transitions of NiI_2, CdI_2:Ni^{2+}, and CoI_2. *Phys. stat. sol. (b)* **1981,** *108*, 187-194.
4. Haumesser, P.-H.; Gaumé, R.; Viana, B.; Antic-Fidancev, E.; Vivien, D. Spectroscopic and crystal-field analysis of new Yb-doped laser materials. *J. Phys.: Cond. Mat.* **2001,** *13*, 5427-5447.
5. Simondi-Teisseire, B. PhD Thesis. Paris VI University, 1996.
6. Mougel, F.; Dardenne, K.; Aka, G.; Kahn-Harari, A.; Vivien, D. Ytterbium-doped $Ca_4GdO(BO_3)_3$: an efficient infrared laser and self-frequency doubling crystal. *J. Opt. Soc. Am. B* **1999,** *16*, 164-172.
7. Mougel, F. PhD Thesis. Paris VI University, 1999
8. Mix, E. PhD Thesis. Hamburg University, 1999.
9. DeLoach, L. D.; Payne, S. A.; Chase, L. L.; Smith, L. K.; Kway, W. L.; Krupke, W. F. Evaluation of absorption and emission properties of Yb^{3+} doped crystals for laser applications. *IEEE J. Quant. Elect.* **1993,** *29*, 1179-1191.
10. Gruber, J. B.; Zandi, B.; Merkle, L. Crystal-field splitting of energy levels of rare-earth ions $Dy^{3+}(4f^9)$ and $Yb^{3+}(4f^{13})$ in M (II) sites in the fluorapatite crystal $Sr_5(PO_4)_3F$. *J. Appl. Phys.* **1998,** *83*, 1009-1017.
11. Payne, S. A.; DeLoach, L. D.; Smith, L. K.; Kway, W. L.; Tassano, J. B.; Krupke, W. F.; Chai, B. H. T.; Loutts, G. Ytterbium-doped apatite-structure crystals: A new class of laser materials. *J. Appl. Phys.* **1994,** *76*, 497-503.
12. Bogomolova, G. A.; Bumagina, L. A.; Kaminskii, A. A.; Malkin, B. Z. Crystal field in laser garnets with TR^{3+} ions in the exchange charge model. *Sov. Phys. Solid State* **1977,** *19*, 1428-1435.
13. Schaffers, K. I.; DeLoach, L. D.; Payne, S. A. Crystal growth, frequency doubling, and infrared laser performance of Yb^{3+}: $BaCaBO_3F$. *IEEE J. Quant. Elect.* **1996,** *32*, 741-748.
14. Montoya, E.; Sanz-Garcıa, J.; Capmany, J.; Bausá, L.; Diening, A.; Kellner, T.; Huber, G. Continuous wave infrared laser action, self-frequency doubling, and tunability of Yb^{3+}: MgO: $LiNbO_3$. *J. Appl. Phys.* **2000,** *87*, 4056-4062.
15. Kuleshov, N. V.; Lagatsky, A. A.; Podlipensky, A. V.; Mikhailov, V. P.; Huber, G. Pulsed laser operation of Yb-doped $KY(WO_4)_2$ and $KGd(WO_4)_2$. *Optics lett.* **1997,** *22*, 1317-1319.
16. Morrison, C. A.; Leavitt, P., Handbook on the physics and chemistry of rare earths, ch 46. Amsterdam: Elsevier: 1982.
17. Wang, P.; Dawes, J. M.; Dekker, P.; Knowles, D. S.; Piper, J. A.; Lu, B. Growth and evaluation of ytterbium-doped yttrium aluminum borate as a potential self-doubling laser crystal. *J. Opt. Soc. Am. B* **1999,** *16*, 63-69.
18. Schwartz, R. W. Electronic structure of the octahedral hexachloroytterbate ion. *Inorg. Chem.* **1977,** *16*, 1694-1698.
19. Kanellakopulos, B.; Amberger, H. D.; Rosenbauer, G. G.; Fischer, R. D. Zur Elektronenstruktur hochsymmetrischer Verbindungen der Lanthanoiden und Actinoiden—V: Paramagnetische Suszeptibilität und elektronisches Raman-Spektrum von $Cs_2NaYb(III)Cl_6$. *J.*

Inorg. Nuc. Chem. **1977,** *39*, 607-611.
20. Malkin, B. Z.; Leushin, A. M.; Iskhakova, A. I.; Heber, J.; Altwein, M.; Moller, K.; Fazlizhanov, I. I.; Ulanov, V. A. EPR and optical spectra of Yb^{3+} in $CsCdBr_3$: Charge-transfer effects on the energy-level structure of Yb^{3+} in the symmetrical pair centers. *Phys. Rev. B* **2000,** *62*, 7063.
21. Tsujii, N.; Imanaka, Y.; Takamasu, T.; Kitazawa, H.; Kido, G. Photoluminescence of Yb^{3+}-doped $CuInS_2$ crystals in magnetic fields. *J. Appl. Phys.* **2001,** *89*, 2706-2710.
22. de Maat-Gersdorf, I. Spectroscopic analysis of erbium-doped silicon and ytterbium doped indium phosphide. University of Amsterdam, 2001.
23. Wyart, J.-F.; Tchang-Brillet, W.-Ü. L.; Spector, N.; Palmeri, P.; Quinet, P.; Biémont, E. Extended Analysis of the Spectrum of Triply-ionized Ytterbium (Yb IV) and Transition Probabilities. *Phys. Scripta* **2001,** *63*, 113-121.
24. De Siena, M. C.; Creutz, S. E.; Regan, A.; Malinowski, P.; Jiang, Q.; Kluherz, K. T.; Zhu, G.; Lin, Z.; De Yoreo, J. J.; Xu, X.; Chu, J.-H.; Gamelin, D. R. Two-Dimensional van der Waals Nanoplatelets with Robust Ferromagnetism. *Nano Lett.* **2020,** *20*, 2100-2106.

Appendix E: Supplementary Information for Chapter 4.3

Luminescence and Covalency in Ytterbium-Doped CrX_3 (X = Cl, Br, I) van der Waals Compounds

Reproduced with permission from Snoeren; T. J.; Pressler, K.; Kluherz, K. T.; Walsh, K. M.; De Yoreo, J. J.; Gamelin, D. R. *J. Am. Chem. Soc.* **2023**, *145*, 17427-17434.

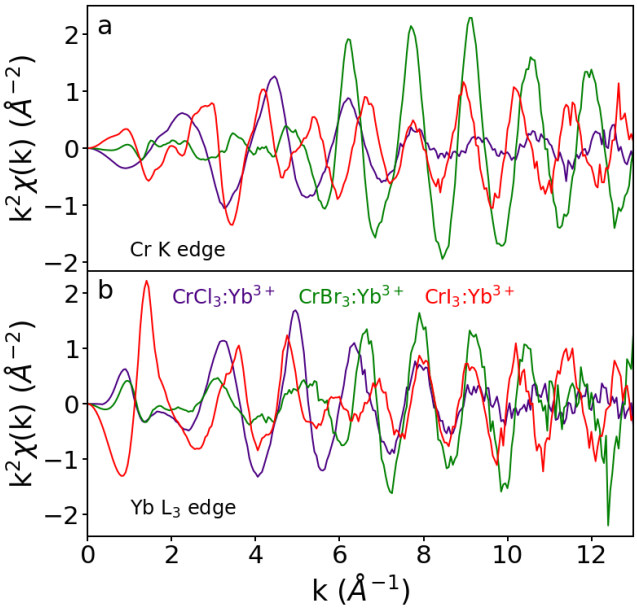

Figure E1. *k*-space EXAFS data from the (a) Cr K- and (b) Yb L_3-edges for $CrX_3:Yb^{3+}$ (X = Cl, Br, I) single crystals, plotted with a *k*-weight of 2. A window from 3 $Å^{-1}$ to 12 $Å^{-1}$ with a d*k* value of 1 $Å^{-1}$ was used for shell-by-shell fitting in Artemis.

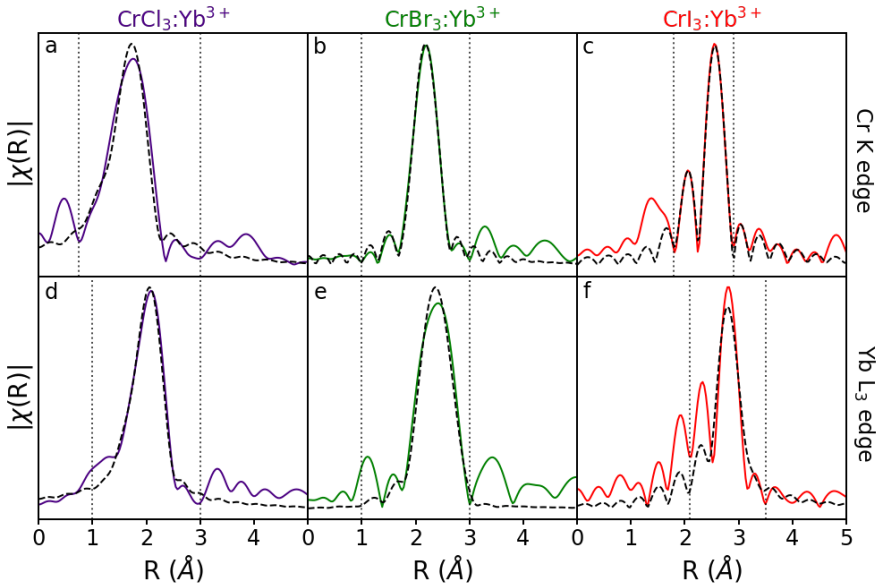

Figure E2. Fourier-transform (real-space) EXAFS data (colored) and fits (black dashed) using the nearest-neighbor halide scatterers for the Cr K edge (top row) and Yb L_3 edge (bottom row) for each sample. (a,d) $CrCl_3:Yb^{3+}$ data (purple); (b,e) $CrBr_3:Yb^{3+}$ data (green); (c,f) $CrI_3:Yb^{3+}$ data (red). Vertical dotted lines in each panel mark the fitting windows used, in R-space. Note that the radial distances have not been corrected for phase shift, in order to compare with the fits.

Table E1. Fitting parameters and bond distances for optimized shell-by-shell fits of EXAFS data for $CrX_3:Yb^{3+}$ (X = Cl, Br, I) single-crystal samples.

	R-factor	χ^2	χ^2_{red}	Debye-Waller	Bond Distance (Å)
Cr K edge					
$CrCl_3:Yb^{3+}$	0.016	1380	239	0.0113	2.252 ±0.015
$CrBr_3:Yb^{3+}$	0.001	69	7	0.0033	2.494 ±0.002
$CrI_3:Yb^{3+}$	0.008	39	18	0.0036	2.715 ±0.006
Yb L_3 edge					
$CrCl_3:Yb^{3+}$	0.017	624	88	0.0108	2.541 ±0.013
$CrBr_3:Yb^{3+}$	0.012	42	11	0.0068	2.806 ±0.019
$CrI_3:Yb^{3+}$	0.007	16	4	0.0040	2.945 ±0.005

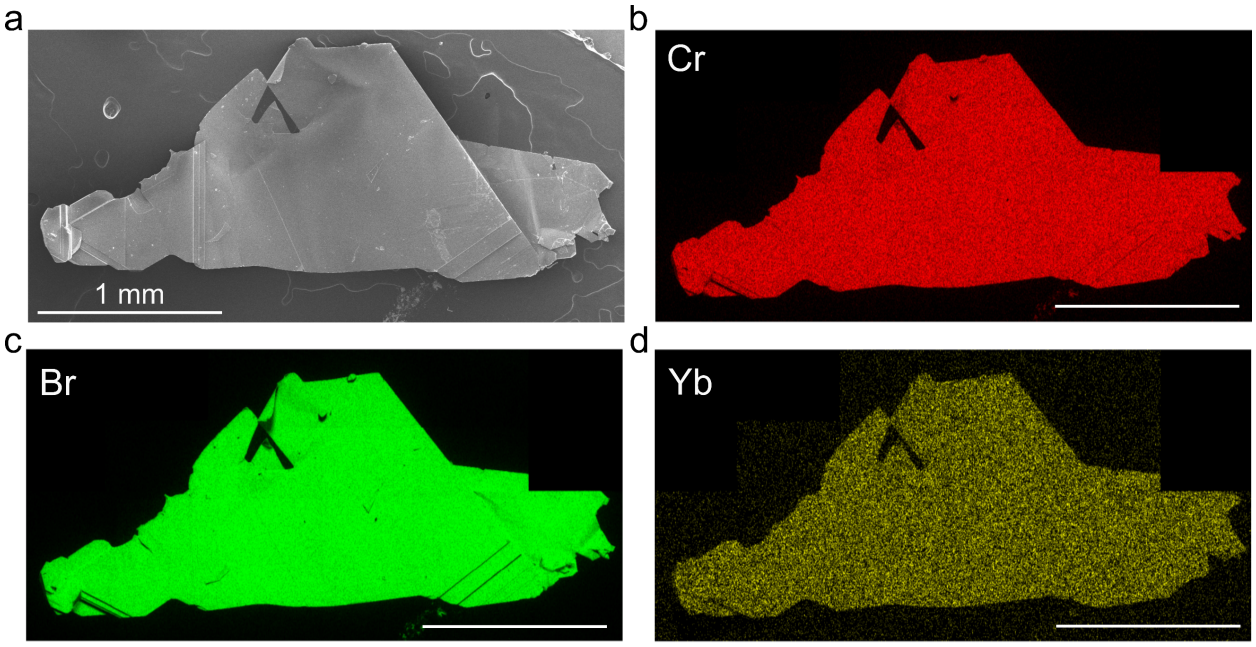

Figure E3. (a) SEM image of a representative $CrBr_3:Yb^{3+}$ flake. (b-d) EDX mapping of the same flake showing an even distribution of Cr, Br, and Yb throughout the material. The low concentration of Yb in this sample leads to worse signal to noise relative to Cr. All scale bars are 1 mm.

Table E2. Summary of Angular Overlap Model (AOM) calculation parameters. All values are in cm^{-1}.

	ζ	e_σ	$e_{\pi,x}$	$e_{\pi,y}$
$CrCl_3:Yb^{3+}$	2883	288.5	198	100.5
$CrBr_3:Yb^{3+}$	2863.5	219.5	212.5	137.5
$CrI_3:Yb^{3+}$	2665	176.5	122.5	122.5

Table E3. Yb^{3+} *f-f* energy levels and ligand-to-metal charge-transfer energies (E_{CT}) in different host lattices. Several of the Yb^{3+} crystal-field energies are collected in an overview paper by Haumesser *et al.*[1] Some charge-transfer energies are collected in an overview paper by Nikl *et al.*[2] Eu^{3+} charge-transfer energies, used to estimate E_{CT} for select Yb^{3+} compounds, are collected in an overview paper by Dorenbos.[3] Charge-transfer energies are rounded to the nearest hundred wavenumbers. All energies in cm^{-1}.

Host Lattice	0	1	2	3	$^2F_{7/2}$ barycenter	0'	1'	2'	$^2F_{5/2}$ barycenter	Δ	Ref.	E_{CT}	Ref.
$LiYF_4$	0	216	371	479	267	10288	10409	10547	10415	10148	4	62900	5
LaF_3	0	72	183	396	163	10268	10442	10668	10459	10296	6	59700[a]	7, 8
CaF_2	0	331	482	669	371	10116	?	?	10412[b]	10042	9	58100	10
YPO_4	0	265	265	841	343	10415	?	?	10607[c]	10264	11	47600	5, 12
$LuPO_4$	0	84	277	277	159.5	10244	10275	10480	10333	10174	6	47600	5
$Y_3Al_5O_{12}$	0	565	612	785	491	10327	10624	10679	10543	10052	13, 14	47600	2, 5
$Lu_3Al_5O_{12}$	0	127	372	601	275	10352	?	?	10500[d]	10224	15	45000	2, 15, 16
$Y_3Ga_5O_{12}$	0	132	330	540	251	10315	?	?	10483[d]	10232	15	44400	15
Sc_2O_3	0	474	634	1076	546	10250	10640	11198	10696	10150	17	44400	5
Y_2O_3	0	536	536	941	503	10235	10526	11050	10604	10101	18	44100	5
$LaPO_4$	0	135	135	551	205	10241	?	?	10356[c]	10151	19, 20	43900	5, 12
Al_2O_3	0	337	550	1020	477	10252	10476	11120	10616	10139	21	43000[a]	22
$YAl_3(BO_3)_4$	0	94	185	581	215	10194	10277	10672	10381	10166	23	43000[a]	24
$Ca_5(PO_4)_3F$	0	409	597	1099	526	10178	10496	11069	10581	10055	6	42800[a]	25
$YAlO_3$	0	209	341	590	285	10220	10410	10730	10453	10168	4	42600	5, 26
$Ca_4GdO(BO_3)_3$	0	423	668	1003	524	10246	10706	11089	10680	10156	27	42300[a]	28
$Sr_5(PO_4)_3F$	0	362	618	1190	543	10150	10512	11108	10590	10048	29	41600[a]	30
$SrLaGa_3O_7$	0	220	386	910	379	10190	10450	11025	10555	10176	31	38500[a]	32
$Cs_2NaYbCl_6$	0	362	362	701	356	10243	10243	10708	10398	10042	33	38300	33
YCl_3	0	318	506	746	393	10392	?	?	10706[b]	10314	34	36500	34
$Na_3Y(PO_4)_2$	0	188	325	722	309	10244	10515	11045	10601	10292	35, 36	34500	35
YBr_3	0	109	332	519	240	10194	?	?	10386[b]	10146	34	29800	34
$CsCdBr_3$	0	159	198	466	206	10125	10139	10598	10287	10081	37	29000	38
ZnS	0	63	108	229	100	10151	?	?	10231[b]	10131	39	28000	39
$NaYS_2$	0	229	229	522	245	10101	?	?	10297[b]	10052	40	26300	40
$CuInS_2$	0	32	87	182	75	10033	10060	?	10095[b]	10020	41	26300	e
$NaInS_2$	0	266	266	582	279	10070	?	?	10293[b]	10014	42	26300	e
$PbIn_2S_4$	0	200	200	549	237	10091	?	?	10281[b]	10044	42	26300	e
Free ion	-	-	-	-	0	-	-	-	10213	10213	43	-	-
CrI_3	0	144	147	400	173	9410	9411	9689	9503	9330	44	17900	f
$CrBr_3$	0	145	237	522	226	10107	10154	10498	10253	10027	This work	29200	f
$CrCl_3$	0	206	321	590	280	10214	10270	10646	10377	10097	This work	36700	f

[a] Calculated from Eu^{3+} charge-transfer energies using the method outlined by Li *et al.*[45]

[b] Calculated from $^2F_{7/2}$ barycenter using $E_{F_{5/2}} = E_{0'} + \sigma E_{F_{7/2}}$, where E_F indicates the barycenter energy, $E_{0'}$ indicates the energy of the lowest-energy crystal-field state of the $^2F_{5/2}$ manifold, and σ = 0.8 (unless stated otherwise), as determined by Pressler *et al.* (SI).[44]

[c] Calculated as described in (b) using σ = 0.56 (from $LuPO_4$)

[d] Calculated as described in (b) using $\sigma = 0.67$ (from $Y_3Al_5O_{12}$)

[e] CT values have not been reported for these lattices, the value used here is for $NaYS_2$ as measured by Hansen *et al*.[40] Error bars are included in the main text figure to indicate expected deviations from this value.

[f] CT values were not reported for these lattices. Values for $[YbX_6]^{3-}$ in solution were used from Ryan and Jørgensen.[46, 47] Estimated error bars are roughly the size of the CrX_3 data points in main text Figure 4.8c.

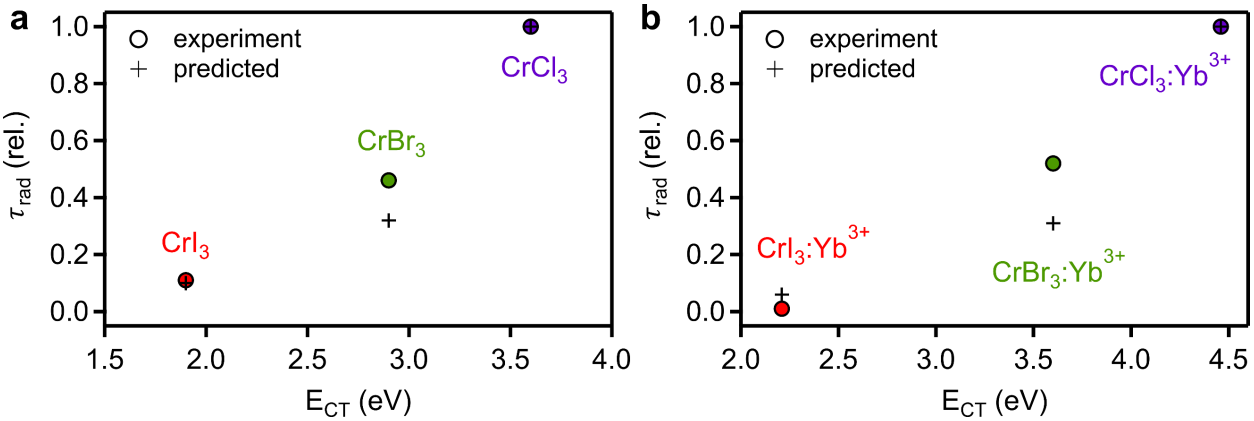

Figure E4. (a) Cr^{3+} PL decay times for CrX_3 compounds plotted *vs* the energy of the first LMCT transition (E_{CT}). Circles: Experimental data from Figure 4.7d of the main text. Crosses: Values predicted using eqs 3 and 4 of the main text. (b) Same as (a) but for Yb^{3+} PL decay times in CrX_3:Yb^{3+} compounds.

References:

1. Haumesser, P.-H.; Gaumé, R.; Viana, B.; Antic-Fidancev, E.; Vivien, D. Spectroscopic and Crystal-Field Analysis of New Yb-Doped Laser Materials. *J. Phys. Condens. Matter* **2001,** *13*, 5427.
2. Nikl, M.; Yoshikawa, A.; Fukuda, T. Charge Transfer Luminescence in Yb^{3+}-Containing Compounds. *Opt. Mater.* **2004,** *26*, 545-549.
3. Dorenbos, P. The Eu^{3+} Charge Transfer Energy and the Relation with the Band Gap of Compounds. *J. Lumin.* **2005,** *111*, 89-104.
4. Morrison, C.; Leavitt, P., *Handbook on the Physics and Chemistry of Rare Earths*. Elsevier: Amsterdam, 1982.
5. Van Pieterson, L.; Heeroma, M.; De Heer, E.; Meijerink, A. Charge Transfer Luminescence of Yb^{3+}. *J. Lumin.* **2000,** *91*, 177-193.
6. DeLoach, L. D.; Payne, S. A.; Chase, L. L.; Smith, L. K.; Kway, W. L.; Krupke, W. F. Evaluation of Absorption and Emission Properties of Yb^{3+} Doped Crystals for Laser Applications. *IEEE J. Quantum Electron.* **1993,** *29*, 1179-1191.
7. Gérard, I.; Krupa, J. C.; Simoni, E.; Martin, P. Investigation of Charge Transfer $O^{2-} \rightarrow Ln^{3+}$ and $F^- \rightarrow Ln^{3+}$ in LaF_3:(Ln^{3+}, O^{2-}) and YF_3:(Ln^{3+}, O^{2-}) Systems. *J. Alloys Compd.* **1994,** *207-208*, 120-127.
8. Mayolet, A.; Krupa, J. C.; Gérard, I.; Martin, P. Luminescence of Eu^{3+} Doped Materials Excited by VUV Synchrotron Radiation. *Mater. Chem. Phys.* **1992,** *31*, 107-109.
9. Kuznetsov, S. V.; Morozov, O. A.; Gorieva, V. G.; Mayakova, M. N.; Marisov, M. A.; Voronov, V. V.; Yapryntsev, A. D.; Ivanov, V. K.; Nizamutdinov, A. S.; Semashko, V. V.; Fedorov, P. P. Synthesis and Luminescence Studies of CaF_2:Yb:Pr Solid Solutions Powders for Photonics. *J. Fluor. Chem.* **2018,** *211*, 70-75.
10. Radzhabov, E. A.; Nepomnyashchikh, A. I.; Kozlovskiĭ, V. Charge-Transfer Bands in Crystals of Alkaline Earth Fluorides with Eu^{3+} and Yb^{3+1}. *Opt. Spectrosc.* **2008,** *105*, 364-368.
11. Li, K.-Y.; Liu, L.-Y.; Wang, R.-Z.; Xiao, S.-G.; Zhou, H.; Yan, H. Broadband Sensitization of Downconversion Phosphor YPO_4 by Optimizing TiO_2 Substitution in Host Lattice Co-Doped with Pr^{3+}-Yb^{3+} Ion-Couple. *J. Appl. Phys.* **2014,** *115*.
12. Van Pieterson, L.; Meijerink, A. Charge Transfer Luminescence of Yb^{3+} in Orthophosphates. *J. Alloys Compd.* **2000,** *300-301*, 426-429.
13. Takaichi, K.; Yagi, H.; Lu, J.; Shirakawa, A.; Ueda, K.; Yanagitani, T.; Kaminskii, A. A. Yb^{3+}-Doped $Y_3Al_5O_{12}$ Ceramics – A New Solid-State Laser Material. *Phys. Status Solidi A* **2003,** *200*, R5-R7.
14. Bogomolova, G. A.; Bumagina, L. A.; Kaminskii, A. A.; Malkin, B. Z. Crystal Field in Laser Garnets with TR^{3+} Ions in the Exchange Charge Model. *Sov. Phys. Solid State* **1977,** *19*, 1428-1435.
15. Kamenskikh, I. A.; Guerassimova, N.; Dujardin, C.; Garnier, N.; Ledoux, G.; Pedrini, C.; Kirm, M.; Petrosyan, A.; Spassky, D. Charge Transfer Fluorescence and f–f Luminescence in Ytterbium Compounds. *Opt. Mater.* **2003,** *24*, 267-274.
16. Ogino, H.; Yoshikawa, A.; Lee, J.-H.; Nikl, M.; Solovieva, N.; Fukuda, T. Growth and Scintillation Properties of Yb-Doped $Lu_3Al_5O_{12}$ Crystals. *J. Cryst. Growth* **2003,** *253*, 314-318.
17. Mix, E. PhD Thesis. Hamburg University, 1999.
18. Kong, J.; Tang, D. Y.; Lu, J.; Ueda, K. Spectral Characteristics of a Yb-Doped Y_2O_3 Ceramic Laser. *Appl. Phys. B* **2004,** *79*, 449-455.
19. Shimizu, T.; Isobe, T. Relation Between Shell Thickness and Near Infrared

Photoluminescence of $LaPO_4:Yb^{3+}/GdPO_4$ Core/Shell Nanoparticles. *Mater. Lett.* **2013,** *110*, 180-183.
20. Kaminska, A.; Duzynska, A.; Suchocki, A.; Bettinelli, M. Spectroscopy of f–f Radiative Transitions of Yb^{3+} Ions in Ytterbium Doped Orthophosphates at Ambient and High Hydrostatic Pressures. *J. Phys. Condens. Matter* **2010,** *22*, 225902.
21. Krebs, J. K.; Happek, U. Yb^{3+} Energy Levels in α-Al_2O_3. *J. Lumin.* **2001,** *94-95*, 65-68.
22. Mariscal, L. B.; Carmona-Téllez, S.; Alarcón-Flores, G.; Meza-Rocha, A. N.; Murrieta, H. S.; Falcony, C. Synthesis of $Al_2O_3:Eu^{3+}$ Powder and PET Films with This Powder Incorporated: A Luminescence Study. *ECS J. Solid State Sci. Technol.* **2015,** *4*, R97.
23. Wang, P.; Dawes, J. M.; Dekker, P.; Knowles, D. S.; Piper, J. A.; Lu, B. Growth and Evaluation of Ytterbium-Doped Yttrium Aluminum Borate as a Potential Self-Doubling Laser Crystal. *J. Opt. Soc. Am. B* **1999,** *16*, 63-69.
24. Blasse, G.; Bril, A. Study of Energy Transfer from Sb^{3+}, Bi^{3+}, Ce^{3+} to Sm^{3+}, Eu^{3+}, Tb^{3+}, Dy^{3+}. *J. Chem. Phys.* **2004,** *47*, 1920-1926.
25. Sahoo, R.; Bhattacharya, S. K.; Debnath, R. A New Type of Charge Compensating Mechanism in $Ca_5(PO_4)_3F:Eu^{3+}$ Phosphor. *J. Solid State Chem.* **2003,** *175*, 218-225.
26. Shim, J. B.; Yoshikawa, A.; Nikl, M.; Solovieva, N.; Pejchal, J.; Yoon, D. H.; Fukuda, T. Growth and Characterization of Yb^{3+}-Doped $YAlO_3$ Fiber Single Crystals Grown By the Modified Micro-Pulling-Down Method. *J. Cryst. Growth* **2003,** *256*, 298-304.
27. Mougel, F.; Dardenne, K.; Aka, G.; Kahn-Harari, A.; Vivien, D. Ytterbium-Doped $Ca_4GdO(BO_3)_3$: An Efficient Infrared Laser and Self-Frequency Doubling Crystal. *J. Opt. Soc. Am. B* **1999,** *16*, 164-172.
28. Dirksen, G. J.; Blasse, G. Tetracalcium Gadolinium Oxoborate ($Ca_4GdO(BO_3)_3$) As a New Host Lattice for Luminescent Materials. *J. Alloys Compd.* **1993,** *191*, 121-126.
29. Gruber, J. B.; Zandi, B.; Merkle, L. Crystal-Field Splitting of Energy Levels of Rare-Earth Ions $Dy^{3+}(4f^9)$ and $Yb^{3+}(4f^{13})$ in M(II) Sites in the Fluorapatite Crystal $Sr_5(PO_4)_3F$. *J. Appl. Phys.* **1998,** *83*, 1009-1017.
30. Jagannathan, R.; Kutty, T. R. N. Anomalous Fluorescence Features of Eu^{2+} in Apatite-Pyromorphite Type Matrices. *J. Lumin.* **1997,** *71*, 115-121.
31. Simondi-Teisseire, B. PhD Thesis. Paris VI University, 1996.
32. Kubota, S.-I.; Izumi, M.; Yamane, H.; Shimada, M. Luminescence of Eu^{3+}, Tb^{3+} and Tm^{3+} in $SrLaGa_3O_7$. *J. Alloys Compd.* **1999,** *283*, 95-101.
33. Schwartz, R. W. Electronic Structure of the Octahedral Hexachloroytterbate Ion. *Inorg. Chem.* **1977,** *16*, 1694-1698.
34. Dorenbos, P.; Josef, A.; de Haas, J. T. M.; Krämer, K. W. Vacuum Referred Binding Energies of the Lanthanides in Chloride, Bromide, and Iodide Compounds. *J. Lumin.* **2019,** *208*, 463-467.
35. Legendziewicz, J.; Guzik, M.; Szuszkiewicz, W. Charge Transfer and f–f Emission of Trivalent Ytterbium Observed in Double Phosphates $M^{I}M^{III}(PO_4)_2$ (M^{I}=Na, Rb; M^{III}=Lu, Y). *J. Alloys Compd.* **2008,** *451*, 165-171.
36. Godlewska, P.; Matraszek, A.; Macalik, L.; Hermanowicz, K.; Ptak, M.; Tomaszewski, P. E.; Hanuza, J.; Szczygieł, I. Spectroscopic and Structural Properties of $Na_3RE(PO_4)_2:Yb$ Orthophosphates Synthesised by Hydrothermal Method (RE=Y, Gd). *J. Alloys Compd.* **2015,** *628*, 199-207.
37. Malkin, B. Z.; Leushin, A. M.; Iskhakova, A. I.; Heber, J.; Altwein, M.; Moller, K.; Fazlizhanov, I. I.; Ulanov, V. A. EPR and Optical Spectra of Yb^{3+} in $CsCdBr_3$ Charge-Transfer

Effects on the Energy-Level Structure of Yb^{3+} in the Symmetrical Pair Centers. *Phys. Rev. B* **2000,** *62*, 7063-7070.
38. Demirbilek, R.; Heber, J.; Sergey, I. N. Charge Transfer and $4f^n$-$4f^{n-1}$ $5d$ Transitions of Trivalent Rare-Earth Ions in $CsCdBr_3$. *Proc.SPIE* **2002,** *4766*, 47-50.
39. Przybylińska, H.; Świątek, K.; Stąpor, A.; Suchocki, A.; Godlewski, M. Recombination Processes in Yb-Activated ZnS. *Phys. Rev. B* **1989,** *40*, 1748-1755.
40. Hansen, P.-A.; Kumar, S.; Meijerink, A. Strong Self-Sensitized Green and NIR Emission in $NaYS_2$ Doped with Pr^{3+} and Yb^{3+} by Inducing Laporte Allowed and Charge Transfer Transitions. *J. Lumin.* **2021,** *235*, 118012.
41. Tsujii, N.; Imanaka, Y.; Takamasu, T.; Kitazawa, H.; Kido, G. Photoluminescence of Yb^{3+}-Doped $CuInS_2$ Crystals in Magnetic Fields. *J. Appl. Phys.* **2001,** *89*, 2706-2710.
42. Creutz, S. E.; Fainblat, R.; Kim, Y.; De Siena, M. C.; Gamelin, D. R. A Selective Cation Exchange Strategy for the Synthesis of Colloidal Yb^{3+}-Doped Chalcogenide Nanocrystals with Strong Broadband Visible Absorption and Long-Lived Near-Infrared Emission. *J. Am. Chem. Soc.* **2017,** *139*, 11814-11824.
43. Wyart, J.-F.; Tchang-Brillet, W.-Ü. L.; Spector, N.; Palmeri, P.; Quinet, P.; Biémont, E. Extended Analysis of the Spectrum of Triply-Ionized Ytterbium (Yb IV) and Transition Probabilities. *Phys. Scr.* **2001,** *63*, 113.
44. Pressler, K.; Snoeren, T. J.; Walsh, K. M.; Gamelin, D. R. Magnetic Amplification at Yb^{3+} "Designer Defects" in the van der Waals Ferromagnet CrI_3. *Nano Lett.* **2023,** *23*, 1320-1326.
45. Li, L.; Zhou, S.; Zhang, S. Relationship Between Charge Transfer Energies of Yb^{3+} and Sm^{3+} and Crystal Environmental Factor. *J. Lumin.* **2009,** *129*, 187-191.
46. Ryan, J. L.; Jørgensen, C. K. Absorption Spectra of Octahedral Lanthanide Hexahalides. *J. Phys. Chem.* **1966,** *70*, 2845-2857.
47. Ryan, J. L. Weak or Unstable Iodo Complexes. I. Hexaiodo Complexes of the Lanthanides. *Inorg. Chem.* **1969,** *8*, 2053-2058.

Appendix F: Chapter Acknowledgements

Chapter 2: Ferromagnetism and Spin-Polarized Luminescence in Lead-Free $CsEuCl_3$ Perovskite Nanocrystals and Thin Films

Support for this research from the US NSF (DMR-1807394) is gratefully acknowledged. K.M.W. thanks UW's Clean Energy Institute for graduate fellowship support. We thank Christian Erickson for assistance with the magneto-optical measurements and Kyle Kluherz for collecting the TEM images. PLE measurements and some PL measurements were performed using the shared user facilities of UW's Molecular Engineering Materials Center, an NSF MRSEC (DMR-1719797). Part of this work was conducted at the Molecular Analysis Facility, a National Nanotechnology Coordinated Infrastructure (NNCI)site at the University of Washington that is supported in part by the National Science Foundation (NNCI-1542101 andNNCI-2025489), the University of Washington, the Molecular Engineering & Sciences Institute, the Clean Energy Institute, and the National Institutes of Health. The authors thank the Research Corporation for Science Advancement (RCSA) for supporting this research via a 2021 Cottrell Fellowships Award (award #27993) to D.R.G. in support of M.J.C.

Chapter 3.2: An Air-Stable and Exfoliable Ferromagnetic Two-Dimensional Perovskite, $(Phenehtylammonium)_2CrCl_4$

This work was primarily supported by the U.S. National Science Foundation through the University of Washington Molecular Engineering Materials Center (MEM-C), a Materials Research Science and Engineering Center (DMR-2308979 to D.R.G. and J.-H.C.). Early stages of this work were performed with the support of NSF DMR-1807394 (to D.R.G.). Additional support from a Clean Energy Institute fellowship and support from an NSF Graduate Research Fellowship (1000356387) to R.T.S. are gratefully acknowledged. Single-crystal XRD measurements were collected using the UW Chemistry X-ray Diffraction Facility with the support of Dr. Werner Kaminsky and Sebastian Krajewski. Exfoliation and AFM experiments were performed using the University of Washington MEM-C Shared Facilities with the assistance of Dr. Xi Wang.

Chapter 3.3: Anion Exchange and Lateral Heterostructure Formation in Ferromagnetic PEA_2CrCl_4 Two-Dimensional Perovskites

This work was supported by the U.S. National Science Foundation, Division of Materials Research (solid state and materials chemistry), through award DMR-2404703. Part of this work was conducted at the Molecular Analysis Facility, a National Nanotechnology Coordinated Infrastructure (NNCI) at the University of Washington with partial support from the National Science Foundation via awards NNCI-2025489 and NNCI-15422101. AFM experiments were performed using the University of Washington MEM-C Shared Facilities. R.T.S. gratefully

acknowledges support from an NSF Graduate Research
Fellowship (1000356387). The authors thank Kimo Pressler for thoughtful discussions on the topic of diffusion kinetics.

Chapter 4.2 Magnetic Amplification at Yb^{3+} "Designer Defects" in the van der Waals Ferromagnet CrI_3

Support of this project by the US NSF (DMR-1807394) is gratefully acknowledged. Initial stages of this work were performed as part of Programmable Quantum Materials, an Energy Frontier Research Center funded by the U.S. Department of Energy (DOE), Office of Science, Basic Energy Sciences (BES), under award DESC0019443. Additional support was received from the UW Clean Energy Institute(graduate fellowships to T.J.S. and K.M.W.). Part of this work was conducted at the Molecular Analysis Facility, a National Nanotechnology Coordinated Infrastructure (NNCI) site at the University of Washington that is supported in part by the National Science Foundation (NNCI-1542101 and NNCI-2025489), the University of Washington, the Molecular Engineering & Sciences Institute, the Clean Energy Institute, and the National Institutes of Health. The authors thank Dr. Werner Kaminsky and Paige M. Gannon for single-crystal XRD measurements, Dr. Xi Wang for assistance with optical microscope measurements, Prof. Jiun-Haw Chu and Dr. Zhaoyu Liu for VSM measurements, and Prof. Robert Glaum, Maximilian Jähnig, and Julia Spitz for provision of and assistance with the BonnMag code.

Chapter 4.3 Luminescence and Covalency in Ytterbium-Doped CrX_3 (X = Cl, Br, I) van der Waals Compounds

Support of this project by the US NSF (DMR-1807394) is gratefully acknowledged. Additional support was received from the UW Clean Energy Institute (graduate fellowships to T.J.S. and K.M.W.). Part of this work was conducted at the Molecular Analysis Facility, a National Nanotechnology Coordinated Infrastructure (NNCI) site at the University of Washington that is supported in part by the National Science Foundation (NNCI-1542101 and NNCI-2025489), the University of Washington, the Molecular Engineering &Sciences Institute, the Clean Energy Institute, and the National Institutes of Health. EXAFS measurements were supported by the UW Molecular Engineering Materials Center, an NSF Materials Research Science and Engineering Center (grant no.DMR-1719797). This research used resources of the Advanced Photon Source, a U.S. Department of Energy (DOE) Office ofScience User Facility operated for the DOE Office of Science by Argonne National Laboratory under Contract no. DE-AC02-06CH11357. We acknowledge S. Heald and S. Kelly from APS Sector 20 (BL 20-BM) (GUP 77348) for collecting these data sets and assistance with data processing. We also thank S. Mergelsberg and S. Saslow for their assistance with EXAFS theory and analysis.